Structures, Statistics and Mechanisms of Low Froude Number Free-Surface Turbulence — A Simulation-Based Study

by

Lian Shen

S.B. in Mechanics and Mechanical Engineering,
University of Science and Technology of China, 1993

Submitted to the Department of Ocean Engineering in partial fulfillment of the requirements for the degree of

Doctor of Science

at the

Massachusetts Institute of Technology

February 2001

Author .....
Department of Ocean Engineering
September 29, 2000

Certified by....
.....
Dick K. P. Yue
Professor of Hydrodynamics and Ocean Engineering
Thesis Supervisor

Accepted by.....
.....
Nicholas M. Patrikalakis
Kawasaki Professor of Engineering
Chairman, Departmental Committee on Graduate Students

Structures, Statistics and Mechanisms of Low Froude Number Free-Surface Turbulence — A Simulation-Based Study

by

Lian Shen

Submitted to the Department of Ocean Engineering
on September 29, 2000, in partial fulfillment of the
requirements for the degree of
Doctor of Science

Abstract

The physics of free-surface turbulence (FST) is essential to many applications such as air-sea interactions, ship hydrodynamics, and industrial processes involving multi-phase flows. In order to obtain a comprehensive understanding of free-surface turbulent flows and to establish the physical basis for the turbulence modeling, we perform a simulation-based study for a turbulent shear flow beneath a free surface at low Froude numbers. The Navier-Stokes equations subject to viscous free-surface boundary conditions are solved numerically using a finite-difference scheme. From an ensemble of such simulations, we obtain substantial understanding of low Froude number FST in terms of surface-layer structure, coherent turbulent vortices, near-surface transport processes, and subgrid-scale modeling.

To elucidate the fundamental dynamics of FST, we identify conceptually and numerically a multi-layer structure adjacent to the surface. The surface inner layer is caused by the tangential free-surface dynamic boundary conditions, and the surface outer layer is due to the kinematic boundary condition. Examination of the effects of these layers on the turbulence statistics of length scales, Reynolds-stress balance, and enstrophy dynamics shows clearly the different turbulence mechanisms operating in the respective near-surface scales.

In order to quantify the surface layers and to establish the physical foundation for FST parameterization, we develop a similarity theory for the momentum diffusion process. The theoretical predictions on the shape and time-scaling behavior of the mean flow, as well as the scaling relations for the thickness of surface layers, are confirmed by numerical results. The similarity theory is then extended for the case of passive scalar and also compares well with our direct simulations of scalar mixing.

In order to illustrate the underlying mechanism for the persistent surface signatures and to identify key transport processes in FST, we study FST coherent vortical structures in detail. The mechanisms for the connection of hairpin vortices to the free surface and the evolution of surface-connected vortices are shown. We also characterize and quantify the contributions of coherent vortical structures to the scalar transport process. It is found that hairpin vortices play a significant role in convecting passive scalars from the bulk flow to the

free surface, while surface-connected vortices transport scalars away from the surface.

Finally we apply the physical insights gained from direct numerical simulations (DNS) to the improved subgrid-scale (SGS) modeling for large-eddy simulation (LES) of free-surface turbulent flows. Based on the unique surface-layer structure and the energy backscattering associated with coherent vortical structures, we develop two novel SGS models for FST, a dynamic free-surface function model (DFFM), and a dynamic anisotropic selective model (DASM). We also model for the first time the surface SGS flux and the dynamic SGS pressure. Our physics-based SGS models are shown to substantially improve the predictions of free-surface turbulent flows over existing models.

Thesis Supervisor: Dick K. P. Yue

Title: Professor of Hydrodynamics and Ocean Engineering

Acknowledgments

I would like to express my sincerest gratitude and appreciation to my advisor, Professor Dick Yue. My education at MIT actually started five months before I came to the United States, with his transpacific phone calls when he first saw my application to graduate school. Ever since then, I have benefited tremendously from his guidance, support, stimulation, and his unending enthusiasm. I am forever grateful to him for the mentor role he played in my transition from a "pupil" into a "fluid mechanician" (in his words).

I have been blessed by the opportunity to work closely with Professor George Triantafyllou at Levich Institute and National Technical University of Athens over the past four years. I will never forget his insightful email discussion, sometimes on daily basis, his expert help with my first conference presentation, and his extension of the visit to the US just to comply with my "D-Day" schedule.

Professor Michael Triantafyllou is highly appreciated for serving as my thesis committee member, for acting as the co-supervisor while Professor Yue was on sabbatical, and for offering profound comments and questions on group meetings. Whenever I walk into his office, I can always obtain kind help with both my academic and personal life.

My sincere appreciation is also expressed to the Department of Ocean Engineering for the excellent academic and research environment it provides, and to Martin A. Abkowitz International Fellowship Fund for the award. I especially want to thank OE Student Administrator, Jean Sucharewicz, for all her kind help with my graduate-student life.

I have been fortunate to work in the MIT Vortical Flow Research Laboratory, where unreserved support is given by all its members. In particular, I owe my gratitude to Lenny, Mel, Kelli and Matt for their help. This turbulent-flow research would never have been possible without their patience and help with the "turbulence" I brought to their laboratory management work, which includes the numerous terminals/computers I broke throughout these years and the tons of CFD data I generated. Of special note, I want to thank Kelli for her help with parallel computing, which increased the size of my CFD data from O(gigabyte) to O(terabyte).

My thanks also go to all my dear friends, who made my life at MIT a truly pleasant experience. In particular, I want to thank my fellow officers on the Ashdown House Social Committee, with whom I had a colorful life; the gang in our exclusive "dining club," through

which I polished my taste for gourmet food and started to sincerely believe I deserve another degree; and all the board members during my term as the president of MIT Chinese Student and Scholar Association, with whose help I had an opportunity to make contributions to MIT community.

Finally, my most special thanks go to my family. My deepest gratitude to my parents for their unbounded love and support. I am indebted to my sister and her family for taking good care of my parents while I am thousands of miles from home. Finally, my sincere appreciation to Haiyan for her support and help with both my daily life and my academic activities, the latter including her brilliant idea of showing the clip of a popular Hollywood movie at the beginning of my thesis defense to motivate the free-surface turbulence research!

Contents

List of Figures

List of Tables

Chapter 1

Introduction

1.1 Motivation

The study of turbulent flows in the vicinity of a free surface is a great scientific challenge. Turbulence itself is the one of the most difficult problems in physical science. Sir Horace Lamb once said (cf. Goldstein 1969):

> *When I die and go to heaven there are two matters on which I hope for enlightenment. One is quantum electrodynamics, and the other is the turbulent motion of fluids. And about the former I am rather optimistic.*

In excess of the usual complexity of turbulence, the presence of a free surface adds additional difficulties to the study of free-surface turbulence (FST) including, to name a few, the respective anisotropic kinematic and anisotropic dynamic constraints of the surface on the velocity and vorticity fields, respectively, the complex geometry of the deformable free surface, the nonlinear interaction between turbulence and surface waves, the generation and consequence of secondary surface vorticity, as well as surfactant dynamics.

In addition to its profound implication for basic scientific research, the study of free-surface turbulence is also essential to the following important applications:

(1) Air–sea interaction and global climate change

The FST research is critical to our understanding of the ocean's role in the global climate change. The oceans have an enormous capacity to absorb heat and gases. The rate at which heat and mass are transferred across the ocean surface greatly affects the weather as well as the long term status of the environment. The accurate estimation of this transfer rate relies on our better understanding of the mechanisms of the turbulent flows near the ocean surface. The development of climatological models requires a thorough study of the various parameters and phenomena which mediate the heat and mass transport across the air–water interface. Therefore, the study of the mechanism and dynamics of free-surface turbulent flows will facilitate and expedite our understanding of the processes affecting the climate.

(2) Marine environment and pollution control

Pollutants enter the oceans worldwide from runoff in rivers and streams as well as from oil spills. Oil spills occur both accidentally (for example, from crashed tankers) or routinely (for example, in the NY-NJ harbor). These hazardous materials directly affect the marine environment and its resources for human on earth in terms of commerce, health, and security, and the evolution of these pollutants is largely determined by the turbulent motions at the upper ocean.

(3) Remote sensing of ship wakes

Recently, the turbulent wakes behind ships have attracted special interest, largely due to the need to interpret the radar observations of ship wakes (cf. Munk, Scully-Power & Zachariasen 1987, and Sarpkaya 1996). Synthetic Aperture Radar images reveal the existence of a narrow V-like wake with a half angle typically between 2° and 3°, which is the most prominent feature in remote sensing and is found to extend some 20km behind a surface ship. This observation does not belong to the Kelvin wake pattern and is believed to be related to short-wave-damping phenomena involving free-surface turbulent flows, surface-active materials, and the redistribution of surface impurities by currents and bubbles. Our ability to interpret the observed narrow V-shaped ship wakes highly depends on the understanding of the relevant fluid mechanics of the turbulent flow in the wake and its interactions with the

free surface.

(4) Ship hydrodynamics and other industrial processes

The study of free-surface turbulence is also of practical importance to many engineering problems. For example, understanding the interaction between the ocean surface currents and ship hulls leads to more efficient maneuverability of maritime vehicles. In industry, the design of contacting equipment such as condensers, evaporators, pipelines, and chemical reactors relies on knowledge of the dynamics of free-surface turbulent flows. Furthermore, the mechanism of free-surface turbulence is essential to the safety analysis of water cooled nuclear reactors during accidents.

1.2 Background

In general, turbulent flows are affected by a free surface by means of two mechanisms, which differ fundamentally from their counterpart, turbulence near a rigid wall. First, in the absence of wind, the tangential stresses at the free surface should be zero, while near a rigid wall, velocity gradient is large, which makes turbulence production and dissipation significant there. Second, the free surface restricts motion in the normal direction only, while a no-slip condition at a rigid wall makes velocity components in all directions vanish.

Much of the work on turbulence in the past has been directed towards wall turbulence. Hunt & Graham (1978) analyzed an interesting variation of the problem of turbulence interaction with a rigid wall, which somewhat resembles a stress-free boundary. They introduced a semi-infinite rigid wall which moves with the same speed as the mean velocity of grid turbulence. Near the wall, they identified two distinct boundary layers: an inner viscous layer and an outer source layer. Their theoretical predictions on the spectra variances and cross-correlations were found to compare well with measurements of turbulence near moving walls by Uzkan & Reynolds (1967) and Thomas & Hancock (1977), and were later further confirmed by the Brumley & Jirka's (1987) measurements of near-surface turbulence in a grid-stirred tank to a large extent.

Although the problem of Hunt & Graham (1978) is strictly not FST, it identifies some

of the features characteristic of free-surface turbulence, and has inspired a number of other investigations in this area. Most of these investigations use the 'rigid lid' or 'free slip' approximation for the free surface, i.e. a flat surface with zero stresses but also zero normal velocity. This corresponds to the problem of free-surface turbulence in the limit of zero Froude number.

Perot & Moin (1995) used a novel idea to study the influence of a rigid wall on turbulence by considering separately two fictitious problems with 'simpler' boundary conditions. The first is a boundary which enforces no-slip but is otherwise permeable. This isolates and elucidates the viscous effects of a rigid wall. The second one they considered is in fact a flat free-slip boundary. This they used to isolate and investigate the kinematic effects that occur near the boundary. They found that it is the imbalance between splats and antisplats that leads to inter-component energy transfer near the surface. This imbalance is controlled by viscous processes and is found to be small for grid FST where there is no mean shear in the bulk flow underneath.

While Perot & Moin (1995) focused on the immediate effect of the presence of a free-slip boundary, Walker, Leighton & Garza-Rios (1996) studied a similar grid FST case but considered the late time development after the imposition of the boundary. They identified two boundary layers where velocity and vorticity respectively are anisotropic and the thicknesses of these two layers are respectively the turbulence length scale and one-tenth of the turbulence length scale. Their analysis of the Reynolds-stress balance and enstrophy budget shows that the flow is fully three-dimensional up to the free surface.

Besides grid FST, another type studied in the past is that of open-channel flow. Experimental measurements were obtained by Komori *et al.* (1982), Komori, Murakami & Ueda (1989a, 1989b), Nakagawa & Nezu (1981), Rashidi & Banerjee (1988, 1990a, 1990b), Rashidi (1997), Ueda *et al.* (1977), among many others. In these experiments, the relation between bursting events at the channel bottom and the surface-renewal eddies at the free surface have been investigated exclusively. Early numerical work on open-channel turbulent flows can be traced back to Handler *et al.* (1991), Lam & Banerjee (1988, 1992) Leighton *et al.* (1991), and Swean *et al.* (1991), who all studied the turbulent flow between a no-slip wall

and a free-slip plate. Leighton *et al.* (1991) investigated the interaction of vorticity with the free surface and proposed two models — the 'spin' model and the 'splat' model, which follow a description by Bradshaw & Koh (1981). Handler *et al.* (1993) studied the Reynolds-stress balance and reported that the dissipation rate exhibits a sharp drop near the surface. Handler *et al.* (1993) also examined the variation of length scales and proposed a 'pancake' model to explain the increase of horizontal length scales and the decrease of vertical scales.

Vortex structures in open-channel flow have been studied numerically by Pan & Banerjee (1995) and experimentally by Kumar, Gupta & Banerjee (1998). They both identified large-scale persistent structures at the free surface, which include 'upwelling', 'downdrafts', and 'attached vortices'. It is found that the attached vortices are particularly long-lived and tend to interact with each other unless destroyed by other upwellings. Both Pan & Banerjee (1995) and Kumar *et al.* (1998) concluded that turbulence structures near the free surface are quasi-two-dimensional.

Based on the understanding of the fluid motions in free-surface turbulence, the transfer of heat and gases across the air–water interface has been investigated by a number of researchers. Among others, Brown, Khoo & Sonin (1990), Khoo & Sonin (1992), Komori *et al.* (1982), Rashidi, Hetsroni & Banerjee (1991), Sonin, Shimko & Chun (1986), and Ueda *et al.* (1977) performed experimental measurements and obtained empirical expressions for the scalar transfer coefficient. Recently, based on the detailed three-dimensional datasets obtained from direct numerical simulations, Nagaosa (1999) and Nagaosa & Saito (1997) showed that the surface renewal events are often associated with streamwise vortex dipoles, while Handler *et al.* (1999) proposed a model based on the hypothesis that hairpin vortex structures dominate the surface renewal processes.

We note that the approximation of the free surface by a flat slip-free plate (zero Froude number limit) facilitates the numerical simulation and has been used extensively in the past (Handler *et al.* 1991, 1993 and 1999, Lam & Banerjee 1988 and 1992, Leighton *et al.* 1991, Pan & Banerjee 1995, Perot & Moin 1995, Swean *et al.* 1991, and Walker *et al.* 1996, among others). A systematic justification of this approximation, as well as an accurate quantification of the effect of finite Froude numbers on the evolution of free-surface surface, however, have

never been provided in the literature. Komori *et al.* (1993) used a non-zero Froude number which is however so small that there are no non-trivial differences from the zero Froude number case. Borue, Orszag & Staroselsky (1995) studied the interaction of surface waves with turbulence in an open channel and found that the effect of non-zero Froude number on the turbulence statistics they examined is weak.

As a general feature of the different types of FST flows studied in the literature above, it is now understood that the evolution of FST is governed by two key effects of the free surface, namely the kinematic restriction of not allowing complete freedom for motions along the vertical direction, and the dynamics requirement that the tangential stresses vanish at the free surface. Near the free surface, turbulence intensity in the horizontal plane is increased at the expense of that in the vertical direction. Furthermore, very near the free surface, vortex filaments attach to the free surface almost perpendicularly, with considerable dissipation of enstrophy. The first effect is attributed primarily to the kinematic boundary condition at the free surface which reduces the vertical velocity fluctuations. The second effect is attributed to the dynamic zero-stress condition. Both properties can be characterized as 'generic' of FST in the sense that they have been observed in all different types of FST flows. One can therefore loosely talk of a 'free-surface boundary layer' as a region of the flow with properties dominated by the effect of the free surface. The elucidation and precise quantification of this surface boundary layer, the characterization of the statistical, structural and dynamical features of the flow field in the boundary layer, as well as the modeling of the key transport processes across the boundary layer, are thus the key to the understanding and parameterization of free-surface turbulent flows, and are the foci of this study.

1.3 Thesis overview

In the present study we investigate the structures, mechanisms and statistical characteristics of free-surface turbulence at low Froude numbers. The main objectives of this research are to:

- develop numerical capabilities of direct numerical simulation (DNS) and large-eddy

simulation (LES) for turbulent flows in the vicinity of a free surface at low Froude numbers;

- improve our understanding of the structure, mechanism and dynamics of free-surface turbulent flows;
- identify and characterize the key transport processes within the free-surface boundary layer;
- establish the physical basis for modeling free-surface turbulent flows; develop, calibrate and validate specific turbulence subgrid-scale models for FST; and finally pave the path for the parameterizations of air–water interaction.

To achieve the above goals, we investigate the interaction between a turbulent flow and a free surface at low Froude numbers in the absence of surface tension effects and winds. As a conical problem, we consider the development of a three-dimensional flow with a two-dimensional mean shear under a free surface. The instability of this flow has been studied by Triantafyllou & Dimas (1989), Longuet-Higgins (1998) and Engevik (2000), and a detailed study on the nonlinear evolution of the instability was reported by Dimas & Triantafyllou (1994). In this free-surface shear flow, turbulence is generated and maintained by the mean shear in the bulk flow and interacts with the free surface.

Our basic research tools are direct numerical simulation (DNS) and large-eddy simulation (LES). With the rapid growth in both the size and speed of modern computers, numerical simulation has become an indispensable tool in turbulence research (cf. the reviews by Moin & Mahesh 1998 and Moin & Kim 97). Once robust numerical capability is established, substantial information on the statistical, structural and dynamical properties of the flow field can be obtained, based on which the key turbulence processes can be characterized, quantified and modeled.

Next we provide an overview of the thesis.

In Chapter 2 we present the numerical tools used in this study, direct numerical simulation (DNS) and large-eddy simulation (LES). For DNS, we first introduce the governing Navier–Stokes equations subject to the free-surface kinematic and dynamics boundary conditions.

The governing equations are then solved numerically using a finite-difference scheme. The numerical method is validated in different aspects. Next we introduce the LES approach for free surface turbulent flows, in which only the large-scale motions are computed directly while the contributions from small scales (subgrid scales, SGS) are modeled. Of special note, we demonstrate the SGS contributions to the free-surface flux and free-surface dynamics pressure, which are unique to the free-surface problem and must be modeled.

Chapter 3 investigates the surface layers in free-surface turbulent flows. We identify conceptually and numerically a multi-layer structure of the free-surface boundary layer. The surface inner layer is a thin region adjacent to the free surface characterized by fast variations of the horizontal vorticity components. This inner layer is caused by the dynamic zero-stress boundary conditions at the free surface and lies inside a much thicker outer layer, which is due to the kinematic boundary condition at the free surface. The importance of the outer layer is manifested mainly in the redistribution of the turbulence intensity, i.e. in the increase of the horizontal velocity fluctuations at the expense of the vertical velocity fluctuation. A prominent feature of FST is vortex connections to the free surface which occur inside the inner layer. It is found that as hairpin-shaped vortex structures approach the free surface, their 'head' part is dissipated quickly in the inner layer, while the two 'legs' connect almost perpendicularly to the free surface. Analysis of the evolution of surface-normal vorticity based on vortex surface-inclination angle shows that both dissipation and stretching decrease dramatically after connection. As a result, vortex structures connected to the free surface are persistent and decay slowly relative to non-connected vorticities. The effects of inner and outer layers on the turbulence statistics of length scales, Reynolds-stress balance, and enstrophy dynamics are examined, which show clearly the different turbulence mechanisms operating in the respective near-surface scales. Finally we investigate the effect of non-zero Froude number on the turbulence statistics. We show that the most significant effect of the presence of the free surface is a considerable reduction of the pressure–strain correlation at this surface, compared to that at a free-slip flat plate. This reduction is finite even for very low values of the Froude number.

Chapter 4 studies numerically and analytically the turbulent diffusion characteristics near a free surface. From an ensemble of such direct numerical simulations, we find that a boundary layer develops at the free surface characterized by a fast reduction in the value of the eddy viscosity. As the free surface is approached, the magnitude of the mean shear initially increases over the boundary (outer) layer, reaches a maximum and then drops to zero inside a much thinner inner layer. To understand and model this behavior, we derive an analytical similarity solution for the mean flow. This solution predicts well the shape and the time-scaling behavior of the mean flow obtained in the direct simulations. The theoretical solution is then used to derive scaling relations for the thickness of the inner and outer layers.

In Chapter 5 we study numerically and analytically the mixing of a passive scalar in turbulent flows with a free surface where the scalar flux vanishes. The Navier–Stokes equations and scalar mixing equation are solved by direct numerical simulations. Initially the scalar concentration profile is prescribed by a smooth function without fluctuation. We find that a boundary layer develops at the free surface characterized by a fast reduction in the value of the turbulent diffusivity of the scalar. As the free surface is approached, for large Schmidt numbers, the magnitude of the mean concentration gradient initially increases over the boundary outer layer, reaches a maximum and then drops to zero inside a much thinner inner layer; for small Schmidt numbers, the mean concentration gradient does not have a local maximum and its value drops to zero directly. To understand and quantify this multi-layer mixing structure and its dependence on the Schmidt number, we derive an analytical solution of a self-similar form for the scalar mean concentration. The thickness of the outer layer is directly proportional to the thickness of the corresponding momentum boundary layer; while the thickness of the inner layer present in high Schmidt number cases is found to be inversely proportional to the square root of the Schmidt number. The maximum value of the concentration gradient is located at the end of the inner layer and is proportional to the square root of the Schmidt number.

In addition to the passive scalar of which the flux rate vanishes at the free surface, Chapter 6 further investigates the transport of passive scalars with two other free-surface boundary conditions. The first is a fixed scalar surface-value case, which models the gas transfer

across the air-water interface; while the second is a fixed scalar surface-flux case, which models the heat transport problem. The effects of surface layers on scalar transport process are elucidated through turbulence statistics. We then investigate the dependence of scalar structure on coherent turbulent motions. With a novel conditional-averaging technique, we are able to identify and quantify the contributions of difference types of coherent turbulent structures to the scalar transport process. It is found that splats convects scalars to the surface from the bulk flow below, while antisplats, to a lesser degree, carry scalars away from the surface. Hairpin vortices play a significant role in the transport of scalars towards the surface, while surface-connected vortices draw scalars down to the bulk flow below.

In Chapter 7 we study the inter-scale energy transfer in free-surface turbulence, in order to obtain the physical understanding necessary for the effective subgrid-scale modeling of free-surface turbulence. The flow field is solved by direct numerical simulation of the Navier–Stokes equations at fine grid. The grid-scale motions are defined by Gaussian filters in the horizontal directions and a discrete filter in the vertical direction. It is found that the amount of energy transferred from the grid scales to the subgrid scales reduces significantly as the free surface is approached. This is a result of energy backscatter associated with the fluid vertical motions. Conditional averaging reveals that the energy backscatter occurs at the splat regions of coherent hairpin vortex structures as they connect to the free surface. The free-surface region is highly anisotropic at all length scales while the energy backscatter is carried out by the horizontal components of the SGS stress only. The physical insights obtained here are essential to the efficacious SGS modeling of LES for free-surface turbulence.

Based on the physical insights obtained from preceeding chapters, we study in Chapter 8 the large-eddy simulation for free-surface turbulence. The SGS contribution to the Dirichlet pressure free-surface boundary condition is modeled with a dynamic form of the Yoshizawa (1986) expression; while the SGS flux that appears in the kinematic boundary condition is modeled by a dynamic scale-similarity model. For the SGS stress, we first examine the existing dynamic Smagorinsky model (DSM), which is found to capture the free-surface turbulence structure only roughly. Based on the special physics of free-surface turbulence, we propose two new SGS models — a dynamic free-surface function model (DFFM) and a

dynamic anisotropic selective model (DASM). The DFFM correctly represents the reduction of the Smagorinsky coefficient near the surface and is found to capture the free-surface boundary layer more accurately. The DASM takes into account both the anisotropic nature of free-surface turbulence and the dependence of energy backscatter on specific coherent vorticity mechanisms, and is found to produce substantially better surface signature statistics. Finally, we show that the combination of the new DFFM and DASM with a dynamic scale-similarity model further improves the results.

Finally, Chapter 9 presents a summary of the main results and contributions of this study. We also discuss future studies there.

Chapter 2

Numerical Simulation of Free-Surface Turbulence

With the advent of the modern computer, numerical simulation has become an indispensable tool in turbulence research. Once robust numerical capability is established, substantial information on the statistical, structural and dynamical properties of the flow field can be obtained, based on which key turbulence processes can be characterized, quantified and modeled. In this chapter we introduce two basic numerical approaches used in the present study, direct numerical simulation (DNS) and large-eddy simulation (LES). DNS applies to low to moderate Reynolds numbers ($R_e \sim O(10^{3-4})$). In DNS, all the turbulence scales are resolved through the Navier–Stokes equations. DNS has the advantage that no *ad hoc* turbulence model is used, and thus provides a description of the flow field with great fidelity. In LES, one only computes the spatial and temporal scales relevant to specific and detail boundary conditions of the problem, while the more universal subgrid-scale (SGS) quantities such as those in the inertial range are modeled. The LES approach can be used at high Reynolds number range ($R_e \sim O(10^{4-7})$).

This chapter is organized as follows. In §2.1 we introduce the DNS approach. We first formulate the governing equations as well as the boundary conditions for the problem of the interaction between a turbulent flow with a free surface at low Froude numbers. We then describe the numerical scheme and computational details. After providing an overview of

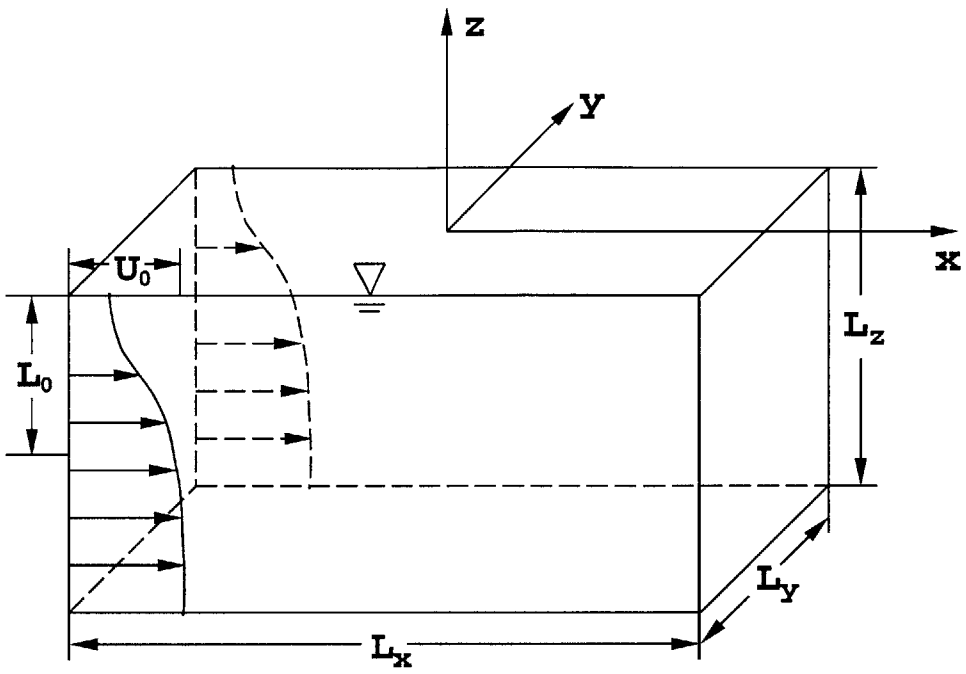

Figure 2-1: Schematic of a turbulent shear flow under a free surface

the flow field, we present validations for the current DNS approach. In §2.2 we present the LES method. We introduce the governing equations for the resolved motions. Of significant importance, we discuss the free-surface boundary conditions in LES, which contain SGS contributions which need to be modeled. Finally we provide numerical details of LES.

2.1 Direct numerical simulation

2.1.1 Mathematical formulation

We consider a turbulent flow with a free surface at low Froude numbers. Referring to Figure 2-1, the frame of reference has axes x, y, z (also denoted as x_1, x_2, x_3 when tensor notation is used), where x and y are horizontal, z is vertical, positive upward, with the $z = 0$ plane coinciding with the undisturbed free surface.

The governing equations for the velocity components u_i (also denoted as u, v, or w) are

the Navier–Stokes equations

$$\frac{\partial u_i}{\partial t} + \frac{\partial (u_i u_j)}{\partial x_j} = -\frac{\partial p}{\partial x_i} + \frac{1}{R_{e0}} \frac{\partial^2 u_i}{\partial x_j \partial x_j}, \quad i = 1, 2, 3, \tag{2.1}$$

and the continuity equation

$$\frac{\partial u_i}{\partial x_i} = 0 \, . \tag{2.2}$$

Here and hereafter, unless otherwise specified, all variables are normalized by the characteristic (macro) length scale L_0 and the characteristic velocity scale U_0 of the flow. The dynamic pressure p is normalized by ρU_0^2, with ρ the fluid density. $R_{e0} \equiv U_0 L_0 / \nu$ is the Reynolds number, with ν the kinematic viscosity.

We assume that the Froude number $F_{r0} \equiv U_0 / (g L_0)^{1/2}$ is small but not zero. Therefore, we use linearized free-surface boundary conditions at the position of undisturbed free surface $z = 0$.

(a) At the free surface, $z = 0$, the tangential stresses vanish:

$$\frac{1}{R_{e0}} \left(\frac{\partial u}{\partial z} + \frac{\partial w}{\partial x} \right) = 0 \qquad \text{on } z = 0 \, , \tag{2.3}$$

$$\frac{1}{R_{e0}} \left(\frac{\partial v}{\partial z} + \frac{\partial w}{\partial y} \right) = 0 \qquad \text{on } z = 0 \, . \tag{2.4}$$

(b) At the free surface, the normal stress vanishes which gives (neglecting surface tension)

$$p = \frac{h}{F_{r0}^2} + \frac{2}{R_{e0}} \frac{\partial w}{\partial z} \qquad \text{on } z = 0 \, , \tag{2.5}$$

where $h(x, y, t)$ is the free-surface elevation.

(c) Finally, the fact that the free surface moves as a material surface gives:

$$\frac{\partial h}{\partial t} = w - u \frac{\partial h}{\partial x} - v \frac{\partial h}{\partial y} \qquad \text{on } z = h \, . \tag{2.6}$$

By linearization we obtain the kinematic boundary condition at the undisturbed free

surface as

$$\frac{\partial h}{\partial t} = w - \frac{\partial}{\partial x}(uh) - \frac{\partial}{\partial y}(vh) \qquad \text{on } z = 0\ . \tag{2.7}$$

At the bottom $z = -D$, we impose free-slip conditions:

$$\frac{\partial u}{\partial z} = \frac{\partial v}{\partial z} = w = \frac{\partial p}{\partial z} = 0\ , \qquad \text{on } z = -D. \tag{2.8}$$

Thus there is no turbulence production at the bottom and turbulence energy is extracted solely from the mean shear in the bulk flow. Finally we impose periodic boundary conditions in both horizontal directions.

For later reference, we define the statistical average over the horizontal plane, where the turbulent flow is statistically homogeneous. For any variable $f(x, y, z, t)$, $\langle f \rangle(z, t)$ stands for the average over the horizontal plane; $f'(x, y, z, t) \equiv f - \langle f \rangle$ denotes the instantaneous fluctuation; and $f^{rms}(z, t) \equiv \langle f^2 \rangle^{1/2}$ its root-mean-square value. As will be defined in §2.2, in LES, $\overline{f}(x, y, z, t)$ denotes the resolved grid-scale portion of $f(x, y, z, t)$, while $f''(x, y, z, t) \equiv f - \overline{f}$ is the subgrid-scale portion.

2.1.2 Numerical scheme

The primitive-variable form of Navier–Stokes equations (2.1) and continuity equation (2.2) are solved numerically as an initial-boundary-value problem. The numerical method we use traces back to the marker and cell (MAC) method developed by Harlow & Welch (1965). We first use a projection method, which couples the continuity equation with the Navier–Stokes equations, to obtain a Poisson equation with a divergence correction for the pressure. The Poisson equation for the pressure is solved at each time-step. The simulation is then advanced explicitly to the next step. More specifically, knowing u_i^n, $i = 1, 2, 3$, at the current timestep, the time-discrete form of (2.1) is

$$\frac{u_i^{n+1} - u_i^n}{\Delta t} + \frac{\partial (u_i u_j)^n}{\partial x_j} = -\frac{\partial p^n}{\partial x_i} + \frac{1}{R_{e0}} \frac{\partial^2 u_i^n}{\partial x_j \partial x_j}\ . \tag{2.9}$$

Taking the divergence of (2.9) on both sides and invoking the continuity equation at the next step:

$$\frac{\partial u_i^{n+1}}{\partial x_i} = 0 \,, \tag{2.10}$$

we obtain the following Poisson equation for the pressure p^n:

$$\frac{\partial^2 p^n}{\partial x_i \partial x_i} = \frac{1}{\Delta t}\frac{\partial u_i^n}{\partial x_i} + \frac{\partial}{\partial x_i}\left(-\frac{\partial (u_i u_j)^n}{\partial x_j} + \frac{1}{R_{e0}}\frac{\partial^2 u_i^n}{\partial x_j \partial x_j}\right) \,. \tag{2.11}$$

This Poisson equation is solved subject to Dirichlet condition (2.5) at the free surface, Neumann condition (2.8) at the bottom, and periodic conditions in the horizontal directions. After the pressure p^n is obtained, velocity components are advanced explicitly in time using (2.9). In this study we use a second-order Runge–Kutta scheme for the time integration.

For space discretization, we use sixth-order finite-differences in the horizontal directions and second-order finite-difference in the vertical direction. To ensure mass conservation to machine accuracy, a staggered-grid system is employed in the vertical direction wherein u, v, and p are assigned at regular grid positions while w is assigned at the positions with a vertical shift of half a grid spacing. In addition, mass conservation also requires that the horizontal operator $\partial^2 p/\partial x^2$ (similar for $\partial^2 p/\partial y^2$) be approximated by

$$\begin{aligned}\left.\frac{\partial^2 p}{\partial x^2}\right|_i &= \frac{1}{3600\Delta x^2}(p_{i-6} - 18_{i-5} + 171p_{i-4} - 810p_{i-3} + 1935p_{i-2} + 828p_{i-1} - 4214p_i \\ &\quad +828p_{i+1} + 1935p_{i+2} - 810p_{i+3} + 171p_{i+4} - 18p_{i+5} + p_{i+6}) + O(\Delta x^6) \,, \end{aligned} \tag{2.12}$$

instead of the conventional form

$$\begin{aligned}\left.\frac{\partial^2 p}{\partial x^2}\right|_i &= \frac{1}{180\Delta x^2}(2p_{i-3} - 27p_{i-2} + 270p_{i-1} - 490p_i + 270p_{i+1} - 27p_{i+2} + 2p_{i+3}) \\ &\quad +O(\Delta x^6) \,. \end{aligned} \tag{2.13}$$

The argument is similar to Kwak *et al.* 's (1975) fourth-order case and will not be repeated here.

It should also be pointed out that the horizontal convection terms in the Navier–Stokes

equations need a special energy-conservative scheme to avoid nonlinear instability (e.g. Kwak *et al.* 1975). Take the term $\partial(uv)/\partial x$, for example:

$$\begin{aligned}\left.\frac{\partial(uv)}{\partial x}\right|_i &= \frac{3}{8\Delta x}(u_{i+1}v_{i+1} - u_{i-1}v_{i-1} + u_i(v_{i+1} - v_{i-1}) + v_i(u_{i+1} - u_{i-1})) \\ &\quad -\frac{3}{40\Delta x}(u_{i+2}v_{i+2} - u_{i-2}v_{i-2} + u_i(v_{i+2} - v_{i-2}) + v_i(u_{i+2} - u_{i-2})) \\ &\quad -\frac{1}{120\Delta x}(u_{i+3}v_{i+3} - u_{i-3}v_{i-3} + u_i(v_{i+3} - v_{i-3}) + v_i(u_{i+3} - u_{i-3})) \\ &\quad +O(\Delta x^6)\ . \end{aligned} \tag{2.14}$$

It can be shown that in the absence of viscous terms and time-differencing errors, this scheme conserves energy to machine accuracy. A similar proof to this can again be found in Kwak *et al.* (1975).

Among the free-surface boundary conditions (2.3)–(2.7), the tangential dynamic conditions (2.3) and (2.4) are used in computing z-derivatives in (2.1); the normal free-surface dynamic condition (2.5) is used in the boundary condition for (2.11); and the kinematic free-surface condition (2.7) is used to update the free-surface elevation h in time.

2.1.3 Computational parameters

In this study, we consider as a canonical problem a three-dimensional incompressible turbulent flow in the presence of a free surface. As shown in Figure 2-1, the turbulent flow has a mean velocity $\langle u\rangle(z,t)$ in the x-direction with the initial profile

$$\frac{\langle u\rangle(z,t=0)}{U_0} = 1 - 0.9988\,\mathrm{sech}^2(0.88137\frac{z}{L_0})\ , \tag{2.15}$$

which is half of the mean velocity profile measured in the wake of a NACA 0003 hydrofoil in unbounded fluid (Mattingly & Criminale 1972). Here and hereafter, the initial mean shear flow depth L_0 and velocity deficit U_0 are used to normalize all the variables. Note that (2.15) is Galilean transformed with U_0 as in the simulations.

The Orr–Sommerfeld stability analysis of the velocity profile (2.15) has been performed by Triantafyllou & Dimas (1989), Longuet-Higgins (1998) and Engevik (2000), and a detailed

study on the nonlinear evolution of the instability is reported by Dimas & Triantafyllou (1994). Unlike open-channel flow, the turbulence in this sheared FST is generated solely from the mean shear in the bulk flow and is especially relevant to applications in naval hydrodynamics, such as ship wakes, and geophysical flows.

In this study, the Reynolds number $R_{e0} = U_0 L_0/\nu$ is 700, 1000, 1400. The $R_{e0} = 1000$ case is used as the basic case to elucidate the free-surface boundary layer in Chapter 3. In Chapter 4, where the effects of molecular viscosity are investigated, all the three Reynolds numbers are considered. In Chapters 5–8, where the asymptotic behavior of the turbulent shear flow in large t and the inter-scale energy cascade are of interest, the largest Reynolds number $R_{e0} = 1400$ is used.

The present study focuses on low Froude numbers. In most cases, we use the Froude number $F_{r0} = U_0/(gL_0)^{1/2} = 0.7$ as the basic case. In Chapter 3, where the Froude number effects are examined, additional Froude number values of 0.35 and 0 are considered.

In Chapter 3, where the free-surface boundary layer is illustrated, we use a 'shallow' computational domain of the size L_x=10.472 $\times$ L_y=10.472 $\times$ L_z=4 with a 128^3 grid. In Chapters 4–8, where the late-stage evolution of the turbulent shear flow is investigated, we use a 'deep' domain of L_x=10.472 $\times$ L_y=10.472 $\times$ L_z=6 with a $128^2 \times 192$ grid. We note that the difference in the near-surface flow characteristics between these two domain sizes is negligible. The reason we employ the deep domain in Chapters 4–8 is that the evolution of the bulk shear flow is of interest there, and thus it is necessary to eliminate the effects of the bottom boundary on the bulk flow at large t. Note that the horizontal domain size 10.472 corresponds to the minimum wavenumber 0.6, which is close to the most unstable mode for the mean shear profile (2.15) (Triantafyllou & Dimas 1989). The simulation is carried out from $t = 0$ to 90, with timestep $\Delta t = 0.005$.

The initial turbulence field in our simulation is implemented by the superposition of divergence-free random velocity noise upon the mean flow (2.15). Initially this random velocity noise is made to vanish at the free surface and the surface elevation is zero. As time goes on, energy is extracted from the mean shear flow to turbulence as the turbulent flow develops. From this point of view, the initial perturbations serve only as 'seeds' for

the turbulence. This is in contrast with the cases of purely decaying turbulence, where the initial turbulence field needs to be constructed carefully, usually to match the experimental measurements.

To obtain convergent results for statistics, we perform repeated simulations using different seeds for the initial random field. Our experience shows that the variances become sufficiently small beyond about 20 simulations. Unless otherwise stated, all the results we present are ensemble averaged over (at least) 20 DNS realizations.

2.1.4 Overview of the flow field

In this subsection, we give an overview of the time evolution of the shear flow. We use the case of $R_{e0} = 1000$ and $F_{r0} = 0.7$ as an example. As pointed out earlier, turbulence is initially absent at the free surface and the surface is calm at $t = 0$. Supplied by the shear flow underneath, turbulence develops at the free surface as time evolves.

Figure 2-2 plots the time evolution of free-surface turbulence kinetic energy $q_0^2 \equiv (\langle u'^2 \rangle + \langle v'^2 \rangle + \langle w'^2 \rangle)|_{z=0}$, the fluctuation of free-surface elevation h'^{rms}, and their standard deviations. Initially, both the free-surface elevation and the turbulence intensity at the surface are zero. As free-surface turbulence develops, the flow reaches a quasi-steady state after about $t = 40$. At this quasi-steady state, the velocity fluctuation at the free surface q_0 is $O(0.1)$, which makes the Reynolds number based on turbulence intensity $R_{eq} \equiv q_0 L_0/\nu \simeq 100$ and the Froude number $F_{rq} \equiv q_0/(gL_0)^{1/2} \simeq 0.07$. The fluctuation of the surface elevation h'^{rms} is about 0.005. Figure 2-2 shows that the free-surface elevation h'^{rms} normalized by F_{r0}^2 is comparable to the free-surface turbulence kinetic energy $q_0^2/2$. This is indicative of the fact that some of the kinetic energy is transformed to potential energy in the surface fluctuations. Figure 2-2 also shows that at later time ($t > 75$), dissipation exceeds the supply from below and the free-surface turbulence decays.

We plot in Figure 2-3 the evolution of the mean shear flow profile $\langle u \rangle(z,t)$ and turbulence intensity profile $q^2(z,t) \equiv \langle u'^2 \rangle + \langle v'^2 \rangle + \langle w'^2 \rangle$. Owing to diffusion, the mean shear flattens as time increases. As expected, the diffusion due to turbulence transport is much larger than would be expected due to laminar diffusion. For a laminar shear flow with the same initial

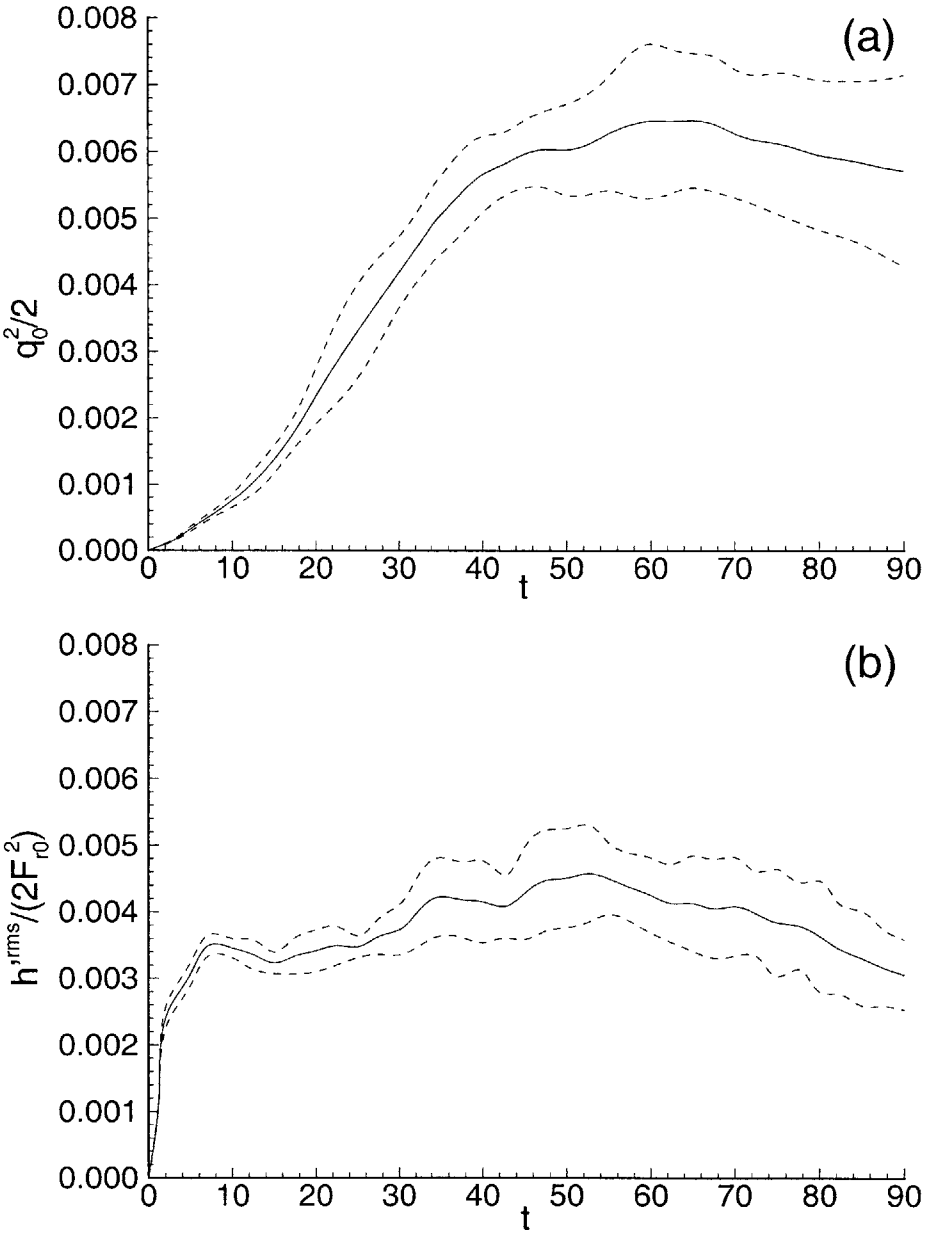

Figure 2-2: Evolution of (a) ———— , free-surface turbulence kinetic energy $q_0^2/2$; - - - - , $q_0^2/2 \pm \sigma$; and (b) ———— , fluctuation of free-surface elevation $h'^{rms}/(2F_{r0}^2)$; - - - - , $h'^{rms}/(2F_{r0}^2) \pm \sigma$. Here σ is the corresponding standard deviation.

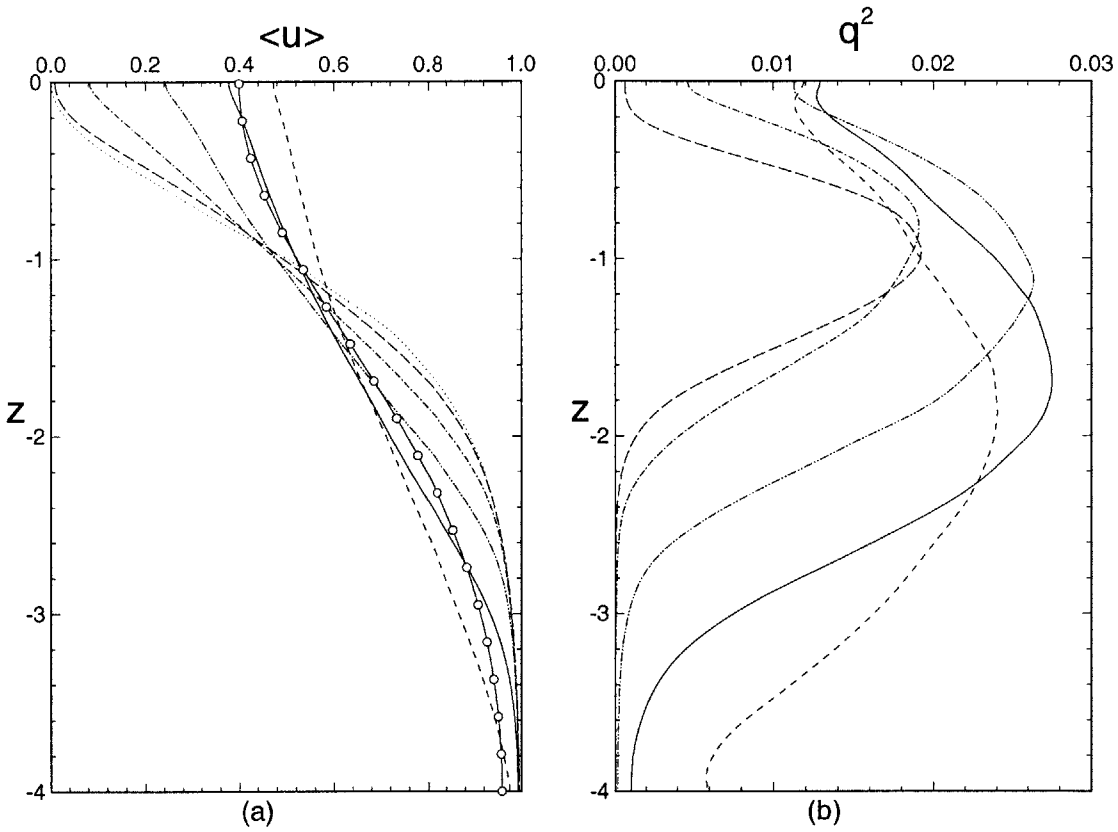

Figure 2-3: Evolution of (a) mean shear flow profile $\langle u \rangle(z,t)$; and (b) turbulence intensity profile $q^2(z,t)$. $\cdots\cdots$, $t=0$; —— ——, $t=5$; $-\cdot-\cdot-$, $t=20$; $-\cdots-\cdots-$, $t=40$; ————, $t=60$; $- - - -$, $t=80$. In (a), ——o—— is the mean flow profile for a laminar shear flow at $t=60$. The laminar flow has the same initial profile (2.15) but Reynolds number $R_{eL}=U_0L_0/\nu$=100.

profile (2.15), we find that an equivalent Reynolds number to obtain a similar evolution of the mean velocity deficit is given by $R_{eL} = U_0 L_0/\nu \approx 100$. This is shown in Figure 2-3(a) which plots the comparison between the mean flow profiles for turbulent flow ($R_{e0} = 1000$) and laminar flow ($R_{eL} = 100$) at $t = 60$.

In this study we focus on the quasi-steady state when the turbulence production from the mean shear is balanced by the turbulence dissipation at the near-surface region. Hereafter, only the results from $t = 40$ to 75 are presented.

2.1.5 Validation of numerical method

A rough estimate based on the theory of isotropic homogeneous turbulence (Tennekes & Lumley 1972) gives the (dimensionless) Kolmogorov scale:

$$\eta \sim \epsilon^{-1/4} R_{e0}^{-3/4} \simeq 0.04 \, . \tag{2.16}$$

Here ϵ is the (dimensionless) dissipation rate for turbulence kinetic energy and is found to be $O(0.0005)$ in our numerical results (Figures 3-15 to 3-17). The grid size in the horizontal directions is

$$\Delta_x = \Delta_y = \frac{10.472}{128} \simeq 0.08 \, ; \tag{2.17}$$

and the grid size in the vertical direction is:

$$\Delta_z = \frac{4}{128} = \frac{6}{196} \simeq 0.03 \, . \tag{2.18}$$

Thus the grid size is of the same order as the Kolmogorov scale.

To ensure that the dynamically significant scales are resolved, we also carry out a high-resolution simulation using a 256^3 grid, with a time step $\Delta t = 0.00125$, as well as a low resolution simulation using a 64^3 grid. Figure 2-4 compares the profiles of the mean flow velocity and the turbulence intensity for different resolutions. The convergence of the turbulence statistics, as the grid resolution increases, is clearly shown. The small difference between the 128^3 and 256^3 cases indicates that the 128^3 grid is sufficient for solving the

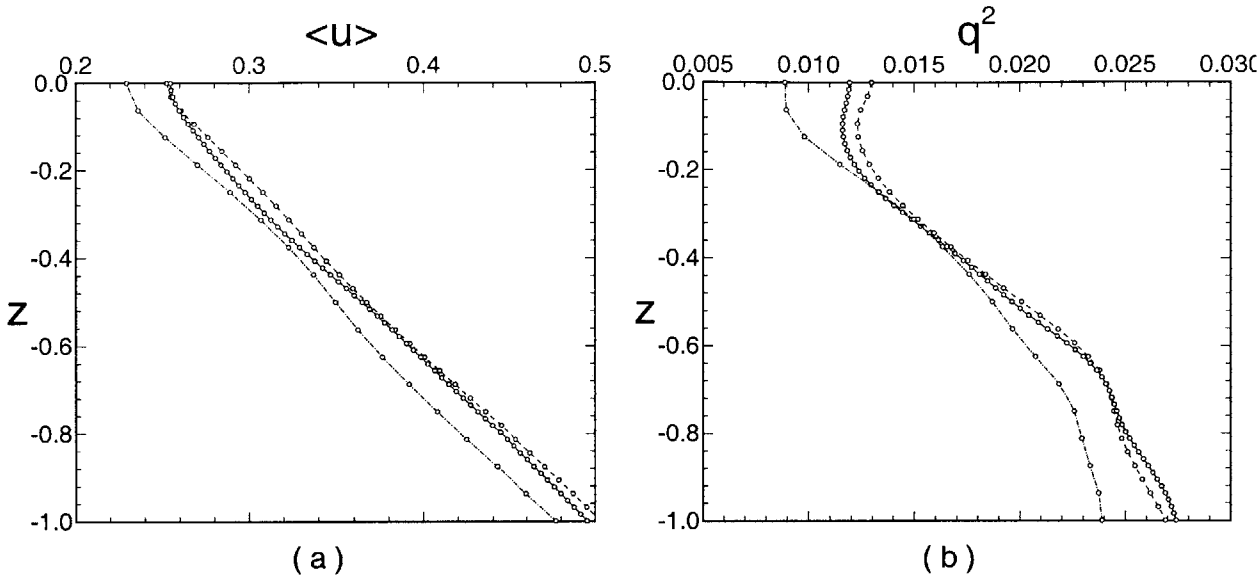

Figure 2-4: Comparison of (a) mean velocity $\langle u \rangle$ and (b) turbulence intensity q^2 at $t = 40$ for different DNS resolutions: $- \cdot - \cdot -$, 64^3 grid; $- - - -$, 128^3 grid; and ————, 256^3 grid.

problem.

As a further validation, we consider the problem of the interaction between a small-amplitude two-dimensional progressive wave and the mean shear flow (2.15) under a free surface. We compare the direct simulation evolution to that obtained from an Orr–Sommerfeld stability analysis of this problem (see Zhang 1996, which is a viscous extension of Triantafyllou & Dimas 1989). Figure 2-5(a) plots the growth rate of the surface wave amplitude as a function of wavenumber. Figure 2-5(b) compares the time-evolution of this amplitude predicted from DNS to the Orr–Sommerfeld analysis for wavenumber 0.6 (which corresponds to the minimum wavenumber for the present DNS horizontal domain size of 10.472). The agreement is quite satisfactory.

Finally, we report that in all our simulations, the total kinetic energy is conserved to less than $O(1)\%$ error and the maximum mass divergence at any grid point is $O(10^{-14})$.

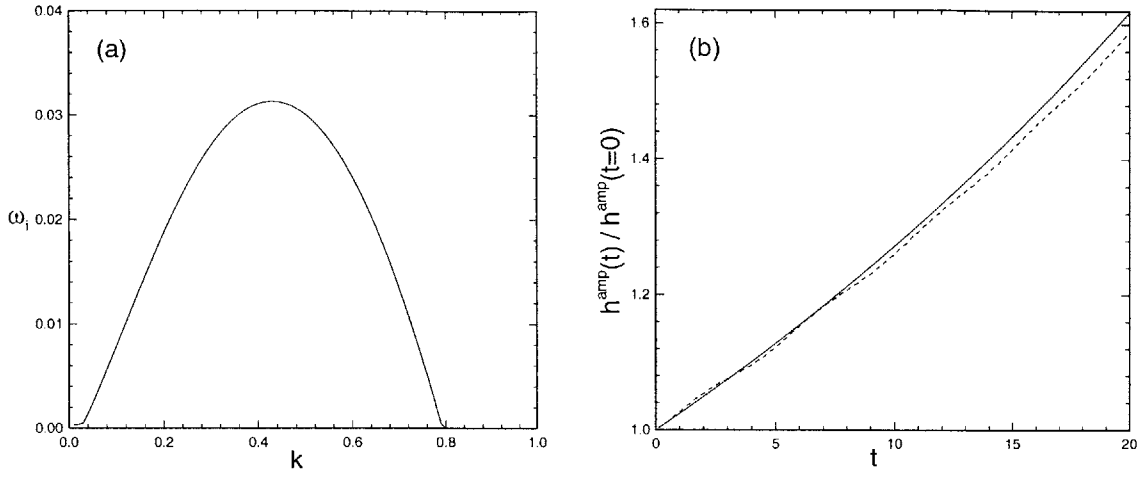

Figure 2-5: (a) Growth rate ω_i (the wave amplitude grows at the rate $\exp(\omega_i t)$) as a function of wavenumber k, obtained from Orr–Sommerfeld analysis of the mean flow (2.15) for R_{e0} = 1000 and F_{r0} = 0.7. (b) Growth in amplitude of a two-dimensional surface progressive wave at wavenumber k=0.6: ———— , Orr–Sommerfeld analysis; – – – – , direct simulation result.

2.2 Large-eddy Simulation

While DNS resolves the essential turbulence scales and thus has the virtue that no *ad hoc* model is needed, it is limited to low Reynolds numbers and simple flow configurations. For most problems of importance to applications, the Reynolds numbers are high, DNS is incapable of covering the full (integral to dissipative) scale range, and turbulence modeling is essential. A promising approach in this case is the method of large-eddy simulation (LES), in which only the large (grid-scale, GS) motions are resolved explicitly, while contributions from subgrid-scale (SGS) motions are modeled. Since the introduction of LES in meteorology (Smagorinsky 1963), LES has been applied with some success to a variety of turbulence problems (cf. reviews on the development and application of LES by Rogallo & Moin 1984, Lesieur & Métais 1996 and Meneveau & Katz 2000). In this subsection we introduce the formulation and numerical scheme for LES of free-surface turbulent flows. The SGS modeling based on the physics of the FST as well as the performance are discussed in Chapter 8.

2.2.1 Governing equations

We consider the resolved grid-scale motions in free-surface turbulence. In this study, for any variable $f(\vec{x})$, its grid-scale portion $\overline{f}(\vec{x})$ is obtained by using a low-pass filter $\overline{G}(\vec{x})$ (cf. e.g. Leonard 1974):

$$\overline{f}(\vec{x}) \equiv \int \overline{G}(\vec{x}-\vec{\xi}) f(\vec{\xi}) \mathrm{d}\vec{\xi} \; ; \tag{2.19}$$

and the subgrid-scale (SGS) portion $f''(\vec{x})$ is defined as

$$f''(\vec{x}) \equiv f(\vec{x}) - \overline{f}(\vec{x}) \; . \tag{2.20}$$

After applying the filter to (2.1) and (2.2), we obtain the governing equations for the grid-scale velocities:

$$\frac{\partial \overline{u}_i}{\partial t} + \frac{\partial \overline{u}_i \overline{u}_j}{\partial x_j} = -\frac{\partial \overline{p}}{\partial x_i} + \frac{1}{R_{e0}} \frac{\partial^2 \overline{u}_i}{\partial x_j \partial x_j} - \frac{\partial \tau_{ij}}{\partial x_j} \; , \quad i = 1, 2, 3, \tag{2.21}$$

and

$$\frac{\partial \overline{u}_i}{\partial x_i} = 0 \; . \tag{2.22}$$

Here τ_{ij} is the SGS stress defined as

$$\tau_{ij} \equiv \overline{u_i u_j} - \overline{u}_i \overline{u}_j \; , \quad i, j = 1, 2, 3 \; , \tag{2.23}$$

which represents the contributions from the subgrid scales and must be modeled in terms of resolved quantities. In flows where only kinematic boundary conditions are imposed, it is conventional to model only the trace-free portion, M_{ij}, of τ_{ij}:

$$M_{ij} \equiv \tau_{ij} - \frac{1}{3} \delta_{ij} \tau_{kk} \; . \tag{2.24}$$

The modeling of M_{ij} is discussed in Chapter 8.

Because of (2.24), the isotropic part of the SGS stress is absorbed into the (dynamic)

pressure. Thus the momentum equation (2.21) becomes

$$\frac{\partial \overline{u}_i}{\partial t} + \frac{\partial \overline{u}_i \overline{u}_j}{\partial x_j} = -\frac{\partial \overline{P}}{\partial x_i} + \frac{1}{R_{e0}} \frac{\partial^2 \overline{u}_i}{\partial x_j \partial x_j} - \frac{\partial M_{ij}}{\partial x_j} , \quad i = 1, 2, 3, \tag{2.25}$$

with the modified pressure

$$\overline{P} \equiv \overline{p} + \frac{1}{3}\tau_{kk}. \tag{2.26}$$

In the presence of a free surface, dynamic conditions on the *total* stress are imposed and the decomposition (2.24) and (2.26) results in an additional SGS scalar, $p_{SGS} \equiv \tau_{kk}/3$, which must be modeled separately. This is discussed in §2.2.2 and the performance of this modeling is evaluated in Chapter 8.

2.2.2 Boundary conditions

After passing the filter (2.19), the bottom boundary conditions for the grid-scale motions (2.8) are obtained as

$$\frac{\partial \overline{u}}{\partial z} = \frac{\partial \overline{v}}{\partial z} = \overline{w} = \frac{\partial \overline{P}}{\partial z} = 0 , \qquad \text{on } z = -L_z. \tag{2.27}$$

The boundary conditions for the deformable free surface are much more complicated. Upon filtering, the dynamic free-surface boundary conditions for the grid-scale motions (2.3)–(2.5) are obtained as follows:

$$\frac{1}{R_{e0}}\left(\frac{\partial \overline{u}}{\partial z} + \frac{\partial \overline{w}}{\partial x}\right) = 0 , \qquad \text{on } z = 0 ; \tag{2.28}$$

$$\frac{1}{R_{e0}}\left(\frac{\partial \overline{v}}{\partial z} + \frac{\partial \overline{w}}{\partial y}\right) = 0 , \qquad \text{on } z = 0 ; \tag{2.29}$$

and

$$\overline{p} = \frac{\overline{h}}{F_{r0}^2} + \frac{2}{R_{e0}} \frac{\partial \overline{w}}{\partial z} , \qquad \text{on } z = 0 . \tag{2.30}$$

Because of the modification (2.26), the normal dynamic free-surface boundary condition

becomes

$$\overline{P} = \frac{\overline{h}}{F_{\tau 0}^2} + \frac{2}{R_{e0}} \frac{\partial \overline{w}}{\partial z} + p_{SGS} \ , \qquad \text{on } z = 0 \ , \tag{2.31}$$

where the subgrid-scale contribution $p_{SGS} \equiv \tau_{kk}/3$ is unknown and needs to be separately modeled.

After filtering, the kinematic free-surface boundary condition (2.7) becomes

$$\frac{\partial \overline{h}}{\partial t} = \overline{w} - \frac{\partial}{\partial x}(\overline{u}\overline{h}) - \frac{\partial}{\partial y}(\overline{v}\overline{h}) - \frac{\partial \tau_u^{kbc}}{\partial x} - \frac{\partial \tau_v^{kbc}}{\partial y} \ , \qquad \text{on } z = 0 \ . \tag{2.32}$$

Here

$$\tau_u^{kbc} \equiv \overline{uh} - \overline{u}\overline{h} \qquad \text{and} \qquad \tau_v^{kbc} \equiv \overline{vh} - \overline{v}\overline{h} \ , \tag{2.33}$$

which are additional unknown subgrid-scale quantities and must again be separately modeled.

The SGS modeling for the free-surface dynamic and kinematic boundary conditions as well as the performance in LES will be discussed together with the SGS stress modeling in Chapter 8.

2.2.3 Numerical scheme and computational parameters

The numerical scheme for the LES is essentially the same as that for DNS. The additional SGS stress terms are assigned at the vertically-staggered grid system, with τ_{11}, τ_{12} (τ_{21}), τ_{22} and τ_{33} at regular grids, and τ_{13} (τ_{31}), τ_{23} (τ_{32}) at staggered grids. To calculate the derivatives of the SGS stress, we use a sixth-order finite difference scheme in the horizontal directions and a second-order finite difference scheme in the vertical direction.

In this study, the grid filter $\overline{G}(\vec{x})$ in (2.19) is defined as Gaussian filters (cf. Kwak, Reynolds & Ferziger 1975) in the horizontal directions and a discrete filter in the vertical direction:

$$\begin{aligned} \overline{G}(\vec{x}) &= \overline{G}_1(x)\overline{G}_2(y)\overline{G}_3(z) \ ; \\ \overline{G}_1(x) &= (6/\pi)^{1/2} \exp[-6x^2/\overline{\Delta}_x^2] \ ; \end{aligned}$$

$$\begin{aligned}\overline{G}_2(y) &= (6/\pi)^{1/2}\exp[-6y^2/\overline{\Delta}_y^2]\ ; \\ \overline{G}_3(z) &= [\delta^D(z-\overline{\Delta}_z)+2\delta^D(z)+\delta^D(z+\overline{\Delta}_z)]/4\ . \end{aligned} \tag{2.34}$$

Here δ^D is the Dirac delta function; and $\overline{\Delta}_x/\Delta_x=\overline{\Delta}_y/\Delta_y=8$ and $\overline{\Delta}_z/\Delta_z=2$ are the horizontal and vertical filter widths, respectively. The overall filter width $\overline{\Delta}$ is set to be:

$$\overline{\Delta} \equiv (\overline{\Delta}_x\overline{\Delta}_y\overline{\Delta}_z)^{1/3} = 0.2992\ . \tag{2.35}$$

The test filter $\widehat{G}$ is similar to $\overline{G}$ and uses Gaussian filters in the (periodic) horizontal directions but no filtering in the vertical direction is now applied. The filter width for $\widehat{G}$ is chosen to satisfy $\widehat{\overline{\Delta}}_x=2\overline{\Delta}_x$ and $\widehat{\overline{\Delta}}_y=2\overline{\Delta}_y$. The overall filter width at the coarse level, $\widehat{\overline{G}}$, is defined as

$$\widehat{\overline{\Delta}} \equiv (\widehat{\overline{\Delta}}_x\widehat{\overline{\Delta}}_y\overline{\Delta}_z)^{1/3} = 0.4749\ . \tag{2.36}$$

For LES simulations, the computational domain size is $L_x \times L_y=10.472^2$ (horizontally) by $L_z=6$ (vertically). The Reynolds number is $R_{e0} = 1400$ and the Froude number is $F_{r0} = 0.7$. To perform direct quantitative comparison with the DNS results which are obtained on a fine grid, LES uses a coarse 32^2 (horizontal) $\times$ 96 (vertical) grid with a larger time step 0.02.

Chapter 3

Surface Layers for Free-Surface Turbulent Flows

In this chapter, we introduce free-surface boundary layer, the key concept in FST study. Through direct numerical simulations, we are able to: (i) identify an inner layer and an outer layer and quantify the dynamics within these layers; (ii) understand the dynamics of surface vortex connections in FST and the underlying mechanisms for the persistence of such connected structures; and (iii) obtain the dominant effects of (even small) Froude numbers on the statistical characteristic of FST as compared to, say, turbulence under a free-slip wall. The elucidation of the inner and outer layers and their dynamics provides a coherent framework for understanding FST which clearly distinguishes it from turbulent flow near a no-slip wall, and, in a not insignificant way, from that near a free-slip wall.

This chapter is organized as follows. In §3.1, the concept of the free-surface inner and outer layers is introduced. In §3.2, we identify the multi-layer structure in our numerical simulations. The spatial and temporal development of the surface layer during vortex surface connection events is studied in §3.3. In §3.4, we present the effects of the surface layers on the turbulence statistics with special emphasis on the turbulence length scales, Reynolds-stress balance and enstrophy dynamics. In §3.5, we investigate the effect of Froude numbers on the FST statistics. For small (non-zero) Froude numbers, we find that the effects are comparably small with the exception of the pressure–strain correlations which show qualitative differences

as a result of the free surface. We conclude in §3.6 with a discussion and a summary.

3.1 The concept of free-surface boundary layer

In this section, we discuss the concept of the boundary layer that develops at a clean free surface. The free-surface dynamic boundary conditions are given in (2.3)–(2.5). For $R_{e0} \gg 1$, the first term on the right-hand side of (2.5) is much larger than the second term, so that the requirement of vanishing normal stress is effectively an inviscid boundary condition. The effect of viscosity is thus manifest primarily through the vanishing of the tangential stresses (2.3) and (2.4). This can be seen most clearly in the horizontal components of the vorticity ω_i at the free surface. Using (2.3) and (2.4), we obtain

$$\omega_x = \frac{\partial w}{\partial y} - \frac{\partial v}{\partial z} = -2\frac{\partial v}{\partial z} = 2\frac{\partial w}{\partial y} \qquad \text{on } z = 0\,, \tag{3.1}$$

$$\omega_y = \frac{\partial u}{\partial z} - \frac{\partial w}{\partial x} = 2\frac{\partial u}{\partial z} = -2\frac{\partial w}{\partial x} \qquad \text{on } z = 0\,. \tag{3.2}$$

For small Froude numbers, h and w at the free surface are small, and it follows that ω_x and ω_y are small at $z = 0$. Finally, using the fact that vorticity is divergence free, we obtain from (3.1) and (3.2) the boundary condition for ω_z on the free surface:

$$\frac{\partial \omega_z}{\partial z} = 0 \qquad \text{on } z = 0\,. \tag{3.3}$$

This simple analysis shows that, for flows with significant vorticity, there exists a region inside which the values of ω_x, ω_y, and $\partial\omega_z/\partial z$ (but not ω_z itself) change from their 'outer' values to the much smaller values specified by (3.1), (3.2) and (3.3).

We note that this surface layer is thin for high Reynolds numbers. For laminar flow, a typical argument of balance between viscous and convection terms in the evolution equations for ω_x or ω_y shows that the thickness of the layer is proportional to the square root of the Reynolds number.

The surface inner layer, which is due to the viscous dynamic boundary conditions, is

distinct from the so-called 'blockage' or 'source' outer layer, which is due to the kinematic boundary condition. The importance of the outer layer is manifested mainly in the redistribution of the turbulence intensity, i.e. in the reduction of the vertical velocity fluctuations and the increase of the horizontal velocity fluctuations. From the continuity equation, the outer layer has a thickness of order macroscale L.

The surface inner layer is unique to free-surface viscous flow, while the outer layer obtains in principle for any flows with a boundary constraining the normal motion, for example, rigid wall flows and free-surface potential flows.

3.2 Identification of the surface layers

The existence of surface inner and outer layers is manifest in our DNS results of shear-flow FST. Figure 3-1 shows these two layers clearly. Figure 3-1(a) plots the vertical variation of $\omega_x'^{rms}$, $\omega_y'^{rms}$, $\omega_z'^{rms}$, and $(\partial\omega_z/\partial z)^{rms}$, which give a clear indication of the inner layer which has a thickness of $O(0.1)$. Figure 3-1(b) plots the vertical profiles of the fluctuation velocity components $u_i'^{rms}$, which show distinctly the outer layer of thickness $O(0.5)$ (the macroscale is $O(1)$).

As mentioned earlier, a free surface affects the underlying turbulent flow by means of two mechanisms: first, the dynamic boundary conditions require that the tangential stresses at the surface vanish; second, the kinematic boundary condition constrains the motion normal to the surface. The inner layer is where the dynamic boundary conditions are felt and the outer layer is where the kinematic boundary condition is felt. Since the inner layer and the outer layer are caused by different mechanisms at the free surface, the roles of these two layers in the FST are distinct from each other. In §3.4, we investigate the effects of each layer on the turbulence statistics in some detail, with the focus on the inner layer since it is unique to FST. Here we demonstrate the variation of the first derivatives of velocity components $\partial u_i/\partial x_j$ and the variation of the strain components $s_{ij} \equiv (\partial u_i/\partial x_j + \partial u_j/\partial x_i)/2$ over these two layers.

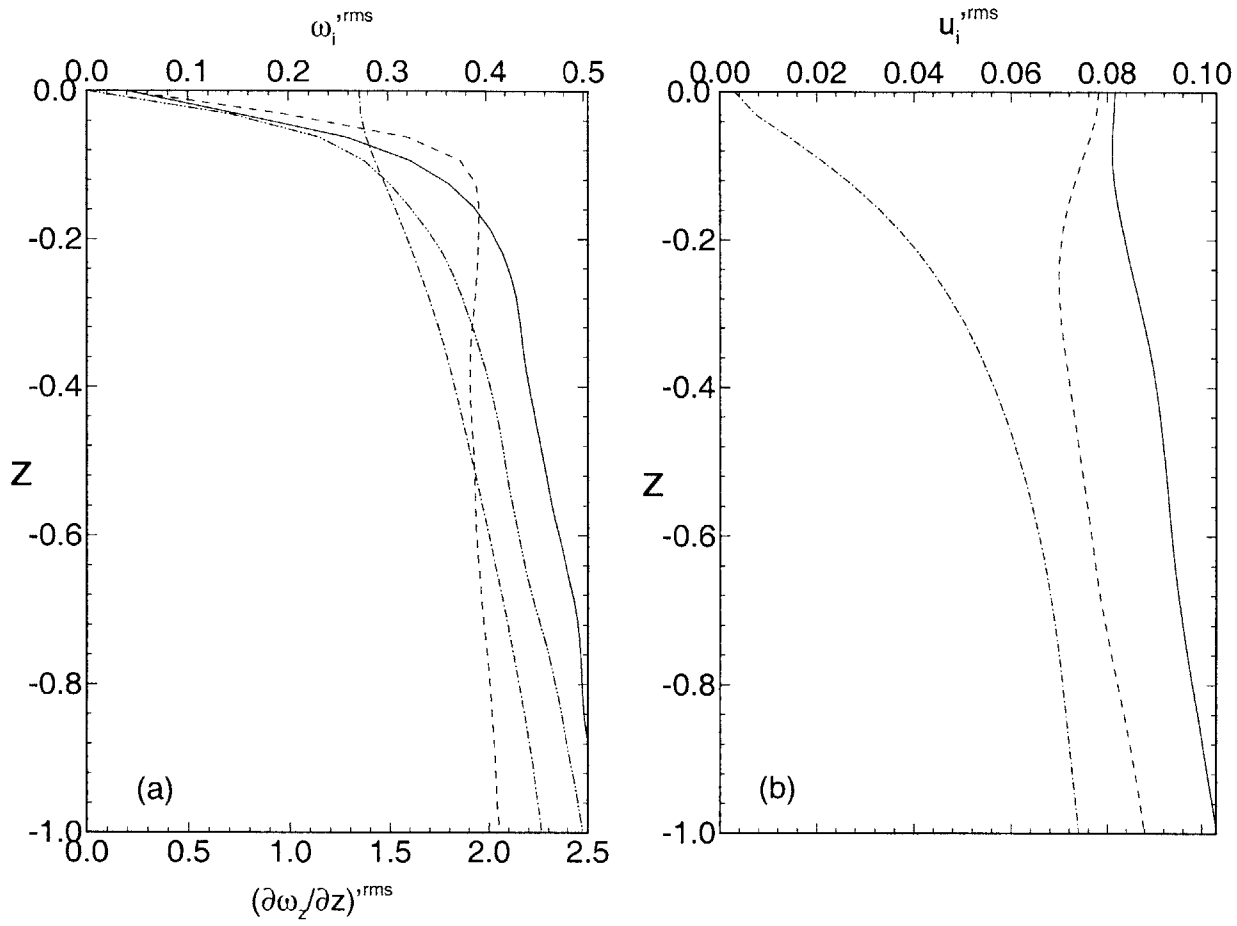

Figure 3-1: Existence of surface inner and outer layers. (a) Inner layer: ———— , $\omega_x^{\prime rms}$; – – – – , $\omega_y^{\prime rms}$; – · – · – , $\omega_z^{\prime rms}$; —··—··— , $(\partial\omega_z/\partial z)^{\prime rms}$; and ($b$) outer layer: ———— , $u^{\prime rms}$; – – – – , $v^{\prime rms}$; – · ·· · – , $w^{\prime rms}$. Results at $t = 60$ are plotted.

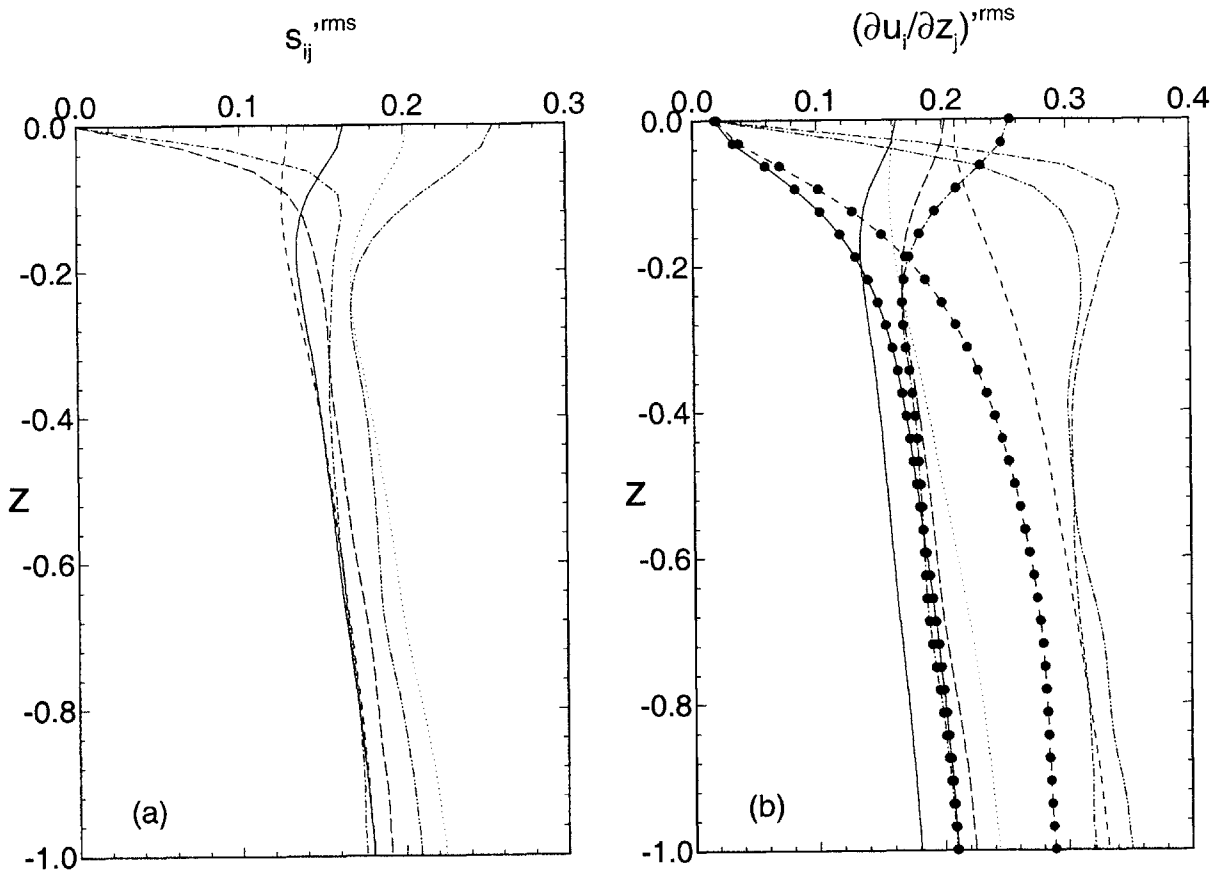

Figure 3-2: Variation of $\partial u_i/\partial x_j$ and s_{ij} over the surface inner and outer layers: (a) ———— , $s_{11}^{'rms}$; – – – – , $s_{12}^{'rms}$; – · – · – , $s_{13}^{'rms}$; · · · · · · · , $s_{22}^{'rms}$; —— —— , $s_{23}^{'rms}$; —··—··— , $s_{33}^{'rms}$. (b) ———— , $(\partial u/\partial x)^{'rms}$; – – – – , $(\partial u/\partial y)^{'rms}$; – · – · – , $(\partial u/\partial z)^{'rms}$; · · · · · · · , $(\partial v/\partial x)^{'rms}$; — — —— , $(\partial v/\partial y)^{'rms}$; —··—··— , $(\partial v/\partial z)^{'rms}$; ——●——, $(\partial w/\partial x)^{'rms}$; – ●– – , $(\partial w/\partial y)^{'rms}$; – · ●· – , $(\partial w/\partial z)^{'rms}$. Results at $t = 60$ are plotted.

The vanishing of the tangential stresses at the free surface (2.3) and (2.4) gives

$$s_{13} = s_{23} = 0 \qquad \text{on } z = 0\,, \tag{3.4}$$

and

$$\frac{\partial u}{\partial z},\ \frac{\partial v}{\partial z} \ll 1 \qquad \text{on } z = 0\,. \tag{3.5}$$

Therefore, s_{13}, s_{23}, $\partial u/\partial z$, and $\partial v/\partial z$ decrease abruptly over the inner layer. This is shown in Figure 3-2.

The term $s_{33} = \partial w/\partial z$, on the other hand, reflects the blockage effects of the surface and varies over the outer layer. It follows from continuity that $s_{11} = \partial u/\partial x$ and $s_{22} = \partial v/\partial y$ also change over the outer layer. In Figure 3-2, the outer layer depth indicated by the above variables appears to be smaller than that in Figure 3-1(b) and that indicated by $\partial w/\partial x$ and $\partial w/\partial y$ in Figure 3-2(b). The reason is that the flow field is inhomogeneous in the vertical direction.

The presence of the surface inner and outer layers can be seen in the results of previous studies. For example, Borue *et al.* (1995), Leighton *et al.* (1991), Pan & Banerjee (1995), and Walker *et al.* (1996) plotted the profile of vorticity components, from which the inner layer can be observed; Borue *et al.* (1995), Handler *et al.* (1993), Perot & Moin (1995), and Walker *et al.* (1996) plotted the velocity component profiles, from which the outer layer can be identified.

3.3 Effects of surface layers on vortex dynamics

In this section, we discuss the vorticity dynamics near the free surface, with emphasis on the role of the surface layers in the reattachment of the vorticity to the free surface.

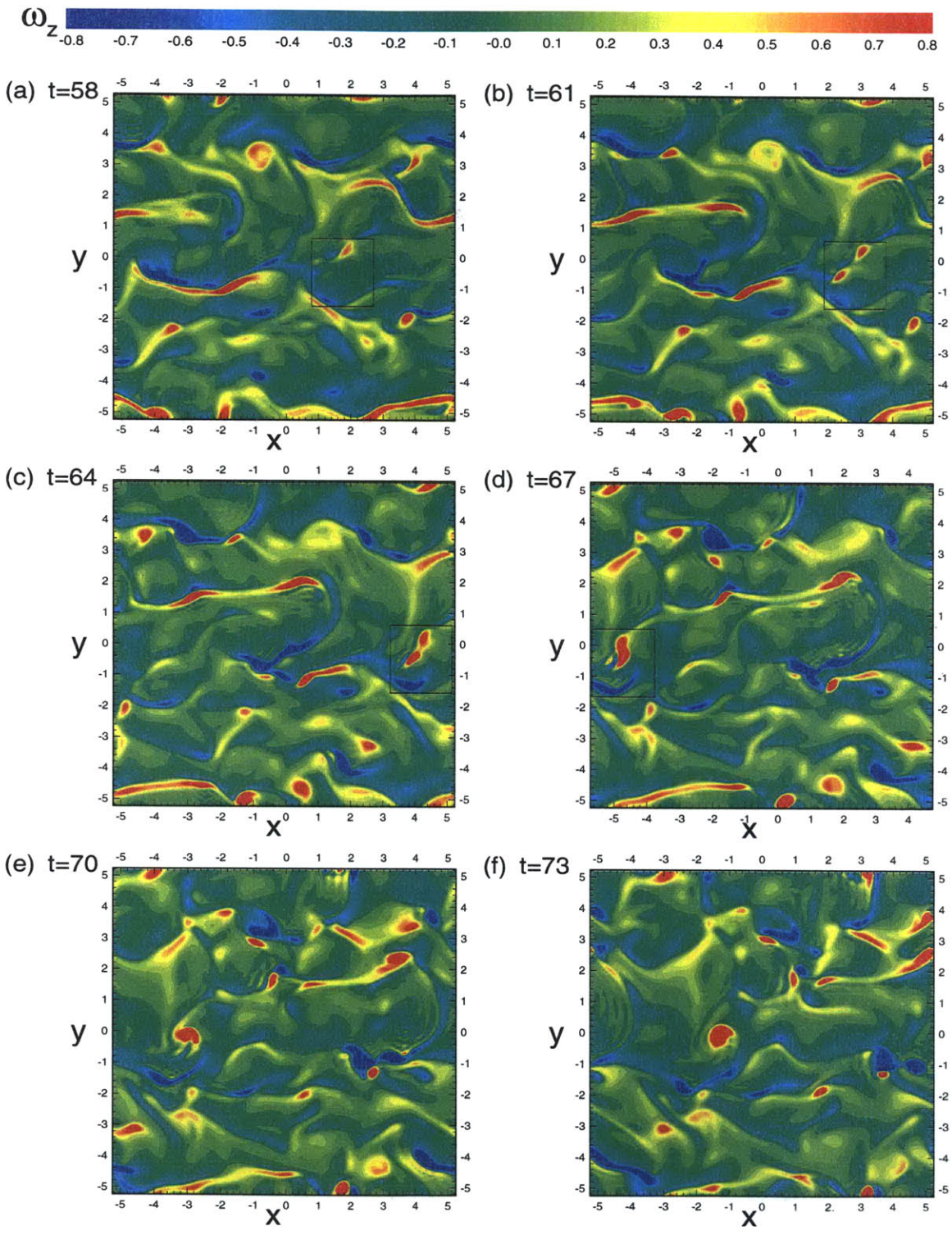

Figure 3-3: Evolution of normal vorticity at the free surface. Surface contours of ω_z are plotted at (*a*) $t = 58$; (*b*) $t = 61$; (*c*) $t = 64$; (*d*) $t = 67$; (*e*) $t = 70$; and (*f*) $t = 73$. The small boxes in (*a*) through (*d*) indicate regions where detailed vortex structures underneath are plotted in Figure 3-4.

3.3.1 Free-surface observables and the underlying vortex structures

It is known that the most prominent surface signature of FST is that due to connected normal vorticity (see e.g. Sarpkaya 1996). Figure 3-3 shows the contours of ω_z at the free surface at six successive time instants t = 58, 61, 64, 67, 70 and 73 from a specific DNS realization. Note that the (periodic) domains plotted in Figure 3-3 are translated with the mean longitudinal velocity (cf. Figure 2-3a). Coherent vortex structures are found scattered on the free surface. If we look at those vortices continuously at smaller time intervals, we can observe that a positive vortex ($\omega_z > 0$) always appears together with a negative vortex ($\omega_z < 0$) and vice versa. Figure 3-3 also shows that the normal vortices at the free surface are persistent with slow overall decay rates.

The presence of the aforementioned vortex structures is due to connection of vortex structures at the free surface. Using the vortex at (−1.4, 0) in Figure 3-3(f) as an example, we show how surface-connected vortices are generated. Figure 3-4 shows the near-surface vortex structures in a small domain of size 2 × 2 × 0.75 at the four earlier time instants t = 58, 61, 64, and 67. The positions of these sub-domains are indicated in Figures 3-3(a) to (d). The vortex structures are represented by tracing a bundle of vortex lines defined as

$$\frac{d\vec{x}}{d\ell} = \frac{\vec{\omega}}{|\vec{\omega}|}\,, \tag{3.6}$$

where ℓ is the arc length of the vortex line. A fourth-order Runge–Kutta integration scheme is used to integrate (3.6).

Figure 3-4 also plots the contours of ω_z at the free surface above the underlying vortex structures to show their correlations.

Figure 3-4(a) (t = 58) shows the presence of a large underlying hairpin-shaped vortex structure (marked 'C' in the figure), which is found to be prevalent in shear-flow FST. The hairpin has the 'head' near the free surface consisting mainly of near-surface horizontal vorticity and the two 'legs' in the bulk flow below. This is opposite to that in rigid-wall-turbulence case, where the legs of the hairpin are close to the boundary and the head is in

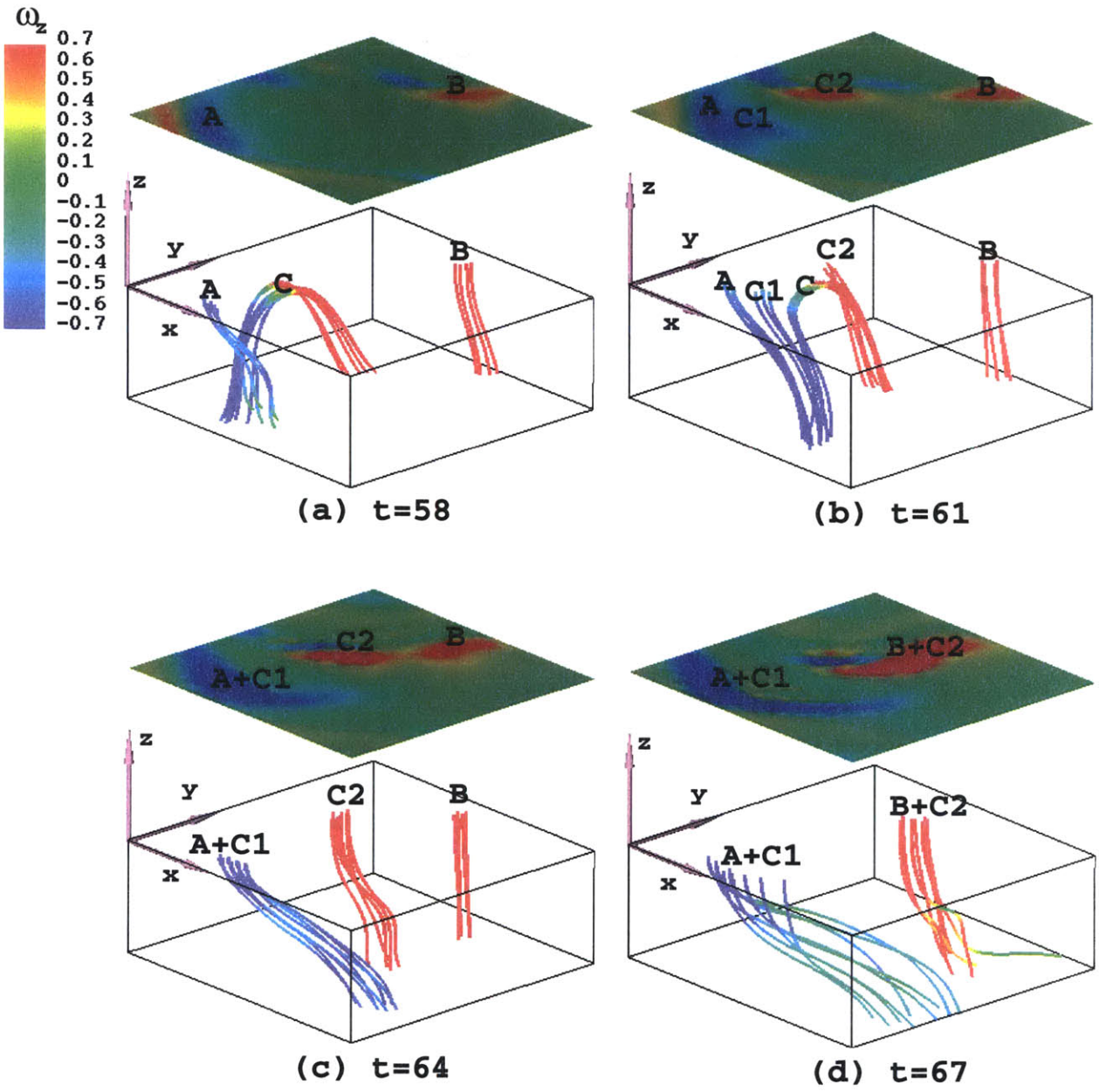

Figure 3-4: Vortex structures in shear-flow FST. Vortex lines and free surface contours of ω_z are plotted. The colors on the vortex lines represent the magnitude of ω_z. The surface contours are plotted above, which correlate with the vortex structures underneath. The domain size is $2 \times 2 \times 0.75$. The position of each domain is shown in Figure 3-3.

the bulk flow (e.g. Moin & Kim 1985). Near the hairpin structure, in this case, there are two other vortices (marked 'A' and 'B' in the figure) which are already connected to the free surface.

As the hairpin vortex structure is swept towards the free surface by the uprising fluid ('splat' event), the head is dissipated quickly in the surface inner layer where the dissipation rate for horizontal vorticities is significantly higher. (The effects of the inner layer on vorticity dissipation are discussed in detail in §3.4.3.) The hairpin vortex begins to break and the two legs connect to the free surface at the 'shoulder.' The mechanism for the connection of a hairpin vortex structure to the free surface is very much the same as the connection of, say, a vortex ring to the surface. The detailed mechanisms have been studied extensively (see e.g. Zhang *et al.* 1999) and will not be repeated here.

Figure 3-4(b) ($t = 61$) shows such a connection occurring: part of the hairpin vortex structure has broken and the two legs (marked 'C1' and 'C2') connect to the free surface. The remaining vortex lines of the hairpin soon also break and connect to the free surface.

The connection is complete at $t = 64$ (Figure 3-4c). The two legs are completely attached to the free surface forming a pair of counter-rotating vortices with opposite signs for the ω_z component. Figure 3-4(c) also shows the merging of connected vortices (in this case 'C1' with a same-signed vortex 'A' which had previously been connected to the surface). At a later time, $t = 67$ in Figure 3-4(d), the opposite-signed leg 'C2' also merges with another surface-connected vortex 'B' of that sign. This coherent vortex ('B+C2') is what we see at $(-1.4,\ 0)$ later at $t = 73$ (Figure 3-3e). The merger of surface-connected vortices is also frequently observed in FST (e.g. Gharib *et al.* 1994 for grid FST; Pan & Banerjee 1995 for open-channel FST).

After the connection, vortices remain attached to the free surface and decay slowly, as shown in Figure 3-3. In low-Froude-numbers cases, the magnitude of the horizontal vorticity components is much smaller than that of the vertical vorticity, so that the vortices are nearly perpendicular to the free surface. In the bulk flow below, the vortices are inclined in the direction of the mean shear flow.

A statistical measure of the structures and mechanisms illustrated above can be obtained

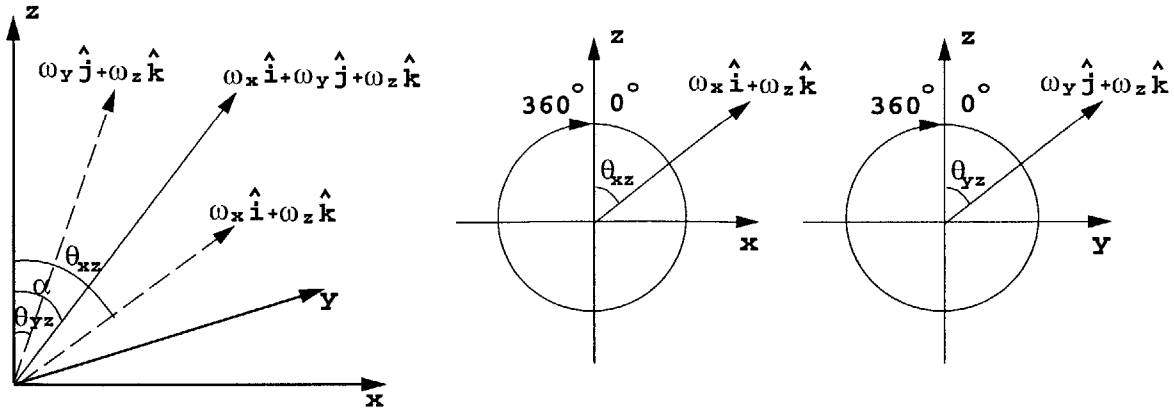

Figure 3-5: Coordinate system and sign convention for vortex inclination angles θ_{xz}, θ_{yz}, and α. θ_{xz} is the angle from the positive-z axis to $\omega_x\vec{i} + \omega_z\vec{k}$ in the (x, z)-plane; θ_{yz} is the angle from the positive-z axis to $\omega_y\vec{j} + \omega_z\vec{k}$ in the (y, z)-plane; α is the angle between the z-axis and $\omega_x\vec{i} + \omega_y\vec{j} + \omega_z\vec{k}$.

by investigating the spatial distribution of two-dimensional vortex inclination angles in a way similar to Moin & Kim (1985). If the vorticity vector is projected onto the (x, z)- and (y, z)-planes, the two-dimensional vortex inclination angles are defined as $\theta_{xz} = \tan^{-1}(\omega_x/\omega_z)$ and $\theta_{yz} = \tan^{-1}(\omega_y/\omega_z)$, respectively, with the sign convention for the angles and coordinate system shown in Figure 3-5. To emphasize the stronger vortices, the inclination angles are weighted by the magnitudes of the respective projections of the vorticity vector (Moin & Kim 1985).

Figures 3-6(a) and 3-6(b) show the histograms of vortex inclination angles θ_{xz} and θ_{yz} at different depths. Near the free surface, θ_{xz} is highly concentrated around 180° and 0°/360°; while θ_{yz} is concentrated around 180°, 0°/360°, and 270°. The concentration of θ_{xz} and θ_{yz} around 180° and 0° (or 360°) indicates the dominance of vertical vorticity, which corresponds to vortices connected to the free surface, while the concentration of θ_{yz} around 270° indicates the dominance of spanwise vorticities pointing in the negative-y direction, which corresponds to the head portion of the hairpin structures. In the bulk flow ($z = -1$), the peaks of θ_{xz} shift towards 120° and 300°, which indicates that the vortices there are inclined with the mean shear flow. The concentration of θ_{yz} at 270° in the bulk reflects the spanwise vorticity of the two-dimensional mean shear flow.

Following Moin & Kim (1985), θ_{xz} and θ_{yz} in Figures 3-6(a) and 3-6(b) are based on

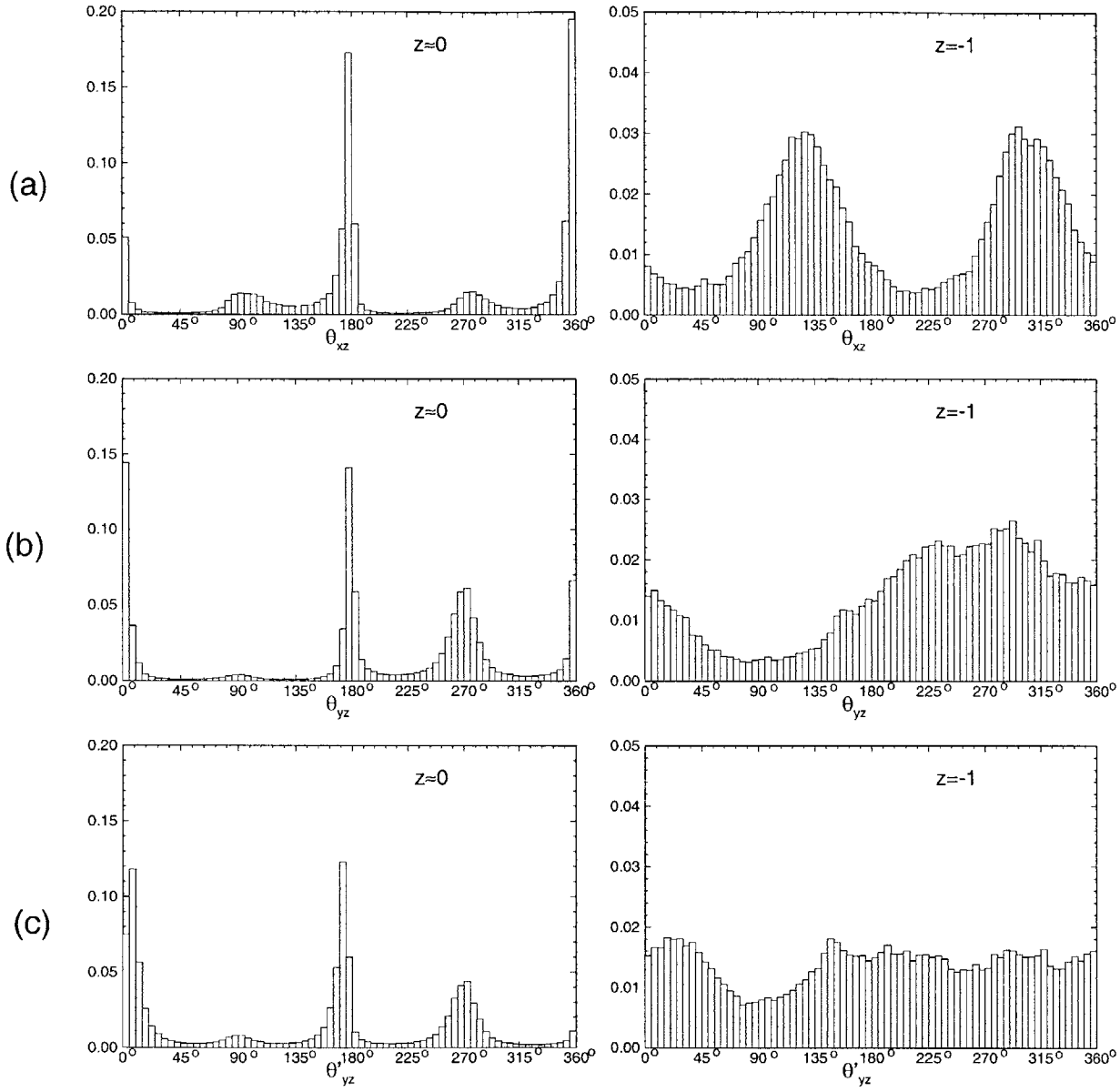

Figure 3-6: Histograms of two-dimensional vortex inclination angles near the surface and in the bulk flow below. (a) θ_{xz} is defined as the angle from the positive-z axis to the instantaneous vorticity $\omega_x\vec{i} + \omega_z\vec{k}$; (b) θ_{yz} is the angle from the positive-z axis to the instantaneous vorticity $\omega_y\vec{j} + \omega_z\vec{k}$; (c) θ'_{yz} is the angle from the positive-z axis to the instantaneous vorticity fluctuation $\omega'_y\vec{j} + \omega'_z\vec{k}$.

instantaneous vorticity which includes the mean vorticity of the shear flow. The two-dimensional vortex inclination angles θ'_{yz} based on instantaneous vorticity fluctuations are plotted in Figure 3-6(c) which shows that, in the bulk flow below ($z = -1$), the concentration of θ_{yz} around 270° is absent for θ'_{yz}, while near the free surface, θ_{yz} and θ'_{yz} are similar. Therefore, coherent horizontal vortex structures (head portion of coherent hairpin structures) do exist near the free surface.

We note that hairpin vortex structures and their connection to the free surface have been reported in open-channel FST (cf. Rashidi 1997), which makes the physics of shear-flow FST and open-channel FST closer to each other than to grid FST. However, the origins of the vortical events in the open-channel FST and the shear-flow FST are different. In open-channel FST, hairpin vortex structures are generated at the boundary layer at the solid bottom and are swept to the surface after ejection from the bottom. In the present flow, vorticity is generated entirely by the shear flow dynamics.

3.3.2 Spatial and temporal development of the surface layers

As we show in §3.1, the surface inner layer is a region of rapid variations for the horizontal vorticity components and the vertical derivative of the vertical vorticity component. The inner layer is, however, not always present: for instance, a uniform flow with a free surface will have no need for a surface inner layer; uniform-strength vortex filaments attached perpendicularly to the free surface also satisfy the boundary conditions (3.1), (3.2), and (3.3) automatically, and the inner layer is not present. In general free-surface vortical flows, the surface inner layer is present whenever and wherever horizontal vortex filaments approach the free surface.

Figure 3-7 shows the development of the surface inner layer during the connection of hairpin vortex structures to the free surface. Using the hairpin vortex in §3.3.1 as an example, Figure 3-7(a) shows the vertical section of the hairpin structure as it approaches the free surface. The head portion of the hairpin is a region of high horizontal vorticity (mainly ω_y) and there exist high gradients between the hairpin head and the free surface where horizontal vorticities given by (3.1) and (3.2) are small. The presence of the surface inner layer at, say,

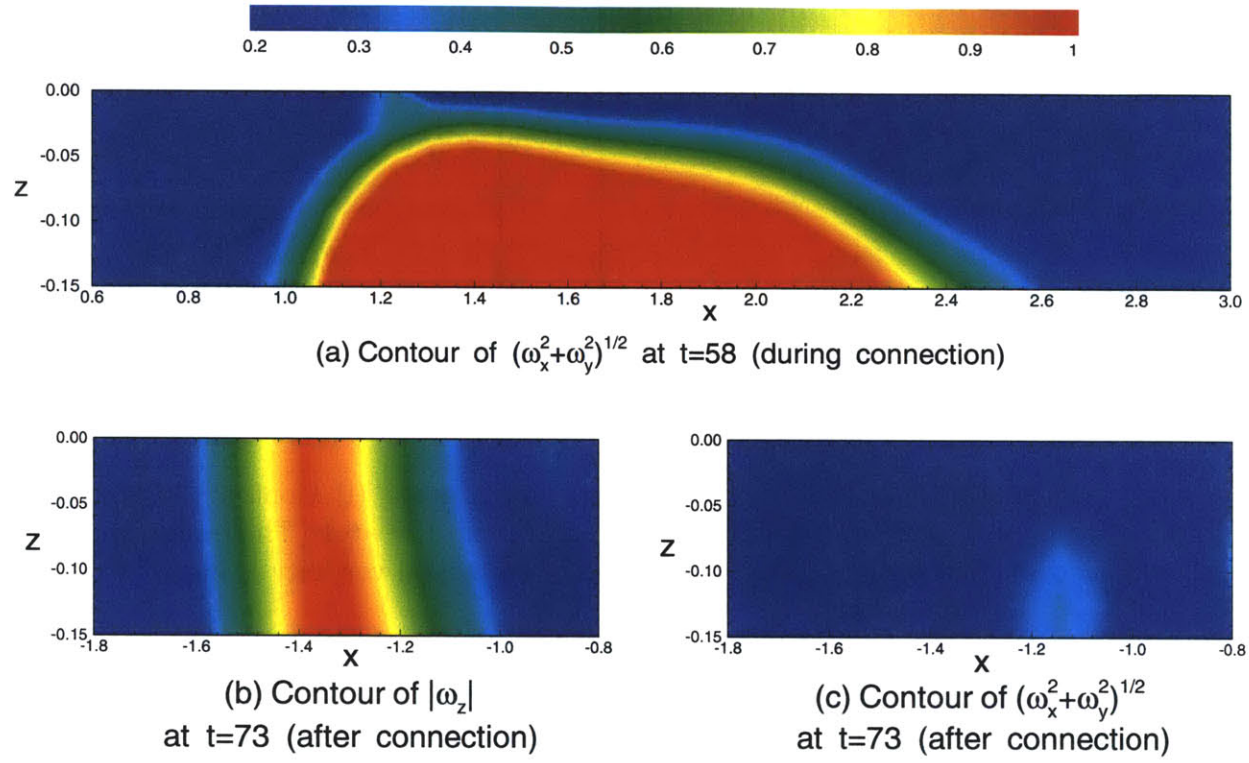

Figure 3-7: Development of the surface inner layer during a vortex connection process. (a) Contours of $(\omega_x^2 + \omega_y^2)^{1/2}$ on the vertical x,z section at y=-0.49, t=58, when the hairpin structure in §3.3.1 approaches the surface. The inner layer is evident in this case. (b), (c) Contours of $|\omega_z|$ and $(\omega_x^2 + \omega_y^2)^{1/2}$ on the vertical x,z section at $y = -0.33$, t=73, when the vortex has connected to the surface. An inner layer is not present in this case. The contour intervals are 0.2 for all three figures.

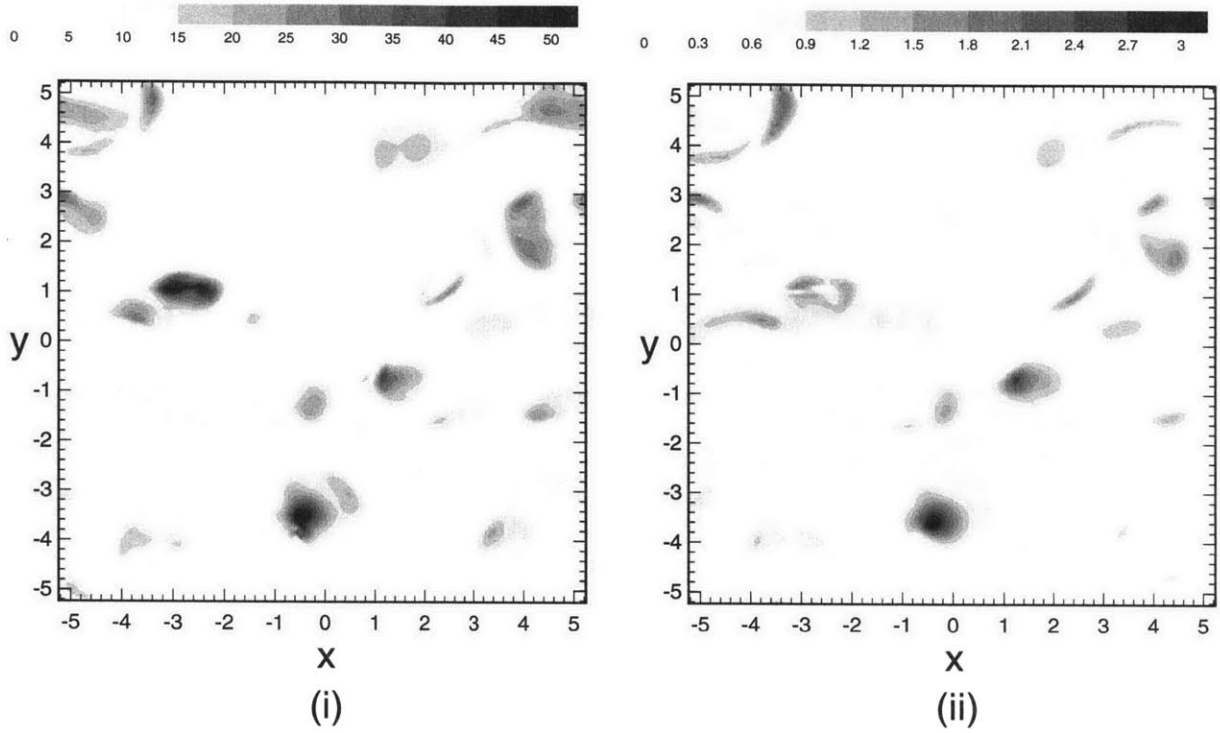

Figure 3-8: Spatial distribution of the surface inner layer. (i) Contours of $[(\partial\omega_x/\partial z)^2 + (\partial\omega_y/\partial z)^2]^{1/2}$ at $z = 0$. (ii) Contours of $(\omega_x^2 + \omega_y^2)^{1/2}$ at $z = -0.1$. The inner layer exists at the dark regions where the vertical derivatives of horizontal vorticity is large.

$x \in \sim (1.1, 2.1)$, is quite evident. Outside such a region, the vertical gradients are not large and the surface inner layer is absent.

After a vortex is connected to the free surface, the vertical gradients are smoothed out and the surface inner layer is, strictly speaking, not present. This is shown in Figure 3-7 where the above vortex has connected to the free surface (see Figure 3-7*b*). Figure 3-7(c) plotting the $(\omega_x^2 + \omega_y^2)^{1/2}$ contours confirms that horizontal vorticity components are small underneath and that, in general, a surface inner layer is absent for a vortex after it has connected to the surface.

Figure 3-8 shows a global picture of the spatial distribution of the surface inner layer. Figure 3-8(i) plots the contours of $[(\partial\omega_x/\partial z)^2 + (\partial\omega_y/\partial z)^2]^{1/2}$ at the surface $z = 0$, while Figure 3-8(ii) plots the contours of $(\omega_x^2 + \omega_y^2)^{1/2}$ at $z = -0.1$. In both figures, the presence of the surface inner layer is indicated by dark regions where the vertical derivatives of horizontal vorticity are large. The light regions are locations where significant near-surface horizontal

vorticity is absent (vorticity itself is either small or has connected to the surface there), and the inner layer is not established there.

In conclusion, a surface inner layer only exists when/where vortex filaments (which should contain horizontal components) approach the free surface. In the present shear-flow FST, connection of vortices to the free surface occurs frequently and the surface inner layer is present over a considerable portion of the free surface (see Figure 3-8) at all times.

The occurrence of hairpin vortex structures in grid FST, on the other hand, is rarer than that in shear-flow FST, and the effect of the surface inner layer is less significant for grid FST than shear-flow FST. This is discussed in §3.4.

Pan & Banerjee (1995) performed an interesting test in their DNS with two different boundary conditions at the bottom: (*a*) they first applied the usual no-slip condition at the bottom; (*b*) after the flow with no-slip bottom was fully developed, they then switched the no-slip bottom to a free-slip bottom. In case (*a*), the ejection from the wall towards the surface is found to be pronounced. In this case, we can regard the occurrence of the surface inner layer to be significant, since the upwelling motions sweep considerable horizontal vortex filaments (which are generated near the wall) to the surface. In case (*b*), Pan & Banerjee's (1995) results show that the mean shear flow becomes flattened out immediately and the upwellings are found to disappear. Their mean shear is much weaker than that in the present study and their flow field (*b*) is more like grid FST than the shear-flow FST here. In that case, few horizontal vortices are swept to the surface and we expect that the surface inner layer is less significant in case (*b*).

3.3.3 Evolution of normal vorticity at the free surface

As pointed out earlier, the surface inner layer has little effect on the vertical vorticity component and the surface-connected vortices are found to be extremely persistent. We analyze here the vorticity equation to reveal the underlying mechanisms for the evolution of surface-connected vortices.

The evolution equation of ω_z can be written as

$$\frac{\partial \omega_z}{\partial t} + \vec{v} \cdot \nabla \omega_z = \vec{\omega} \cdot \nabla w + \frac{1}{R_{e0}} \nabla^2 \omega_z \ , \tag{3.7}$$

where the first term on the right represents vortex turning and stretching, and the second term, vortex diffusion due to viscosity.

Defining $\nabla' \equiv (\partial/\partial x, \partial/\partial y, 0)$ and invoking continuity, we obtain

$$\frac{\partial \omega_z}{\partial t} + \nabla' \cdot (\omega_z \vec{v} - w\vec{\omega}) = \frac{1}{R_{e0}} \nabla^2 \omega_z \ . \tag{3.8}$$

At the free surface, tangential stresses vanish as in (2.3) and (2.4):

$$\frac{\partial u}{\partial z} + \frac{\partial w}{\partial x} = \frac{\partial v}{\partial z} + \frac{\partial w}{\partial y} = 0 \qquad \text{on } z = 0 \ . \tag{3.9}$$

It follows that

$$\nabla' \cdot (w\vec{\omega}) = \frac{\partial}{\partial x}(\frac{\partial w^2}{\partial y}) - \frac{\partial}{\partial y}(\frac{\partial w^2}{\partial x}) = 0 \qquad \text{on } z = 0 \ , \tag{3.10}$$

and (3.8) reduces to

$$\frac{\partial \omega_z}{\partial t} + \nabla' \cdot (\omega_z \vec{v}) = \frac{1}{R_{e0}} \nabla^2 \omega_z \qquad \text{on } z = 0 \ . \tag{3.11}$$

If we consider an arbitrary region $\mathcal{F}$ on the free surface, it follows from (3.11)

$$\frac{d}{dt} \int\int_{\mathcal{F}} \omega_z dx dy = \frac{1}{R_{e0}} \int\int_{\mathcal{F}} \nabla^2 \omega_z dx dy \qquad \text{on } z = 0 \ . \tag{3.12}$$

If $\mathcal{F}$ is taken to be the entire (periodic) domain, (3.12) becomes trivial since both integrals involving ω_z over $\mathcal{F}$ vanish.

We now consider the more general form of (3.8) under the condition (3.9). Multiplying (3.11) by $n\omega_z^{n-1}$, $n = 1, 2, ...$, we obtain

$$\frac{\partial \omega_z^n}{\partial t} + n\omega_z^{n-1} \nabla' \cdot (\omega_z \vec{v}) = \frac{n}{R_{e0}} \omega_z^{n-1} \nabla^2 \omega_z \qquad \text{on } z = 0 \ . \tag{3.13}$$

After some manipulation we obtain

$$\frac{\partial \omega_z^n}{\partial t} + \nabla' \cdot (\omega_z^n \vec{v}) = (n-1)\omega_z^n \frac{\partial w}{\partial z} + \frac{n}{R_{e0}} \omega_z^{n-1} \nabla^2 \omega_z \qquad \text{on } z = 0 \,. \tag{3.14}$$

In the region $\mathcal{F}$ we have

$$\frac{d}{dt} \int\int_{\mathcal{F}} \omega_z^n dxdy = (n-1) \int\int_{\mathcal{F}} \omega_z^n \frac{\partial w}{\partial z} dxdy + \frac{n}{R_{e0}} \int\int_{\mathcal{F}} \omega_z^{n-1} \nabla^2 \omega_z dxdy \qquad \text{on } z = 0 \,. \tag{3.15}$$

Therefore, for $n > 1$, $\int\int_{\mathcal{F}} \omega_z^n dxdy$ over the entire free surface, is, in general, no longer conserved. Of special interest is the case $n = 2$ which governs the enstrophy:

$$\begin{aligned} & \frac{d}{dt} \int\int_{\mathcal{F}} \omega_z^2 dxdy \\ = \; & \int\int_{\mathcal{F}} \omega_z^2 \frac{\partial w}{\partial z} dxdy + \frac{2}{R_{e0}} \int\int_{\mathcal{F}} \omega_z \nabla^2 \omega_z dxdy \\ = \; & \underbrace{\int\int_{\mathcal{F}} \omega_z^2 \frac{\partial w}{\partial z} dxdy}_{\text{stretching}} \underbrace{- \int\int_{\mathcal{F}} \frac{2}{R_{e0}} \nabla \omega_z \cdot \nabla \omega_z dxdy}_{\text{dissipation}} + \underbrace{\int\int_{\mathcal{F}} \frac{1}{R_{e0}} \nabla'^2 \omega_z^2 dxdy}_{\text{horizontal diffusion}} + \underbrace{\int\int_{\mathcal{F}} \frac{1}{R_{e0}} \frac{\partial^2 \omega_z^2}{\partial z^2} dxdy}_{\text{vertical diffusion}} . \end{aligned} \tag{3.16}$$

In (3.16), the first term is a vortex stretching term, which produces enstrophy. The second is a dissipation term while the third is the horizontal diffusion out of the region $\mathcal{F}$. If $\mathcal{F}$ is the entire (periodic) free surface, this horizontal diffusion is exactly zero. The fourth term is the vertical diffusion of the enstrophy. Therefore, over the entire free surface the enstrophy is, in general, not conserved except for a quasi-steady state in which the stretching term approximately cancels those due to dissipation and diffusion.

To investigate the evolution of surface-connected vorticity, we first examine the time evolution of the surface-inclination angle of these vortices. The three-dimensional vortex surface-inclination angle α is defined as

$$\alpha \equiv \tan^{-1}((\omega_x^2 + \omega_y^2)^{1/2} / |\omega_z|), \quad \alpha \in (0°,\, 90°), \quad z = 0 \,, \tag{3.17}$$

i.e. α is the angle between the z-axis and the vorticity vector $\omega_x \vec{i} + \omega_y \vec{j} + \omega_z \vec{k}$, as shown in

Figure 3-5.

As expected, α is found to generally decrease as a surface-connected vortex evolves: as a vortex connects to the free surface, the horizontal components of vorticity (in the head portion of the hairpin) are not small compared to the vertical component and the inclination angle is large. After connection, the horizontal vorticity is dissipated away because of the surface inner layer. The vertical vorticity dominates and the surface-inclination angle becomes small. This is shown in Figure 3-9 for typical surface-connected vortices (cf. Figure 3-3). The vortex surface-inclination angle thus provides a useful measure of the 'age' of a vortex in the connecting/connected process: large α corresponds to early stages of the evolution and small α later stages.

To examine the roles of the different terms in (3.16) in the evolution of surface-connected vortices, we perform conditional averaging over the free surface, first for $\omega_z \geq C\omega_z^{rms}$, where $C = 2$, say, to select the stronger surface vortices, and then for specific values of α so that the contributions at different stages of the evolution are separated: i.e. $\langle \bullet \mid \omega_z \geq 2\omega_z^{rms}; \alpha \rangle$ where $\bullet$ is a term in (3.16).

Figure 3-10 plots the conditional-averaged terms in (3.16) as a function of vortex surface-inclination angle α. Note that *negative* stretching, i.e. $-\int\int_{\mathcal{F}} \omega_z^2 \partial w/\partial z dx dy$ is plotted in Figure 3-10. It is shown that both vortex stretching and dissipation are strongly dependent on α, and their magnitudes drop dramatically as α decreases. This is reasonable since the flow field is more three-dimensional during the early phase of connection (large α). Also at the early phase, stretching is dominant. The supplementing of enstrophy by vortex stretching exceeds the reduction due to dissipation and diffusion and therefore the enstrophy increases. At the late stage of evolution (small α), both stretching and dissipation decrease and the role of horizontal diffusion becomes more and more important. (Note that due to conditional averaging, there always exists horizontal diffusion into the area where vorticity is weaker.) The vertical diffusion is always negligible.

The disparate behaviors of vortex stretching at different stages of connection is manifested in Figure 3-11 which plots the surface contours of ω_z, $\partial w/\partial z$, and $\omega_z^2 \partial w/\partial z$, as well as the underlying vortex lines for the vortex examined in §3.4.1 at respectively $t = 64$ (early stage

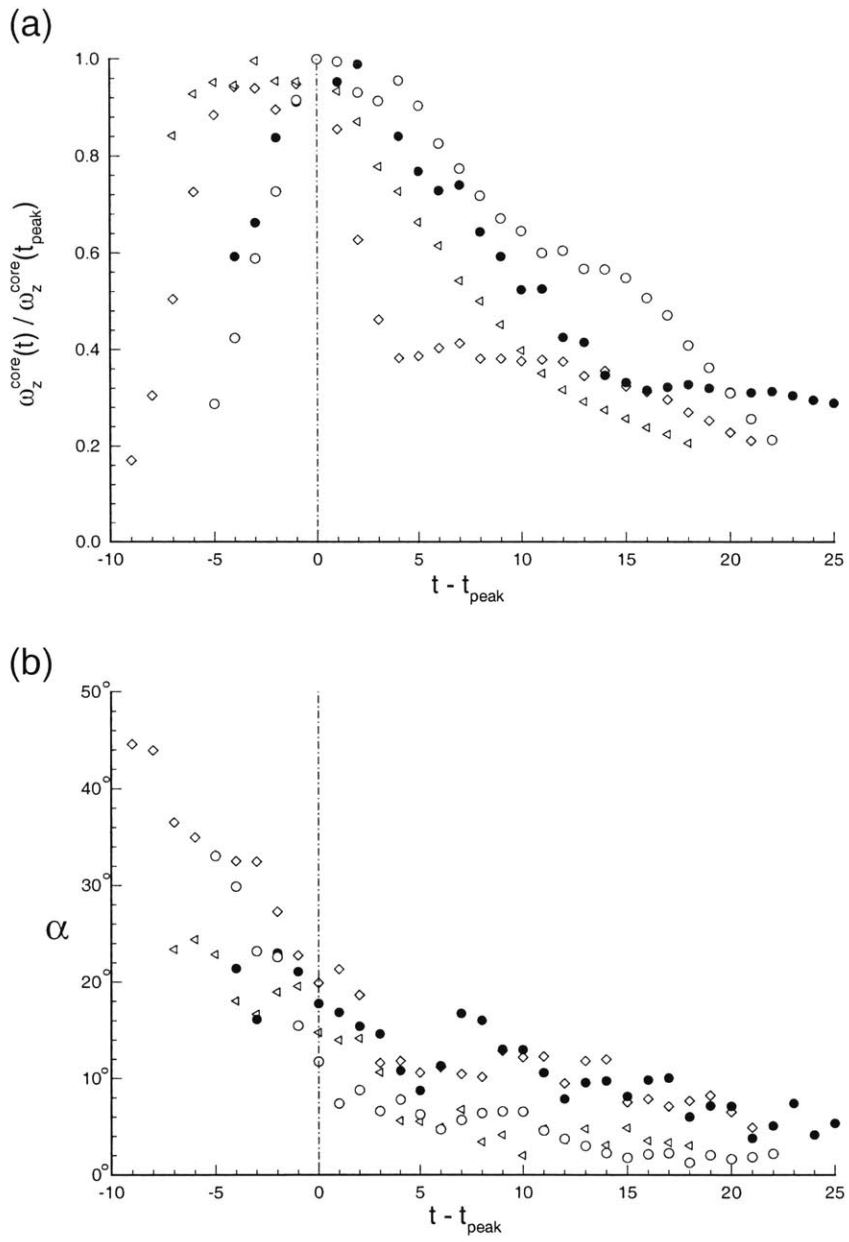

Figure 3-9: Time evolution of (a) core vorticity; and (b) surface-inclination angle α; for typical surface-connected vortices in Figure 3-3. The vortex inclination angle for each vortex is averaged over a region defined by $\omega_z \geq 0.05\omega_z^{core}$, and t_{peak} is the time when ω_z^{core} reaches its maximum. Different symbols represent different connected vortices located in Figure 3-3(e) (at $t = 70$) at: $\diamond$, $(-3, -0.2)$; $\triangleleft$, $(-3.8, -1.6)$; $\circ$, $(-1.9, 3.8)$; $\bullet$, $(-4.6, -3.2)$.

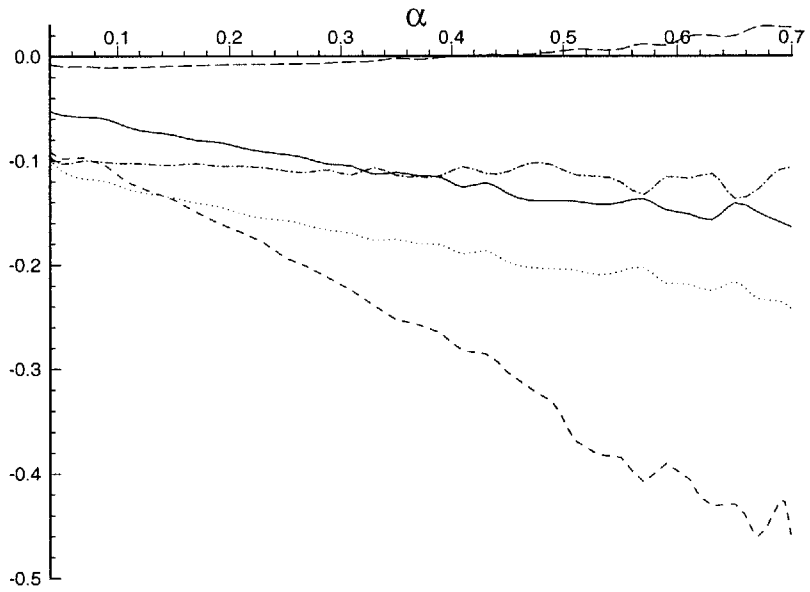

Figure 3-10: Conditional average of the evolution of surface-normal enstrophy. Terms in (3.16) normalized by ω_z^2 are plotted as a function of vortex surface-inclination angle α for vortices $\omega_z \geq 2\omega_z^{rms}$: – – – – , (negative) stretching; ———— , dissipation; – · – · – , horizontal diffusion; —— —— , vertical diffusion; and ····· , dissipation for the entire free surface without the condition $\omega_z \geq 2\omega_z^{rms}$.

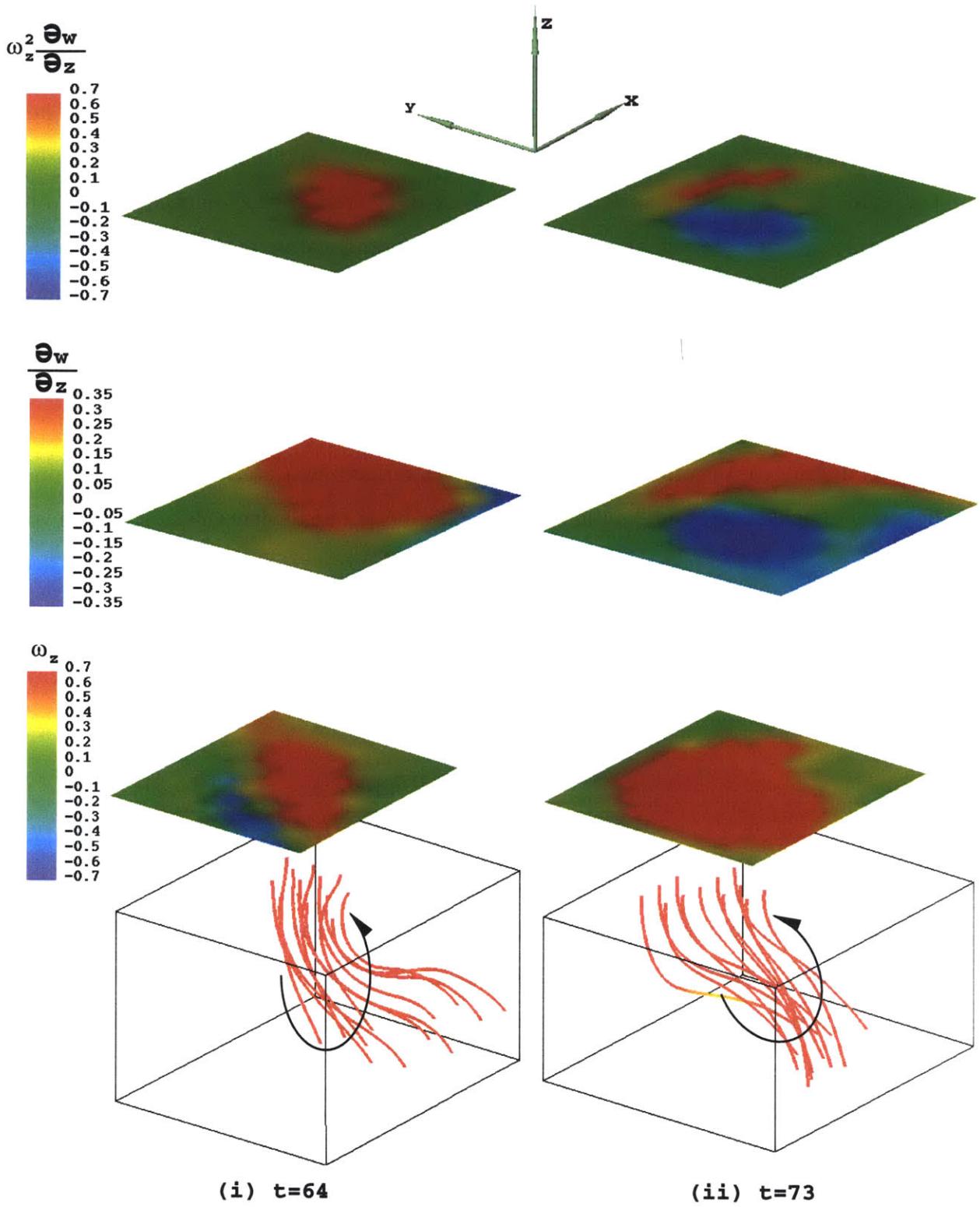

Figure 3-11: Vortex stretching for a surface-connected vortex at different stages of evolution. The vortex presented here is the one shown in §3.3.1. Surface contours of ω_z, $\partial w/\partial z$, and $\omega_z^2 \partial w/\partial z$ and the underlying vortex lines are plotted at (i) $t = 64$ (early stage of evolution) and (ii) $t = 73$ (late stage of evolution).

of evolution) and $t = 73$ (late stage). Note that the strain rate $\partial w/\partial z$, which governs vortex stretching, is always positive for the whole surface-connected vortex during the early stage of evolution but becomes small when integrated over the vortex at a later stage. The latter is controlled by the underlying vortex structure which generally does not remain (nearly) perpendicular to the free surface in the shear flow below. The induced strain rate over the surface connection region is thus, in general, approximately antisymmetric with a small net integral. This is illustrated in Figure 3-11(ii). The overall consequence is that vortex stretching $\int\int_{\mathcal{F}} \omega_z^2 \partial w/\partial z dx dy$ is strong/weak during the early/late stage of the connection. The decrease of both vortex stretching and viscous dissipation in the later phase makes horizontal viscous diffusion relatively important.

It is instructive to compare the evolution of a surface-connected vortex to that predicted by a two-dimensional Lamb laminar vortex which has an analytical solution for the vorticity given by

$$\omega(r, t_d) = \frac{\Gamma R_{e0}}{4\pi t_d} e^{-r^2 R_{e0}/4t_d} , \tag{3.18}$$

where r is the distance from the vortex center, Γ the total circulation, and t_d the decay time. The vorticity at the center ω^{core} is given by

$$\omega^{core}(t_d) = \frac{\Gamma R_{e0}}{4\pi t_d} . \tag{3.19}$$

To effect comparison, we define an initial time t' for the connected vortex using the criterion $\alpha \leq 20°$, obtain Γ by the integration of ω_z over the region $\omega_z \geq 0.05\omega_z^{core}$ at that time, and obtain the time scale $\tau = t_d$ by solving (3.19) using these values and the observed ω^{core} at this (initial) time. The diffusion time is then given by $t_d = t - t' + \tau$.

Figure 3-12 compares the decay rates of surface-connected vortices to that of a Lamb vortex (solid line) assuming either the actual Reynolds number $R_{e0} = 1000$ (Figure 3-12*a*), or one based on eddy viscosity (Figure 2-3*a*) with Reynolds number $R_{eT} \approx 100$ (Figure 3-12*b*). The figures show that the decay rate of surface-connected vortices is substantially slower than that predicted by eddy viscosity and is in fact more comparable to that due to laminar diffusion (at $R_{e0} = 1000$). This reflects the fact that for a vortex which has

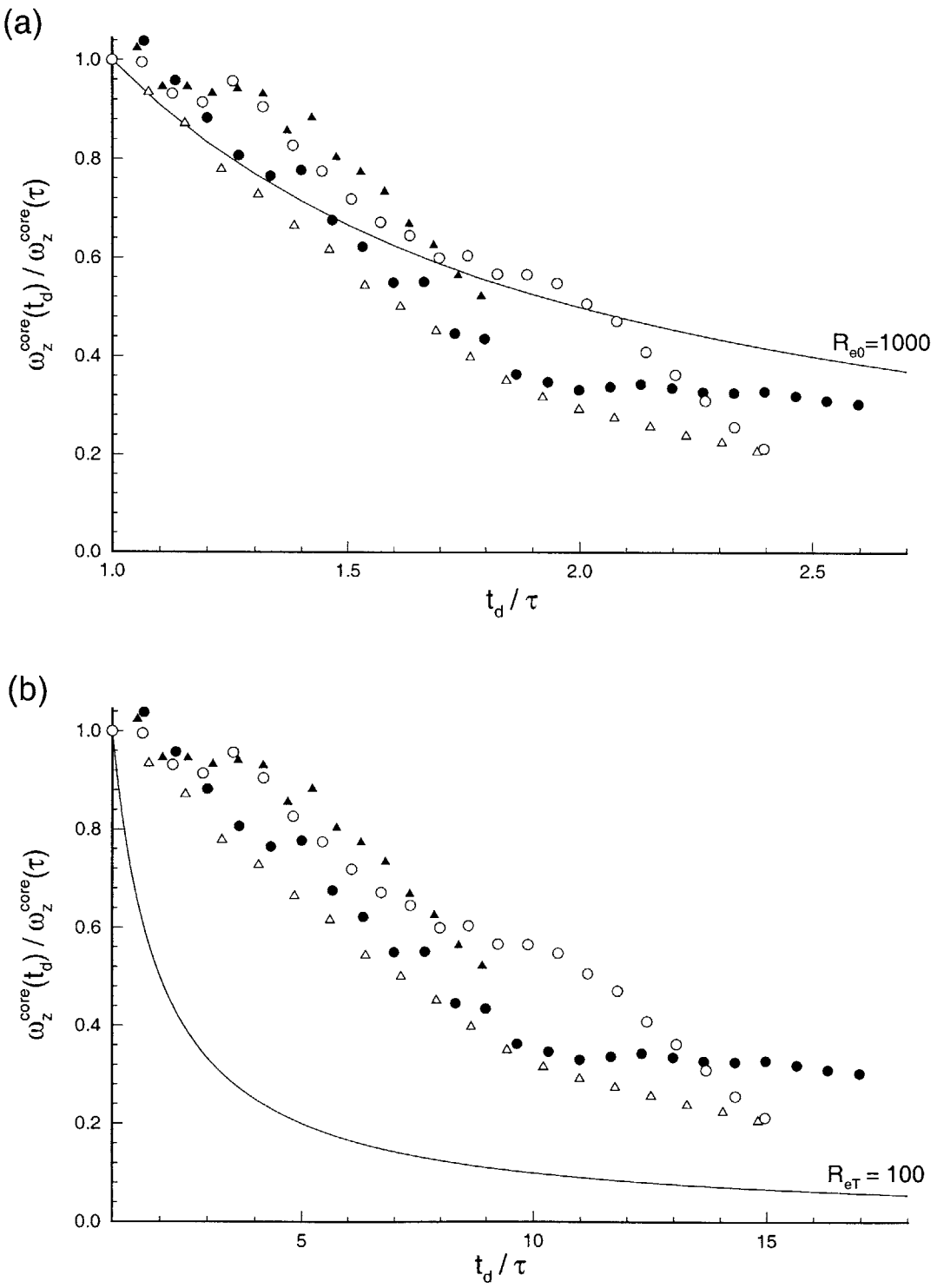

Figure 3-12: Comparison of the decay rate between surface-connected vortices and a two-dimensional Lamb laminar vortex which is at (a) the same Reynolds number $R_{e0} = 1000$; and (b) $R_{eT} \approx 100$ based on eddy viscosity. The symbols represent different surface-connected vortices in Figure 3-3 whose positions are given in Figure 3-9.

connected to the surface, dissipation is small as shown in Figure 3-10 (the dissipation for strong coherent vortices, say conditioned by $\omega_z \geq 2\omega_z^{rms}$, is even smaller than the average value for all vortices.) The conclusion is that, relative to surface-parallel vorticity which dissipates rapidly in the surface inner layer, connected surface-normal vortices decay slowly and thus remain persistent on the surface. This persistence of connected vortices has been reported in experiments (see e.g. Sarpkaya, 1996).

We point out that vortex stretching remains a dominant process during most of vortex connection and the net effect diminishes only as the connection is established (the net effects that remain help maintain the strength of the connected vorticity). The three-dimensional effects associated with vortex stretching are thus an important aspect of FST, and quasi-two-dimensional hypotheses (e.g. Gharib *et al.* 1994, Pan & Banerjee 1995) do not in general obtain. The three-dimensionality of FST has also been argued by Walker *et al.* (1996) who based their conclusion solely on turbulence statistics, which we discuss in the next section.

3.4 Effects of surface layers on turbulence statistics

In this section we discuss the roles of the surface inner and outer layers in the statistics of turbulence scales, Reynolds-stress balance, and enstrophy dynamics.

3.4.1 Turbulence scales

The velocity two-point correlation function is defined as

$$R_{lm}(r,z) = \frac{\langle u_l(\vec{x}_p) u_l(\vec{x}_p + \vec{e}_m r)\rangle}{\langle u_l'^2\rangle}, \quad l = 1,2,3, \quad m = 1,2\,, \tag{3.20}$$

where $\vec{e}_m$ is the unit vector in the m-direction and r the distance between the two points. Summation notation is *not* implied for $l = 1,2,3$.

The Taylor microscale is

$$\lambda_{lm}(z) \;=\; \left[-\frac{2}{(\partial^2 R_{lm}(r,z)/\partial r^2)\,|_{r=0}} \right]^{1/2}$$

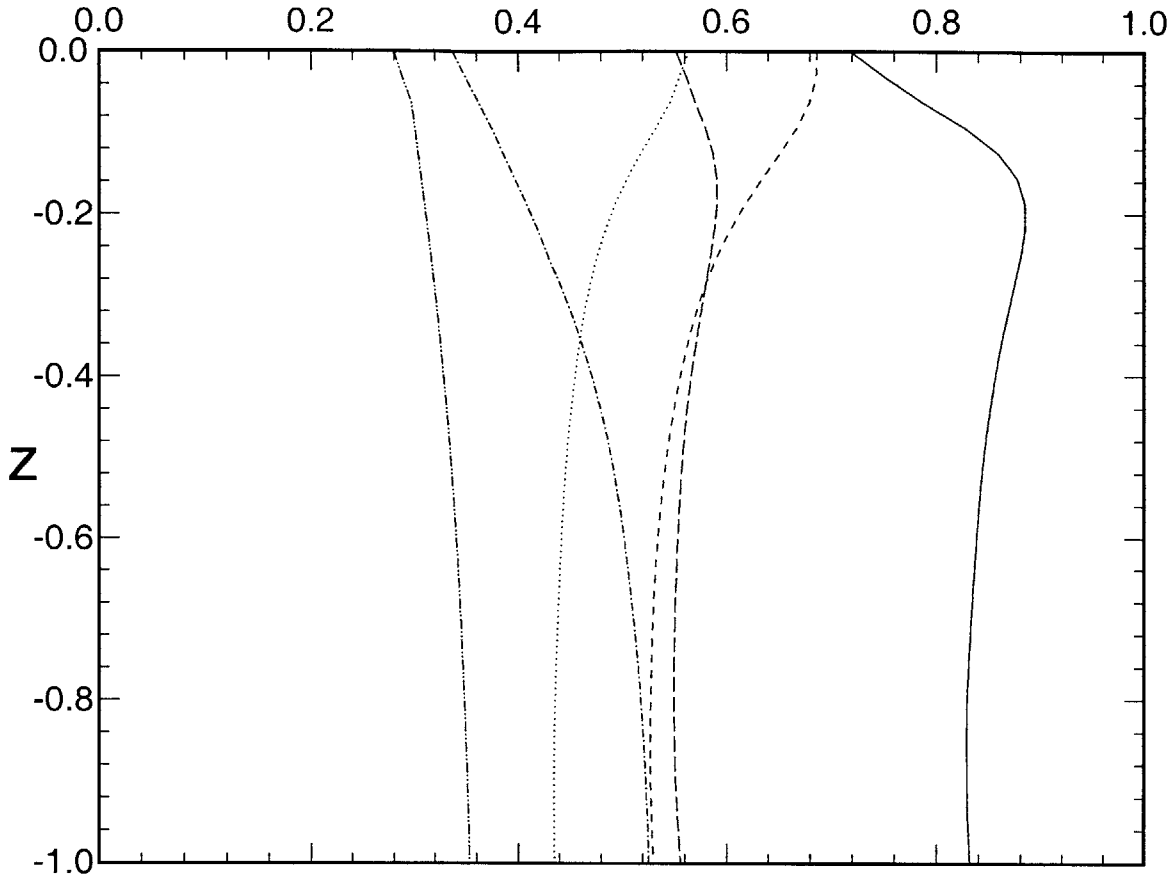

Figure 3-13: Vertical variations of Taylor microscales: ———— , λ_{11}; – – – – , λ_{21}; – · – · – , λ_{13}; · · · · · · · , λ_{12}; —— —— , λ_{22}; —··—··— , λ_{32}.

$$= \left[\frac{2\langle u_l'^2\rangle}{\langle(\partial u_l'/\partial x_m)^2\rangle}\right]^{1/2} . \tag{3.21}$$

Figure 3-13 plots the vertical variations of Taylor microscales λ_{lm}. The streamwise scale associated with the spanwise velocity λ_{21} and the spanwise scale associated with the streamwise velocity λ_{12} increase as the free surface is approached. This phenomenon is consistent with what Handler *et al.* (1993) have found (although the rate of increase in shear-flow FST here is smaller than that in open-channel FST). To explain it, Handler *et al.* (1993) proposed a 'pancake' model which states that eddy structures get flattened as they impinge the free surface. To show this picture more clearly, we look at the Taylor microscale λ_{lm}^{ω} which is de-

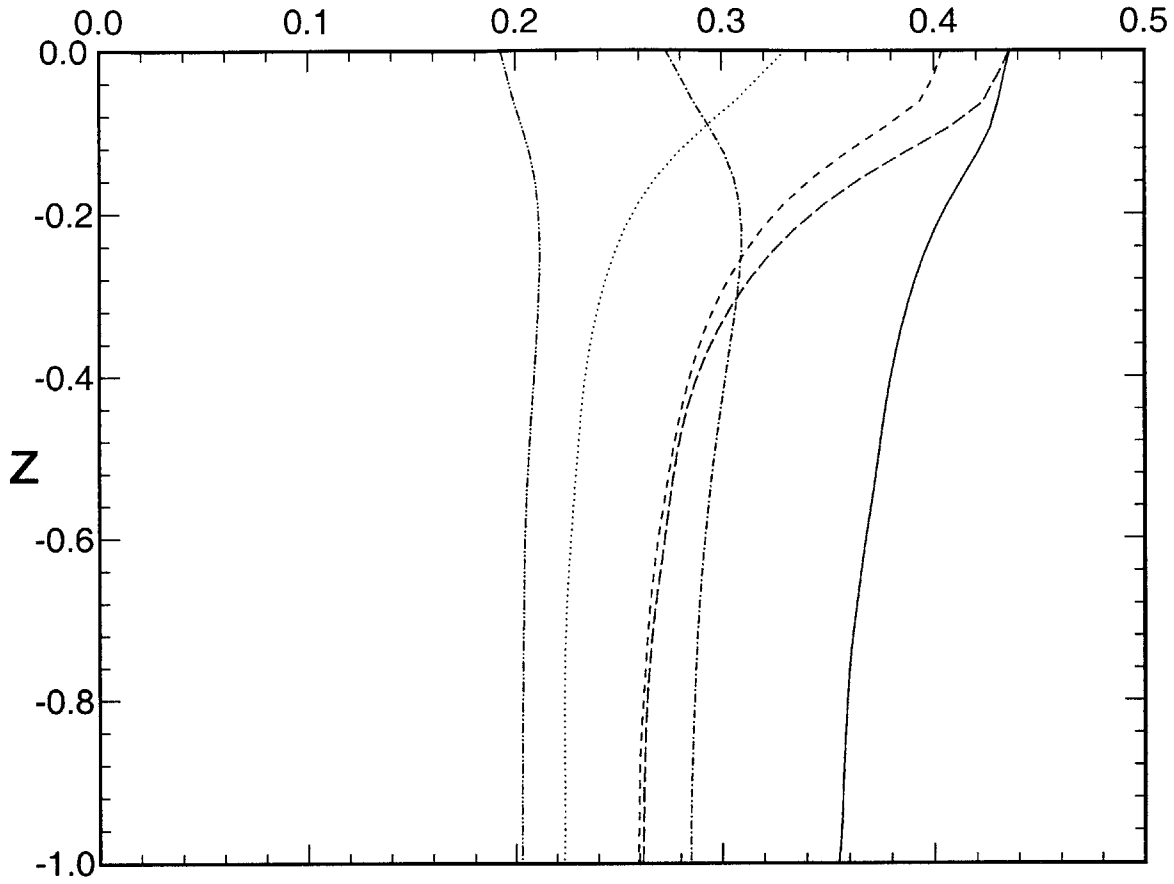

Figure 3-14: Vertical variations of Taylor microscales for vorticity: ———— , λ_{11}^{ω}; - - - - , λ_{21}^{ω}; - · - - · - , λ_{13}^{ω}; · · · · · · · , λ_{12}^{ω}; —— —— , λ_{22}^{ω}; —··—··— , λ_{32}^{ω}.

fined in terms of vorticity instead of velocity in (3.21). As shown in Figure 3-14, the scales of horizontal vorticity increase within the outer layer. The decrease of vertical vorticity scales is believed to be caused by the stretching of surface-normal vorticity.

Thus, the vertical variations of Taylor microscales (of velocity, and especially of vorticity) support the 'pancake' model proposed by Handler *et al.* (1993). Apparently, the 'pancake' (vortex structure) gets flattened because of the blockage effect of the surface when it is swept to the surface by upwelling motions. Therefore, the 'pancake' model is a result of the outer layer.

3.4.2 Reynolds-stress balance

For FST with a two-dimensional mean shear, the equations for the primary components of the Reynolds stresses $\langle u'^2\rangle$, $\langle v'^2\rangle$ and $\langle w'^2\rangle$ are (see e.g. Hinze 1975, p. 323)

$$\frac{\partial\langle u'^2\rangle}{\partial t} = \underbrace{2\langle p'\frac{\partial u'}{\partial x}\rangle}_{I} + \underbrace{\frac{1}{R_{e0}}\frac{\partial^2\langle u'^2\rangle}{\partial z^2}}_{II} \underbrace{-\frac{2}{R_{e0}}\langle\frac{\partial u'}{\partial x_k}\frac{\partial u'}{\partial x_k}\rangle}_{III} \underbrace{-\frac{\partial}{\partial z}\langle u'^2w'\rangle}_{IV} \underbrace{-2\langle u'w'\rangle\frac{\partial\langle u\rangle}{\partial z}}_{V}, \tag{3.22}$$

$$\frac{\partial\langle v'^2\rangle}{\partial t} = \underbrace{2\langle p'\frac{\partial v'}{\partial y}\rangle}_{I} + \underbrace{\frac{1}{R_{e0}}\frac{\partial^2\langle v'^2\rangle}{\partial z^2}}_{II} \underbrace{-\frac{2}{R_{e0}}\langle\frac{\partial v'}{\partial x_k}\frac{\partial v'}{\partial x_k}\rangle}_{III} \underbrace{-\frac{\partial}{\partial z}\langle v'^2w'\rangle}_{IV}, \tag{3.23}$$

$$\frac{\partial\langle w'^2\rangle}{\partial t} = \underbrace{2\langle p'\frac{\partial w'}{\partial z}\rangle}_{I} + \underbrace{\frac{1}{R_{e0}}\frac{\partial^2\langle w'^2\rangle}{\partial z^2}}_{II} \underbrace{-\frac{2}{R_{e0}}\langle\frac{\partial w'}{\partial x_k}\frac{\partial w'}{\partial x_k}\rangle}_{III} \underbrace{-\frac{\partial}{\partial z}\langle w'^3\rangle - 2\frac{\partial}{\partial z}\langle p'w'\rangle}_{IV}. \tag{3.24}$$

Here I are the pressure–strain correlation terms, II the viscous diffusion terms, III the dissipation terms, IV the transport terms, and V the shear flow production terms.

Figures 3-15 to 3-17 show the vertical profiles of the above terms. Most are similar to those in open-channel FST (Handler *et al.* 1993). Compared with grid FST, however, many are qualitatively different.

Turbulence production

A fundamental difference between shear-flow FST (or open-channel FST) and grid FST is that the former has turbulence production from the mean shear, while the latter purely decays. For the two-dimensional mean shear $\langle u\rangle(z)$ studied in this paper, (3.22)–(3.24) show that only the u' equation has the production term $-2\langle u'w'\rangle\partial\langle u\rangle/\partial z$, which means that only the streamwise velocity component obtains energy directly from the mean shear flow. Therefore, u' is larger than v' and w', which is shown in Figure 3-1(b).

Figure 3-15 shows that turbulence production decreases as the free surface is approached. This decrease is a result of two effects: (i) the reduction of the vertical velocity w', as a result of the blockage effect, as the free surface is approached; and (ii) more importantly, the reduction of the mean velocity shear $\partial\langle u\rangle/\partial z$ inside the surface inner layer. In fact,

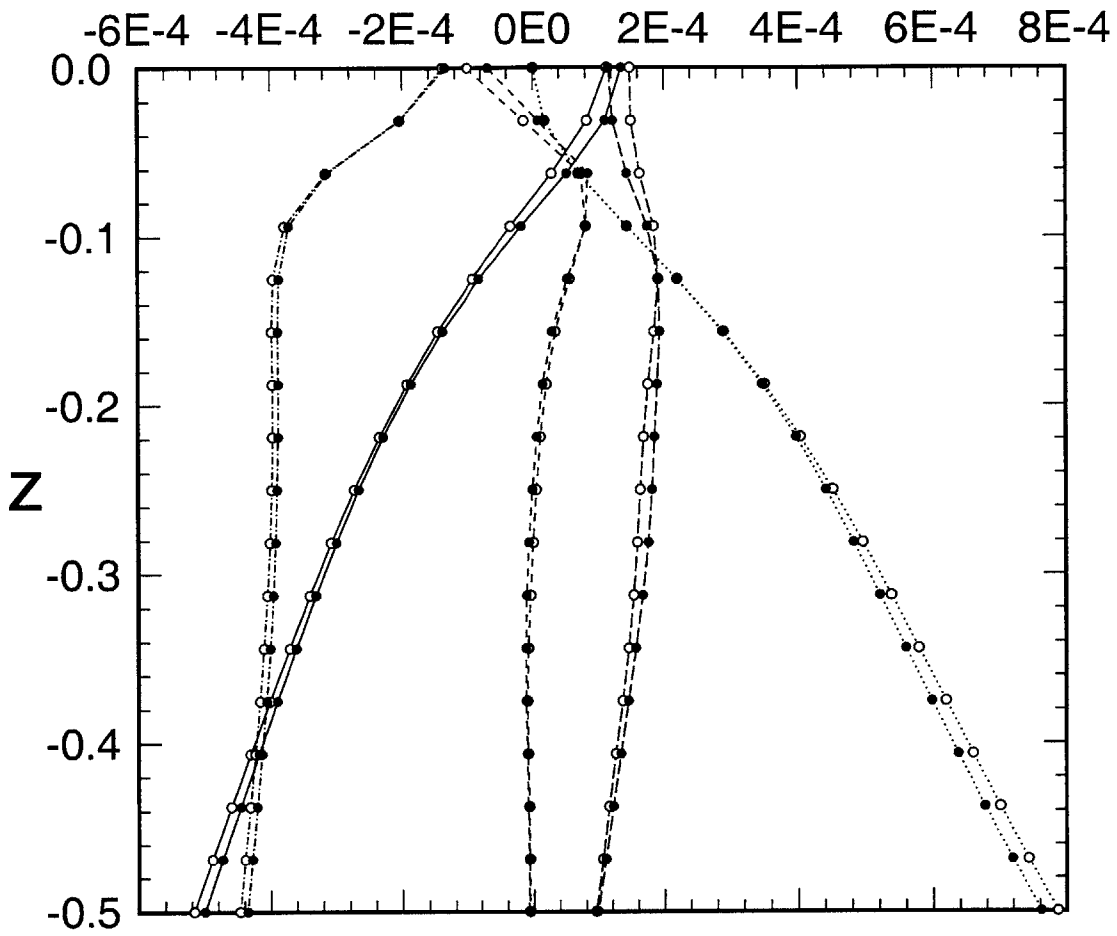

Figure 3-15: Terms in the Reynolds-stress equation for $\langle u'^2 \rangle$: ———— , pressure–strain correlation term $2\langle p' \partial u'/\partial x \rangle$; – – – – , viscous diffusion term $(1/R_{e0})\partial^2 \langle u'^2 \rangle / \partial z^2$; – · – · – , dissipation term $-(2/R_{e0})\langle \partial u'/\partial x_k \cdot \partial u'/\partial x_k \rangle$; —— —— , transport term $-\partial \langle u'^2 w' \rangle / \partial z$; ····· , shear flow production term $-2\langle u'w' \rangle \partial \langle u \rangle / \partial z$. The symbol ∘ corresponds to F_{r0}=0.7; and • to F_{r0}=0. Froude number effects are discussed in §3.5.

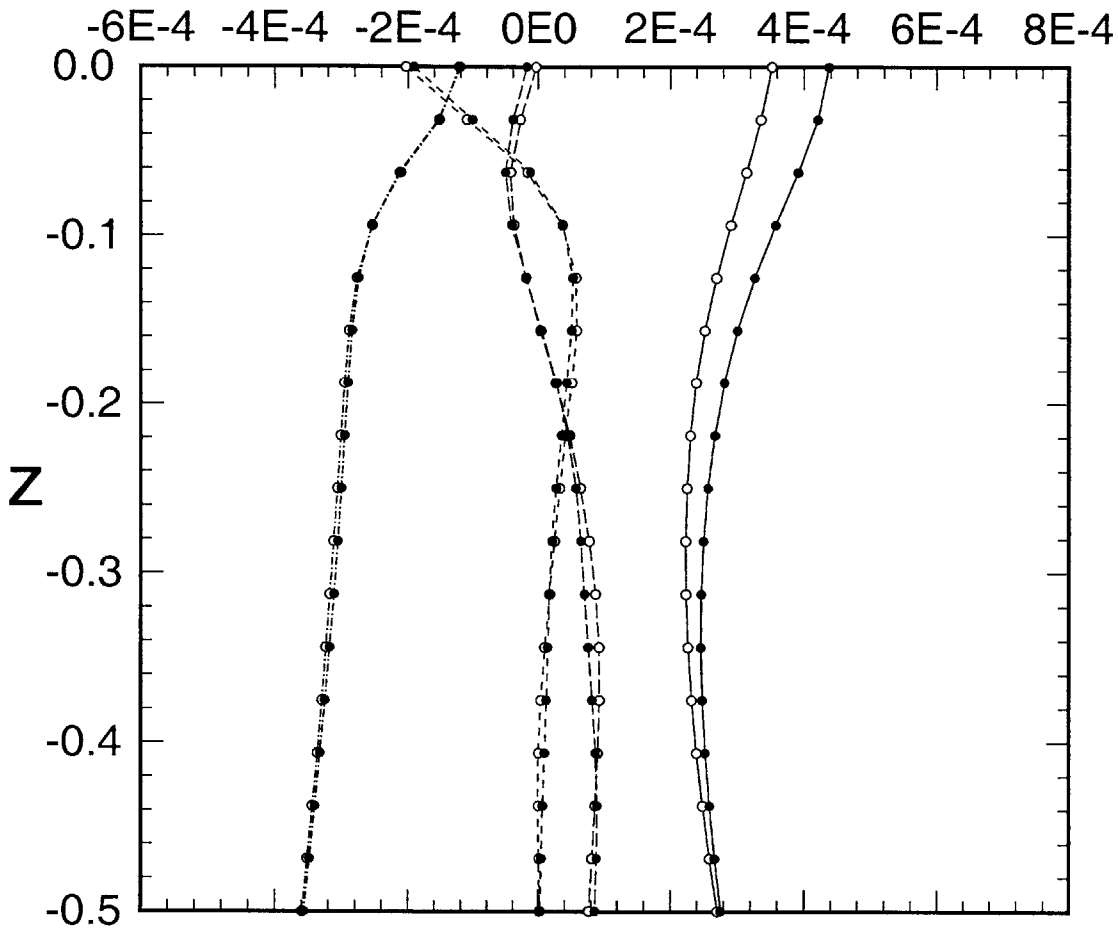

Figure 3-16: Terms in the Reynolds-stress equation for $\langle v'^2 \rangle$: ———— , pressure–strain correlation term $2\langle p' \partial v'/\partial y \rangle$; – – – – , viscous diffusion term $(1/R_{e0})\partial^2 \langle v'^2 \rangle / \partial z^2$; – · – · – , dissipation term $-(2/R_{e0})\langle \partial v'/\partial x_k \cdot \partial v'/\partial x_k \rangle$; — — , transport term $-\partial \langle v'^2 w' \rangle / \partial z$. The symbol ○ corresponds to F_{r0}=0.7; and • to F_{r0}=0. Froude number effects are discussed in §3.5.

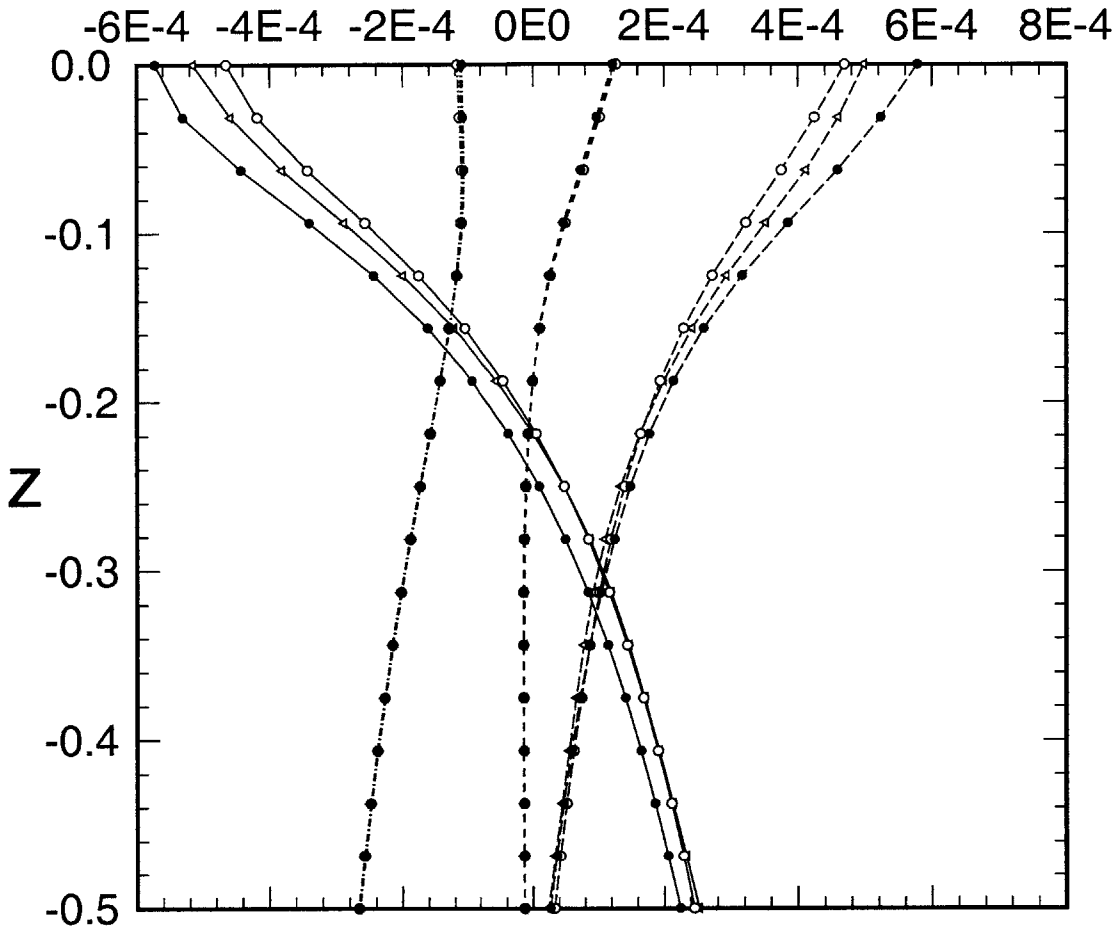

Figure 3-17: Terms in the Reynolds-stress equation for $\langle w'^2 \rangle$: ———— , pressure–strain correlation term $2\langle p' \partial w'/\partial z \rangle$; – – – – , viscous diffusion term $(1/R_{e0})\partial^2 \langle w'^2 \rangle / \partial z^2$; – · – · – , dissipation term $-(2/R_{e0})\langle \partial w'/\partial x_k \cdot \partial w'/\partial x_k \rangle$; —— —— , transport term $-\partial \langle w'^3 \rangle / \partial z - 2\partial \langle p' w' \rangle / \partial z$. The symbol ○ corresponds to F_{r0}=0.7; '◁' to F_{r0}=0.35; and ● to F_{r0}=0. Froude number effects are discussed in §3.5.

at the free surface, the mean shear becomes zero in accordance with the zero mean stress requirement at $z = 0$.

Dissipation

For the dissipation term, there is a significant reduction within the surface inner layer for both the horizontal components u' and v' (Figures 3-15 and 3-16). The decrease in the dissipation is a direct result of the zero stress condition at the free surface. More specifically, if we write explicitly the expression for the dissipation, say for the u' component

$$-\frac{2}{R_{e0}}\langle\frac{\partial u'}{\partial x_k}\frac{\partial u'}{\partial x_k}\rangle = -\frac{2}{R_{e0}}\langle(\frac{\partial u'}{\partial x})^2\rangle - \frac{2}{R_{e0}}\langle(\frac{\partial u'}{\partial y})^2\rangle - \frac{2}{R_{e0}}\langle(\frac{\partial u'}{\partial z})^2\rangle \; ; \tag{3.25}$$

we see from §3.2 that the value of $\partial u'/\partial x$ increases over the outer layer and the variation of $\partial u'/\partial y$ is small. It is the last term $\partial u'/\partial z$ that must decrease abruptly inside the surface layer to reach the value dictated by the boundary condition (3.5), which is shown in Figure 3-2(b). The reduction in the overall dissipation is thus due to the decrease of this term near the free surface.

Unlike in Figures 3-15 and 3-16, the surface inner layer has no visible effect on the dissipation of w' (Figure 3-17). The dissipation for the w' component is

$$-\frac{2}{R_{e0}}\langle\frac{\partial w'}{\partial x_k}\frac{\partial w'}{\partial x_k}\rangle = -\frac{2}{R_{e0}}\langle(\frac{\partial w'}{\partial x})^2\rangle - \frac{2}{R_{e0}}\langle(\frac{\partial w'}{\partial y})^2\rangle - \frac{2}{R_{e0}}\langle(\frac{\partial w'}{\partial z})^2\rangle \; . \tag{3.26}$$

Figure 3-2(b) shows that over the outer layer, $\partial w'/\partial x$ and $\partial w'/\partial y$ decrease while $\partial w'/\partial z$ increases. Thus the surface inner layer has little effect on the dissipation of w'.

If we now sum the dissipation of u', v', and w', we obtain the conclusion that the total turbulent kinetic energy dissipation

$$\epsilon = \frac{1}{R_{e0}}(\langle\frac{\partial u'}{\partial x_k}\frac{\partial u'}{\partial x_k} + \frac{\partial v'}{\partial x_k}\frac{\partial v'}{\partial x_k} + \frac{\partial w'}{\partial x_k}\frac{\partial w'}{\partial x_k}\rangle) \tag{3.27}$$

decreases within the inner layer. Therefore most of the kinetic energy dissipation occurs outside the inner layer. This result is in contrast with the boundary layer next to a wall where the opposite is true.

The decreased dissipation at the free surface was first observed by Handler *et al.* (1993) and further discussed by Perot & Moin (1995) and Walker *et al.* (1996). Perot & Moin (1995) conjectured that the two-componentality of the turbulence near the surface and therefore the lack of the usual energy cascade leads to the reduction of dissipation. Walker *et al.* (1996) explained the reduction by the decrease of horizontal vorticity, which is in the same spirit as the present explanation (3.25) and (3.26), although their explanation is slightly more complicated. Walker *et al.* (1996) wrote the kinetic energy dissipation as

$$\epsilon = \frac{1}{R_{e0}}(s_{ij}s_{ji} + \frac{1}{2}\omega_i\omega_i) \ , \tag{3.28}$$

and showed that the decrease in dissipation results from the reduction in the enstrophy $\omega_i\omega_i$. We would like to point out that the reduction in two of the components of $s_{ij}s_{ji}$: $s_{13}s_{31}$ and $s_{23}s_{32}$, in the surface inner layer (Figure 3-2*a*), also contributes to the decrease of dissipation. From our DNS data, it is found that the variation in enstrophy is responsible for about 70% of the reduction in dissipation, while the variation in s_{13} and s_{23} is responsible for the remaining 30%.

Pressure–strain correlation

Since energy is extracted from the mean shear flow to u', u' is larger than v' and w'. In order to return to isotropy, energy is further transfered from u' to v' and w' through pressure–strain correlation terms. Figures 3-15 to 3-17 show that $2\langle p'\partial u'/\partial x\rangle$ is in general negative, while $2\langle p'\partial v'/\partial y\rangle$ and $2\langle p'\partial w'/\partial z\rangle$ are in general positive (except near the free surface where $2\langle p'\partial w'/\partial z\rangle$ becomes negative). Thus u' in general loses energy to v' and w'.

Figure 3-17 shows that $2\langle p'\partial w'/\partial z\rangle$ becomes negative near the free surface, which means that w' loses energy to the two horizontal velocity components. As pointed out by Perot & Moin (1995), near the surface, the inter-component energy transfer is controlled by both splat and antisplat events: splats transfer energy from w' to u' and v' but antisplats transform the energy back immediately. It is the imbalance between the splats and antisplats that results in the inter-component energy transfer; and this imbalance is controlled by viscous processes such as dissipation and diffusion. Perot & Moin (1995) found that for grid FST,

the viscous effects and therefore the inter-component energy transfer is small. The results obtained by Walker *et al.* (1996) have also confirmed the relatively small inter-component energy transfer in grid FST.

The situation in shear-flow FST is, however, substantially different. If we assume that the viscous effects in shear-flow FST are small, as in the case of grid FST, the energy w' loses to u' and v' should be small. If we further take into account the extra energy transfered from u' to v' and w' because of the mean flow production, the energy that w' loses should be even smaller (or w' may in fact gain energy). However, Figure 3-17 shows that $2\langle p'\partial w'/\partial z\rangle$ is not negligible at the surface. As a matter of fact, the inter-component energy transfer is significant for shear-flow FST. Therefore, the imbalance between splats and antisplats near the free surface is not insignificant for shear-flow FST.

The inter-component energy transfer is also important for open-channel FST (e.g. Handler *et al.* 1993). The main difference in inter-component energy between shear-flow FST/open-channel FST and grid FST can be understood as follows. Both shear-flow FST and open-channel FST are characterized by strong splat motions (which sweep horizontal vorticity filaments to the surface and make the surface inner layer clear) and antisplat motions, although the causes in these two types of flow are different. The former emerges from the sheared bulk flow while the latter is due to ejections from the rigid wall. Our experience in grid FST shows that splats and antisplats are quite rare compared to shear-flow FST and open-channel FST. A good example is the 'switch-bottom test' by Pan & Banerjee (1995), which we discussed in §3.3.2. Therefore, the inter-component energy transfer in shear-flow FST and open-channel FST is much more important than that in grid FST.

Viscous diffusion and transport

The viscous diffusion terms in shear-flow FST are similar to those in open-channel and grid FST. Diffusion is directly related to the turbulence fluctuation profile, which is shown in Figure 3-1(b). Diffusion is small in the bulk flow below and becomes comparable to other dominant terms only near the surface. For u' and v', the fluctuation increases not only because of the blockage effect of the surface, but also because of the reduction of dissipation

in the surface inner layer. Viscous diffusion is most significant in the inner layer. Figures 3-15 and 3-16 show that diffusion transports energy from the near-surface-region to the deep region for u' and v'. For w', since its profile is mainly affected by the blockage effect of the surface, diffusion is appreciable inside the outer layer instead of the inner layer. Figure 3-17 shows that w' diffusion moves energy from the deep region to the surface.

The transport terms represent the vertical energy transfer due to turbulence velocity fluctuations (and pressure fluctuation in the case of w'). Since the transport terms reflect the subtle variations in the fluctuation profile, we believe they are highly dependent on the specific problem being studied.

Finally, we remark that the summation of all the right-hand-side terms in (3.22)–(3.24), which gives the time-rate-of-change of the Reynolds stresses, is small since the near-surface region is quasi-steady. This is as expected and is in contrast with grid FST which is purely decaying.

3.4.3 Enstrophy dynamics

We have seen that the surface inner layer is manifest primarily in the horizontal vorticity components rather than in the vertical vorticity component. It is thus natural to expect that the inner layer will have disparate effects on the dynamics of the horizontal versus vertical enstrophy components.

The equation for the balance of the enstrophy components is given by (e.g. Tennekes & Lumley 1972 p. 87; Balint *et al.* 1988)

$$\frac{\partial\langle\omega_x'^2\rangle}{\partial t} = \underbrace{-\frac{\partial\langle\omega_x'^2 w'\rangle}{\partial z}}_{II} \underbrace{+2\langle(\omega_x'^2\frac{\partial u'}{\partial x}+\omega_x'\omega_y'\frac{\partial u'}{\partial y}+\omega_x'\omega_z'\frac{\partial u'}{\partial z})\rangle}_{III} \tag{3.29}$$

$$\underbrace{+2\langle\omega_x'\omega_z'\rangle\frac{\partial\langle u\rangle}{\partial z}}_{IV} \underbrace{+2\frac{\partial\langle u\rangle}{\partial z}\langle\omega_x'\frac{\partial u'}{\partial y}\rangle}_{V} + \underbrace{\frac{1}{R_{e0}}\frac{\partial^2}{\partial z^2}\langle\omega_x'^2\rangle}_{VI} \underbrace{-\frac{2}{R_{e0}}\langle\frac{\partial\omega_x'}{\partial x_k}\frac{\partial\omega_x'}{\partial x_k}\rangle}_{VII},$$

$$\frac{\partial\langle\omega_y'^2\rangle}{\partial t} = \underbrace{-2\langle\omega_y'w'\rangle\frac{\partial^2\langle u\rangle}{\partial z^2}}_{I} \underbrace{-\frac{\partial\langle\omega_y'^2w'\rangle}{\partial z}}_{II} \underbrace{+2\langle(\omega_x'\omega_y'\frac{\partial v'}{\partial x}+\omega_y'^2\frac{\partial v'}{\partial y}+\omega_y'\omega_z'\frac{\partial v'}{\partial z})\rangle}_{III} \quad (3.30)$$
$$\underbrace{+2\frac{\partial\langle u\rangle}{\partial z}\langle\omega_y'\frac{\partial v'}{\partial y}\rangle}_{V} \underbrace{+\frac{1}{R_{e0}}\frac{\partial^2}{\partial z^2}\langle\omega_y'^2\rangle}_{VI} \underbrace{-\frac{2}{R_{e0}}\langle\frac{\partial\omega_y'}{\partial x_k}\frac{\partial\omega_y'}{\partial x_k}\rangle}_{VII},$$

$$\frac{\partial\langle\omega_z'^2\rangle}{\partial t} = \underbrace{-\frac{\partial\langle\omega_z'^2w'\rangle}{\partial z}}_{II} \underbrace{+2\langle(\omega_x'\omega_z'\frac{\partial w'}{\partial x}+\omega_y'\omega_z'\frac{\partial w'}{\partial y}+\omega_z'^2\frac{\partial w'}{\partial z})\rangle}_{III} \quad (3.31)$$
$$\underbrace{+2\frac{\partial\langle u\rangle}{\partial z}\langle\omega_z'\frac{\partial w'}{\partial y}\rangle}_{V} \underbrace{+\frac{1}{R_{e0}}\frac{\partial^2}{\partial z^2}\langle\omega_z'^2\rangle}_{VI} \underbrace{-\frac{2}{R_{e0}}\langle\frac{\partial\omega_z'}{\partial x_k}\frac{\partial\omega_z'}{\partial x_k}\rangle}_{VII}.$$

Here the terms are: I, gradient production; II, transport by velocity fluctuations; III, production due to the gradients of velocity fluctuation; IV, production due to mean shear; V, mixed production; VI, viscous diffusion; and VII, dissipation.

The vertical variation of the above terms is plotted in Figures 3-18 to 3-20. The results are largely consistent with the open-channel FST figures of Leighton *et al.* (1991). Comparing with the grid FST results (Walker *et al.* 1996), the terms related to hairpin vortex structures are different.

The most significant effects of the presence of the free surface in all these cases are the large vertical variations of the viscous diffusion term (VI) and dissipation term (VII) for the horizontal vorticity within the surface inner layer where vertical gradients of horizontal vorticities are high. Hence, both diffusion and dissipation increase sharply in the inner layer. In the limit of zero Froude number, it can be shown that diffusion and dissipation must be in balance at the surface (this is also true for $\langle w'^2\rangle$). For small Froude numbers, such a balance must still approximately obtain.

Unlike the horizontal enstrophy components, the viscous diffusion and dissipation terms for $\langle\omega_z'^2\rangle$ are not affected by the surface layer (Figure 3-20). This is consistent with our

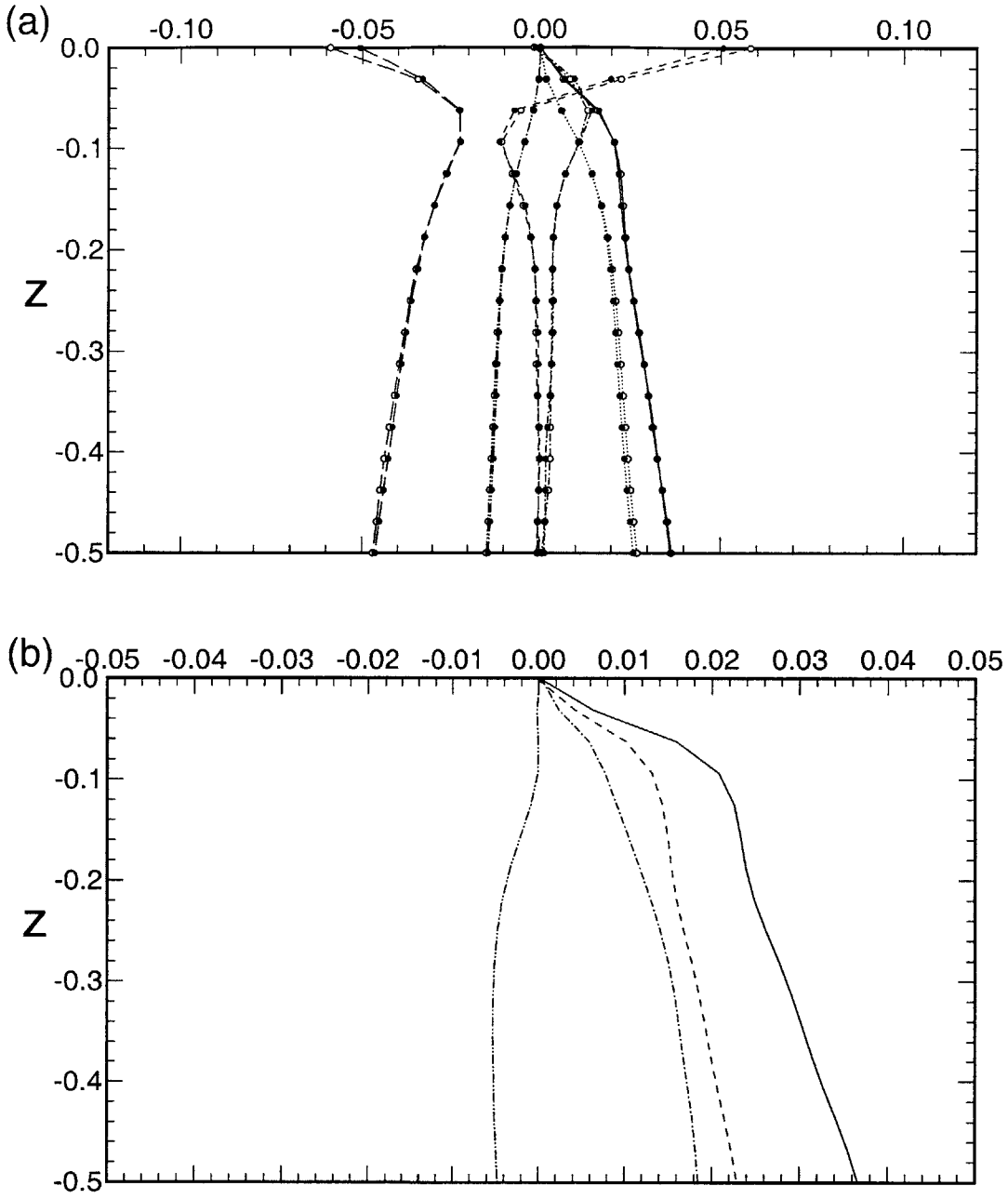

Figure 3-18: Terms in the enstrophy evolution equation for $\langle \omega_x'^2 \rangle$: ($a$) $- \cdot - \cdot -$, transport by velocity fluctuations $-\partial \langle \omega_x'^2 w' \rangle / \partial z$; ———— , production due to the gradients of velocity fluctuation $2\langle (\omega_x'^2 (\partial u'/\partial x) + \omega_x' \omega_y' (\partial u'/\partial y) + \omega_x' \omega_z' (\partial u'/\partial z)\ ) \rangle$; $\cdots\cdots$, production due to mean shear $2\langle \omega_x' \omega_z' \rangle \partial \langle u \rangle / \partial z$; $-\cdots-\cdots-$, mixed production $2(\partial \langle u \rangle / \partial z) \langle \omega_x' (\partial u'/\partial y) \rangle$; $- - - -$, viscous diffusion $(1/R_{e0}) \partial^2 \langle \omega_x'^2 \rangle / \partial z^2$; —— —— , dissipation $-(2/R_{e0}) \langle (\partial \omega_x'/\partial x_k)(\partial \omega_x'/\partial x_k) \rangle$. ($b$) ———— , The total production due to the gradients of velocity fluctuation; $- - - -$, $2\langle \omega_x'^2 (\partial u'/\partial x) \rangle$; $- \cdot - \cdot -$, $2\langle \omega_x' \omega_y' (\partial u'/\partial y) \rangle$; $-\cdots-\cdots-$, $2\langle \omega_x' \omega_z' (\partial u'/\partial z) \rangle$. The symbol $\circ$ corresponds to F_{r0}=0.7; and $\bullet$ to F_{r0}=0. Froude number effects are discussed in §3.5.

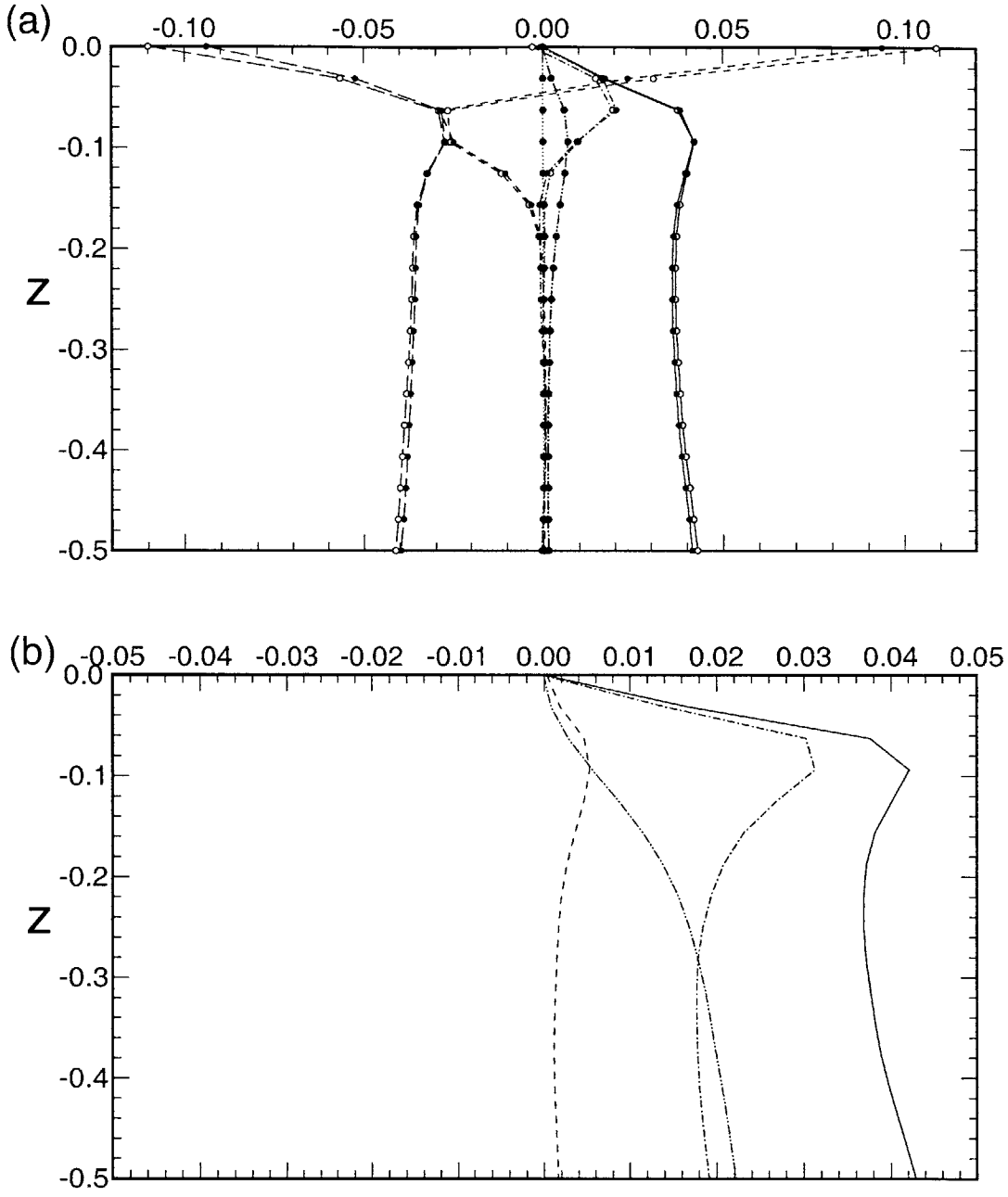

Figure 3-19: Terms in the enstrophy evolution equation for $\langle \omega_y'^2 \rangle$: (a) - · - · - , transport by velocity fluctuations $-\partial\langle \omega_y'^2 w' \rangle / \partial z$; ———— , production due to the gradients of velocity fluctuation $2\langle (\omega_x'\omega_y'(\partial v'/\partial x) + \omega_y'^2(\partial v'/\partial y) + \omega_y'\omega_z'(\partial v'/\partial z)\ )\rangle$; · · · · · · · , gradient production $-2\langle \omega_y' w' \rangle (\partial^2\langle u \rangle / \partial z^2)$; —·—·— , mixed production $2(\partial\langle u \rangle/\partial z)\langle \omega_y'(\partial v'/\partial y)\rangle$; - - - - , viscous diffusion $(1/R_{e0})\partial^2\langle \omega_y'^2 \rangle / \partial z^2$; —— —— , dissipation $-(2/R_{e0})\langle (\partial\omega_y'/\partial x_k)(\partial\omega_y'/\partial x_k)\rangle$. (b) ———— , The total production due to the gradients of velocity fluctuation; - - - - , $2\langle \omega_x'\omega_y'(\partial v'/\partial x)\rangle$; - · - · - , $2\langle \omega_y'^2(\partial v'/\partial y)\rangle$; —··—··— , $2\langle \omega_y'\omega_z'(\partial v'/\partial z)\rangle$. The symbol ∘ corresponds to F_{r0}=0.7; and • to F_{r0}=0. Froude number effects are discussed in §3.5.

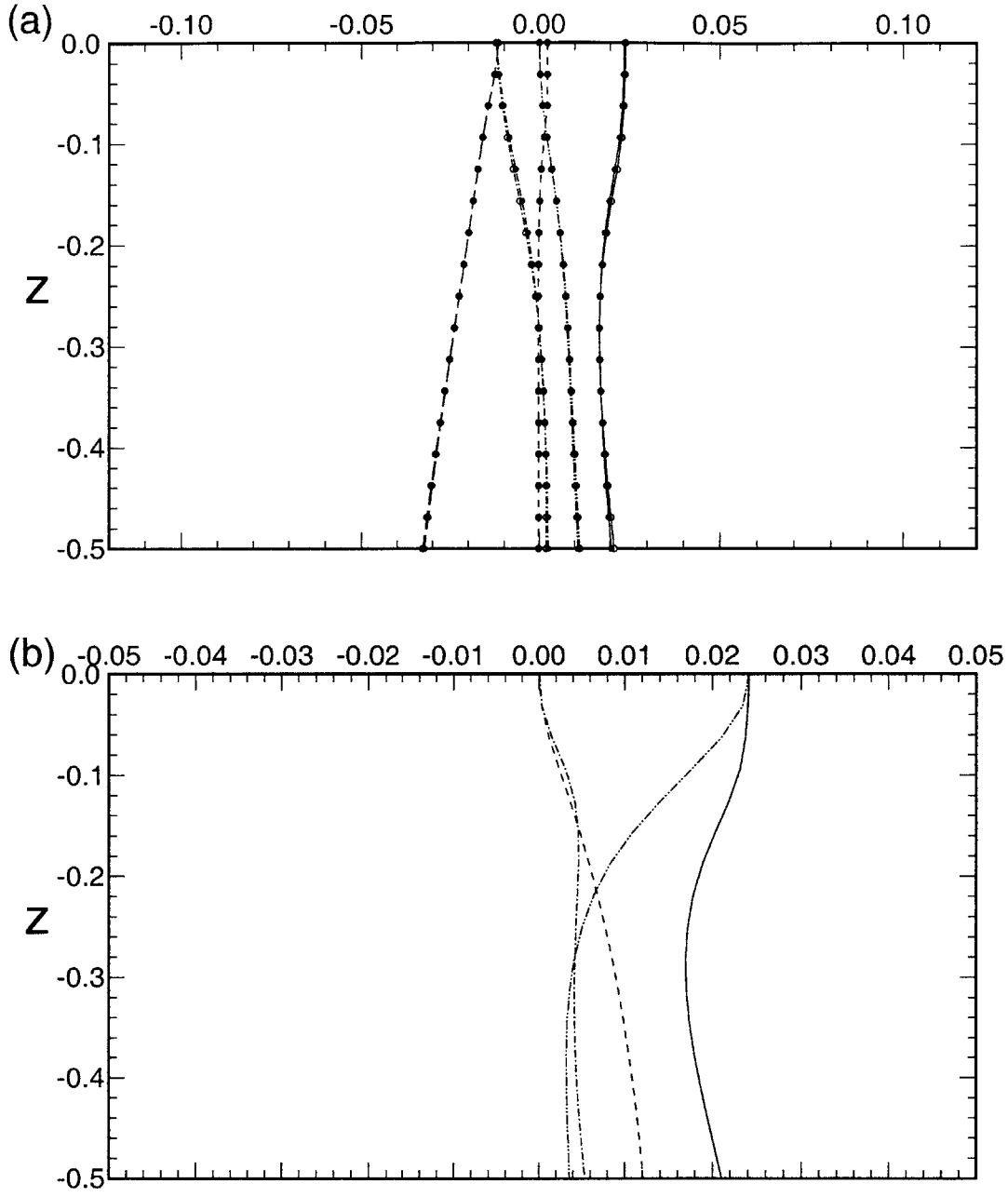

Figure 3-20: Terms in the enstrophy evolution equation for $\langle \omega_z'^2 \rangle$: (a) $- \cdot - \cdot -$, transport by velocity fluctuations $-\partial \langle \omega_z'^2 w' \rangle / \partial z$; ———— , production due to the gradients of velocity fluctuation $2\langle (\omega_x' \omega_z' (\partial w'/\partial x) + \omega_y' \omega_z' (\partial w'/\partial y) + \omega_z'^2 (\partial w'/\partial z)\ ) \rangle$; $- \cdots - \cdots -$, mixed production $2(\partial \langle u \rangle / \partial z) \langle \omega_z' (\partial w'/\partial y) \rangle$; $- - - -$, viscous diffusion $(1/R_{e0}) \partial^2 \langle \omega_z'^2 \rangle / \partial z^2$; —— —— , dissipation $-(2/R_{e0}) \langle (\partial \omega_z'/\partial x_k)(\partial \omega_z'/\partial x_k) \rangle$. (b) ———— , The total production due to the gradients of velocity fluctuation; $- - - -$, $2\langle \omega_x' \omega_z' (\partial w'/\partial x) \rangle$; $- \cdot - \cdot -$, $2\langle \omega_y' \omega_z' (\partial w'/\partial y) \rangle$; $- \cdots - \cdots -$, $2\langle \omega_z'^2 (\partial w'/\partial z) \rangle$. The symbol $\circ$ corresponds to F_{r0}=0.7; and $\bullet$ to F_{r0}=0. Froude number effects are discussed in §3.5.

earlier observations that the variation of ω_z is small over the surface inner layer since it is not ω_z but $\partial\omega_z/\partial z$ that is controlled by the inner layer.

The different behaviors of viscous diffusion/dissipation for horizontal vorticity and vertical vorticity explain the rapid vanishing of the head portion of hairpin vortices within the surface inner layer in contrast to the persistence of surface-connected vortices as discussed in §3.3.

For the same reason, the transport term (II), which reflects the vertical variation of the intensity of vorticity fluctuation, also has disparate behavior for horizontal and vertical vorticity components. The transport for $\langle\omega_x'^2\rangle$ and $\langle\omega_y'^2\rangle$ becomes significant in the surface inner layer where ω_x' and ω_y' attenuate rapidly, and ω_x' and ω_y' enstrophy is transported from below to the surface inner layer. The transport term for $\langle\omega_z'^2\rangle$, on the other hand, becomes important in the outer layer instead of the inner layer, since the fluctuation of ω_z' varies over the outer layer.

Both the inner layer effects and the outer layer effects are manifest in the production due to the gradients of velocity fluctuation term (III). To show the mechanisms more clearly, Figures 3-18(b), 3-19(b), and 3-20(b) plot each component of III. As shown, the production due to stretching ($2\langle\omega_x'^2(\partial u'/\partial x)\rangle$, $2\langle\omega_y'^2(\partial v'/\partial y)\rangle$, and $2\langle\omega_z'^2(\partial w'/\partial z)\rangle$) is dominant near the surface. Their significant increase in the outer layer is due to the increase in stretching ($\partial u'/\partial x$, $\partial v'/\partial y$, and $\partial w'/\partial z$) there. (Leighton *et al.* 1991 and Walker *et al.* 1996 explained this by using the 'splat' concept. Walker *et al.* 1996 further argued that FST is fully three-dimensional up to the surface based on the vertical stretching $\partial w'/\partial z$.)

The inner layer makes $2\langle\omega_x'^2(\partial u'/\partial x)\rangle$ and $2\langle\omega_y'^2(\partial v'/\partial y)\rangle$ different from $2\langle\omega_z'^2(\partial w'/\partial z)\rangle$. For horizontal components, the stretching of horizontal vorticity decreases sharply over the inner layer since ω_x and ω_y diminish at the free surface. The stretching of vertical vorticity, on the other hand, continues to increase up to the free surface, since ω_z does not need to decrease in the inner layer.

An important observation is the significance of the ω_y stretching (Figure 3-19b). It increases inside the outer layer and reaches its peak just outside the inner layer. This peak is more prominent than that of ω_x (Figure 3-18b); it is also much larger than the horizontal

stretching in grid FST (Walker *et al.* 1996). The significance of the ω_y stretching in shear-flow FST is due to the hairpin vortex structures investigated in §3.3. The head portion of hairpin vortices corresponds to the enhanced spanwise vorticity ω_y, which is shown in Figure 3-1(b). As the hairpin head enters the outer layer, it is stretched by the diverging flow due to the blockage effect of the surface ('pancake' model or 'splat' model). Therefore, the above difference in ω_x and ω_y stretching is consistent with the hairpin vortex structures discussed in §3.3.

The remaining terms are characteristic of shear-flow FST and not present in grid FST. The gradient production term (I) exchanges enstrophy between mean vorticity and the vorticity fluctuation and only the ω_y equation has this term. The production due to mean shear (IV) is similar to the production term in the Reynolds-stress equation and only ω_x has this term. The mixed production (V) is present for all the three components of vorticity. An interesting observation from Figures 3-18 to 3-20 is that the summation of all the mixed production for each vorticity component is close to zero, which means that the mixed production somehow redistributes the enstrophy among the vorticity components.

3.5 The effects of the Froude number

3.5.1 Overview

In the study of FST of small Froude numbers, it is often suggested that the free surface can be approximated as a flat free-slip plate, in which case free-slip boundary conditions apply at $z = 0$:

$$\frac{\partial u}{\partial z} = \frac{\partial v}{\partial z} = 0 \,, \tag{3.32}$$

$$w = 0 \,, \tag{3.33}$$

$$\frac{\partial p}{\partial z} = 0 \,. \tag{3.34}$$

These are obtained also from (2.3), (2.4), (2.5), and (2.7) (and (2.1)) in the limit $F_{r0} \to 0$.

Since the free-slip-plate approximation does not involve motions of the free surface, the

	$z=0$		$z=-0.125$		$z=-1$	
	$F_{r0}=0.7$	$F_{r0}=0$	$F_{r0}=0.7$	$F_{r0}=0$	$F_{r0}=0.7$	$F_{r0}=0$
$\langle u\rangle$	$0.3771E0$	$0.3763E0$	$0.3924E0$	$0.3921E0$	$0.5206E0$	$0.5221E0$
u'^{rms}	$0.8171E{-}1$	$0.8196E{-}1$	$0.8154E{-}1$	$0.8170E{-}1$	$0.1031E0$	$0.1041E0$
v'^{rms}	$0.7825E{-}1$	$0.7946E{-}1$	$0.7301E{-}1$	$0.7397E{-}1$	$0.8793E{-}1$	$0.8811E{-}1$
w'^{rms}	$0.3003E{-}2$	0	$0.2732E{-}1$	$0.2666E{-}1$	$0.7396E{-}1$	$0.7359E{-}1$
q	$0.1132E0$	$0.1139E0$	$0.1132E0$	$0.1135E0$	$0.1546E0$	$0.1549E0$
$\omega_x'^{rms}$	$0.3961E{-}1$	0	$0.3624E0$	$0.3510E0$	$0.5180E0$	$0.5073E0$
$\omega_y'^{rms}$	$0.3664E{-}1$	0	$0.3903E0$	$0.3913E0$	$0.4147E0$	$0.4382E0$
$\omega_z'^{rms}$	$0.2710E0$	$0.2656E0$	$0.2972E0$	$0.2929E0$	$0.4572E0$	$0.4527E0$
ω_q	$0.2789E0$	$0.2663E0$	$0.6122E0$	$0.6039E0$	$0.8065E0$	$0.8102E0$
$\langle p\rangle-\langle p\rangle_{bottom}$	$-0.9018E{-}5$	0	$-0.7464E{-}3$	$-0.7108E{-}3$	$-0.5470E{-}2$	$-0.5415E{-}2$
p'^{rms}	$0.8434E{-}2$	$0.8448E{-}2$	$0.8519E{-}2$	$0.8526E{-}2$	$0.1143E{-}1$	$0.1145E{-}1$
h'^{rms}	$0.4251E{-}2$	0	—	—	—	—

Table 3.1: Comparison between free-surface turbulence ($F_{r0}=0.7$) and free-slip-plate turbulence ($F_{r0}=0$) at $t=60$.

question remains whether free-surface effects on the turbulent flow are indeed negligible for relatively small Froude numbers. To study this, we compare our DNS results for the free-surface case (F_{r0}=0.7) with another set of (twenty) simulations under identical conditions but using free-slip-plate (F_{r0}=0) boundary conditions (3.32)–(3.34).

Table 3.1 shows the comparison of relevant turbulence statistics between the two cases. In Table 3.1, $\omega_q \equiv ((\omega_x'^{rms})^2+(\omega_y'^{rms})^2+(\omega_z'^{rms})^2)^{1/2}$ is the fluctuation intensity of enstrophy; and $\langle p\rangle$ is the horizontal average of pressure which satisfies

$$\langle p\rangle - \langle p\rangle_{bottom} = -\langle w^2\rangle + \langle w^2_{bottom}\rangle = -\langle w^2\rangle \ . \tag{3.35}$$

Equation (3.35) is obtained by averaging the z-component of the Navier–Stokes equations (2.1) over the (x,y)-plane and integrating with respect to z.

We remark that F_{r0}=0.7 is based on the initial mean velocity deficit U. A more appropriate scale here is the turbulence velocity fluctuation at the surface $q_0 \simeq 0.1U$, which yields the Froude number $F_{rq} \simeq 0.07$. Thus, the difference between the free-slip-plate turbulence and the free-surface turbulence is expected to be quite small, in particular for all the quantities considered in Table 3.1.

The exception to the above observation turns out to be quite subtle. Figure 3-18 shows that inside the surface inner layer, the variations of dissipation and diffusion for horizontal vorticity in the F_{r0}=0.7 case is slightly larger than those in the F_{r0}=0 case. This implies that the vertical gradients of horizontal vorticities increase for the F_{r0}=0.7 case. The outer layer effects, on the other hand, are weakened by the free surface. This can be seen most clearly in Figure 3-17: the pressure–strain correlation term and the transport term in the free-surface case are considerably smaller than those in the F_{r0}=0 case, even for such small Froude numbers.

In the following subsections, we discuss the effects of (small) Froude numbers on the surface inner and outer layers, respectively.

3.5.2 Effects of Froude number on the inner layer

The horizontal vorticity ω_x and ω_y at the surface is given by (3.1) and (3.2). At a free-slip plate, ω_x and ω_y are both zero. At a free surface, however, the surface vorticity components ω_x and ω_y are non-zero, although the magnitude is small for low Froude numbers.

Figure 3-21 shows the free-surface elevation and surface vorticity induced by an underlying vortical structure (we use, as an example, the vortex structure in Figure 3-7*a*). The coherent vortex structure in the Figure (dashed lines) is the cross-section of a hairpin head, whose ω_y component is negative. As the hairpin approaches the free surface, secondary surface vorticity is induced. This can be seen most clearly at the position ($x = 1.2,\ z = 0$). The free surface is depressed and the induced surface vorticity has a positive ω_y component, which is opposite in sign to the main vortex underneath. These observations are consistent with those for laminar vortex interaction with a free surface (see Marcus & Berger 1989, Lugt & Ohring 1994, and Zhang *et al.* 1999).

The opposite signs of the surface vorticity and the one underneath which generates it are confirmed by statistics. The correlation between the vorticity at the surface and the one underneath is defined as:

$$Cor\langle\omega_i(0),\omega_i(z)\rangle \equiv \frac{\langle\omega_i(0)\omega_i(z)\rangle}{\omega_i^{rms}(0)\omega_i^{rms}(z)},\quad i=1,2,3\,, \tag{3.36}$$

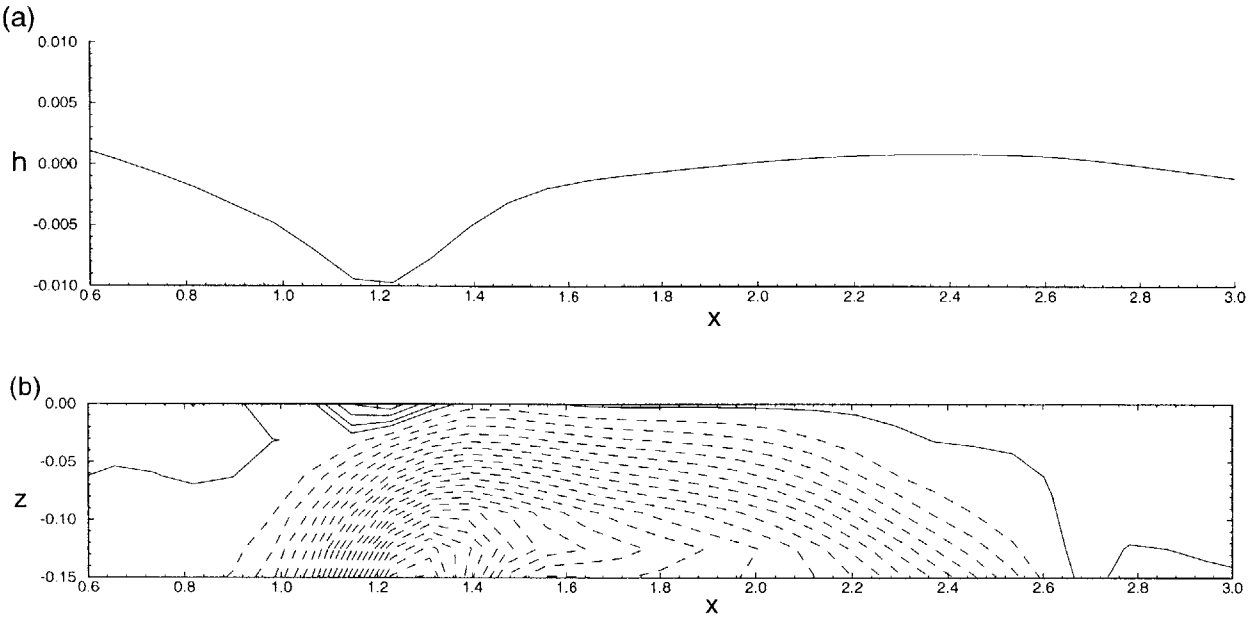

Figure 3-21: (a) Free-surface elevation h and (b) surface vorticity ω_y, induced by an underlying vortex approaching the free surface. The position and time is the same as in Figure 3-7(a). In (b), solid lines represent positive contour values while dashed lines represent negative values. The contour increment is 0.1.

where no summation notation is implied, and $\omega_i(0) \equiv \omega_i|_{z=0}$ and $\omega_i(z) \equiv \omega_i|_{z=z}$ etc.

Figure 3-22 plots the correlation function (3.36) for ω_x, ω_y, and ω_z. $Cor\langle\omega_z(0), \omega_z(z)\rangle$ decreases slowly over the outer layer, which means that the surface-normal vorticity is well correlated with the vortex structures underneath. The correlation functions for ω_x and ω_y, on the other hand, decrease sharply over the surface layer which shows that the structure of horizontal vorticity changes dramatically near the free surface. This result is of fundamental importance when information from surface sensing (such as the imaging of a ship wake) is used to deduce structures of the underlying flow.

Figure 3-22 shows that the correlation functions for ω_x and ω_y are negative for small z. The surface inner layer is the region where horizontal vorticity changes from 'outer' values to the small values at the surface inner layer. Comparing this with the F_{r0}=0 case where surface vorticity is zero, the free surface produces surface vorticity which has signs opposite to those underneath. Therefore, the vertical gradients in the free-surface case are larger than those in the free-slip-plate case. This explains why the surface inner layer effects are slightly

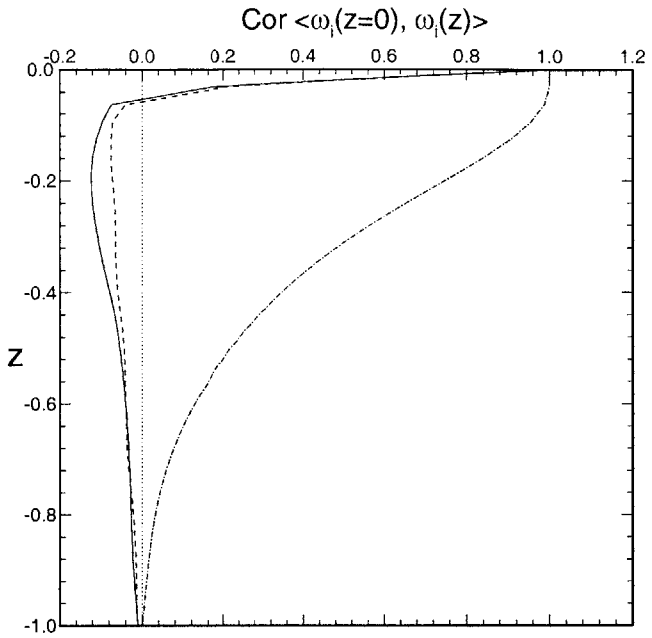

Figure 3-22: Correlation between the vorticity at the surface and vorticity underneath. ——— , $Cor\langle\omega_x(0),\omega_x(z)\rangle$; – – – – , $Cor\langle\omega_y(0),\omega_y(z)\rangle$; – · – · – , $Cor\langle\omega_z(0),\omega_z(z)\rangle$.

larger for FST in Figures 3-18(a) and 3-19(a).

It should be pointed out that surface vorticities at low Froude numbers are small compared to the vorticities of underlying vortex structures. Therefore, the effects of small Froude numbers on the inner layer is not pronounced. The Froude number effects on the outer layer is, however, much more prominent, which we investigate next.

3.5.3 Effects of Froude number on the outer layer

As we pointed out, quantities associated with the pressure distribution have considerable difference between the free-slip-plate turbulence and free-surface turbulence, even for small Froude numbers.

Figure 3-17 of §3.4.2 plots the vertical variation of the terms in the Reynolds-stress equation for $\langle w'^2\rangle$, for both the free-surface (F_{r0}=0.7) case and the free-slip plate (F_{r0}=0) case. To provide a further check, we plot here also the results for F_{r0}=0.35. As shown in Figure 3-17, the effects of Froude numbers on dissipation and diffusion are negligible.

However, the differences in the pressure–strain correlation term and transport term are significant.

The transport term can be written as

$$-\frac{\partial}{\partial z}\langle w'^3\rangle - 2\frac{\partial}{\partial z}\langle p'w'\rangle = -\langle 3w'^2\frac{\partial w'}{\partial z}\rangle - 2\langle w'\frac{\partial p'}{\partial z}\rangle - 2\langle p'\frac{\partial w'}{\partial z}\rangle \,. \tag{3.37}$$

The first two terms on the right are negligible for small Froude numbers while the third term cancels the pressure–strain correlation term. As a result, at the free-surface, the transport term approximately balances the pressure–strain correlation term for small Froude numbers. (The balance is exact for zero Froude number.) We thus focus our attention on the pressure–strain correlation and perform a detailed analysis of the blockage effects of the free surface relative to a free-slip surface.

As fluid particles approach the free surface, they are forced to diverge and move in the horizontal directions. This is called the *splat* event. Based on the conservation of mass, the motion approaching the free surface must be balanced by the motion leaving the surface. The latter is called *antisplat* event. Splat and antisplat events are discussed by Perot & Moin (1995) for the zero Froude number case. Here we investigate the effects of the Froude number on these events.

The splat and antisplat events are manifested in the DNS results. Figure 3-23 shows a typical example. In a splat event (left side of Figure 3-23), fluid moving towards the free surface turns near the surface and diverges horizontally. In an antisplat event (right side of Figure 3-23), fluid particles moving towards each other at the surface meet and leave the surface. The centers of the splats and antisplats in Figure 3-23(a) appear as respectively outward and inward nodal points of the velocity field in the (x, y)-plane and are therefore points of high pressure. In regions between splats and antisplats, horizontal velocities are high and the pressure is generally low (Figure 3-23a).

It should be pointed out that there exists another form of antisplat, which is the stretching of surface-connected vortices shown in §3.3.3 (as well as another form of splat for the half-compression of surface-connected vortices at late evolution stages). Unlike that in Figure 3-23, the antisplat occurring at a surface-connected vortex is characterized by high horizontal

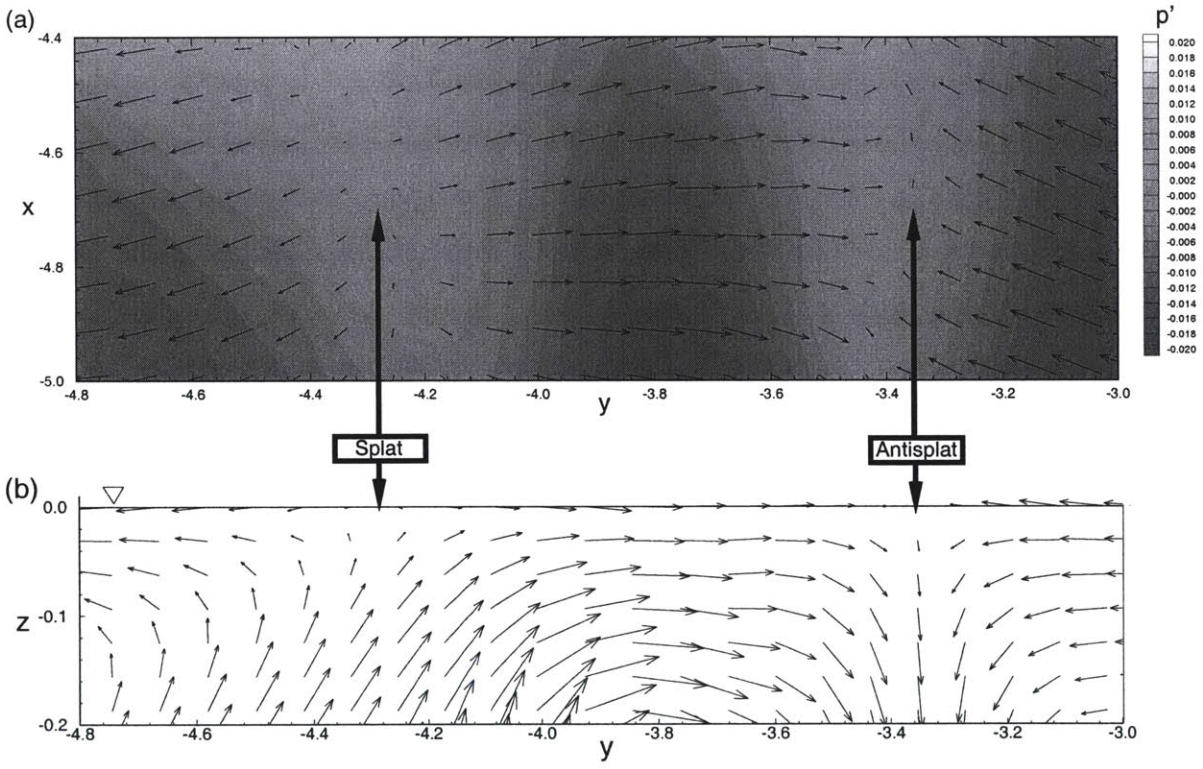

Figure 3-23: Splat and antisplat processes in FST. (a) Horizontal velocity vector (u', v') at the free surface. The background shows contours of the pressure fluctuation. (b) Velocity vector (v', w') in a vertical (y, z) section (at $x = -4.7$).

velocity and low pressure.

The splat event in Figure 3-23 corresponds to the 'upwellings' described by Pan & Banerjee (1995) or the 'splat' model Leighton *et al.* (1991) used. The antisplat event in Figure 3-23 corresponds to the 'downdrafts' of Pan & Banerjee (1995). The aforementioned surface-connected vortices are the same as the 'spin' model of Leighton *et al.* (1991). To understand the effects of Froude number on pressure–strain correlation, we focus on the first two since they are responsible for most of the differences due to Froude number in the inter-component energy transfer.

To investigate the statistics of splat and antisplat events over the free surface, we perform conditional averaging based on different stages of the splat and antisplat processes. The condition for such averaging is specified at each grid point on the free surface by the value of $-(\partial u'/\partial x + \partial v'/\partial y)^*/q^*$. Here the superscript * indicates that the quantity is normalized by its r.m.s. value. Positive/negative $\partial u'/\partial x + \partial v'/\partial y$ (negative/positive $\partial w'/\partial z$) corresponds to splat/antisplat respectively. This value, further divided by velocity fluctuation $q \equiv (u'^2 + v'^2 + w'^2)^{1/2}$, quantifies the splat and antisplat processes. Large values indicate that the fluid particle is close to the core of a splat/antisplat (large horizontal velocity divergence but small velocity at the stagnant points) while small values correspond to the neutral region between a splat and an antisplat (small divergence but large velocity when traveling along the surface).

Figure 3-24 shows the area histogram according to the above criterion. It is shown that most grid points at the free surface are located in the neutral region between splats and antisplats. It is also seen that the area of the antisplat region is larger than that of the splat region. (The ratio is about 55% to 45%.)

Figure 3-25 shows the conditional average of turbulence kinetic energy and pressure fluctuation at each stage of splat/antisplat processes. At the free surface, following a fluid particle from splat to antisplat (from left to right in Figure 3-23), the pressure is high at the splat while the kinetic energy is low there; in the middle between the splat and antisplat, the kinetic energy is high but the pressure is low; at the antisplat, the kinetic energy returns to a low value and the pressure increases again. This is consistent with Figure 3-23.

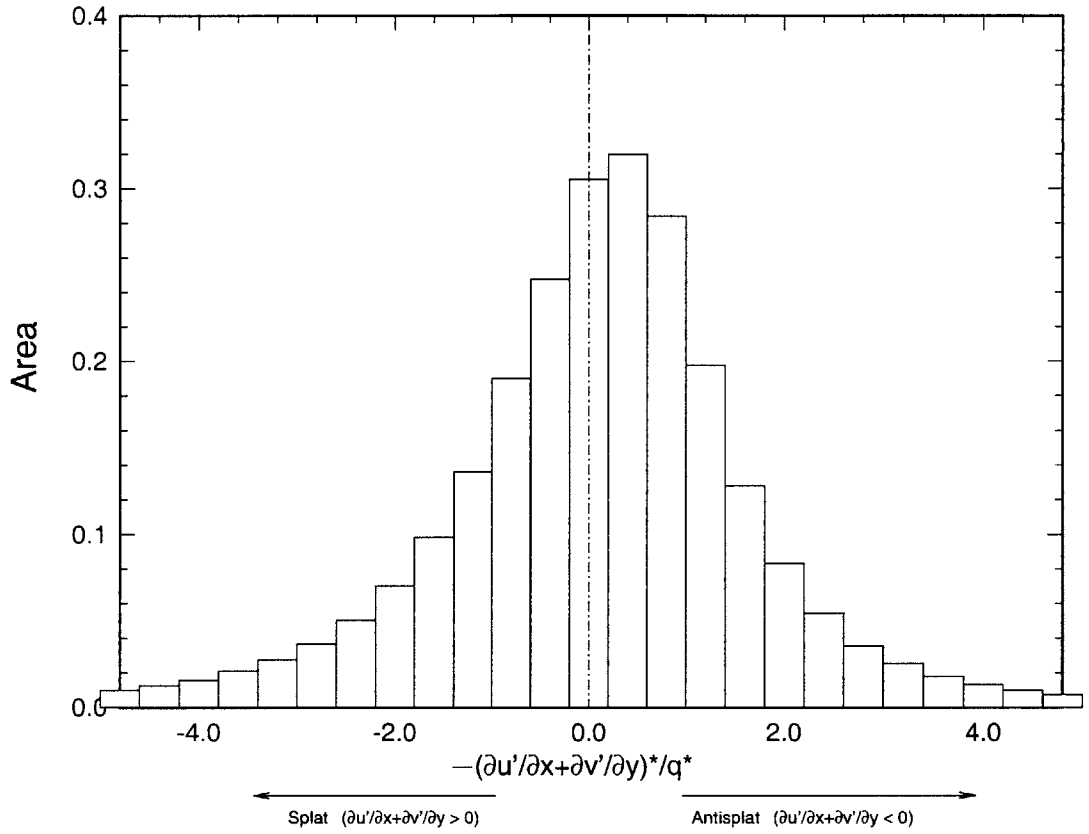

Figure 3-24: Area histogram based on the conditional average of splat and antisplat processes.

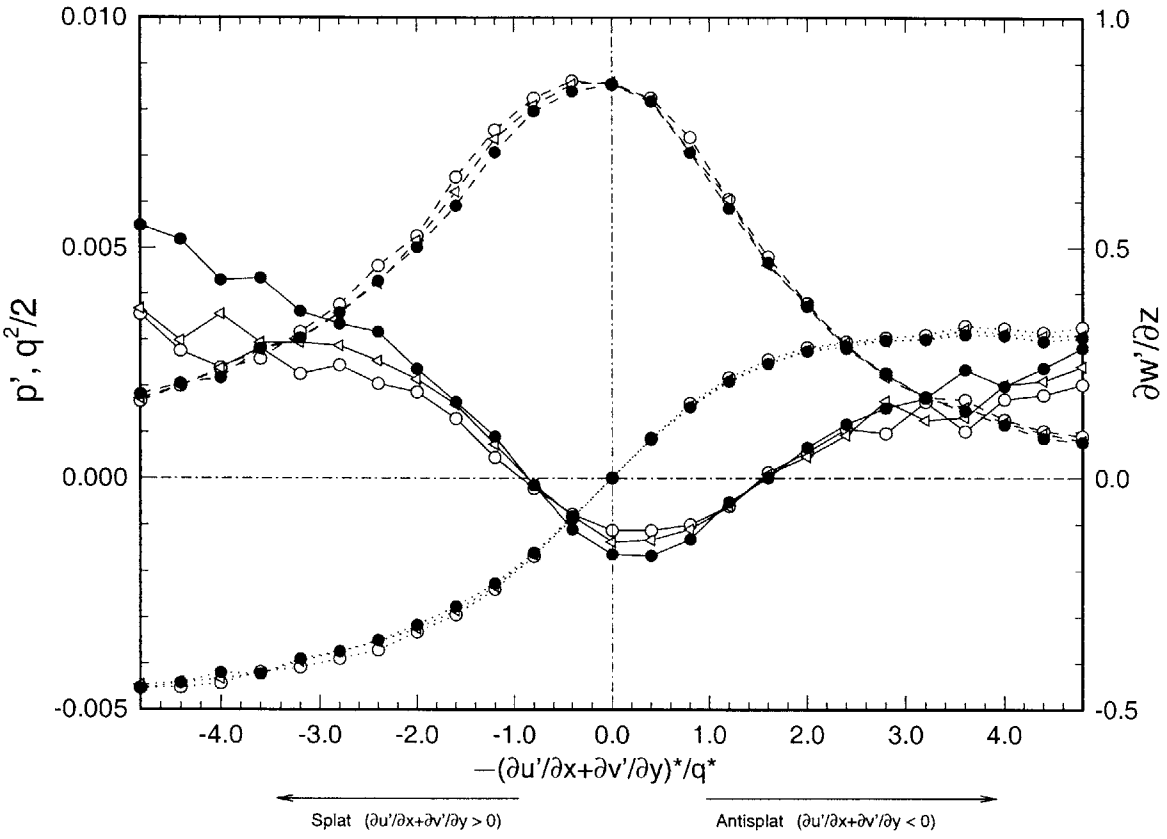

Figure 3-25: Conditional average of pressure fluctuation p', turbulence kinetic energy $q^2/2 = (u'^2 + v'^2 + w'^2)/2$, and $\partial w'/\partial z$ during splat and antisplat processes: ———— , p'; – – – – , $q^2/2$; · · · · · · · , $\partial w'/\partial z$. The symbol ○ refers to F_{r0}=0.7, ◁ to F_{r0}=0.35, and ● to F_{r0}=0.

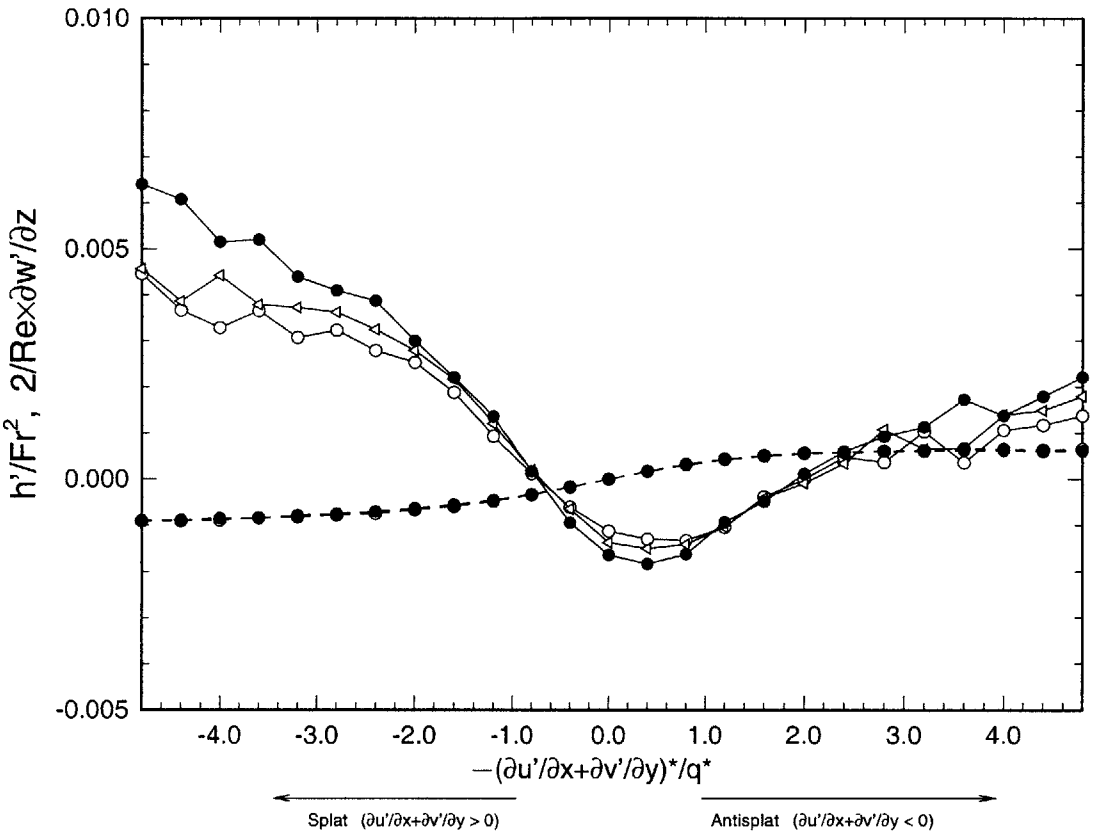

Figure 3-26: Conditional average of free-surface elevation h'/F_{r0}^2 and viscous stress $(2/R_{e0})\partial w'/\partial z$ during splat and antisplat processes: ———— , h'/F_{r0}^2; – – – – , $(2/R_{e0})\partial w'/\partial z$. The symbol ○ refers to F_{r0}=0.7, ◁ to F_{r0}=0.35; and '●' to F_{r0}=0. Here h'/F_{r0}^2 is undefined for F_{r0}=0 where we plot the value $p' - (2/R_{e0})\partial w'/\partial z$ instead.

It is important to point out that the curve of pressure fluctuation in Figure 3-25 as well as the area histogram in Figure 3-24 are not left–right symmetric; and the curve of $\partial w'/\partial z$ in Figure 3-25 is not left–right anti-symmetric. Otherwise the overall integration of the pressure–strain correlation $\langle p'\partial w'/\partial z\rangle$ will be zero. It should also be mentioned that the region of surface-connected vortices is located near the central part in Figure 3-25 since q is large for surface-connected vortices.

Figure 3-27 plots the histogram of pressure–strain correlation, which is the product of pressure fluctuation and $\partial w'/\partial z$ (Figure 3-25) weighted by the area under Figure 3-24. The histogram is not left–right anti-symmetric about the splat and antisplat. The integration gives the overall negative pressure–strain correlation at the free surface (Figure 3-17), which indicates that the net energy transfer is from the vertical velocity component to horizontal components.

An important observation from Figure 3-25 is that, although features like $(u'^2+v'^2+w'^2)/2$ and $\partial w'/\partial z$ do not depend very much on the Froude number, the pressure distribution during the splat and antisplat process is sensitive to the Froude number. It is shown that the pressure at splats and antisplats in the free-surface case is considerably lower than that in the free-slip-plate case. The reduction of the pressure in the free-surface case shows that the deformable free surface relieves such impinging. Figure 3-25 also shows that due to the motions of the free surface, the pressure distribution at the free surface is smoother than that at the free-slip plate.

It should be noted that the reduction and smoothing of the pressure during splat/antisplat at a deformable surface does not cause an obvious reduction in the global statistics of pressure fluctuation p'^{rms} (Table 3.1). This issue is subtle: the deformable free surface only changes the *local distribution* of pressure in the splats/antisplats process. Therefore, only when we use the conditional averaging technique to highlight the distribution in the splat/antisplat process, does the difference caused by different Froude numbers appear as shown in Figure 3-25.

The difference in the pressure distribution is caused by the distribution of free-surface elevation. The free-surface dynamic boundary condition (2.5) states that the pressure fluc-

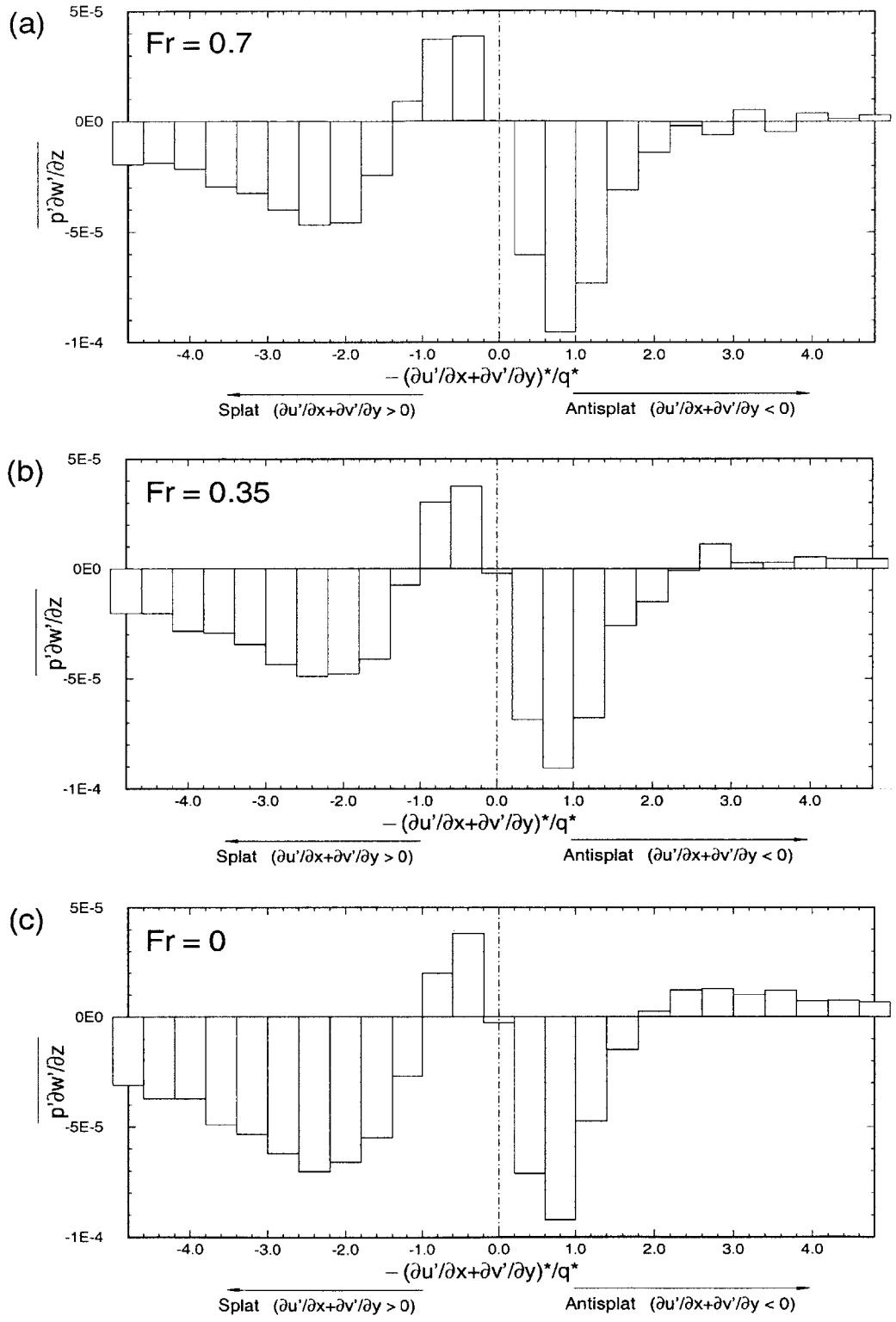

Figure 3-27: Histogram of pressure–strain correlation $\langle p'\partial w'/\partial z\rangle$ based on the conditional average of splat and antisplat processes: (a) F_{r0}=0.7; (b) F_{r0}=0.35; and (c) F_{r0}=0.

tuation p' at $z = 0$ is given by two parts: the hydrostatic pressure h'/F_{r0}^2 and the viscous stress $(2/R_{e0})\partial w'/\partial z$. Figure 3-26 plots the distribution of h'/F_{r0}^2 and $(2/R_{e0})\partial w'/\partial z$ during the splat and antisplat process. During a splat ($\partial w'/\partial z < 0$), p' is smaller than h'/F_{r0}^2, while during an antisplat ($\partial w'/\partial z > 0$), p' is larger than h'/F_{r0}^2. As Figure 3-26 shows, the dependence of $(2/R_{e0})\partial w'/\partial z$ on the Froude number is negligible. It is the hydrostatic pressure h'/F_{r0}^2 that is sensitive to the Froude number. Note that, similar to the pressure distribution, the r.m.s. value of h'/F_{r0}^2 for the whole (x, y)-plane does not differ much as the Froude number changes, i.e. h'^{rms} is scaled by F_{r0}^2. It is the *local distribution* of h'/F_{r0}^2 that is sensitive to the Froude number which is only shown using the conditional averaging in Figure 3-26.

Since the pressure distribution over the splat/antisplat process depends on the Froude number, the pressure–strain correlation is directly affected. Figures 3-27(a to c) compare the histogram of $\langle p'\partial w'/\partial z\rangle$ among the F_{r0}=0.7, 0.35, and 0 cases. It is shown that the free surface transfers considerably less energy from the vertical velocity component to horizontal components than the free-slip-plate. As shown in Figure 3-17, the effect of Froude number on the pressure–strain correlation is felt throughout the outer layer.

In conclusion, it is shown that the local distribution of pressure (free-surface elevation) during the splat/antisplat process is sensitive to the Froude number. Accordingly, the pressure–strain correlation in free-surface turbulence is considerably less than that in free-slip-plate turbulence, even at low Froude numbers. Although the difference in pressure–strain correlation is partially balanced by the corresponding variations in the remaining terms in the Reynolds-stress equations (Figures 3-15 to 3-17) and the eventual influence on Reynolds-stresses is small, as shown in Table 3.1, the sensitivity of the pressure–strain correlation to the Froude number indicates the essentially different physics in the inter-component energy transfer for FST. This is important for the modeling of FST. Moreover, the Froude number effects on the pressure field are of fundamental importance for the generation of surface waves. The effects revealed here are of leading order and should still obtain (and be stronger) for higher Froude numbers where other mechanisms such as those associated with nonlinear free-surface effects are present.

3.6 Conclusions

In this chapter we identify a three-layer structure which is essential to understanding free-surface turbulence: the deeply submerged part of the flow, an outer layer (thin compared to the vertical extent of the shear in the flow), and a much thinner inner layer immediately under the free surface. The outer layer results from the kinematic boundary condition at the free surface, and the inner layer is caused by the dynamic zero-stress conditions.

The outer layer is manifested in the vertical velocity fluctuations, which decrease to the values imposed by the kinematic boundary condition at the surface. This reduction of the vertical velocity fluctuation occurs without any appreciable increase of kinetic energy dissipation, and is primarily compensated by an increase of the horizontal velocity fluctuations. This effect has been observed in different flows with a free surface (e.g. Handler *et al.* 1993, Pan & Banerjee 1995, Walker *et al.* 1996), and can therefore be considered as a generic feature of free-surface turbulence.

The inner layer is indicated by the sharp transition of the two horizontal vorticity components and the vertical derivative of the vertical vorticity component, which are reduced from their bulk (isotropic) values to those imposed by the zero-stress conditions at the free surface. As a result, the inner layer is a region of decreased kinetic energy dissipation and increased enstrophy dissipation. The latter increase is highly localized around vortex connection events. In fact, once an attachment event is completed, the enstrophy dissipation is locally reduced, resulting in significantly slower decay of the attached vortex. Since attachment events occur on a continuous basis, the enstrophy dissipation averaged over the horizontal plane shows an increase inside the inner layer as a permanent and prominent feature.

The surface inner layer makes it possible for vorticity features at the free surface to differ substantially not only from those in the bulk but also from those inside the outer layer. This result is important for practical applications when information from surface sensing is used to deduce characteristics of the underlying flow.

Finally, we identify the importance of non-zero Froude number on free-surface turbulence. We show that, even for very low Froude numbers, there is a finite reduction of the pressure–

strain correlation at the free surface relative to that obtained using a free-slip flat plate as a model for the free surface. This is due to the free-surface elevation which can cause pressure variations comparable to turbulent pressure fluctuations. This should be taken into account in the modeling of free-surface turbulence when the details of the near-surface hydrodynamics are of interest (for example, in the spreading of surfactants).

Chapter 4

Turbulent Diffusion near a Free Surface

In Chapter 3, the features of a free-surface turbulent shear flow in the near-surface region were examined in detail including the distinction and elucidation of an outer layer and an inner layer at the free surface. Chapter 3, however, did not provide quantitative definitions of these free-surface layers, which are important to the modeling of the FST.

The main goal of this chapter is to *quantitatively* study the free-surface boundary layer in order to obtain insights necessary for turbulent modeling of free-surface flows. To do this, we investigate here the mechanism of turbulent diffusion near a free surface. The turbulent diffusion near a free surface has been studied in the past by Hunt (1954), Ellison (1960), Levich (1962), Jobson & Sayre (1970), Davis (1972), Lee & Gill (1977), and Ueda *et al.* (1977). More recently there has been renewed interest in the problem of free-surface turbulence (FST) spurred by the availability of high-resolution numerical simulations and state-of-the-art experimental techniques. Numerical simulations of FST have been performed, for example, by Lam & Banerjee (1988), Handler *et al.* (1991, 1993), Leighton *et al.* (1991), Swean *et al.* (1991), Borue *et al.* (1995), Dimas & Triantafyllou (1995), Pan & Banerjee (1995), Perot & Moin (1995), and Walker *et al.* (1996); while experimental measurements were obtained by Komori *et al.* (1982, 1989), Nakagawa & Nezu (1981), Rashidi & Banerjee (1988, 1990), Gharib *et al.* (1994), and Rashidi (1997), among many others.

In this study, we use a combination of numerical simulation and theoretical analysis. Direct numerical simulation (DNS) is used to expound and quantify the FST boundary layer and also to confirm and calibrate the analytical solution. We adopt an eddy viscosity model and obtain an analytical similarity solution of the horizontally-averaged equation. The theoretical solution predicts well the surface layer behaviors obtained from DNS and is then used to predict the scaling properties of the free-surface boundary layer.

This chapter is organized as follows. In §4.1 we provide the mathematical formulation for diffusion of the mean flow near a free surface. Based on the characteristics of momentum diffusion, we obtain a quantitative definition of the free-surface boundary layer in §4.2. In §4.3, we derive a similarity solution of the horizontally-averaged equation, confirm it against the DNS results, and use it to obtain scaling properties of the free-surface inner and outer layers. Finally in §4.4, we present the conclusions.

4.1 Mathematical formulation

Our present interest is the effects of the free-surface boundary layer on the near-surface turbulent diffusion. To quantify these effects, the mean shear, rather than the mean velocity, is the main quantity of interest since the zero-stress boundary condition at the free surface requires it to vanish there.

For the mean (horizontally averaged) velocity, lateral symmetry of the problem yields that $\langle v \rangle = 0$. Moreover, upon averaging (2.2), we obtain

$$\frac{\partial \langle w \rangle}{\partial z} = 0 \,. \tag{4.1}$$

Far below the free surface, $\langle w \rangle \to 0$. Thus, $\langle w \rangle = 0$ everywhere.

Upon averaging the y-momentum equation, (2.1) for i=2, we obtain

$$\frac{\partial \langle v \rangle}{\partial t} + \frac{\partial (\langle v \rangle \cdot \langle w \rangle)}{\partial z} + \frac{\partial \langle v'w' \rangle}{\partial z} = \nu \frac{\partial^2 \langle v \rangle}{\partial z^2} \,. \tag{4.2}$$

Since $\langle v \rangle = \langle w \rangle = 0$ everywhere, we conclude that $\partial \langle v'w' \rangle / \partial z = 0$, and consequently that

$\langle v'w' \rangle$ is constant. Far below the free surface $\langle v'w' \rangle \to 0$, therefore $\langle v'w' \rangle = 0$ everywhere. Thus the turbulent diffusion in the vertical direction is completely specified by the Reynolds stress $\langle -u'w' \rangle$.

Averaging the x-momentum equation, (2.1) for i=1, yields

$$\frac{\partial \langle u \rangle}{\partial t} + \frac{\partial \langle u'w' \rangle}{\partial z} = \nu \frac{\partial^2 \langle u \rangle}{\partial z^2} \; . \tag{4.3}$$

We define the eddy viscosity ν_e as usual:

$$\nu_e \equiv \frac{\langle -u'w' \rangle}{\partial \langle u \rangle / \partial z} \; . \tag{4.4}$$

We can now re-write (4.3) as follows:

$$\frac{\partial \langle u \rangle}{\partial t} = \frac{\partial}{\partial z}((\nu + \nu_e)\frac{\partial \langle u \rangle}{\partial z}) \; . \tag{4.5}$$

Note that since the mean shear vanishes at the free surface (upon horizontal averaging of (2.3)):

$$\frac{\partial \langle u \rangle}{\partial z} = 0, \qquad \text{on } z = 0; \tag{4.6}$$

equation (4.4) requires (for finite ν_e) that $\langle -u'w' \rangle$ also vanishes at z=0. Applying l'Hopital's rule to (4.4), we obtain the limiting value of the eddy viscosity:

$$\nu_e|_{z=0} = \frac{\partial \langle -u'w' \rangle / \partial z|_{z=0}}{\partial^2 \langle u \rangle / \partial z^2|_{z=0}} \; . \tag{4.7}$$

The eddy viscosity is an even function of z, hence

$$\left. \frac{\partial \nu_e}{\partial z} \right|_{z=0} = 0 \; . \tag{4.8}$$

Equation (4.7) gives, in general, a non-zero value of the eddy viscosity at the free surface, proportional to the flux of the momentum tensor at the free surface. In the special case of a two-dimensional flow in the (x, z)-plane, where $v' = 0$, the right-hand side of (4.7) vanishes.

In summary then, for a two-dimensional flow, we have

$$\nu_e|_{z=0} = \left.\frac{\partial \nu_e}{\partial z}\right|_{z=0} = 0 \,. \tag{4.9}$$

4.2 Quantitative definition of the free-surface boundary layer

The thin inner layer of fast variation of the vorticity shown in Figure 3-1 is not the only region that is influenced by the free surface (but it is the most obvious to see). There is a wider region which is also influenced by the surface. A good indicator of this is the variation of the eddy viscosity — far from the surface, the eddy viscosity reaches an almost constant value, whereas, close to the free surface, the eddy viscosity is reduced abruptly to its surface value. This free-surface outer layer can be seen in Figures 4-1 and 4-2. Figure 4-1 shows the variation of the eddy viscosity with depth at various times and indicates the spatial extent of the outer layer. Figure 4-2 shows the variation of the eddy viscosity with time at various depths, and thus indicates the time required in our simulation for the surface layer to obtain the quasi-steady form ($t \tilde{>} 60$ for $R_{e0} = 1000$; this is also the case for $R_{e0} = 700$ and 1400; these results are not plotted here.)

The reduction of the eddy viscosity in a region near the free surface has also been seen in the measured data of Ueda *et al.* (1977) for open-channel flow. In that study, the value of the eddy viscosity at the free surface is assumed to be zero. This turns out to be not completely valid since the mixing length does not vanish at the free surface. The surface value of ν_e is, in fact, small and comparable to that of molecular viscosity ν. This is indicated from scaling arguments (see §4.3.3) and is verified by our direct simulations. The value of ν_e at the free surface is exactly zero only in the limit of a strictly two-dimensional flow ($v{=}v'{=}0$).

For later reference, we denote the thickness of the outer layer by ℓ_a, and the value of the eddy viscosity outside ℓ_a in the bulk of the flow by ν_{ea}. From dimensional analysis, a

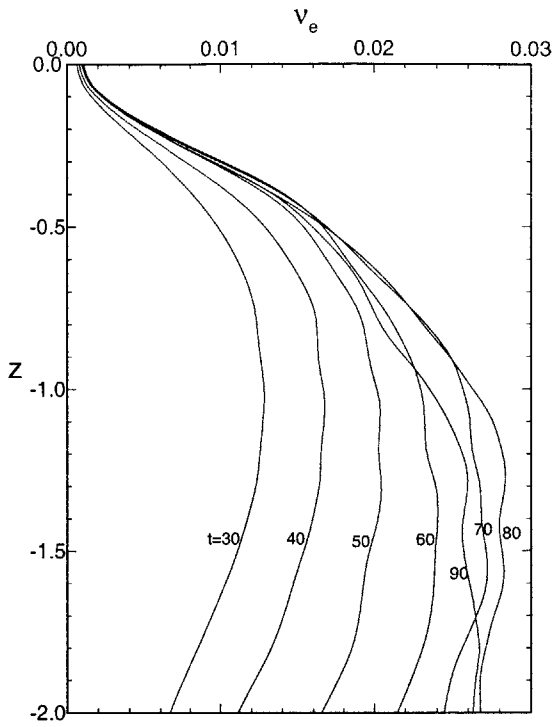

Figure 4-1: Profiles of eddy viscosity ν_e at different times. $R_{e0} = 1000$ and $F_{r0} = 0.7$.

quantitative estimate for ℓ_a can be obtained and is given by

$$\ell_a^2 \sim \frac{2\nu_{ea}}{\partial^2 \nu_e / \partial z^2|_{z=0}} . \tag{4.10}$$

Another important observation here is the vertical variation of the mean shear over the free-surface boundary layer (see Figure 4-3*a*). As the free surface is approached, the magnitude of the mean shear initially increases, and then drops rapidly to zero at the free surface. The magnitude of the mean shear thus exhibits two extrema near the free surface: a local minimum, and, much closer to the free surface, a local maximum.

The above features can be understood if we connect the depth variation of the mean shear to that of the eddy viscosity: inside the outer layer, the eddy viscosity decreases (Figure 4-1) at a rate faster than that of the Reynolds stress (Figure 4-3*b*). As a result, the magnitude of the mean shear is increased. Inside a much thinner inner layer, the mean shear then drops abruptly to zero in order to satisfy the zero-stress condition (4.6) at the free surface.

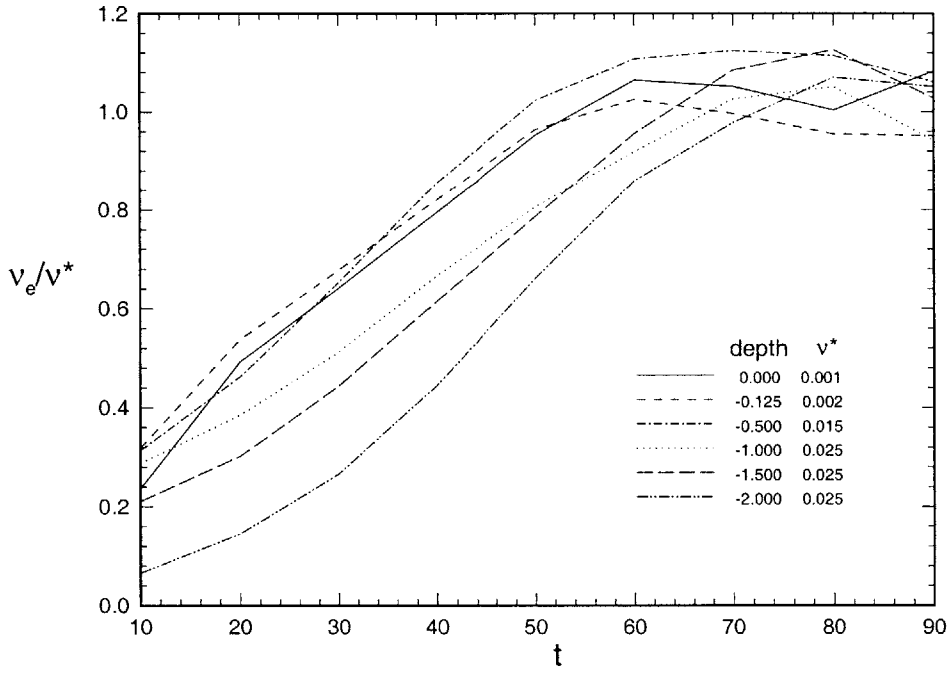

Figure 4-2: Time evolution of eddy viscosity ν_e at different depths. $R_{e0} = 1000$ and $F_{r0} = 0.7$. Note that different scaling constants ν^* are used for different depths to allow the results to be fitted on the same plot.

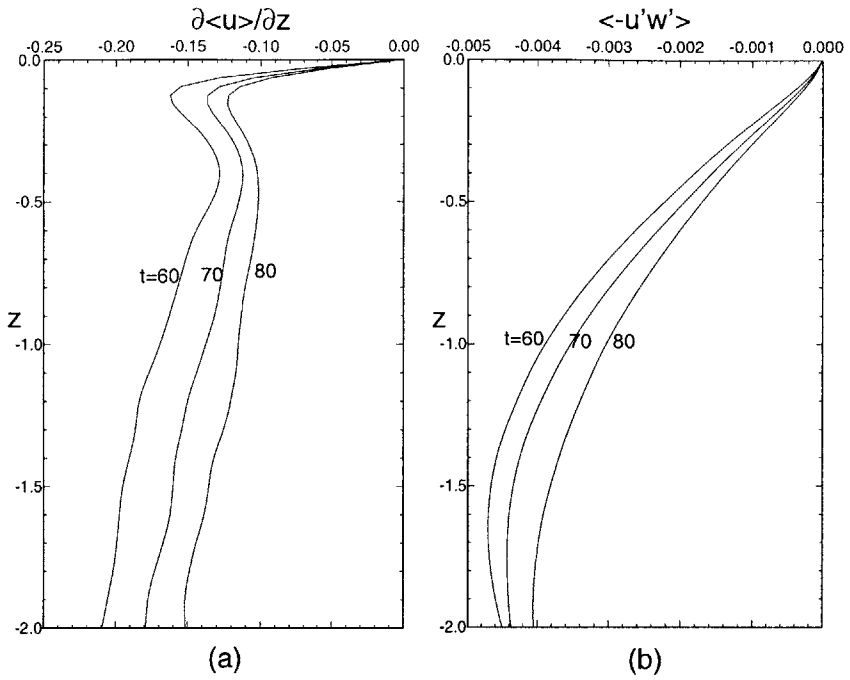

Figure 4-3: (a) Mean shear profiles $\partial\langle u\rangle/\partial z$; and ($b$) Reynolds stress profile $\langle -u'w'\rangle$ at different times. $R_{e0} = 1000$ and $F_{r0} = 0.7$.

Based on this understanding, the thickness of the inner layer at the free surface can be defined as the distance from the free surface to the local maximum of the mean shear. Correspondingly, for the outer layer, the thickness can be defined as the distance of the local minimum of the mean shear from the free surface, which is physically more direct than the estimate (4.10) in terms of the curvature of ν_e at the free surface. Thus, with these definitions, the thicknesses of the surface layers can be obtained directly, for example, from an experimental determination of the mean velocity profile alone.

4.3 Analytical similarity solution

4.3.1 Similarity solution

From Figure 4-1, one can observe that, at large times, the flow generally approaches a self-similar state: the temporal variation of the eddy viscosity in the bulk of the flow below is small, while the length scale of the spatial variation of the eddy viscosity increases with time.

This suggests that one may look for a self-similar solution, say, of the form

$$\frac{U_\infty - \langle u \rangle}{U_d} = f(\eta) \ , \tag{4.11}$$

where $U_\infty \equiv \langle u \rangle|_{z \to -\infty}$, $U_d = U_\infty - \langle u \rangle|_{z=0}$ is the velocity deficit, and η is the similarity variable

$$\eta = z/b \ , \tag{4.12}$$

with b measuring the extent of the mean shear in the flow. Note that both U_d and b are generally functions of time. This is done in order for the similarity solution to be comparable with the results of the simulation which refers to a temporally evolving flow. Extension of the similarity solution methodology to spatially evolving flows, which may better correspond to certain experimentally measured conditions, is straightforward and will not be done here.

The mean velocity $\langle u \rangle$ satisfies (4.5) subject to the boundary condition (4.6) on the free surface. For the eddy viscosity, it is important to take into account its variation with depth, in other words, the dependence of ν_e on U_d, b, the distance from the free surface z, and the molecular viscosity ν. Dimensional analysis then yields

$$\frac{\nu_e}{U_d b} = \psi \left(\eta; \frac{U_d b}{\nu} \right) \ , \tag{4.13}$$

where ψ is some function of the similarity variable assumed known. We denote by ψ_a the value of ψ well below the free surface, i.e. outside the outer layer; and by ψ_0 the value of ψ at the free surface. One important point here is that near the free surface, i.e. inside the outer layer, ψ should also depend on the Reynolds number, whereas far below the free surface, ψ should be independent of the Reynolds number.

Following the usual procedure (see e.g. Lesieur 1997), we find that U_d and b are related by

$$U_d b = C_0 \ , \tag{4.14}$$

where C_0 is some constant. For the function $f(\eta)$, we find that it satisfies the ordinary

differential equation

$$\eta f' + f = -\left(b\,\frac{\mathrm{d}b}{\mathrm{d}t}\right)^{-1}\,\frac{\mathrm{d}}{\mathrm{d}\eta}\left[(\nu + U_d b\psi)f'\right]\,, \tag{4.15}$$

subject to the boundary conditions

$$f(0) = 1, \qquad f'(0) = 0, \qquad \text{and} \quad f'(-\infty) = 0\,. \tag{4.16}$$

It remains to specify the value of $f''(0)$. The appropriate choice can be made by writing (4.15) at η=0:

$$(\nu + U_d b\psi_0)f''(0) = -b\frac{\mathrm{d}b}{\mathrm{d}t}\,. \tag{4.17}$$

The length b is the extent of the shear flow, which should be much greater than that of the outer layer. Consequently b should diffuse at a rate proportional to the value of the eddy viscosity in the bulk of the flow. This dictates the following choice:

$$f''(0) = -\frac{\nu + U_d b\psi_a}{\nu + U_d b\psi_0}\,, \tag{4.18}$$

and (4.17) becomes

$$b\frac{\mathrm{d}b}{\mathrm{d}t} = \nu + U_d b\psi_a\,. \tag{4.19}$$

Upon integration of (4.19), we obtain that b evolves in time as follows:

$$b = \sqrt{2(\nu + U_d b\psi_a)t + Q}\,, \tag{4.20}$$

where Q is a constant of integration. The velocity deficit U_d is given by

$$U_d = \frac{C_0}{\sqrt{2(\nu + U_d b\psi_a)t + Q}}\,. \tag{4.21}$$

Moreover by integrating (4.15) twice (subject to (4.16) and (4.18)) with respect to η we

obtain the following expression:

$$f(\eta) = \exp\left(-\int_0^\eta \frac{s(\nu + U_d b\psi_a)}{\nu + U_d b\psi(s)}\mathrm{d}s\right) . \tag{4.22}$$

Thus, we find that the length scale increases like the square root of t and the velocity deficit decreases at the inverse of this rate, as one may expect from a similarity solution. We note however that the choice (4.18) (which is based on physical reasoning) implies that $f''(0)$ is a large number since $\nu_{ea} = U_d b\psi_a$ is much greater than $\nu_{e0} \equiv \nu_e|_{z=0}$ and ν. Consequently $f'(\eta)$ has a region of fast variation in the vicinity of $\eta = 0$ which corresponds to the free-surface inner layer.

The similarity solution (4.22) provides us with a clear picture of the mean flow, and contains the basic physical features of interest. It remains to see how well it can fit the results of direct numerical simulation.

4.3.2 Comparison between theoretical similarity solution and direct simulations

In order to compare (4.22) with the results of direct numerical simulations, we propose a simple Gaussian fit to the eddy viscosity (the validity of this particular choice will be subsequently supported by numerical results):

$$\psi = \frac{\nu_e}{U_d b} = \psi_a - (\psi_a - \psi_0)\exp(-\eta^2/a^2) , \tag{4.23}$$

where a is proportional to the non-dimensional thickness of the outer layer (i.e. $a \sim \ell_a/b$). Using (4.23) we obtain from (4.22)

$$f(\eta) = \exp\left(-\eta^2/2\right)\left[\frac{1/R_e + \psi_0}{1/R_e + \psi_a - (\psi_a - \psi_0)\exp(-\eta^2/a^2)}\right]^{a^2/2} , \tag{4.24}$$

where R_e is the Reynolds number based on U_d and b (note the difference from R_{e0}):

$$R_e = \frac{U_d b}{\nu} . \tag{4.25}$$

	R_{e0}=700			R_{e0}=1000			R_{e0}=1400		
t	U_d	b	C_0	U_d	b	C_0	U_d	b	C_0
60	0.680	1.529	1.040	0.612	1.669	1.021	0.602	1.684	1.014
65	0.644	1.617	1.041	0.587	1.744	1.024	0.575	1.753	1.008
70	0.621	1.683	1.045	0.566	1.815	1.027	0.557	1.816	1.012
75	0.591	1.768	1.045	0.544	1.874	1.019	0.536	1.880	1.008
80	0.566	1.853	1.049	0.527	1.939	1.022	0.518	1.939	1.004

Table 4.1: Variation with time of the mean velocity deficit U_d, the mean shear extent b, and the product $C_0 = U_d b$, for different R_{e0}.

Note that, because of (4.14), R_e is independent of time for large times.

The eddy viscosity profile (4.23), the mean velocity profile (4.24) and its first derivative (i.e. the mean shear profile) are compared with results from direct numerical simulations after quasi-steady states are reached. The comparisons are performed as follows. The velocity deficit U_d is obtained directly from numerical results. The value of ψ_0 is obtained based on the eddy viscosity at the free surface; ψ_a is obtained based on the averaged eddy viscosity in the bulk of the flow; while b is determined by matching $f(\eta)$ in (4.24) with the numerical value at the depth $\eta = -1$, and the value of a is obtained by a least-square best fit of (4.23).

The values of U_d and b thus obtained at various times are listed in Table 4.1. In agreement with (4.14), the product $C_0 = U_d b$ approaches a constant value at large times (the fluctuation in C_0 is less than 1% for $\tilde{>}$ 60). Figure 4-4 shows the comparisons of the time evolution of U_d and b between the theoretical behaviors given by (4.20), (4.21) and those obtained from direct simulations (the values of C_0, ψ_a and Q used are listed in Table 4.2). For the range of Reynolds numbers considered, the analytical solutions fit the computed behaviors of decreasing U_d and increasing b with time with remarkable accuracy.

Figure 4-5 compares the eddy viscosity given by (4.23) with DNS results at t=60, 70, 80. There are small differences in the deep region, which can be attributed to the use of

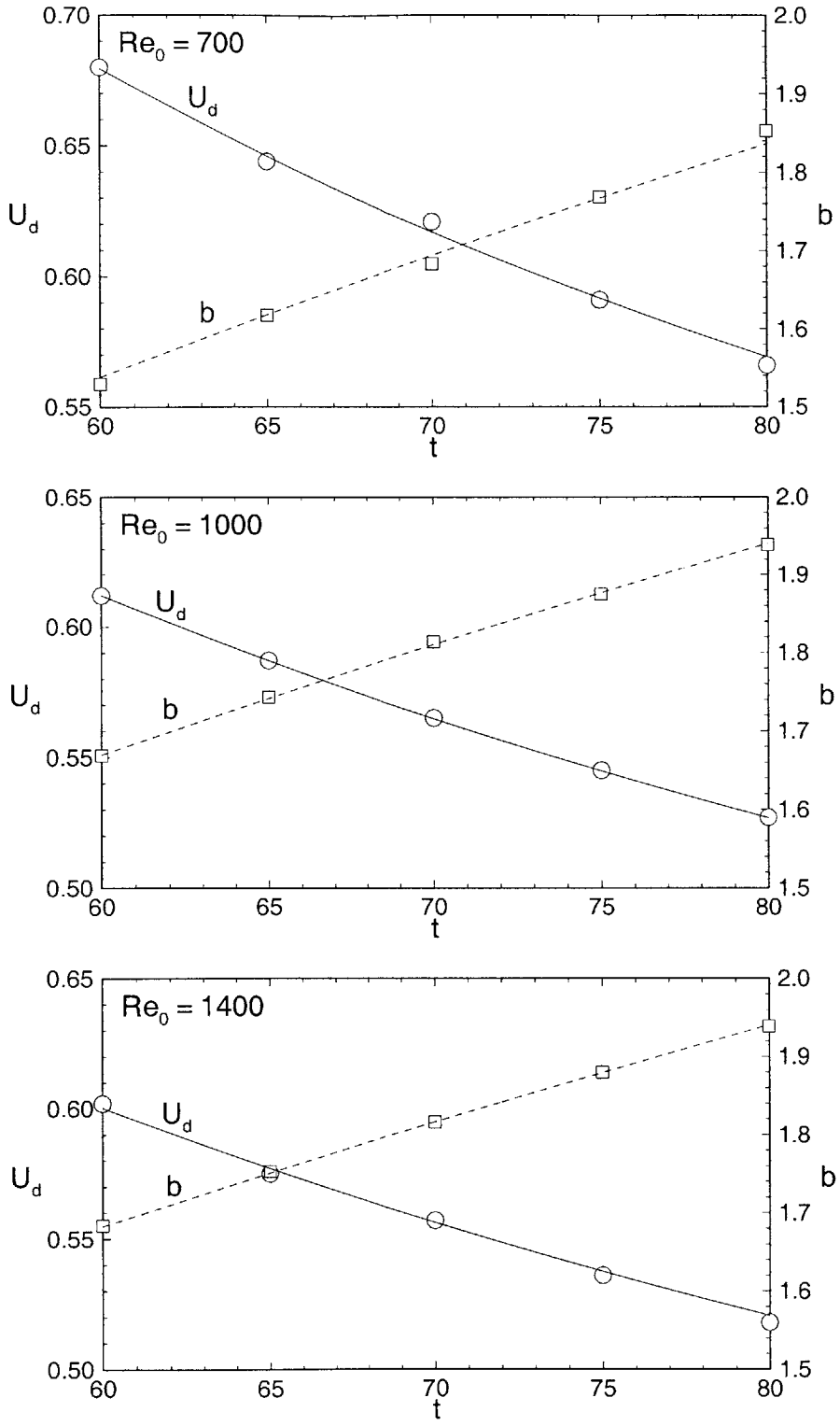

Figure 4-4: Time evolution of U_d and b for $R_{e0} = 700$, 1000, and 1400 for: DNS results ($\circ$ for U_d, $\square$ for b; and similarity solution (———— for U_d, – – – – for b).

R_{e0}	C_0	R_e	ψ_a	ψ_0	ν_{e0}/ν	Q	a	$a(\nu/\nu_{ea})^{-1/2}$
700	1.04	728	0.0228	0.0014	1.05	-0.65	0.305	1.24
1000	1.02	1020	0.0229	0.00098	1.00	-0.14	0.251	1.21
1400	1.01	1414	0.0224	0.00078	1.10	-0.03	0.215	1.22

Table 4.2: Values of C_0, R_e, ψ_a, ψ_0, ν_{e0}/ν, Q, a and $a(\nu/\nu_{ea})^{-1/2}$, for different R_{e0}.

a constant eddy viscosity in the similarity solution there. Our main interest is the region near the free surface where Figure 4-5 shows that the Gaussian profile (4.23) fits the DNS ν_e well in the near-surface region. As will be seen, (4.23) is sufficient to describe the detailed characteristics of the turbulent diffusion near the free surface.

Figure 4-6 shows similar comparisons for the mean velocity and Figure 4-7 the mean shear rate. The agreement is quite good in both cases. (Note that small differences in the deeper region are due to the fact that the DNS turbulent flow underneath is not perfectly statistically homogeneous. Our main interest is in the near-surface region.) These two figures also confirm the similarity assumption that the mean flow approaches a universal shape at large times, although the physical values of the mean flow itself change with time (Figures 2-3*a* and 4-3*a*).

4.3.3 Scaling properties of the free-surface boundary layer

As pointed out in §4.3.1, one anticipates that the parameters a and ψ_0 should depend on the Reynolds number (since they describe properties of the outer layer), while ψ_a should be independent of the Reynolds number, as it describes the value of the eddy viscosity outside the outer layer. These are confirmed in Table 4.2.

On the right-hand side of (4.24), the first (Gaussian) factor is what one would obtain in a constant eddy viscosity model, while the second factor is associated with the variation of eddy viscosity near the surface and, in particular, contains the essential information about

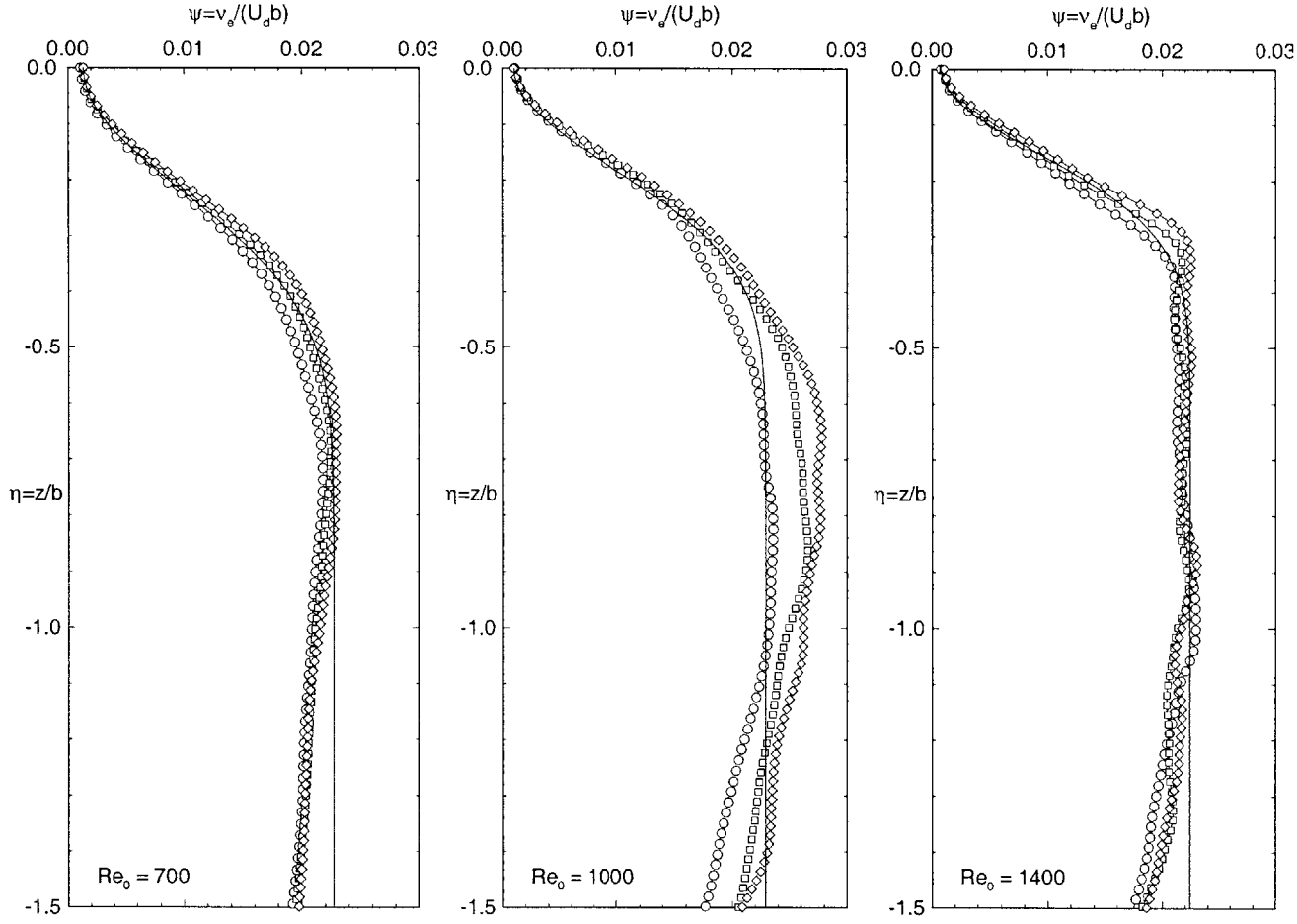

Figure 4-5: Comparison of the eddy viscosity profile between the similarity solution (———) and the DNS results at: ○, t=60; □, t=70; and ◇, t=80; for R_{e0} = 700, 1000, and 1400.

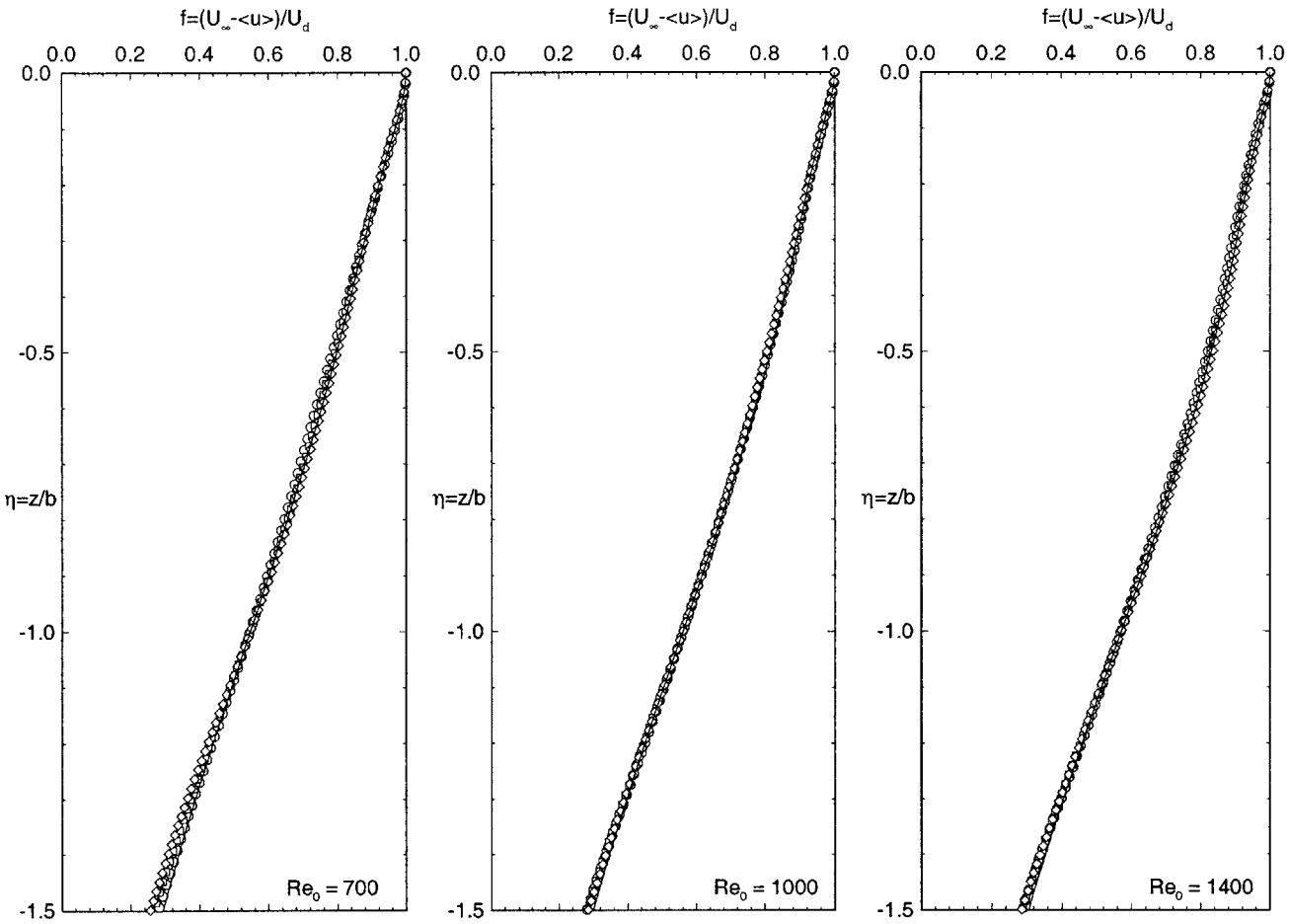

Figure 4-6: Comparison of the mean velocity profile between the similarity solution (——) and the DNS results at: ○, t=60; □, t=70; and ◇, t=80; for R_{e0} = 700, 1000, and 1400.

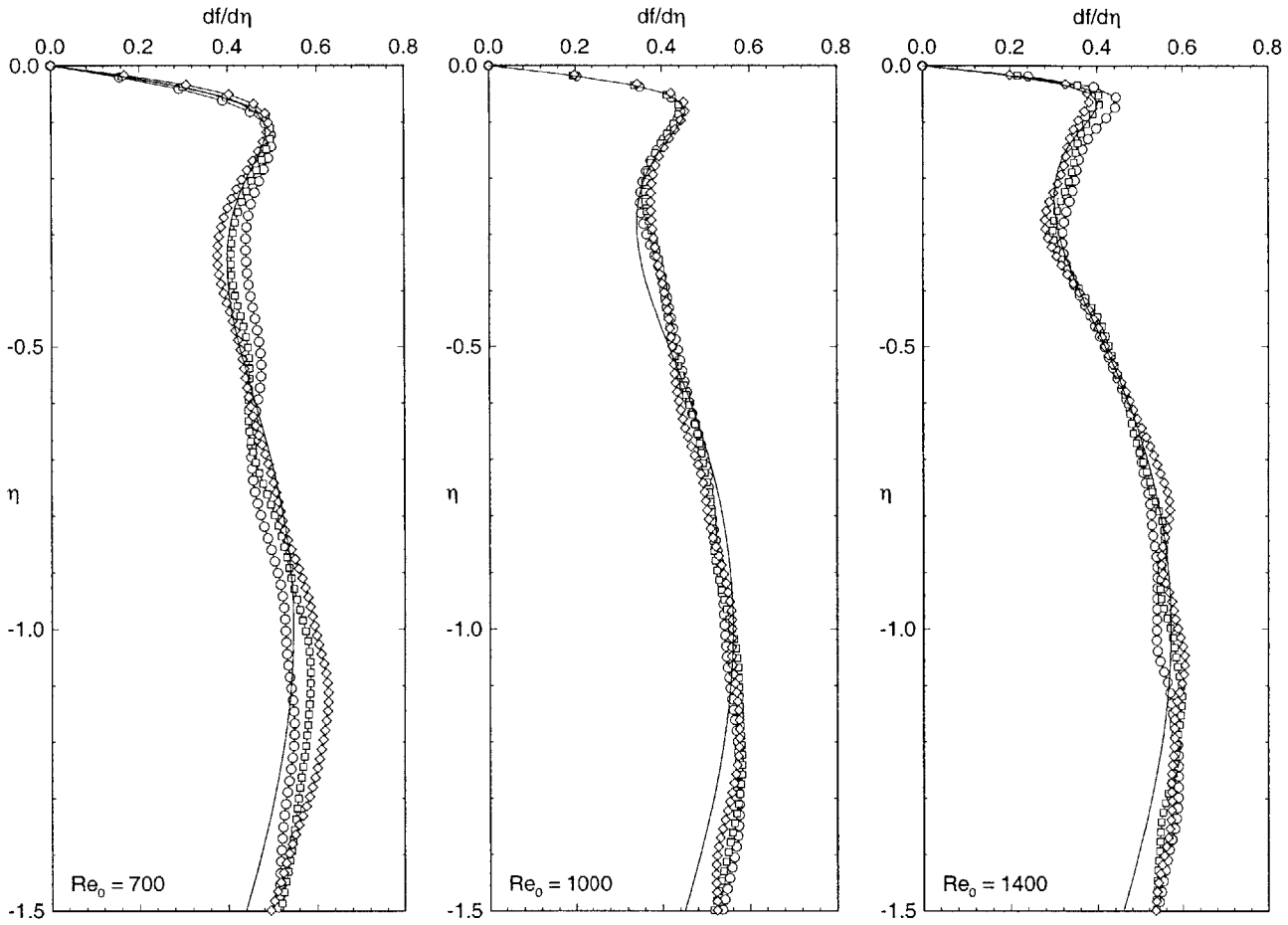

Figure 4-7: Comparison of the mean shear profile between the similarity solution (————) and the DNS results at: ○, t=60; □, t=70; and ◇, t=80; for R_{e0} = 700, 1000, and 1400.

the inner layer. Using a small-η ($\eta \ll a$) expansion of (4.24) we obtain

$$f(\eta) \approx \left[\frac{1/R_e + \psi_0}{1/R_e + \psi_0 + (\psi_a - \psi_0)\eta^2/a^2}\right]^{a^2/2} (1 - \eta^2/2) \; . \tag{4.26}$$

Let ϵ be the non-dimensional thickness of the inner layer. Upon substitution of $\eta = \epsilon\zeta$ (with ζ being of order one) into (4.26), and using a dominant balance argument for the expression in the denominator of the right-hand side of (4.26), we obtain

$$\epsilon \sim a \left(\frac{1/R_e + \psi_0}{\psi_a - \psi_0}\right)^{1/2} \; , \tag{4.27}$$

or equivalently,

$$\epsilon \sim a \left(\frac{\nu + \nu_{e0}}{\nu_{ea} - \nu_{e0}}\right)^{1/2} \; . \tag{4.28}$$

Equation (4.28) shows that the thickness of the inner layer, ϵ, is scaled by the thickness of the outer layer, a. It also shows that the value of the eddy viscosity at the free surface, ν_{e0}, enters into the estimate of the inner layer, and is therefore an important physical parameter of the problem.

We now turn to the dependence of ν_{e0} on the parameters of the problem. Based on (4.7), we can assume that the value of ν_{e0} depends on the following parameters: (i) the horizontal turbulence intensity at the free surface, q_0; (ii) the characteristic lateral size of the vortical structures attached on the free surface, λ_0; and (iii) the molecular viscosity, ν. It follows from dimensional analysis that

$$\frac{\nu_{e0}}{\nu} = F\left(R_{e\lambda} \equiv \frac{q_0\lambda_0}{\nu}\right) \; . \tag{4.29}$$

For a given free-surface shear-flow turbulence characterized by $R_{e\lambda}$, (4.29) indicates that the value of the eddy viscosity at the free surface scales like the value of the molecular kinematic viscosity. This fact is confirmed by our DNS data where the factor of proportionality between ν_{e0} and ν is found to be close to unity for a range of R_{e0} (see Table 4.2).

Interestingly, the similarity theory provides us also with a scaling relationship for the

thickness of the outer layer. The estimate comes out in an indirect manner, through the requirement that the mean shear in the flow remains bounded at all Reynolds numbers.

Consistently with our discussion so far, and supported by DNS results, we assume that $\psi_a \gg 1/R_e$, whereas ψ_0 is comparable to $1/R_e$. Based on this and using the small-argument approximation, we find that the location of the maximum shear near the free surface is

$$\eta_m \approx -a \left[\frac{1/R_e + \psi_0}{(1+a^2)\psi_a - \psi_0} \right]^{1/2} . \tag{4.30}$$

Therefore the maximum mean shear $s_m \equiv f'|_{max}$ is

$$s_m \approx a\,(R_e\psi_a)^{1/2}\, \frac{(1+a^2-\psi_0/\psi_a)^{1/2}\,(1+(R_e\psi_a)^{-1})}{(2+a^2-2\psi_0/\psi_a)(1+R_e\psi_0)^{1/2}}. \tag{4.31}$$

Given that ψ_0 has the same order of magnitude as $1/R_e$, we conclude that s_m remains bounded for $R_e \to \infty$ only if $a(R_e\psi_a)^{1/2}$ is at most order one, i.e. a is at most

$$a \sim (R_e\psi_a)^{-1/2} = \left(\frac{\nu}{\nu_{ea}} \right)^{1/2} . \tag{4.32}$$

The decrease of the outer layer thickness as the Reynolds number increases is evident in Figures 4-5 and 4-7 for the DNS results. A more quantitative DNS confirmation is provided in Table 4.2 which shows that the product $a(\nu/\nu_{ea})^{-1/2}$ is approximately constant.

It should be noted that the scaling relations (4.27) and (4.32) are not particular to the eddy viscosity fitting (4.23). In fact they can be obtained directly from (4.22) by expanding $\psi(\eta)$ for small argument. Writing $\psi(\eta) = \psi_0 + \psi''(0)\eta^2/2 + \ldots$, and noting that in general the non-dimensional thickness of the outer layer a is proportional to $\psi_a/\psi''(0)$ (because of (4.10)), the derivation follows along the same lines as those we presented above.

Finally, we note that our DNS verification of the theoretical scaling results is limited to small Reynolds numbers. It would be very desirable to seek more complete/systematic numerical confirmation of these results. This is difficult primarily because of the fundamental limitations of DNS for high Reynolds numbers. Further examination using other approaches and especially experimental measurements would be helpful.

4.4 Conclusions

In this chapter we investigate the process of turbulent diffusion in a shear flow under a free surface. We obtain an ensemble of simulation results using DNS. Using these data, we identify the free-surface boundary layer structures: an outer layer characterized by the reduction of the eddy viscosity and an accompanying increase of the mean shear rate; and an inner layer characterized by the rapid decrease of the mean shear rate to reach its vanishing value at the free surface. We find that quantitative definitions of the outer and inner thicknesses can be obtained directly from the mean shear profile corresponding respectively to first its local minimum and then its local maximum as the free surface is approached.

Guided by DNS results, we derive a similarity theory for the vertical turbulent diffusivity problem. An important feature of the similarity solution is the specification of a universal shape for the mean velocity profile. This and other predictions of the similarity theory are confirmed by direct comparisons to DNS. Significantly, the similarity solution provides the scaling for the thickness of the inner and outer surface layers as a function of the Reynolds number: the inner layer thickness is proportional to the outer layer thickness; the outer layer thickness is proportional to the mean shear depth; and the factors of proportionality in both cases scale as the square root of the ratio of the molecular viscosity to the bulk eddy viscosity. Thus, the free-surface boundary layers define the region of the flow which remains Reynolds-number-dependent at high Reynolds numbers.

The above results provide a fundamental basis for the modeling of turbulence at a free surface. As will be shown in Chapter 8, we propose a free-surface function model (FFM) for large-eddy simulation of FST. This new model incorporates the expected near free-surface behavior of the turbulence diffusivity and is an improvement over classical models using constant coefficients.

Chapter 5

Mixing of a Passive Scalar near a Free Surface

The mixing of a passive scalar in turbulent flows with a free surface is of interest to geophysical and environmental applications. Examples of applications include the spreading of pollutants and the transfer of gases along an air-water interface. In the past, considerable effort has been made towards the quantification and prediction of the turbulent mixing process near the free surface, for example, the theoretical work by Danckwerts (1951), Hunt (1954), Ellison (1960), Levich (1962), Fortescue & Person (1967), Davis (1972) and Theofanous (1984), the experimental measurements by Jobson & Sayre (1970), Ueda *et al.* (1977), Komori *et al.* (1982), Brown, Khoo & Sonin (1990) and Rashidi, Hetsroni & Banerjee (1991), and the recent numerical simulations by Khoo, Patera & Sonin (1989), Komori *et al.* (1993), van Haarlem, Boersma & Nieuwstadt (1998), Nagaosa (1999) and Handler *et al.* (1999).

The mixing of scalars near the free surface is due to the combined effects of turbulent and molecular diffusion. Turbulent flows are affected by a free surface by two mechanisms: (i) the surface constrains flow motions in the normal direction while motions in the surface-tangential direction are allowed; (ii) the shear stress vanishes at the surface in order to satisfy the stress balance across the free surface. These two mechanisms result in a multi-level free-surface boundary layer which is characterized by unique features such as the splat and antisplat motions, the vanishing of surface-parallel vorticity and the connecting of surface-

normal vorticity to the free surface (cf. Shen *et al.* 1999). Understanding the structure of the underlying turbulent flows is of fundamental importance to the modeling of free-surface scalar mixing process.

As the surface is approached, turbulent mixing in the vertical direction decreases and the effect of molecular diffusion becomes important. As expected, there exists a thin layer adjacent to the surface which is controlled by molecular diffusion. For gas transfer between the ocean and atmosphere, due to the small value of molecular diffusivity (high Schmidt number), this layer is only 20 to 200 μm in thickness (Jähne & Hauβecker 1998), which makes measurements extremely difficult. Hence there is a critical need to accurately quantify the scalar mixing process near the free surface.

In this chapter we study numerically and analytically the mixing of a passive scalar in free-surface turbulence. This study is an extension of our work on the free-surface boundary layer for momentum diffusion in Chapter 4. In Chapter 4, we quantified the multi-layer structure of the turbulent momentum diffusion with an analytical similarity solution. The theoretical predictions on the shape and time-scaling behavior of the mean flow have been found to agree with results of direct numerical simulation (DNS) with remarkable accuracy. In the present study, we perform DNS for the mixing of passive scalars at Schmidt numbers ranging from 0.25 to 4. An analytical solution of a self-similar form is derived for the scalar surface layer. The main goal of this study is to characterize and to quantify the free-surface scalar boundary layer, to elucidate its relation with the free-surface momentum boundary layer, and to obtain its scaling properties.

This chapter is organized as follows: in §5.1 we provide the mathematical formulation for the problem of scalar mixing near a free surface; in §5.2 we outline the numerical scheme for the DNS of scalar mixing and present the DNS results; a similarity theory for the scalar mixing is developed in §5.3 and its predictions are compared to the DNS results; in §5.5 we discuss the scaling properties of the free-surface boundary layer for scalar mixing; and finally in §5.5, we present our conclusions.

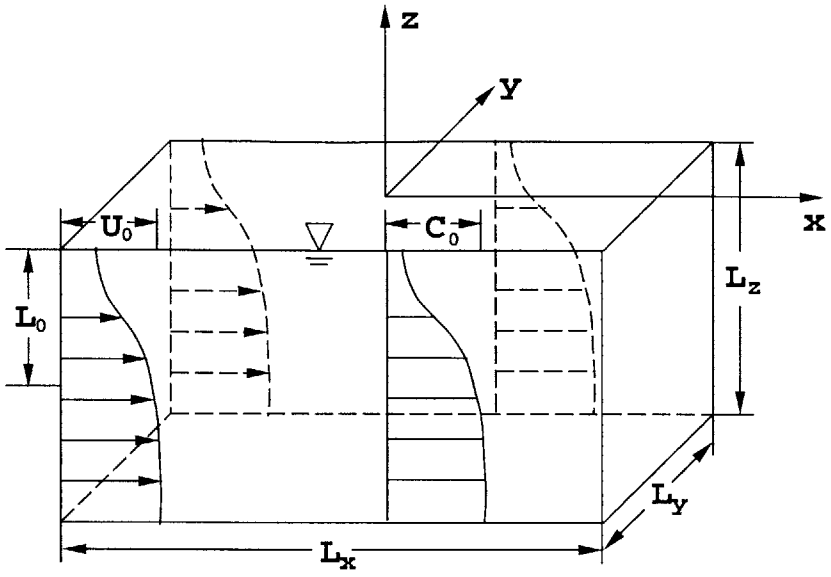

Figure 5-1: Schematic of the mixing of a passive scalar by a turbulent shear flow under a free surface.

5.1 Mathematical formulation

5.1.1 Governing equations and boundary conditions

We consider the mixing of a passive scalar by a turbulent shear flow underneath a free surface at zero Froude number. As shown in Figure 5-1, the frame of reference has axes x, y, and z, where x-axis points in the mean flow direction, y-axis in the spanwise direction, and z-axis is positive upward. The origin is located at the free surface. The mean shear is two dimensional and is in the (x, z)-plane. In this flow, turbulence is generated and maintained by the mean shear, and the passive scalar is transported by the turbulent motion.

The fluid motions are governed by the Navier–Stokes and continuity equations:

$$\frac{\partial u_i}{\partial t} + \frac{\partial (u_i u_j)}{\partial x_j} = -\frac{1}{\rho}\frac{\partial p}{\partial x_i} + \nu \frac{\partial^2 u_i}{\partial x_j \partial x_j} , \tag{5.1}$$

$$\frac{\partial u_i}{\partial x_i} = 0 . \tag{5.2}$$

Here u_i is the velocity components in x_i-direction; p is the dynamic pressure, ρ the density, and ν the kinematic viscosity.

For the zero Froude number, we use the free-slip boundary conditions on z=0:

$$\frac{\partial u}{\partial z} = \frac{\partial v}{\partial z} = w = \frac{\partial p}{\partial z} = 0 \ . \tag{5.3}$$

The space-time evolution for the concentration c of the passive scalar is governed by the following advection–diffusion equation:

$$\frac{\partial c}{\partial t} + \frac{\partial (u_j c)}{\partial x_j} = D \frac{\partial^2 c}{\partial x_j \partial x_j} \ , \tag{5.4}$$

where D is the molecular diffusivity of the scalar. We define the Schmidt number S_c as the ratio of ν over D:

$$S_c \equiv \frac{\nu}{D} \ . \tag{5.5}$$

In this study, we consider the case of zero scalar-flux at the free surface:

$$\left. \frac{\partial c}{\partial z} \right|_{z=0} = 0 \ . \tag{5.6}$$

We remark that this boundary condition applies to situations where the flux rate of the scalar across the free surface is negligible compared to the value in the bulk flow below, for example, the spreading of pollutants in the ocean. For other cases where the surface flux is significant, a boundary condition with a specified scalar concentration value or a specified scalar gradient is more appropriate. The zero-flux condition (5.6) greatly facilitates the derivation of an analytical similarity solution.

For both the flow and the scalar, we use periodic boundary conditions in horizontal directions. At the bottom, we use free-slip conditions for the flow motions and a Dirichlet condition for the scalar:

$$c|_{z=-L_z} = C_0 \ . \tag{5.7}$$

5.1.2 Plane-averaged properties

In view of the statistical homogeneity in horizontal directions, in this study we use the spatial averaging over the (x,y)-plane to define a mean value. For later reference, for any variable $f(x,y,z,t)$, its mean value is denoted as $\langle f\rangle(z,t)$; $f'(x,y,z,t) \equiv f - \langle f\rangle$ is its fluctuation and $f^{rms}(z,t) \equiv \langle f^2\rangle^{1/2}$ is the root-mean-square variation.

By taking average of (5.1) and (5.4) and invoking the horizontal periodicity, we obtain the governing equations for the mean flow and the scalar mean concentration:

$$\frac{\partial\langle u\rangle}{\partial t} = \frac{\partial}{\partial z}\left((\nu+\nu_e)\frac{\partial\langle u\rangle}{\partial z}\right) , \tag{5.8}$$

$$\frac{\partial\langle c\rangle}{\partial t} = \frac{\partial}{\partial z}\left((D+\gamma)\frac{\partial\langle c\rangle}{\partial z}\right) . \tag{5.9}$$

Here ν_e and γ are eddy viscosity and turbulent diffusivity, respectively, which are respectively defined as

$$\nu_e \equiv \frac{\langle -u'w'\rangle}{\partial\langle u\rangle/\partial z} , \qquad \gamma \equiv \frac{\langle -c'w'\rangle}{\partial\langle c\rangle/\partial z} . \tag{5.10}$$

Note that from (5.3) and (5.4), the gradients for both the mean velocity and mean scalar concentration vanish at the free surface:

$$\left.\frac{\partial\langle u\rangle}{\partial z}\right|_{z=0} = 0 , \qquad \left.\frac{\partial\langle c\rangle}{\partial z}\right|_{z=0} = 0 . \tag{5.11}$$

Hence the definitions (5.10) have special forms at z=0, by using the l'Hopital's rule:

$$\nu_e|_{z=0} \equiv \frac{\partial\langle -u'w'\rangle/\partial z|_{z=0}}{\partial^2\langle u\rangle/\partial z^2|_{z=0}} , \qquad \gamma|_{z=0} \equiv \frac{\partial\langle -c'w'\rangle/\partial z|_{z=0}}{\partial^2\langle c\rangle/\partial z^2|_{z=0}} . \tag{5.12}$$

In Chapter 4 we studied the spatial variation of the fluid properties ν_e and $\langle u\rangle$. In this chapter we investigate the variation of the scalar property γ and the consequent effect on $\langle c\rangle$ distribution. The dependence of γ and $\langle c\rangle$ variations on the flow field as well as the Schmidt number effects will be quantified via an analytical similarity solution.

5.2 Direct numerical simulations

5.2.1 Numerical method

For the fluid motions, the governing equations (5.1) and (5.2) subject to the free-surface boundary condition (5.3) are solved numerically as an initial-boundary-value problem. The numerical method as well as its validation are provided in detail in Chapter 2 and will not be taken up here.

For the advection and diffusion of the passive scalar, the governing equation (5.4) is discretized by finite difference. In horizontal directions, a sixth-order finite-difference scheme is used, while a second-order finite-difference scheme is used in the vertical direction. The free-surface boundary condition (5.6) is employed to obtain the values of c at the imaginary points one grid above the free surface, which are used in the calculation of vertical derivatives in (5.4) at z=0. As for time integration, a second-order Runge-Kutta scheme is used. At each sub-timestep, the value of the velocity in (5.4) is provided by the DNS of the fluid motions.

As in Chapter 4, DNS for the fluid motions is performed from t=0 to 90. In this study, we simulate the mixing of the scalar from t=30 to 70. At t=30, the initial profile of the scalar concentration is given by a prescribed function

$$\frac{c(z,t=30)}{C_0} = 1 - \mathrm{sech}^2\left(0.88137\frac{z}{L_0}\right) , \tag{5.13}$$

where L_0 is a measure of the vertical extent of scalar concentration variation, which has the same value as the one used in the initial mean velocity (cf. Chapter 2). Initially the scalar concentration is uniform in horizontal directions. As the simulation carries on, the scalar is subsequently mixed by turbulence. It found that a fully mixed scalar field develops between t=60 and 70, on which period the present study focuses.

It should be noted that the choice of the initial profile of c is not critical. We are interested in the asymptotic behavior (in a self-similar form) of the scalar distribution at large t. We choose (5.13) simply because it satisfies the boundary conditions at z=0 and z=$-L_z$, and

because this profile yields a well-developed turbulent scalar field faster than other initial profiles we have tested, a fact which needs to be taken into account to reduce computational cost.

All the results presented in this chapter are normalized by L_0, C_0, and the initial shear-flow velocity deficit U_0. The Reynolds number $Re \equiv U_0 L_0/\nu$ is 1400. To investigate Schmidt number effects, in this study we have considered five Schmidt numbers S_c=0.25, 0.5, 1, 2, and 4. In order to obtain converged statistics, for each Schmidt number we perform 25 realizations of DNS with different turbulent flow fields, the latter produced by different sets of random seeds for the turbulence generation. All the statistics presented in this chapter are the ensemble average of the plane-averaged values obtained in the 25 realizations.

As in Chapter 4, the computational domain size is L_x=L_y=10.472, L_z=6. A $128^2 \times 196$ grid is used. The timestep is 0.005.

5.2.2 Numerical results

Figures 5-2 to 5-6 plot the statistic of the scalar field obtained from DNS. To illustrate the Schmidt number effects, we show here the S_c=1, 4, and 0.25 cases in Figures (b), (c), and (d), respectively. For reference, the corresponding equivalences in velocity statistics are plotted in Figures (a).

Figures 5-2(b) to (d) show the time evolution of scalar fluctuation profiles. As pointed out earlier, initially (t=30) c is a function of depth only and there is no scalar fluctuation at each horizontal plane. Under the action of turbulent fluid motions, the scalar is mixed up quickly. It is found that $\langle c'^2 \rangle$ reaches its maximum around t=39 (not shown here). After that, $\langle c'^2 \rangle$ decays due to dissipation. Smaller Schmidt numbers cause faster decay, as shown in Figures 5-2(b) to (d).

We plot the turbulent scalar flux $\langle -c'w' \rangle$ in Figures 5-3(b) to (d). Similar to the Reynolds stress $\langle -u'w' \rangle$ (Figure 5-3a), $\langle -c'w' \rangle$ decreases as the free surface is approached. This is expected because the vertical velocity w diminishes towards the surface due to blockage effects.

The turbulent diffusivity γ, defined by (5.10) and (5.12), is plotted in Figures 5-4(b)

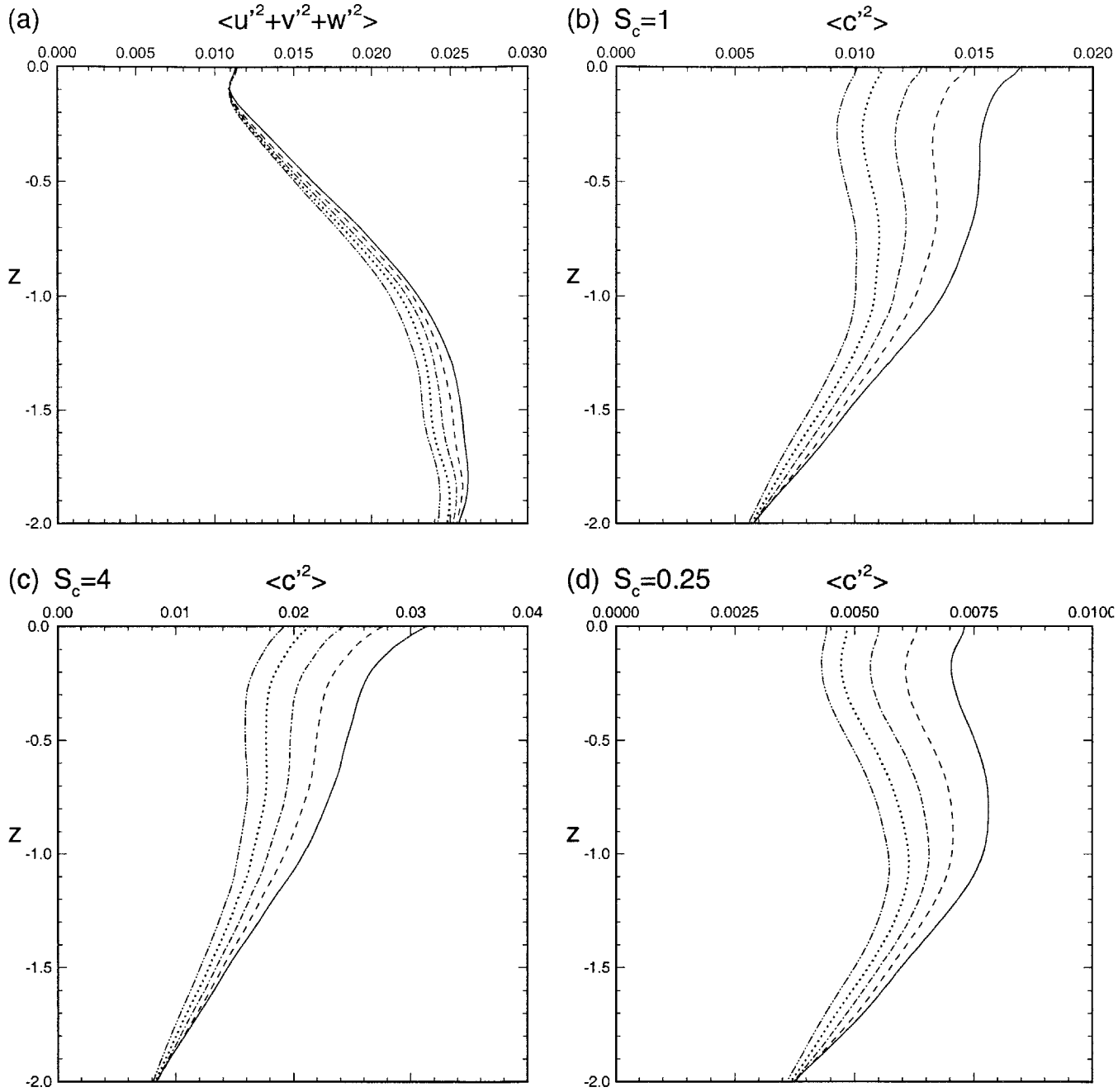

Figure 5-2: Profiles of (a) turbulent velocity fluctuation $\langle u'^2+v'^2+w'^2\rangle$, and scalar fluctuation $\langle c'^2\rangle$ for: (b) S_c=1, (c) S_c=4, and (d) S_c=0.25. ———— , t=60; - - - - , t=62.5, - · - · - , t=65, · · · · · · · , t=67.5, —··—··— , t=70.

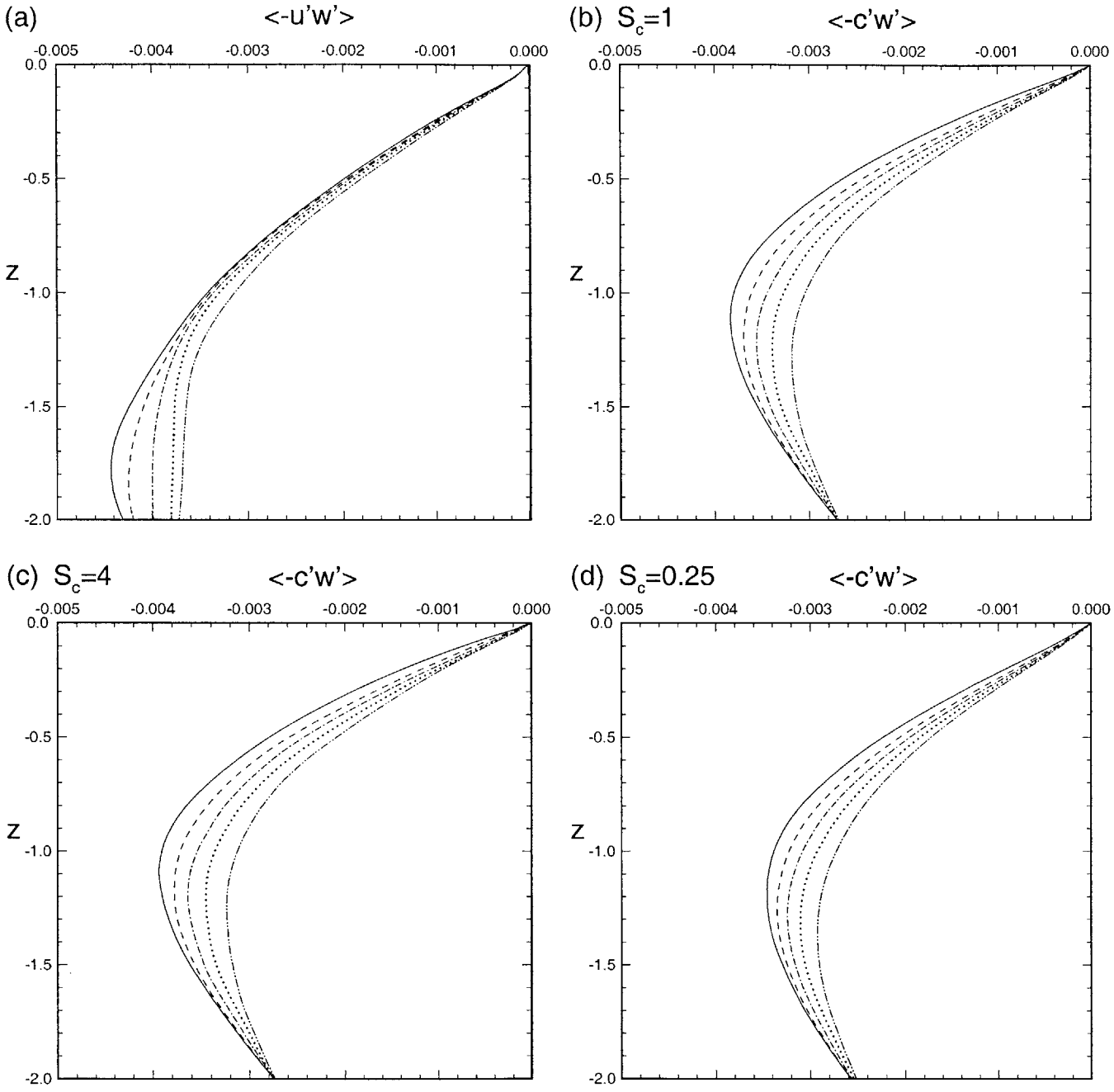

Figure 5-3: Profiles of (a) Reynolds stress $\langle -u'w' \rangle$, and turbulent scalar flux $\langle -c'w' \rangle$ for: (b) S_c=1, (c) S_c=4, and (d) S_c=0.25. ———— , t=60; - - - - , t=62.5, - · - · - , t=65, ····· , t=67.5, —··—··— , t=70.

to (d). In the bulk flow below, γ does not vary with depth. The difference between the magnitude of γ for different Schmidt numbers is negligible. The value of γ is comparable to the eddy viscosity ν_e (Figure 5-4a) because the diffusion mechanisms for the velocity and scalar are similar in the bulk shear flow (Tennekes and Lumley 1972).

The free-surface boundary layer for the scalar mixing is manifest in Figures 5-4(b) to (d). As the free surface is approached, γ decreases rapidly, in a manner similar to ν_e (Figure 5-4a). The decrease of γ and ν_e can be attributed to the constraint on vertical motions by the free surface. From Figure 5-4 we obtain two important observations: (i) Schmidt number does not affect the location from which γ begins to decrease, which is same as the one in the ν_e case. This implies that the thickness of the free-surface (outer) boundary layer for scalar mixing does not depend on the molecular diffusivity of the scalar, and it scales as the free-surface outer layer for momentum diffusion. (ii) As γ decreases towards the free surface, it approaches a surface value γ_0 which is, however, highly dependent on the Schmidt number. We find that the surface value of turbulent diffusivity is proportional to the molecular diffusivity (as will be shown in §5.4, the factor of proportionality is around 2).

In Figure 5-5 we compare the profiles of the mean velocity $\langle u \rangle$ and the mean scalar concentration $\langle c \rangle$ for various Schmidt numbers. As time evolves, both $\langle u \rangle$ and $\langle c \rangle$ profiles flatten out through turbulent diffusion. The difference in the profiles for different Schmidt numbers is noticeable: near the free surface, $\langle c \rangle$ has a hump for high S_c (Figure 5-5c); while for low S_c (Figure 5-5d), $\langle c \rangle$ is rather smooth.

The effect of the Schmidt number on the gradient of the mean concentration is shown in Figure 5-6. Figure 5-6(b) shows the S_c=1 case. It is found that as the free surface is approached, $\partial\langle c \rangle/\partial z$ initially increases, reaching a local maximum and then decreases rapidly over a much thinner inner layer to obtain the zero-gradient value at the free surface. This variation is very similar to the mean shear case (Figure 5-6a). The latter clearly shows the multi-layer structure in turbulent momentum diffusion near a free surface and was investigated extensively in Chapter 4. For the scalar mixing, we find that the Schmidt number substantially affects the near-surface profiles of $\partial\langle c \rangle/\partial z$. Higher S_c greatly increases the maximum value of $\partial\langle c \rangle/\partial z$ and makes the near-surface variation more dramatic (Figure

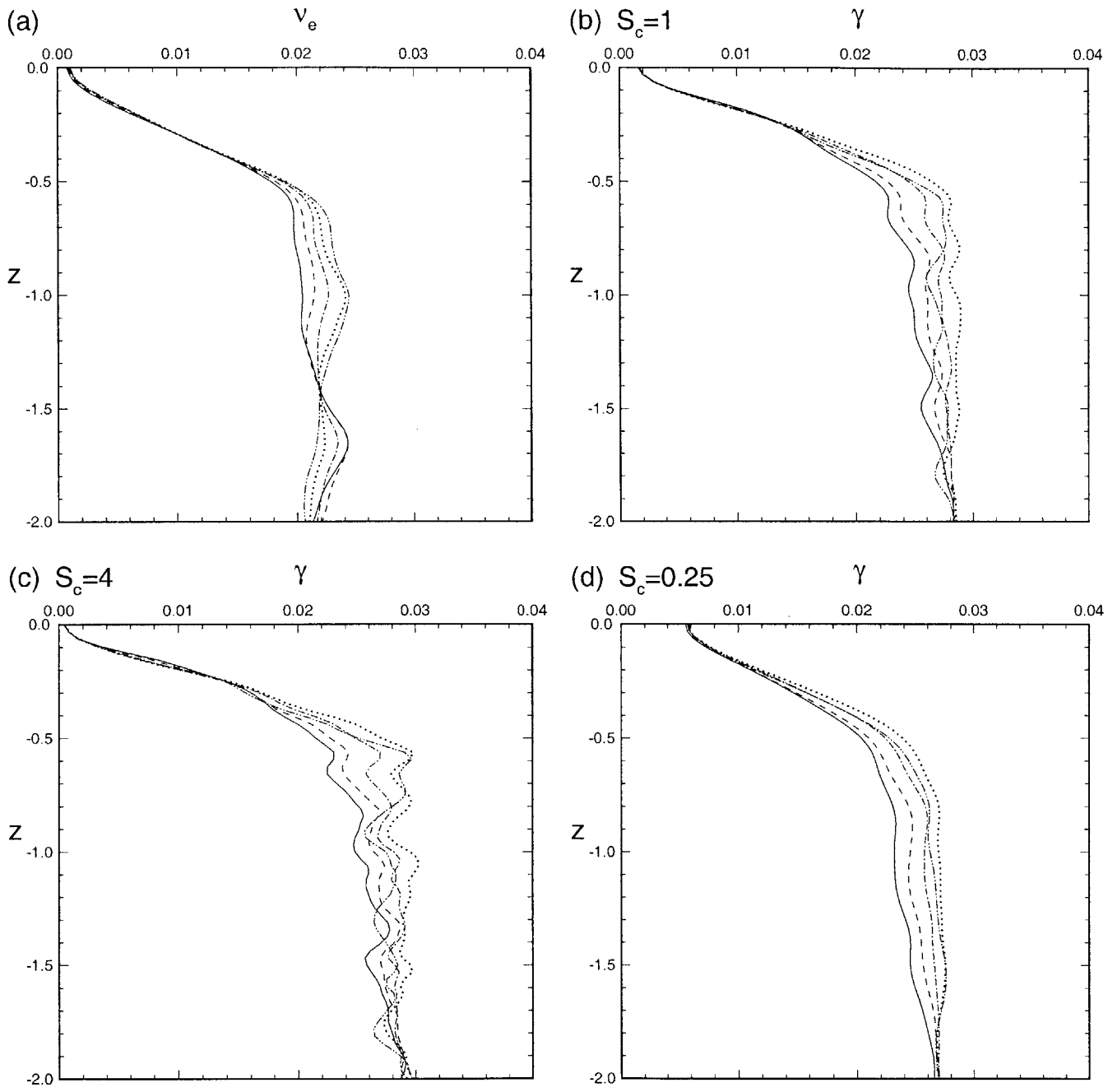

Figure 5-4: Profiles of (a) eddy viscosity ν_e, and turbulent diffusivity γ for: (b) S_c=1, (c) S_c=4, and (d) S_c=0.25. ———— , t=60; – – – – , t=62.5, – · – · – , t=65, ····· , t=67.5, —··—··— , t=70.

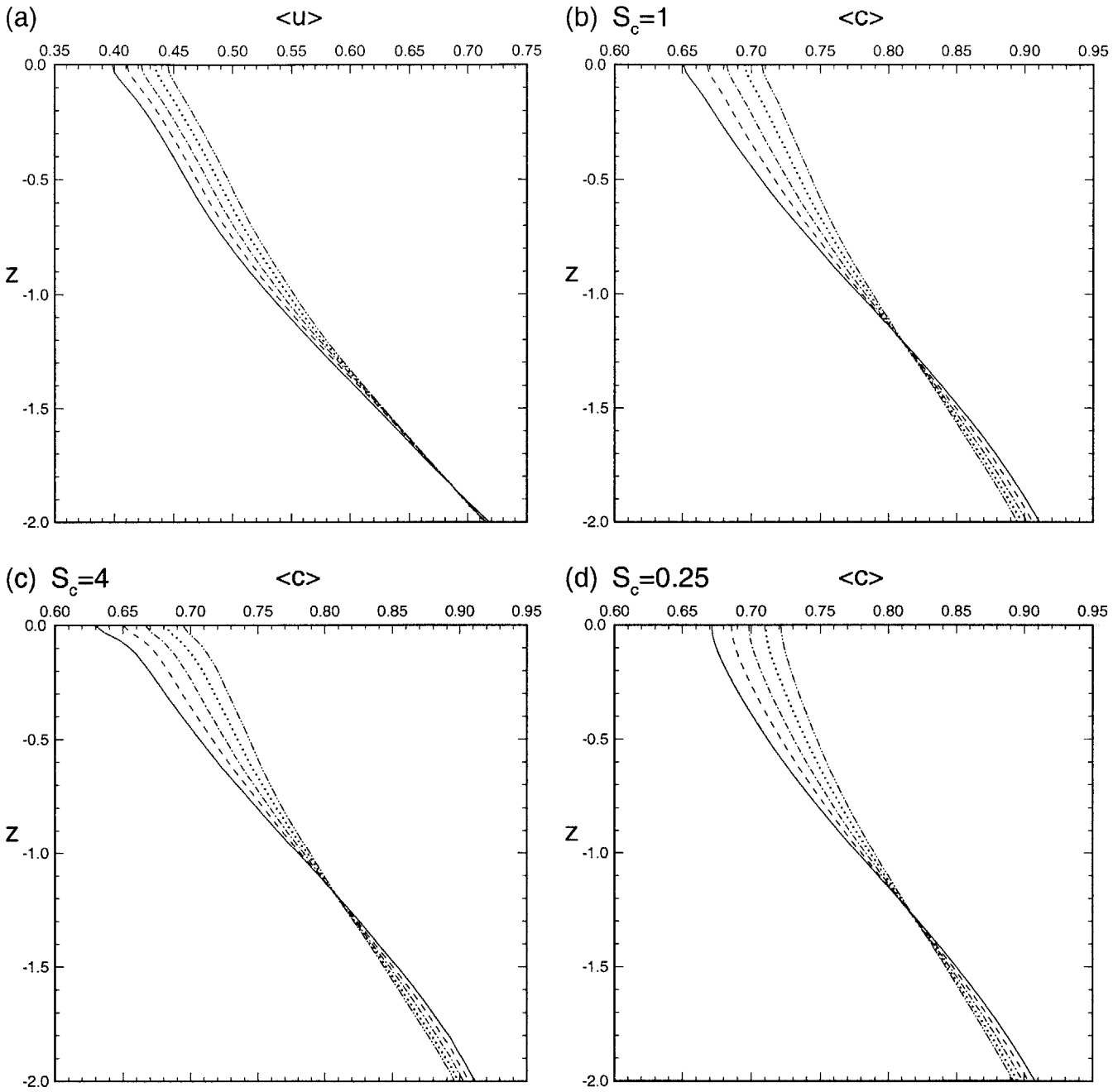

Figure 5-5: Profiles of (a) mean velocity $\langle u \rangle$, and mean scalar concentration $\langle c \rangle$ for: (b) S_c=1, (c) S_c=4, and (d) S_c=0.25. ———— , t=60; – – – – , t=62.5, – · – · – , t=65, ····· , t=67.5, —··—··— , t=70.

5-6c); while at lower S_c, the variation is suppressed and the local maximum even disappears for S_c=0.25 (Figure 5-6d).

5.3 Theoretical interpretation

5.3.1 Analytical similarity solution for scalar mixing

We observe that, mathematically, the governing equations for the problems of momentum diffusion (5.8) and scalar mixing (5.9) are of the same form and they satisfy the same free-surface boundary conditions (5.11). The problem for the evolution of the mean concentration is therefore analogous to that for the evolution of the mean velocity. Following Chapter 4, then, we seek a self-similar solution to the scalar mixing problem. Specifically, we look for solutions of the form:

$$\frac{C_\infty - \langle c \rangle}{C_d} = f(\xi) \,, \tag{5.14}$$

where $C_\infty \equiv \langle c \rangle|_{z\to-\infty}$, C_d=$C_\infty - \langle c \rangle|_{z=0}$ is the maximum concentration difference, and ξ is the similarity variable:

$$\xi = \frac{z}{b_c} \,, \tag{5.15}$$

with b_c the lateral extent of the concentration gradient in the flow. From the conservation of the total scalar we obtain

$$C_d b_c = K_c = \text{const.} \tag{5.16}$$

As shown in §5.2.2, the surface value of the turbulent diffusivity γ_0 is of the same order of magnitude as the molecular diffusivity D. Far from the free surface, on the other hand, the value of γ approaches a constant γ_a, which is determined by the turbulent mixing mechanism in the bulk flow and is independent of D. From dimensional analysis we expect that γ_a should be proportional to the product $U_d b$. Hence we obtain

$$\frac{\gamma}{U_d b} = \psi_c(\xi; \frac{U_d b}{D}) \,. \tag{5.17}$$

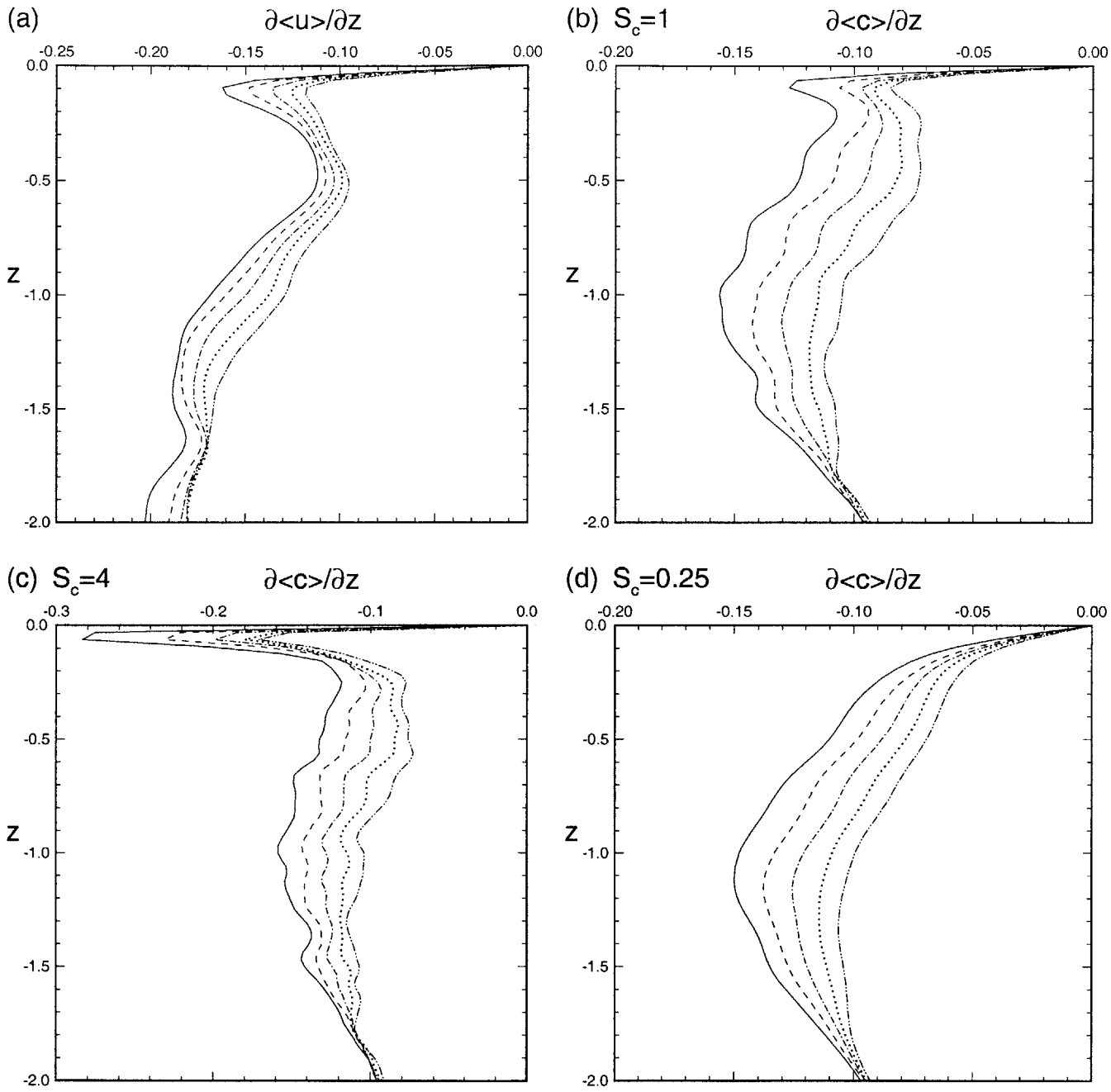

Figure 5-6: Profiles of (a) mean shear $\partial\langle u\rangle/\partial z$, and mean scalar concentration gradient $\partial\langle c\rangle/\partial z$ for: (b) S_c=1, (c) S_c=4, and (d) S_c=0.25. ———— , t=60; – – – – , t=62.5, – · – · – , t=65, · · · · · · · , t=67.5, —··—··— , t=70.

Based on the observation from Figure 5-4, we fit ψ_c with the following curve:

$$\psi_c = \psi_{ca} - (\psi_{ca} - \psi_{c0}) \exp\left(-\xi^2/a_c^2\right) , \tag{5.18}$$

where the parameter a_c is the non-dimensional scale of variation of the turbulent diffusivity; ψ_{ca} and ψ_{c0} are values of the non-dimensional turbulent diffusivity in the bulk flow and at the free surface, respectively.

For the self-similar expression (5.14), the partial differential equation (5.9) is transformed into an ordinary differential equation as

$$\xi f_c' + f_c = -\left(b_c \frac{\mathrm{d}b_c}{\mathrm{d}t}\right)^{-1} \frac{\mathrm{d}}{\mathrm{d}\xi}\left[(D + U_d b \psi_c) f_c'\right] . \tag{5.19}$$

Based on the same physical reasoning as in the momentum case (Chapter 4), we argue that b_c diffuses at a rate proportional to γ_a. Hence we obtain

$$b_c = \sqrt{2(D + U_d b \psi_{ca})t + Q_c} , \tag{5.20}$$

$$C_d = \frac{K_c}{\sqrt{2(D + U_d b \psi_{ca})t + Q_c}} , \tag{5.21}$$

with Q_c a constant; and by integrating (5.19) we obtain the self-similar solution as

$$f_c(\xi) = \exp\left(-\int_0^\xi \frac{s(D + U_d b \psi_{ca})}{D + U_d b \psi_c(s)} \mathrm{d}s\right) . \tag{5.22}$$

For the Gaussian profile (5.18), the above solution can be explicitly expressed as

$$f_c(\xi) = \exp\left(-\xi^2/2\right) \left[\frac{1/(R_e S_c) + \psi_{c0}}{1/(R_e S_c) + \psi_{ca} - (\psi_{ca} - \psi_{c0}) \exp(-\xi^2/a_c^2)}\right]^{a_c^2/2} \tag{5.23}$$

5.3.2 Comparison between similarity solution and DNS result

We next compare the analytical solution with the results of the simulation. The comparison is performed as follows: in the similarity solution, C_d is obtained directly from the DNS values; ψ_{c0} and ψ_{ca} are determined based on the surface and bulk values of turbulent diffusivity; b_c

is obtained by matching $f_c(\xi)$ to the numerical value at $\xi = -1$; and a_c is determined by a least-square fit of (5.23).

Figures 5-7 to 5-11 summarize the results for all Schmidt numbers considered. The profiles of non-dimensional turbulent diffusivity ψ_c, mean concentration f_c, and mean concentration gradient $\partial f_c/\partial\xi$ are compared in Figures (a), (b), and (c), respectively. It is shown that the Gaussian profile (5.18) describes well the variation of turbulent diffusivity near the free surface. The agreement between the analytical curve (5.23) and numerical results of the mean concentration is satisfying. The aforementioned difference between high and low Schmidt numbers close to the free surface is captured accurately. This is shown more clearly in the comparison of $\partial f_c/\partial\xi$ (Figures 5-7 to 5-11c). As revealed in §5.2.2, at high S_c, the scalar gradient initially increases towards the free surface and then decreases, resulting in a local maximum; while as S_c decreases, the hump in the scalar gradient becomes less obvious and finally disappears. These phenomena are represented well by the similarity solution. For high S_c, both the location and the magnitude of the maximum gradient is captured by the theoretical prediction with remarkable accuracy. Figures 5-7 to 5-11 show that by proper scaling with (5.14), all the physically-different profiles of the scalar mean quantities at different times (cf. Figures 5-5 and 5-6) collapse to a single curve. This holds for all Schmidt numbers considered in this study.

Next we examine the time scaling behavior of the scalar mixing. Figure 5-12 plots the time evolution of the product of C_d and b_c obtained from DNS. In agreement with (5.16), $C_d b_c$=K_c remains almost constant in time with a variation of less than 3.5%. Figures 5-13(a) to (e) compare numerical values of C_d and b_c with the theoretical predictions (5.20) and (5.21). In the latter, K_c is set to the time-averaged value of $C_d b_c$ shown in Figure 5-12; Q_c is determined by a least-square fit and is found to be -1.94, -1.94, -1.96, -1.98, and -2.03 for S_c=0.25, 0.5, 1, 2, and 4, respectively.

As Figure 5-13 shows, (5.20) and (5.21) predict well the variation of C_d and b_c in time. From (5.20) and (5.21), we conclude that at large t, the mean scalar concentration difference C_d decays proportionally to $t^{-1/2}$, while the vertical extent of mean scalar concentration variation b_c increases proportionally to $t^{1/2}$. For reference, we also plot in Figure 5-13(f) the

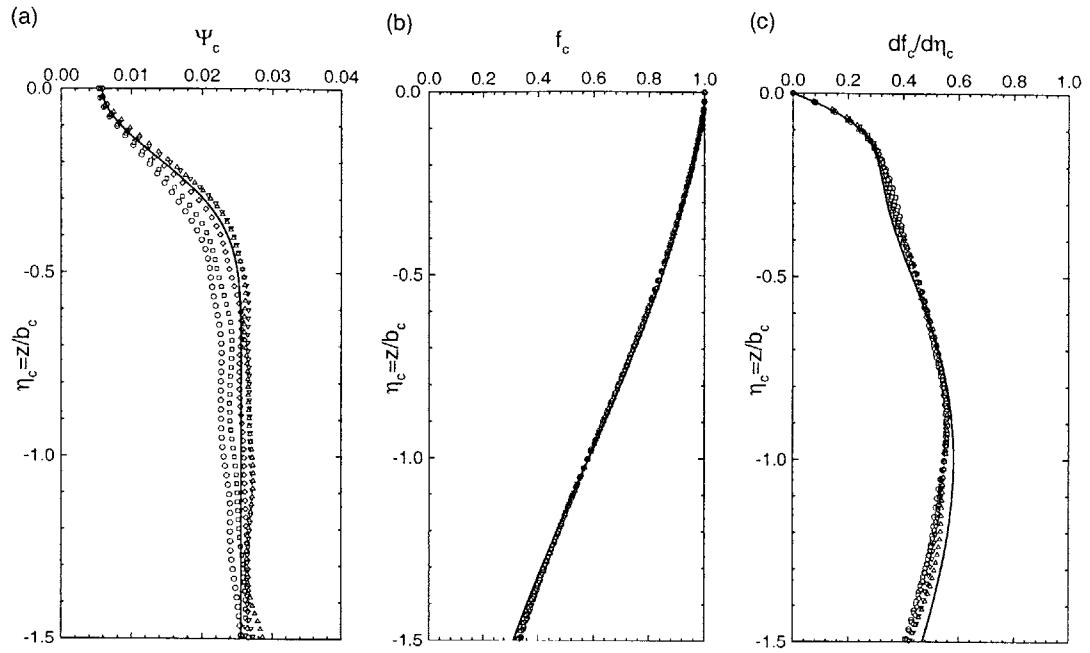

Figure 5-7: Comparison of profiles of (a) turbulent diffusivity, (b) mean concentration, and (c) mean concentration gradient, between the similarity solution (————) and the DNS results at: ○, t=60; □, t=62.5; ◇, t=65; ∇, t=67.5; △, t=70. S_c=0.25.

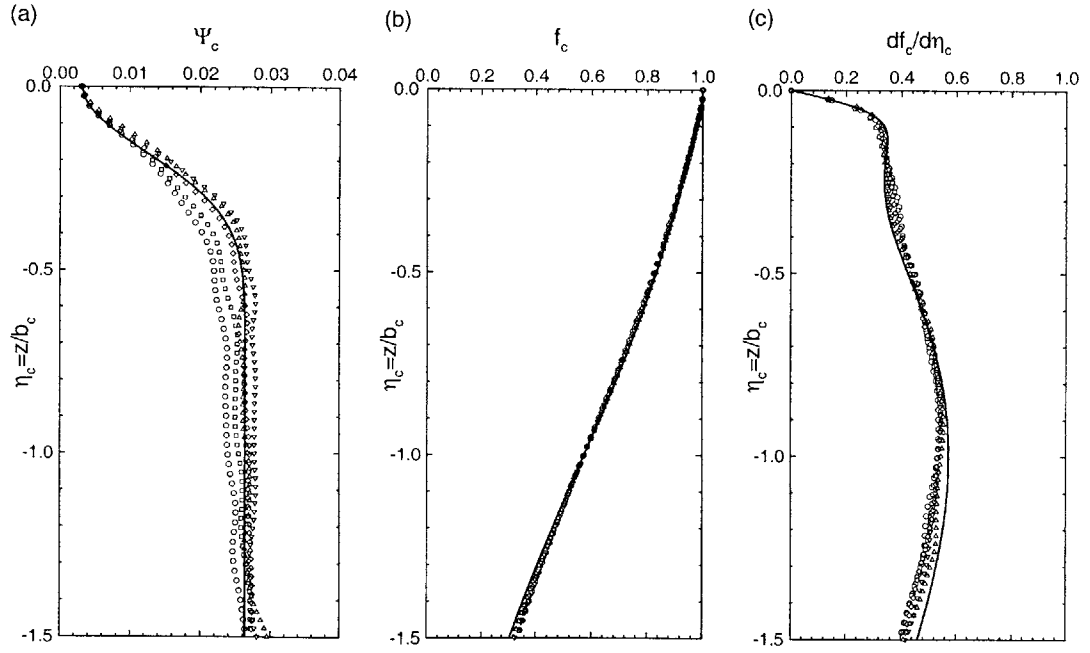

Figure 5-8: Comparison of profiles of (a) turbulent diffusivity, (b) mean concentration, and (c) mean concentration gradient, between the similarity solution (————) and the DNS results at: ○, t=60; □, t=62.5; ◇, t=65; ∇, t=67.5; △, t=70. S_c=0.5.

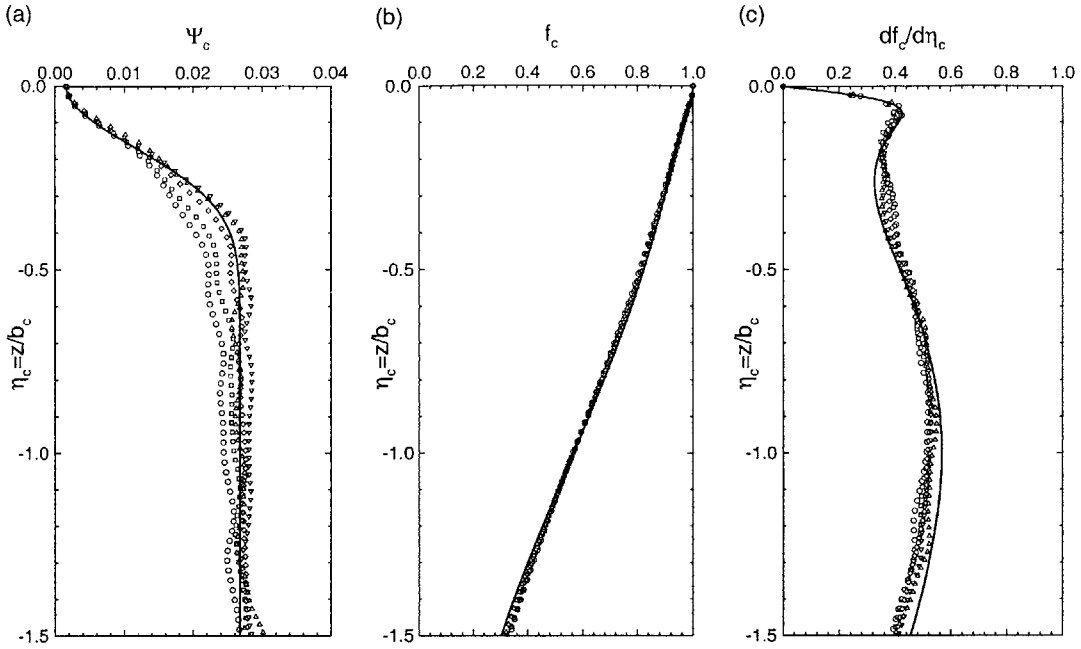

Figure 5-9: Comparison of profiles of (a) turbulent diffusivity, (b) mean concentration, and (c) mean concentration gradient, between the similarity solution (—————) and the DNS results at: ○, t=60; □, t=62.5; ◇, t=65; ∇, t=67.5; △, t=70. S_c=1.

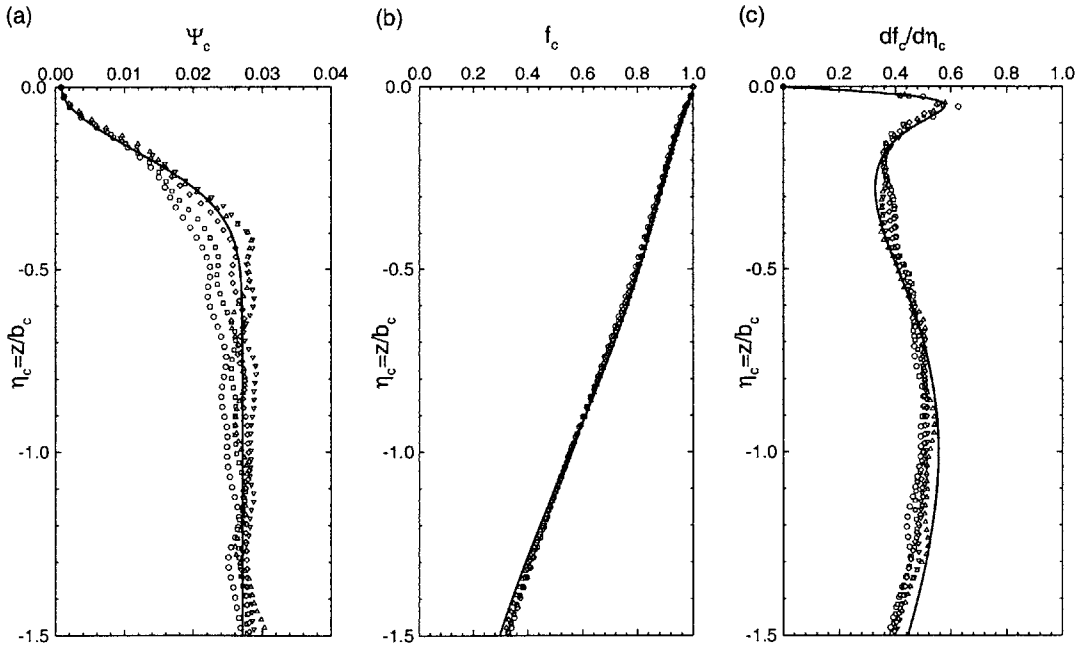

Figure 5-10: Comparison of profiles of (a) turbulent diffusivity, (b) mean concentration, and (c) mean concentration gradient, between the similarity solution (—————) and the DNS results at: ○, t=60; □, t=62.5; ◇, t=65; ∇, t=67.5; △, t=70. S_c=2.

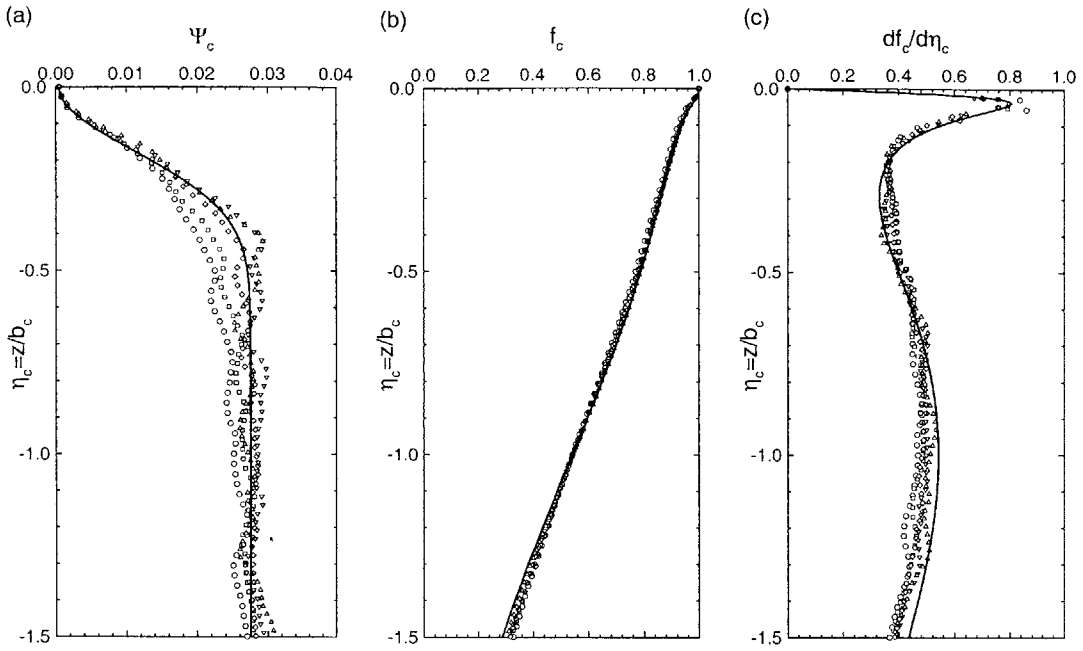

Figure 5-11: Comparison of profiles of (a) turbulent diffusivity, (b) mean concentration, and (c) mean concentration gradient, between the similarity solution (—————) and the DNS results at: ○, t=60; □, t=62.5; ◇, t=65; ▽, t=67.5; △, t=70. S_c=4.

time evolution of the momentum properties, U_d and b_c, which is also predicted well by (4.20) and (4.21). This is further discussed in §5.4.

5.4 Scaling properties of free-surface scalar layer

From the proceeding sections it is shown that the problem of free-surface scalar mixing is characterized by the following three length scales: (i) the lateral extent of the concentration gradient in the flow b_c, (ii) the thickness of the free-surface scalar *outer* boundary layer ℓ_c=$a_c b_c$, over which the turbulent diffusivity decreases, and (iii) the thickness of the free-surface scalar *inner* sublayer δ_c=$\epsilon_c b_c$. Note that ℓ_c and δ_c are the 'physical' measurement. (Although they are normalized by L_0 in the results presented in this chapter, L_0 is chosen in the initial condition and is the same for all the cases. Thus ℓ_c and δ_c differ from the physical value by a constant only.) On the other hand, a_c and ϵ_c are the non-dimensional value normalized by b_c, which is different for each cases and varies in time.

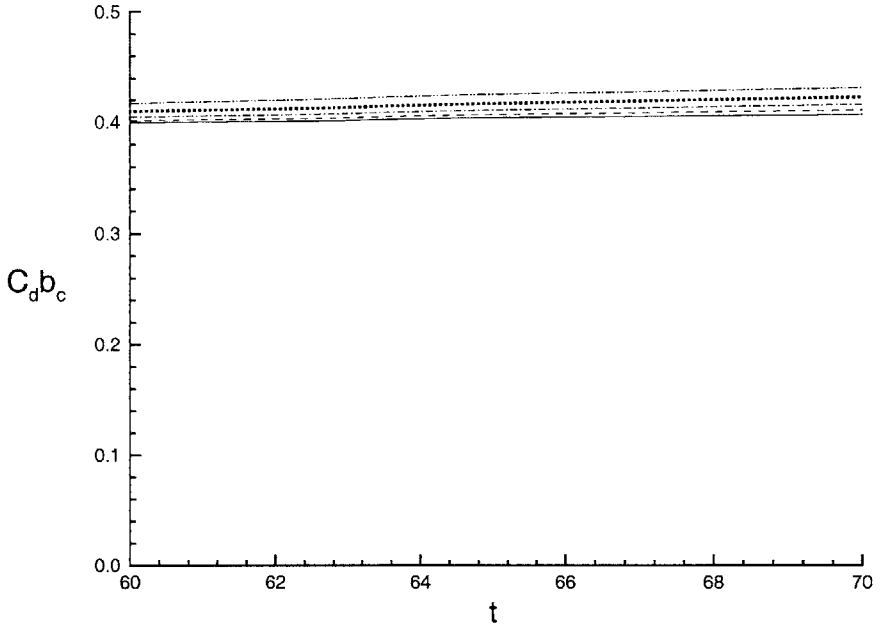

Figure 5-12: Time evolution of $C_d b_c$ for S_c=: 0.25 (————), 0.5 (– – – –), 1 (– · – · –), 2 (· · · · · · ·), and 4 (—··—··—).

We next discuss the scaling properties of the above characteristic length scales in fully mixed flows (large t). By comparing (4.20) and (5.20) we have the following scaling for b_c:

$$b_c \sim b \, . \tag{5.24}$$

We conclude in other words that the extent of scalar concentration gradient is proportional to the extent of shear in the flow, which is shown in Figure 5-13. Note that the difference between b and b_c are mainly caused by the difference in the integration constants Q and Q_c in (4.20) and (5.20) ($Q \approx 0.12$ while $Q_c \approx -2.0$). The difference in the integration constants represent initial effects: for example, the flow begins at t=0 while the scalar mixing begins at t=30; the fluctuation development mechanism for velocity is different from that for the scalar. As t becomes large, the contribution of integration constants decreases and the influence of the bulk eddy viscosity ν_{ea}=$U_d b \psi_a$ and the bulk turbulent diffusivity γ_a=$U_d b \psi_{ca}$ dominates. The values of ν_{ea} and γ_a are close to each other (cf. Figure 5-4) because the turbulent diffusion mechanisms are the same in the bulk shear flow. Hence the factor of

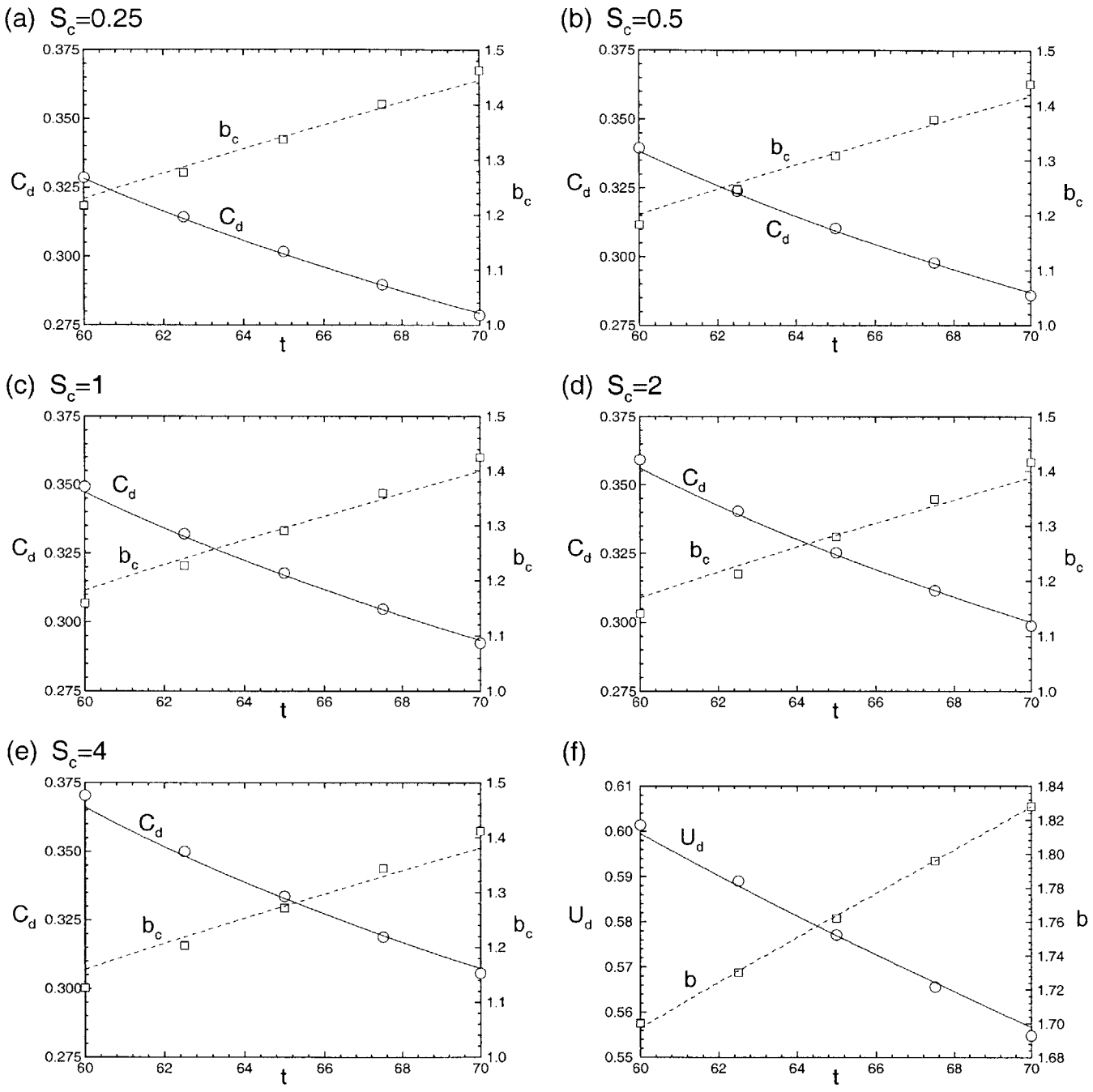

Figure 5-13: Time evolution of C_d and b_c for (*a*) S_c=0.25, (*b*) S_c=0.5, (*c*) S_c=1, (*d*) S_c=2, and (*e*) S_c=4 for: DNS results (○ for C_d, □ for b_c); and similarity solution (———— for C_d, – – – – for b_c). (*f*) Time evolution of U_d and b for DNS results (○ for U_d, □ for b) and similarity solution (———— for U_d, – – – – for b).

proportionality in (5.24) is close to 1.

Likewise, since the mixing of the scalar is caused by turbulence, we assume that the characteristic length scale of variation of the turbulent diffusivity ℓ_c depends only on the characteristic scale of variation of the eddy viscosity ℓ. Dimensional analysis then gives:

$$\ell_c \sim \ell \,. \tag{5.25}$$

For the length scales ℓ=ab and b which characterize the turbulent diffusion of momentum we have the following scaling relation (Chapter 4):

$$\frac{\ell}{b} = a \sim (\frac{U_d b}{\nu})^{-1/2} = R_e^{-1/2} \,. \tag{5.26}$$

We combine (5.24)–(5.26) and obtain the following relation:

$$\frac{\ell_c}{b_c} = a_c \sim R_e^{-1/2} \,, \tag{5.27}$$

For inner layer thickness, on the other hand, we use the small ξ expansion of equation (5.23) and obtain the following estimate:

$$\frac{\delta_c}{\ell_c} = \frac{\epsilon_c}{a_c} \sim (\frac{1/(R_e S_c) + \psi_{c0}}{\psi_{ca} - \psi_{c0}})^{1/2} = (\frac{D + \gamma_0}{\gamma_a - \gamma_0})^{1/2} \,. \tag{5.28}$$

Here the surface value of turbulent diffusivity γ_0 enters into the problem. The results of the numerical simulation consistently show that the value of the turbulent mixing coefficient at the free surface is proportional to the molecular diffusion coefficient. As shown in Table 5.1, the ratio between γ_0 and D is found to be abound 2 for all the Schmidt numbers investigated in the present study throughout the time range considered here.

Since γ_0 scales with D and since $\gamma_c \sim U_d b \gg \gamma_0$, from (5.28) we obtain

$$\frac{\delta_c}{\ell_c} = \frac{\epsilon_c}{a_c} \sim (\frac{D}{U_d b})^{1/2} = R_e^{-1/2} S_c^{-1/2} \,. \tag{5.29}$$

Next we investigate the maximum concentration gradient near the free surface for large

	S_c=0.25	S_c=0.5	S_c=1	S_c=2	S_c=4
t=60	1.93	2.17	2.24	2.30	2.45
t=62.5	2.00	2.26	2.35	2.43	2.59
t=65	2.03	2.29	2.40	2.50	2.68
t=67.5	2.08	2.30	2.42	2.56	2.80
t=70	2.18	2.31	2.48	2.56	2.82

Table 5.1: Ratio of surface value of turbulent diffusivity over molecular diffusivity γ_0/D.

S_c cases. Differentiating (5.23) with respect to ξ and using small-argument approximation, we find that the maximum gradient occurs at

$$\xi_m \approx -a_c \left[\frac{1/(R_e S_c) + \psi_{c0}}{(1+a_c^2)\psi_{ca} - \psi_{c0}} \right]^{1/2} , \tag{5.30}$$

and the maximum concentration gradient $f_c'|_{max}$ is:

$$f_c'|_{max} \approx a_c \left(R_e S_c \psi_{ca}\right)^{1/2} \frac{\left(1 + a_c^2 - \psi_{c0}/\psi_{ca}\right)^{1/2} \left(1 + (R_e S_c \psi_{ca})^{-1}\right)}{(2 + a_c^2 - 2\psi_{c0}/\psi_{ca})(1 + R_e S_c \psi_{c0})^{1/2}} \propto S_c^{1/2} . \tag{5.31}$$

The scaling relations (5.27), (5.29) and (5.31) agree excellently with our numerical results, the latter listed in Table 5.2. In large Schmidt number cases, the inner layer thickness is defined as the distance from the free surface to the location where $f_c'|_{max}$ occurs. As shown in Table 5.2, the outer layer thickness is not affected by the Schmidt number. The inner layer thickness, on the other hand, depends on S_c and is found to scale like $S_c^{-1/2}$. The maximum concentration gradient $f_c'|_{max}$ is also dependent on S_c and $S_c^{-1/2}$ $f_c'|_{max}$ is found to be constant.

Note that in Table 5.2, the inner layer thickness is defined as the distance from the free surface to the location where $f_c'|_{max}$ occurs. As pointed out earlier, as the Schmidt number decreases the mean concentration gradient curve becomes smooth and the near-surface maximum disappears. From the similarity solution (5.23) we obtain a critical Schmidt number S_c=0.40 below which $f_c'|_{max}$ is not present, while in numerical results $f_c'|_{max}$ has

	scalar					velocity
	S_c=0.25	S_c=0.5	S_c=1	S_c=2	S_c=4	
a_c (a)	0.25	0.25	0.24	0.24	0.25	0.22
ϵ_c/a_c	N/A	N/A	0.32	0.22	0.15	N/A
$S_c^{1/2}$ ϵ_c/a_c	N/A	N/A	0.32	0.31	0.31	N/A
$f_c'\|_{max}$	N/A	N/A	0.42	0.58	0.81	N/A
$S_c^{-1/2}$ $f_c'\|_{max}$	N/A	N/A	0.42	0.41	0.40	N/A

Table 5.2: Characteristic scales of free-surface boundary layer.

already become ambiguous at S_c=0.5 (Figure 5-8c). For $S_c \geq 1$, however, $f_c'|_{max}$ is quite distinct (Figures 5-9c to 5-11c) and provides a clear definition for the scalar mixing boundary layer.

Finally, we remark that although the similarity expressions for the free-surface momentum boundary layer (4.24) and the scalar boundary layer (5.23) look similar, the underlying physics are different. In the case of momentum surface layer, both the outer layer thickness and the inner layer thickness are dependent on the Reynolds number. It is found that both $\ell/b = a$ and $\epsilon/a = \delta/\ell$ scale as $R_e^{-1/2}$ and the maximum mean shear remains approximately a constant as R_e increases (cf. Chapter 4). For scalar mixing, the outer layer is controlled by the turbulent motion and its thickness a_c scales with the momentum outer layer thickness a (Table 5.2). The value of molecular diffusivity (in other words, the Schmidt number) does not affect a_c. The scalar inner layer, on the other hand, is the region where the molecular diffusivity is felt. It is found that the scalar inner layer thickness scales as $S_c^{-1/2}$. The maximum concentration gradient, which occurs at the lower limit of the inner layer, scales as $S_c^{1/2}$. Hence, unlike the maximum shear which is bounded as R_e increases, the maximum concentration gradient increases as S_c increases.

5.5 Conclusions

In this chapter we investigate the mixing process of a passive scalar in a turbulent shear flow under a free surface. We perform direct numerical simulations for the Navier–Stokes equations and the scalar convection–diffusion equation. From an ensemble of simulation results, we identify a multi-layer structure for the scalar mixing near the free surface: an inner layer characterized by the decrease of the mean concentration gradient to obtain its vanishing value at the free surface; and an outer layer characterized by the reduction of the turbulent diffusivity.

Guided by numerical results, we derive a similarity theory for this problem. In particular, the similarity solution specifies a universal shape for the mean concentration profile. This and other predictions of the similarity theory are well confirmed by direct comparisons to DNS. Significantly, the similarity solution provides the scaling for the thickness of the inner and outer surface layers as a function of the Reynolds number and the Schmidt number. We find that very close to the free surface (at a distance equal to the thickness of the inner layer) there is a local maximum of the concentration gradient which is proportional to the square root of the Schmidt number. Therefore, we have the interesting conclusion that for high Schmidt numbers high concentration gradients exist very close to the free surface despite the zero flux condition. We find that the near-surface maximum in the concentration gradient is present for Schmidt numbers larger than 0.4, which is the case for most substances (for example, the Schmidt numbers for most gases of environmental interest is $O(10^{2-3})$; the Prandtl number for heat transfer is $O(10^{1-2})$; cf. Lide 2000).

The analytical similarity solution provides a fundamental basis for the quantification of the free-surface scalar-mixing boundary layer. The analytical solution matches the results of the simulation remarkably well. We remark that the range of the Schmidt numbers (from 0.25 to 4) tested in our numerical simulations is constrained by the fundamental limitation of the DNS approach. To obtain more complete/systematic confirmation of the theoretical predictions, it would be very desirable to seek experimental measurements and other simulation approaches such as large-eddy simulation or the scalar-particle Lagrangian-tracking approach (see e.g. Papavassiliou & Hanratty 1997).

Chapter 6

Transfer of a Passive Scalar at a Free Surface

The problem of passive scalar transfer near a free surface is of great importance to many applications. An accurate estimate of the transfer rate of greenhouse gases across the air-sea interface helps our understanding of environmental issues such as the global warming. Many industrial processes, including the gas absorption and evaporation equipments, also require knowledge of free-surface scalar-transfer mechanism.

The problem of turbulent scalar transfer near a free surface has been studied experimentally by Jobson & Sayre (1970), Ueda *et al.* (1977), Komori *et al.* (1982), Brown, Khoo & Sonin (1990) and Rashidi, Hetsroni & Banerjee (1991). Recently, Nagaosa (1999) and Handler *et al.* (1999) performed numerical simulations of turbulent open-channel flows with passive scalars convected by the flow. Nagaosa (1999) showed the relation between surface-renewal events and the quasi-streamwise vortex tubes emanating from the solid bottom. Handler *et al.* (1999) proposed a two-timescale model for surface renewal, which assumes a fast hydrodynamic scale and a slow diffusional scale. It was proposed that coherent hairpin eddies are the dominant kinematic structure responsible for surface renewal. Handler *et al.* (1999), however, were unable to quantify the overall contribution of hairpin eddies to the transport process to support their conjecture, nor did they investigate other turbulence structures.

In this chapter we investigate the statistical characteristics and structures of passive scalars in free-surface turbulence. In Chapter 5 we use DNS to study the problem of scalar mixing near a free surface where the scalar flux vanishes. In this chapter we further consider two others cases, namely a fixed scalar surface-concentration case and a fixed (non-zero) scalar surface-flux case. In both these two cases, the transfer rate of the scalar across the free surface is of interest. The main objectives of this chapter is to elucidate the structure of the FST passive scalar field and to understand the relation between the mechanism of scalar transfer and the dynamics of FST .

This chapter is organized as follows: we first define the problem in §6.1; in §6.2 we investigate the statistical characteristics of the scalar field; we discuss in §6.3 the structures of the scalar field and their dependence on the FST coherent vortices; in §6.4, we identify and quantify the scalar transport processes in free-surface turbulent flows; finally in §6.5, we present the conclusions.

6.1 Problem definition

Similar to Chapter 5, we consider the transport of passive scalars in a turbulent shear flow underneath a free surface (cf. Figure 5-1). The governing equations for the fluid motions as well as the scalar transport are given in §5.1. In Chapter 5, we investigate the case where the scalar concentration c has zero gradient at the free surface:

$$\frac{\partial c}{\partial z} = 0, \qquad \text{on } z = 0 \,, \tag{6.1}$$

which corresponds to situations where there is no scalar flux across the surface, e.g. the transport of most pollutants for which the surface adsorption and desorption rates are low.

In addition to the zero-flux case, we further consider here two other free-surface boundary conditions:

$$c = 0, \qquad \text{on } z = 0 \,, \tag{6.2}$$

and

$$\frac{\partial c}{\partial z} = -1, \qquad \text{on } z = 0\ . \tag{6.3}$$

The fixed-concentration condition (6.2) models the gas transfer between the air and water, in which case the gas transport process is mainly controlled by the water motions and the gas concentration at the air side can be regarded as a constant. The fixed-flux condition (6.3) models the heat transfer problem, where the heat flux rates, controlled by factors such as wind and evaporation, can be reasonably approximated as a constant while the temperature distribution at the water side needs to be investigated.

At the bottom, we apply a fixed-concentration boundary condition:

$$c|_{z=-L_z} = 1. \tag{6.4}$$

In the horizontal directions, period boundary condition is used.

In this chapter we investigate the transport processes of the scalars subject to the free-surface boundary conditions (6.1), (6.2), and (6.3), respectively. The numerical scheme is essentially the same as in Chapter 5 and will not be taken up here. For each cases, we consider five different Schmidt numbers $S_c = 0.25$, 0.5, 1, 2, and 4, in order to investigate the effect of molecular diffusivity.

6.2 Statistics of passive scalar transfer

In view of the horizontal homogeneity, in this chapter we use plane-averaging unless otherwise pointed out. Figures 6-1 to 6-7 plot the statistical properties of the scalar fields, with Figures (a), (b), (c) corresponding to the zero surface-flux, fixed surface-value, and fixed surface-flux cases, respectively. For reference, we also plot in (a) the equivalence in velocity quantities.

Figure 6-1 plots the mean scalar concentration profiles. For the zero surface-flux case (Figure a), the difference between each Schmidt number is negligible in the bulk flow below. Near the free surface, however, the molecular diffusivity affects the $\langle c \rangle$ profile (cf. Chapter 5). For both the fixed surface-value case (Figure b) and the fixed surface-flux case (Figure c),

the effects of molecular diffusivity are much more obvious. For the former, higher Schmidt number produces steeper concentration gradient and a thinner scalar boundary layer, while for the latter, higher Schmidt number results in a higher scalar surface-concentration value.

The effects of the Schmidt number on the scalar concentration distribution can be seen more clearly in the concentration gradient profile (Figure 6-2). The zero surface-flux case (Figure *a*) has been studied extensively in Chapter 5 and will not be taken up here. For the fixed surface-value case (Figure *b*), higher Schmidt number (smaller molecular diffusivity value) is accompanied with higher gradient, in order to maintain the molecular flux value which dominates near the surface in a way similar to the wall boundary layer. For the fixed surface-flux case (Figure *c*), the scalar gradient variation penetrates much deeper into bulk flow for larger molecular diffusivity values (smaller Schmidt numbers).

The scalar fluctuation magnitude is plotted in Figure 6-3. For both the zero surface-flux case and the fixed surface-value case, $\langle c'^2 \rangle$ increases over the surface layer because of the reduction in dissipation there, in a way very similar to the velocity case (cf. Chapter 3). The boundary condition of a fixed surface-value requires the scalar fluctuation to vanish at the surface. However, just underneath the surface, the fluctuation magnitude reaches its peak value because of the large production (large concentration gradient), in analogy to the velocity equivalence near a solid wall.

Figures 6-4 and 6-5 plot the profiles of scalar turbulent flux and molecular flux, respectively. Due to the constraint of the surface on the vertical motion, the turbulent flux $\langle c'w' \rangle$ diminishes as the free surface is approached. Near the free surface, the contribution of molecular flux increases for both the fixed surface-value case and the fixed surface-flux case. The contributions from the turbulent flux and molecular flux can be seen more clearly from Figure 6-6, where each contribution as well as the summation is plotted. As shown, for the fixed surface-value case, the reduction in the turbulent flux is much compensated by the increase of molecular flux.

Finally in Figure 6-7 we plot the turbulent diffusivity profiles. For the zero surface-flux case, the turbulent diffusivity at the free-surface is nonzero and its value is comparable to the molecular diffusivity (cf. Chapter 5). For the other two cases, however, the turbulent

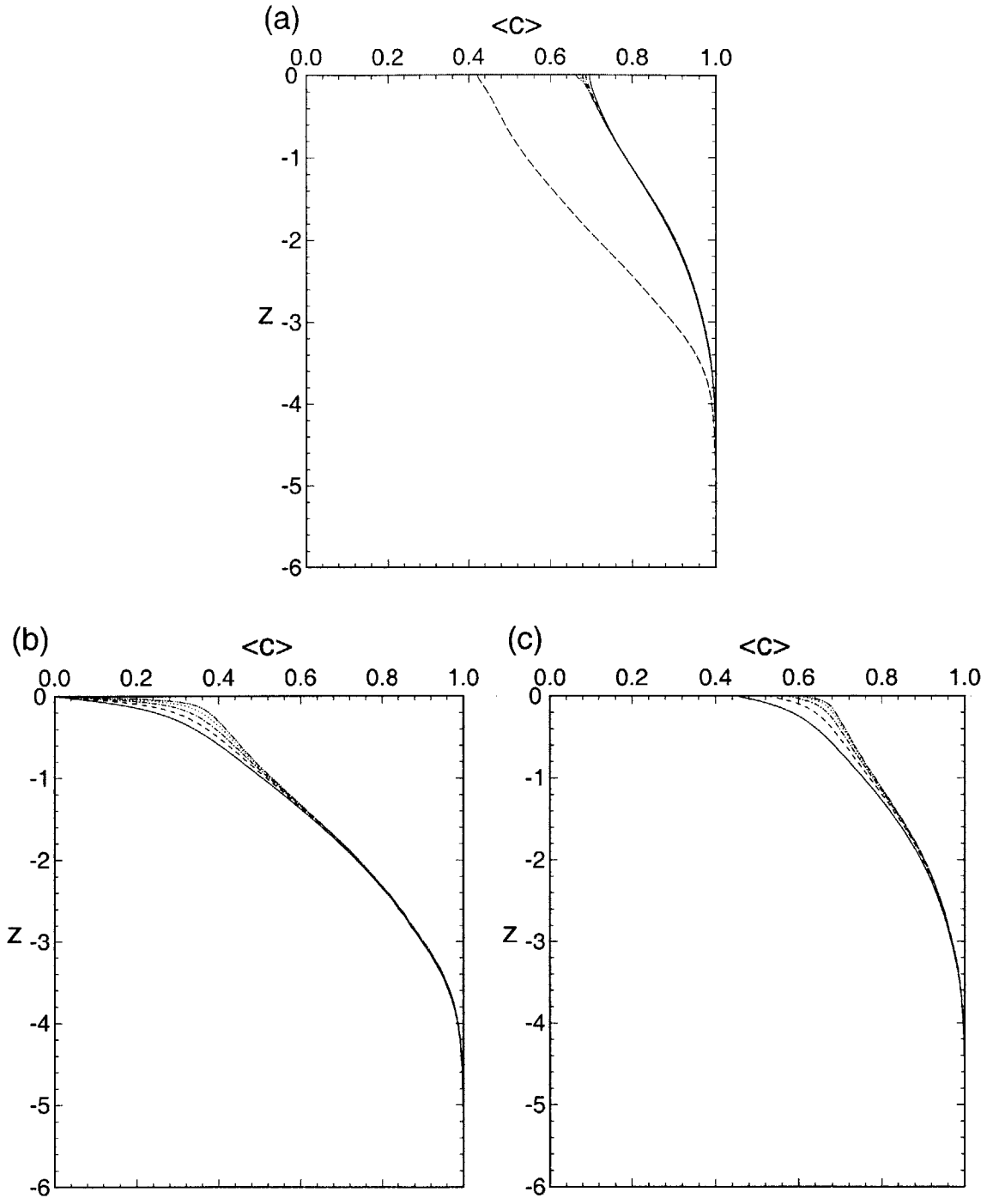

Figure 6-1: Profiles of scalar mean concentration $\langle c \rangle$ for (a) zero surface-flux case, (b) fixed surface-value case, and (c) fixed surface-flux case. ———— , $S_c = 0.25$; - - - - , $S_c = 0.5$; - · - · - , $S_c = 1$; · · · · · · · , $S_c = 2$; —··—··— , $S_c = 0.25$. In (a), —— —— represents the corresponding velocity quantity $\langle u \rangle$.

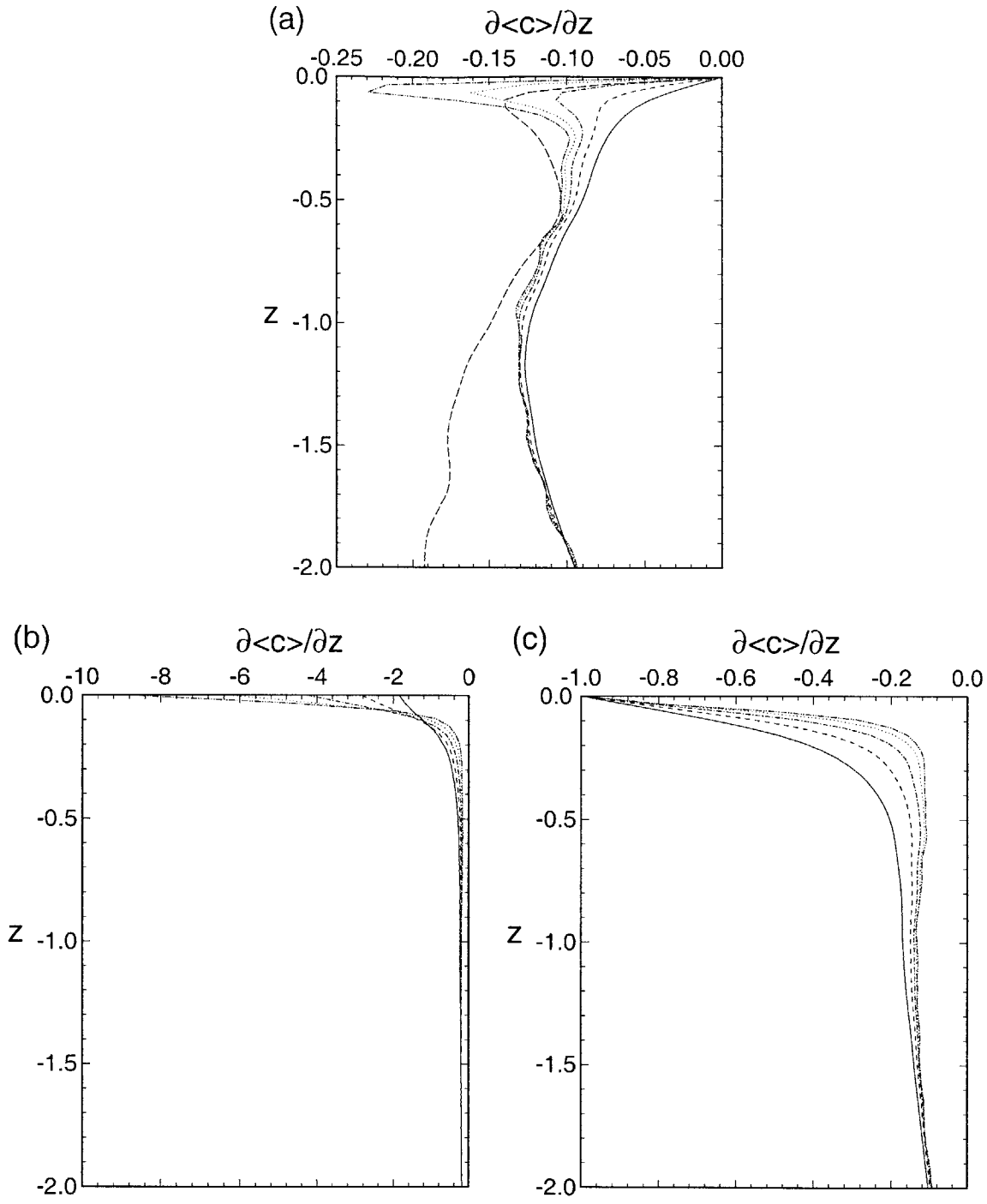

Figure 6-2: Profiles of scalar mean gradient $\partial\langle c\rangle/\partial z$ for (a) zero surface-flux case, (b) fixed surface-value case, and (c) fixed surface-flux case. ———— , $S_c = 0.25$; – – – – , $S_c = 0.5$; – · – · – , $S_c = 1$; · · · · · · · , $S_c = 2$; –··–··– , $S_c = 0.25$. In (a), —— —— represents the corresponding velocity property $\partial\langle u\rangle/\partial z$.

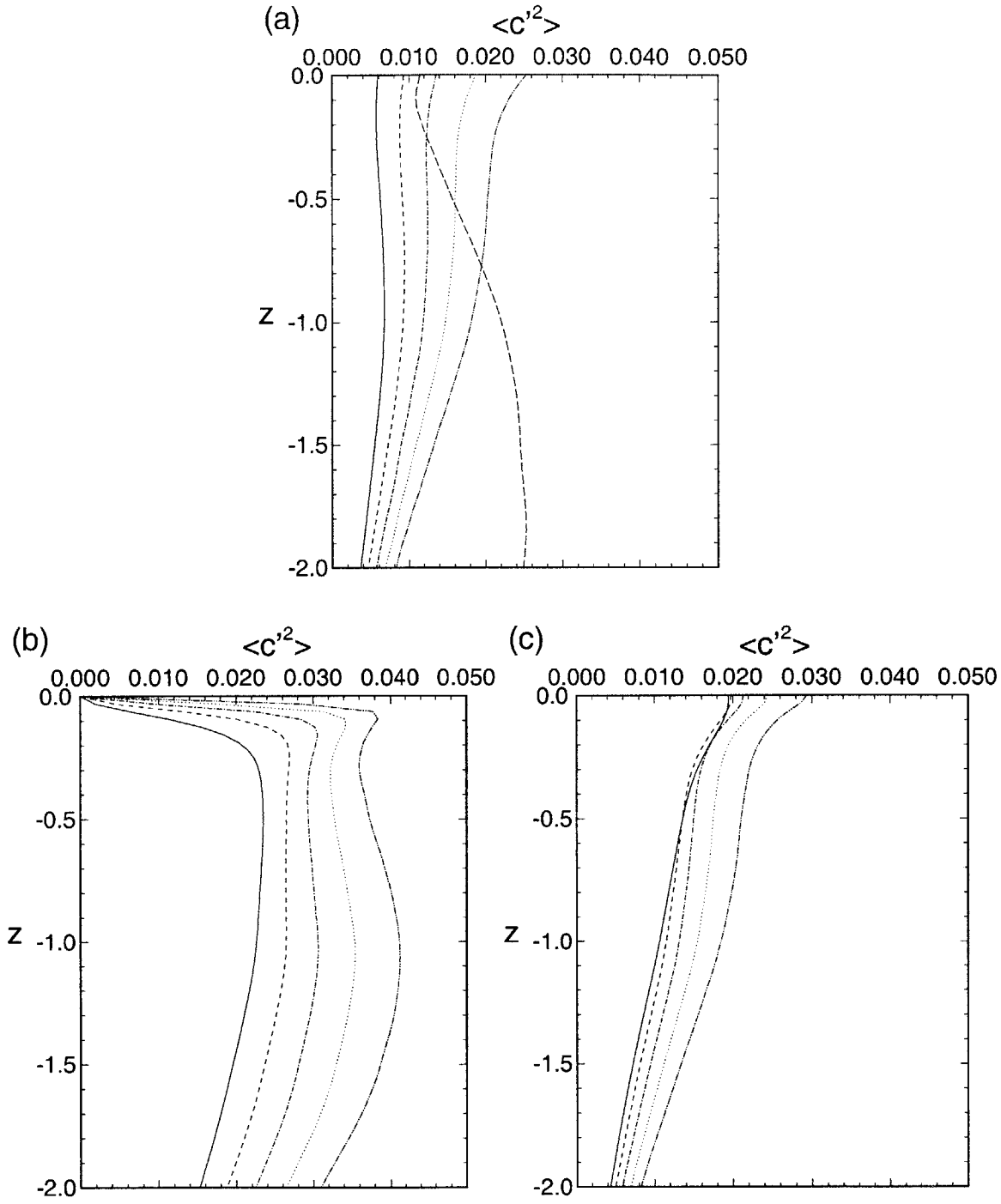

Figure 6-3: Profiles of scalar fluctuation magnitude $\langle c'^2 \rangle$ for (a) zero surface-flux case, (b) fixed surface-value case, and (c) fixed surface-flux case. ———— , $S_c = 0.25$; - - - - , $S_c = 0.5$; - · - · - , $S_c = 1$; ····· , $S_c = 2$; —··—··— , $S_c = 0.25$. In (a), —— —— represents the corresponding velocity property $\langle u'^2 + v'^2 + w'^2 \rangle$.

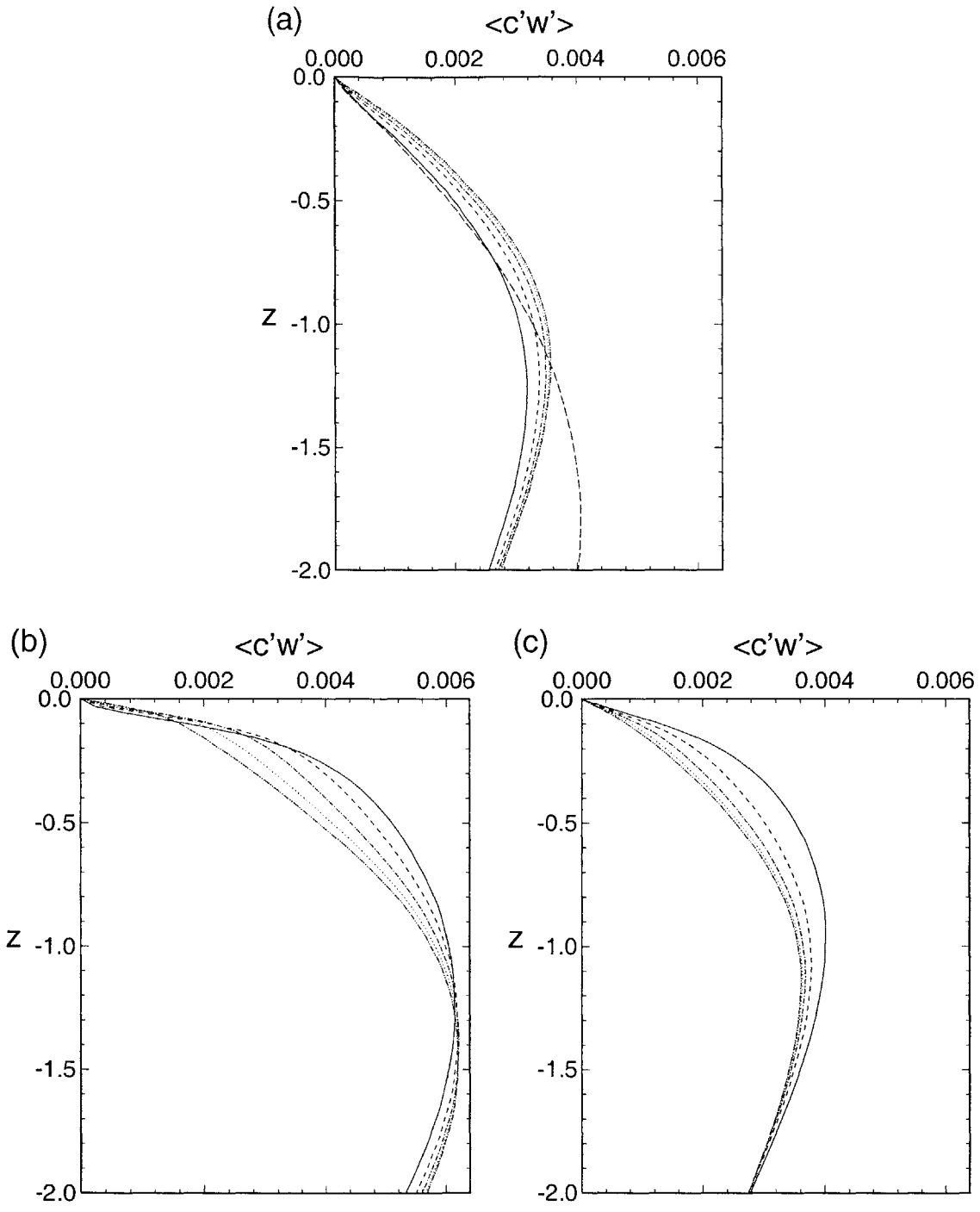

Figure 6-4: Profiles of scalar turbulent flux $\langle c'w' \rangle$ for (a) zero surface-flux case, (b) fixed surface-value case, and (c) fixed surface-flux case. ———— , $S_c = 0.25$; – – – – , $S_c = 0.5$; – · – · – , $S_c = 1$; · · · · · · · , $S_c = 2$; –··–··– , $S_c = 0.25$. In (a), —— —— represents the corresponding velocity property $\langle u'w' \rangle$.

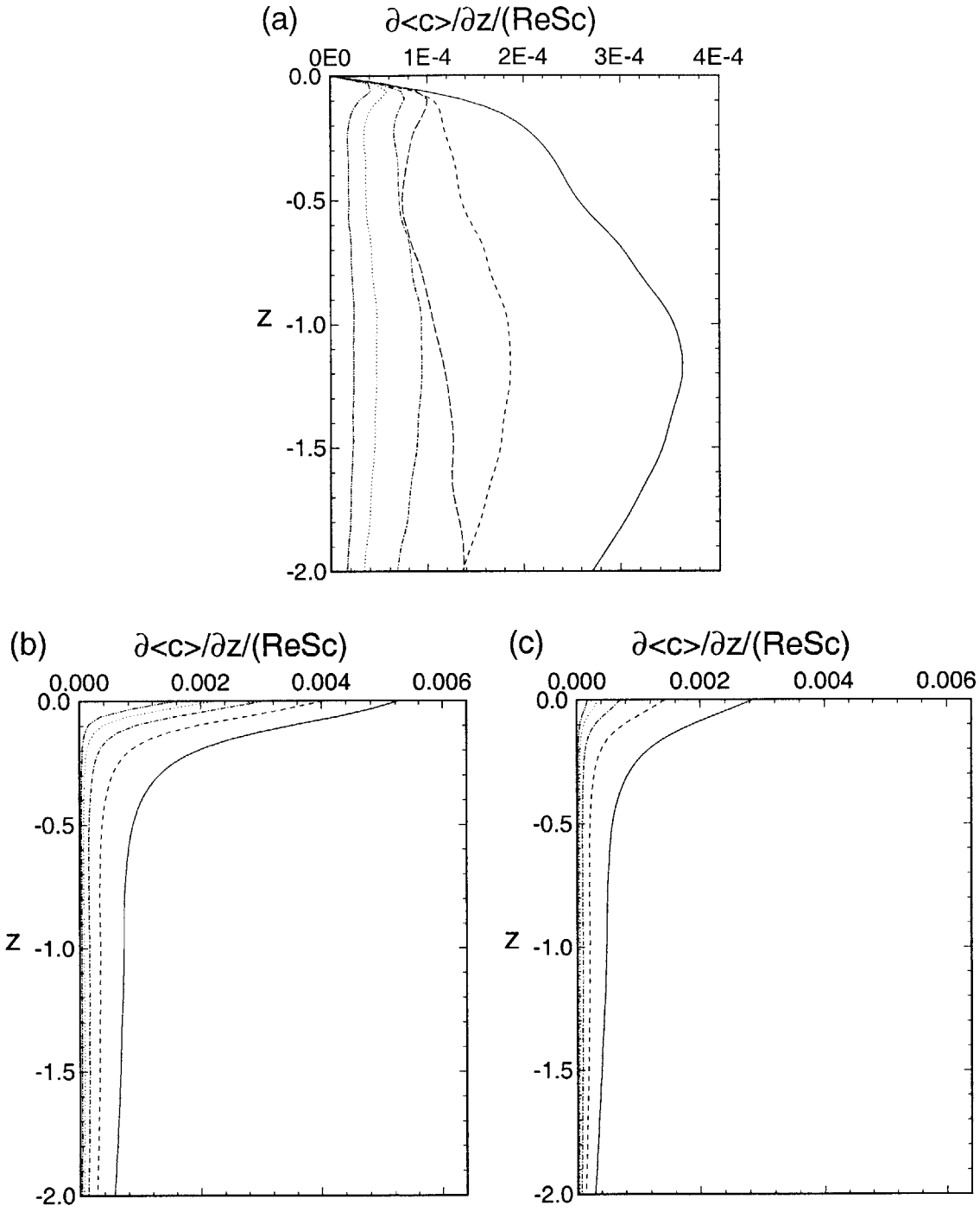

Figure 6-5: Profiles of scalar molecular flux $\partial\langle c\rangle/\partial z/(R_e S_c)$ for (a) zero surface-flux case, (b) fixed surface-value case, and (c) fixed surface-flux case. ———— , $S_c = 0.25$; - - - - , $S_c = 0.5$; - · - · - , $S_c = 1$; · · · · · · , $S_c = 2$; —··—··— , $S_c = 0.25$. In (a), —— —— represents the corresponding velocity property $\partial\langle u\rangle/\partial z/(R_e)$.

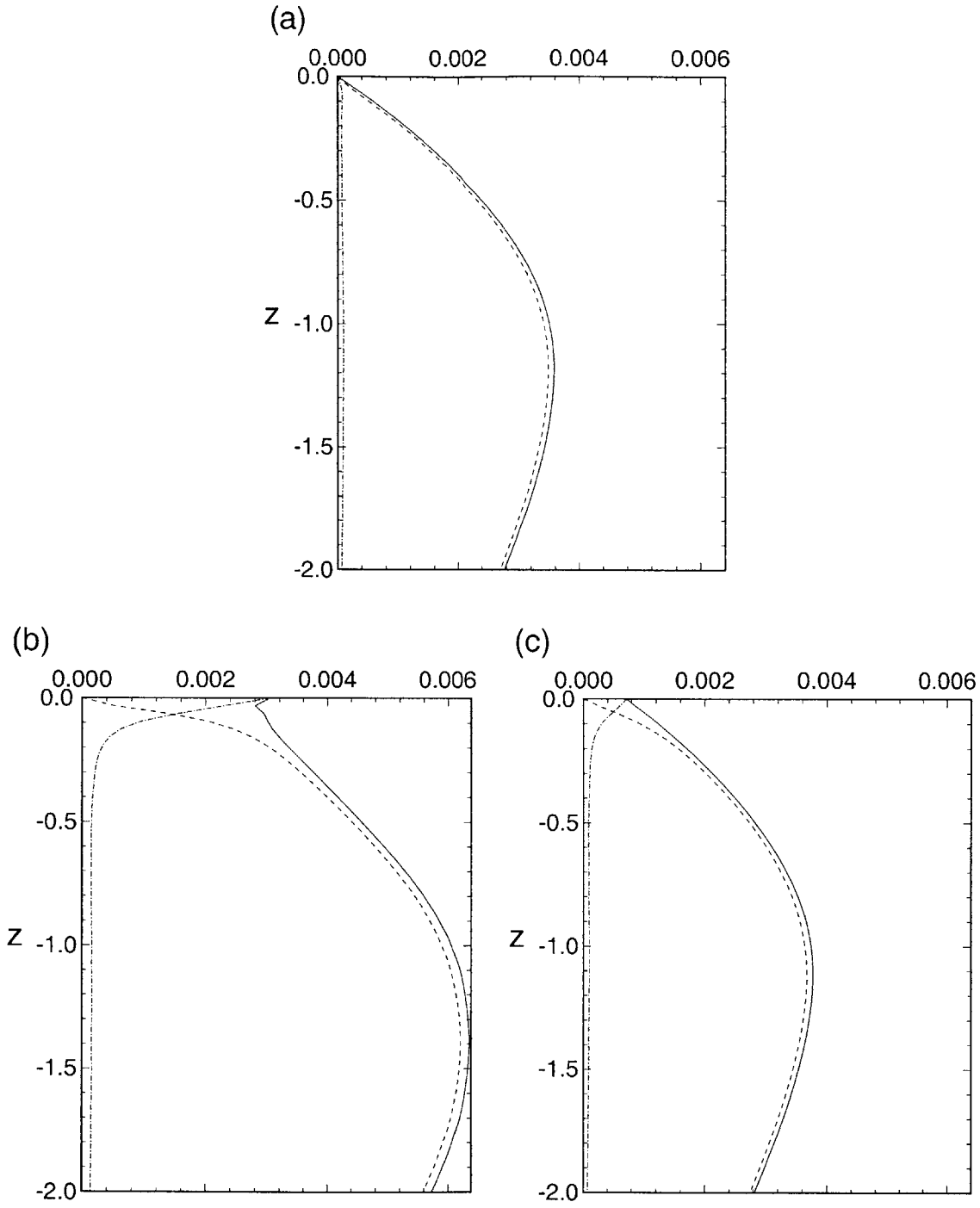

Figure 6-6: Profiles of scalar total flux $\langle c'w' \rangle + \partial \langle c \rangle / \partial z / (R_e S_c)$ for (a) zero surface-flux case, (b) fixed surface-flux case, and (c) fixed surface-flux case. ———— , total flux $\langle c'w' \rangle + \partial \langle c \rangle / \partial z / (R_e S_c)$; - - - - , turbulent flux $\langle c'w' \rangle$; - · - · - , molecular flux $\partial \langle c \rangle / \partial z / (R_e S_c)$. $S_c = 1$.

diffusivity vanishes at the free surface. The reason is that while the turbulent flux $\langle c'w' \rangle$ vanishes, the mean scalar gradient $\partial\langle c \rangle / \partial z$ is zero for the zero surface-flux case but nonzero for the other two cases. Besides the difference at the free surface, the deviation in the turbulent diffusivity in the bulk flow below is negligible. Of special importance is the fact that the scalar surface outer layer is not affected by either the Schmidt number or the scalar boundary conditions. As pointed out by Chapter 5, it is purely controlled by the momentum outer layer.

6.3 Structures of passive scalar transport

In this section we investigate the relation between the scalar transport and the fluid motions in free-surface turbulence. As shown in Chapter 3, free-surface turbulent flows are characterized by events such as splats (upwellings), anti-splats (downdroughts), surface-connected coherent vortices, and coherent hairpin vortices. From first principle, splats convect scalar from the bulk flow to the free surface while anti-splats carry scalar away from the surface. One main objective of this chapter is to identify and quantify the contributions of different flow motions to the scalar transport process.

In order to obtain reliable quantification, we employ the conditional averaging technique of variable-interval space-averaging (VISA), which was developed by Kim (1983) following the variable-interval time-averaging (VITA) method of Blackwelder & Kaplan (1976). In order to capture a strong event which is characterized by a significant value in the quantity f, we first define its variable-interval space averaging $\underline{f}$ as

$$\underline{f}(x, y, z, t, W) \equiv \frac{1}{4W^2} \int_{x-W}^{x+W} \int_{y-W}^{y+W} f(\xi, \zeta, z, t) \mathrm{d}\xi \mathrm{d}\zeta \,, \tag{6.5}$$

where W is the half width of the averaging window, which should be comparable to the macro length-scale of f. To identify strong f events, a localized variance is introduced:

$$f^{var}(x, y, z, t, W) \equiv f^2(x, y, z, t) - \underline{f}^2(x, y, z, t, W) \,, \tag{6.6}$$

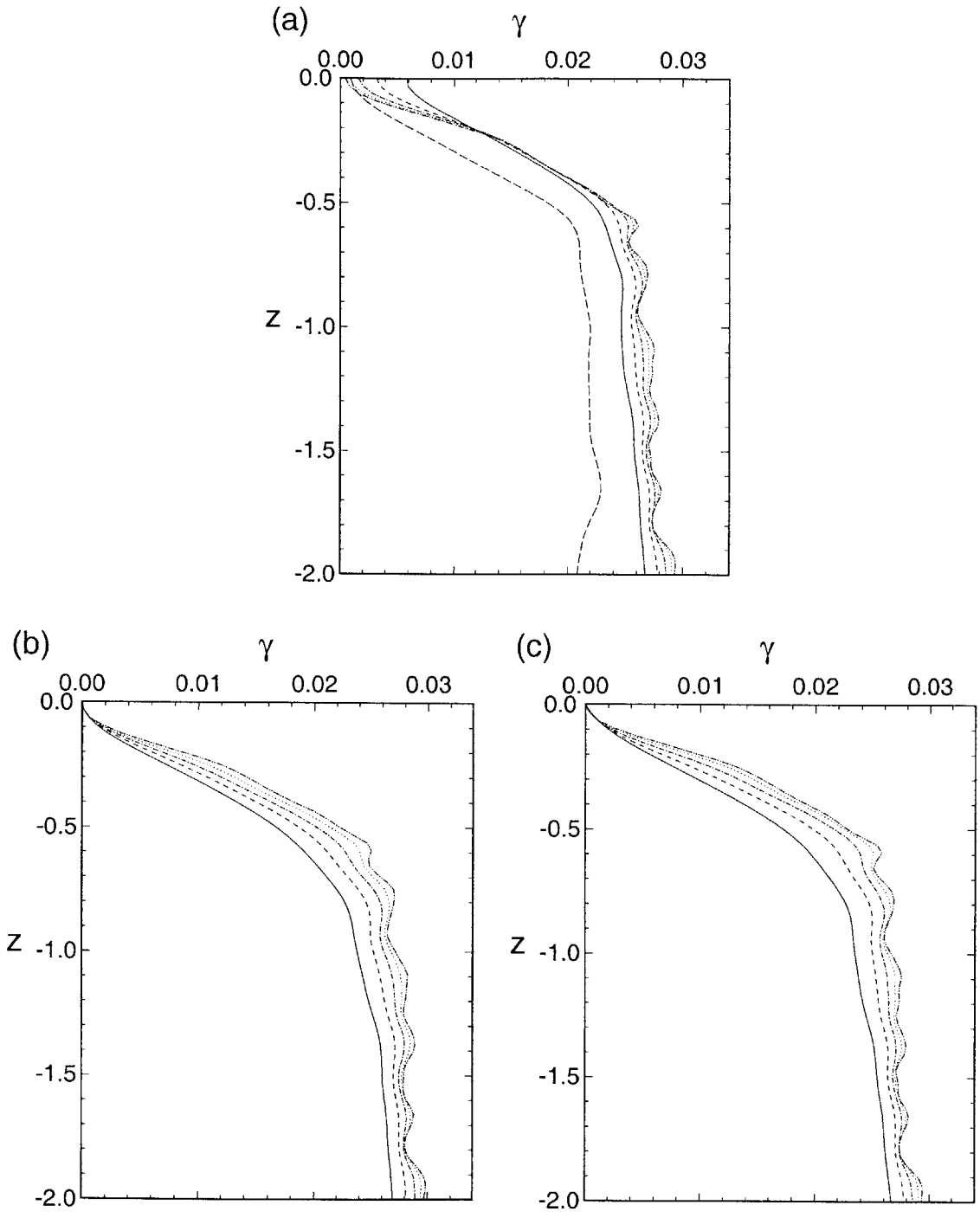

Figure 6-7: Profiles of scalar turbulent diffusivity γ for (a) zero surface-flux case, (b) fixed surface-value case, and (c) fixed surface-flux case. ———— , $S_c = 0.25$; – – – – , $S_c = 0.5$; – · – · – , $S_c = 1$; · · · · · · · , $S_c = 2$; —··—··— , $S_c = 0.25$. In (a), —— —— represents the corresponding velocity property ν_e.

and the strong event is detected using the following criterion:

$$\mathcal{D}(x,y,z,t) = \begin{cases} 1, & \text{if } f^{var} > K(f^{rms})^2, \\ 0, & \text{otherwise.} \end{cases} \tag{6.7}$$

Here the detection function $\mathcal{D}(x,y,z,t)$=1 if the event exists; f^{rms} is the root-mean-square variation of f at the horizontal plane; and K is the threshold level.

In this study, we use the large-magnitude positive and negative plane divergence, $\partial u/\partial x + \partial v/\partial y = -\partial w/\partial z$ at $z = 0$, to detect splats and anti-splats, respectively. Large ω_z at $z = 0$ is used to detect surface-connected vortices, while large negative ω_y at $z = -0.125$ is used to detect hairpin vortices.

The conditionally-averaged field for the flow and scalar are plotted in Figures 6-8 to 6-18. We first consider the splat events. Figure 6-8 plots the vertical (x, z)- and (y, z)-section of the splat, which is located at the center of the domain. As the fluids are convected towards the free surface, the surface does not allow complete freedom on the vertical motions and the fluids are turned into horizontal directions, which is clearly shown in Figure 6-8. Subsequently, the scalars are convected towards the free surface by the upwelling motions, resulting in a high scalar concentration for the zero or fixed surface-flux cases, and high scalar gradient for the fixed surface-value case.

Figure 6-9 plots the surface features around the splats. Since the fluids coming towards the surface are turned into horizontal directions, the plane divergence $\partial u/\partial x + \partial v/\partial y = -\partial w/\partial z$ is positive, which is clearly shown in Figure 6-9(a). Also shown clearly are the enhanced scalar concentration (Figures b and d) and enhanced scalar gradient (Figure c).

Anti-splats are plotted in Figures 6-10 and 6-11. As the counterpart of splats, anti-splats are expected to transport scalar away from the surface to the bulk flow below. In free-surface turbulence, however, the roles of splats and anti-splats should not be equal as the upward and downward motions in an unbounded shear flow: splats can come from a certain distant underneath while the origins of anti-splats are limited by the free-surface location. As a result, the effect of anti-splats is much less significant compared to splats. We also observe from the (x, z)-sections in Figure 6-10 that strong spanwise vortical motions are

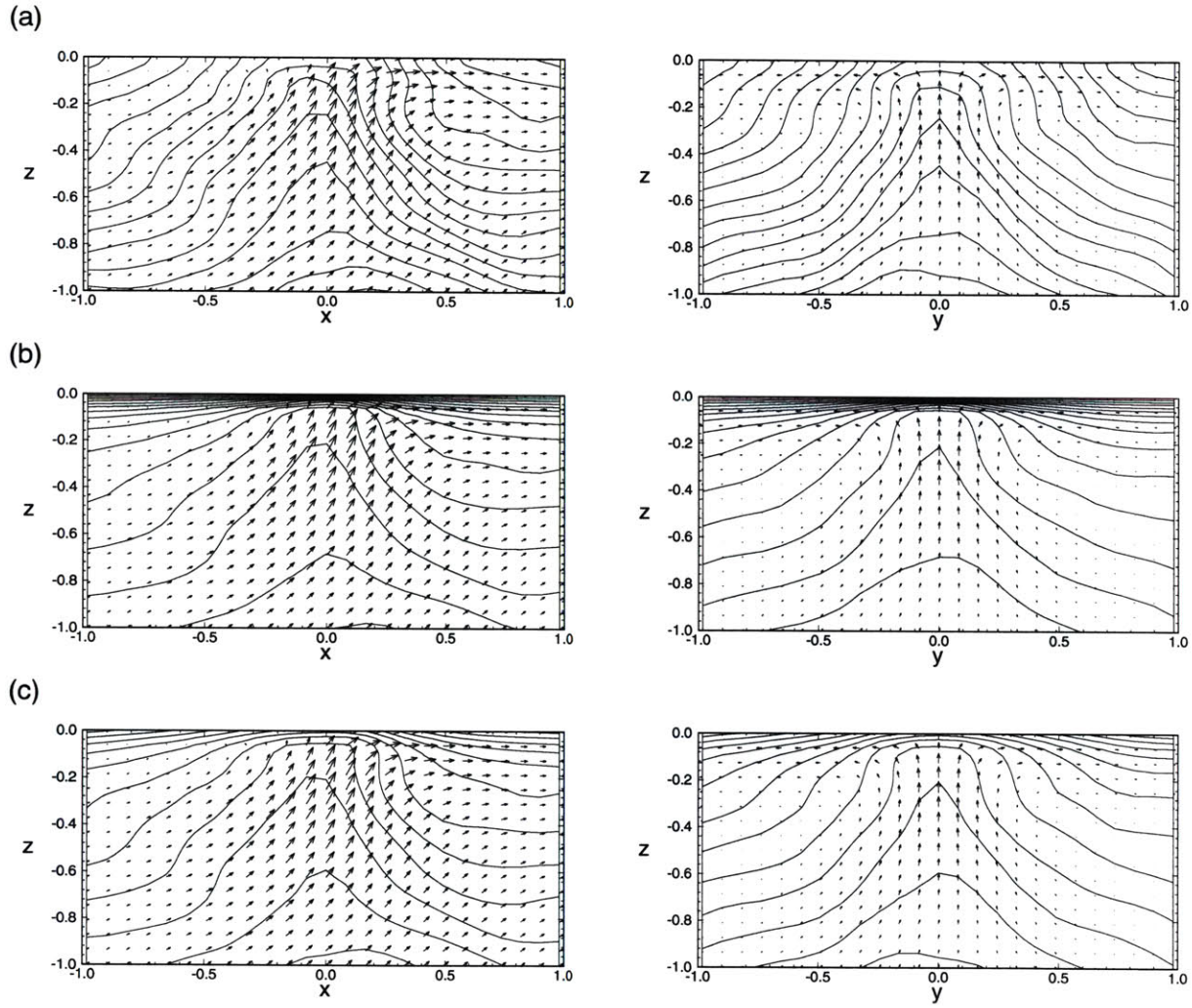

Figure 6-8: Vertical sections of the conditionally-averaged field around splats for (a) the zero surface-flux case, (b) the fixed surface-value case, and (c) the fixed surface-flux case. Plotted are the line contours of c with intervals 0.01, 0.04, and 0.02, respectively, and projections of velocity vectors on the cross-sections.

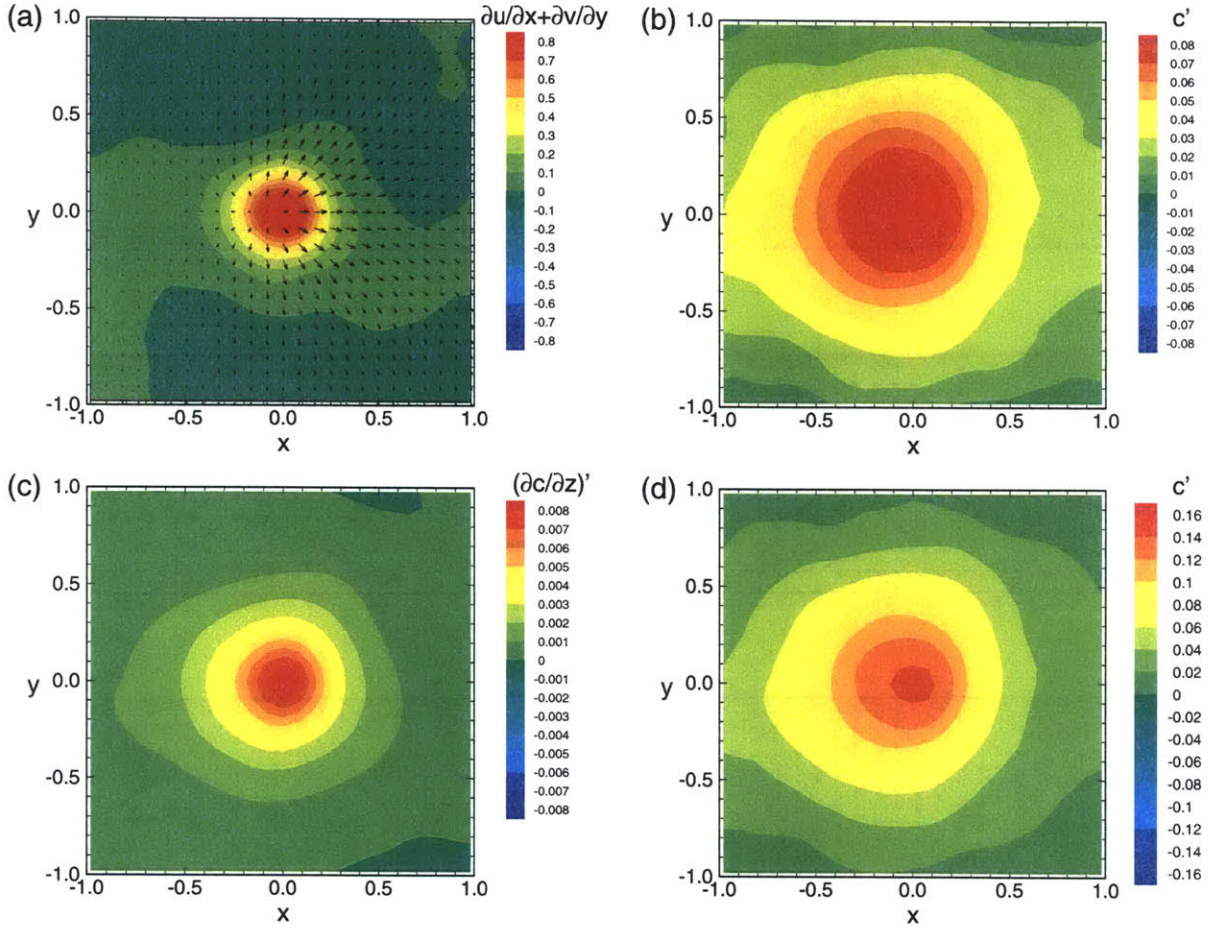

Figure 6-9: Free-surface features of the conditionally-averaged field around splats: (a) contours of plane divergence $\partial u/\partial x + \partial v/\partial y = -\partial w/\partial z$ with velocity vectors (u', v'); (b) contours of c for the zero surface-flux case; (c) contours of $\partial c/\partial z/(R_e S_c)$ for the fixed surface-value case; and (d) contours of c for the fixed surface-flux case.

also present in the conditionally-averaged field. Inducted by the spanwise vortex, the fluids convect the scalar towards the surface at the downstream region. All these factors make the contributions from anti-splats less significant than the splats.

We next investigate the roles of coherent vortical structures, namely the hairpin vortices and the surface-connected vortices, in the scalar transport process. The color contours of spanwise vorticity ω_y are plotted in Figure 6-12, which clearly shows the strong vortex (head portion of hairpin eddy) pointing in the negative y-direction. Induced by this vortex, fluids on the right are convected to the surface, while the fluids on the left are transported away from the surface. Also due to the induction by the two hairpin legs, which are inclined to the positive x-direction (cf. Chapter 3), the upward convection on the right is stronger than the downward convection on the left, as shown in Figure 6-13(a). Because of the upward convection, scalars are transport to the free surface (Figures 6-12), resulting in higher scalar concentration for the cases of zero or fixed surface-flux and enhanced scalar gradients for the fixed surface-value case (Figures 6-13 b to d).

We next consider the surface-connected vortices, which are plotted in Figures 6-14 and 6-17 for positive vortices and in Figures 6-15 and 6-18 for negative vortices. Because of symmetry, the contributions from positive and negative surface-connected vortices are equal. An important observation from Figures 6-14 (and 6-15) (a) to (c) is that surface-connected vortices draw fluid from the surface down to the bulk flow below, like a up-side-down hurricane (Figure 6-16). As a result, scalars are transported away from the surface through the vortex core. Figures 6-17 and 6-18 show that the downdroughts inducted by the surface-connected vortices are significant for all the three cases investigated in this study.

6.4 Quantification of scalar transport process in free-surface turbulent flows

A critical need in the study of free-surface turbulence is to quantify the dependence of transport process on the flow hydrodynamics. As shown in §6.3, splats enhance the convection of scalar towards the free surface, while anti-splats carry the scalar away from the surface.

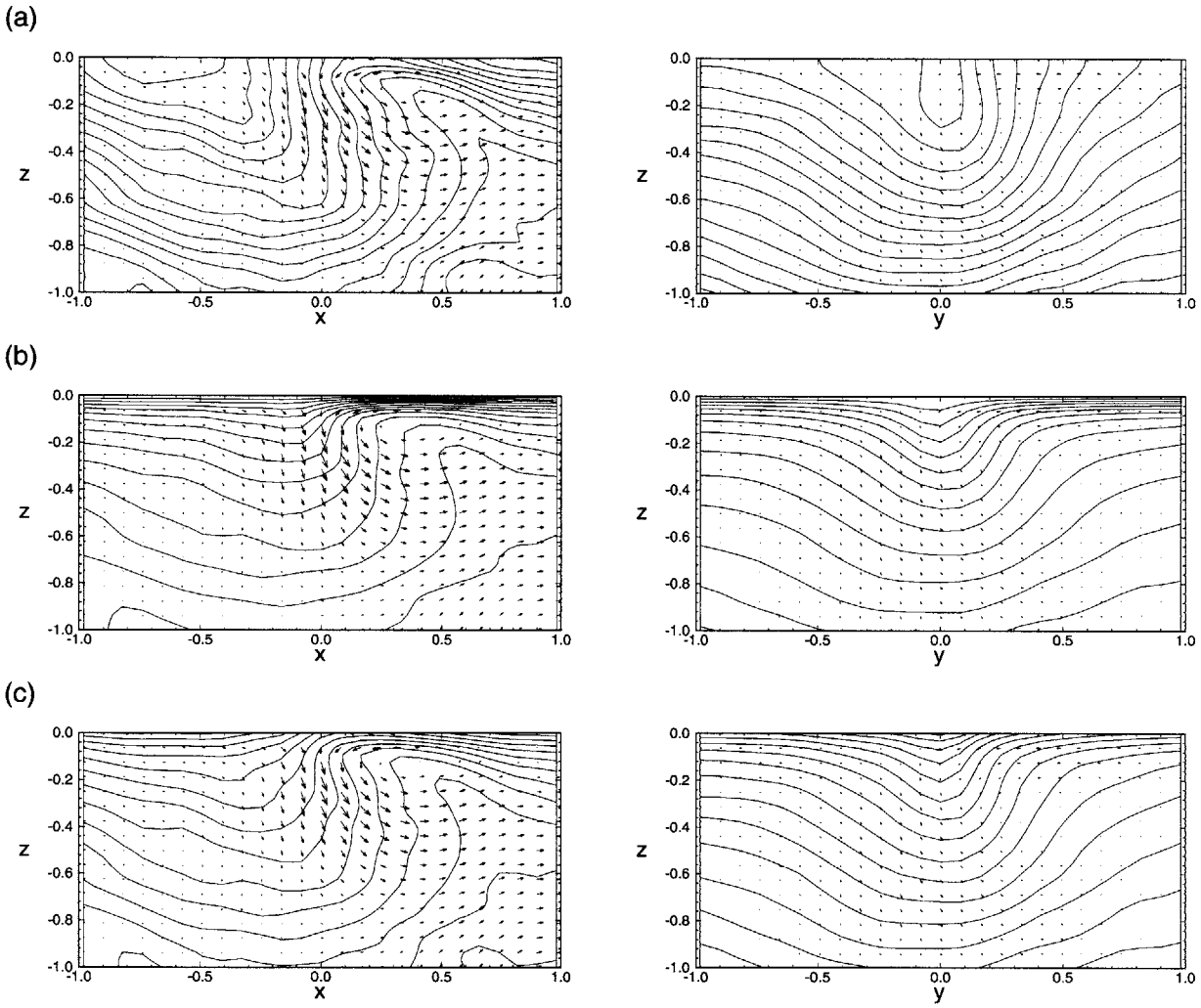

Figure 6-10: Vertical sections of the conditionally-averaged field around anti-splats for (a) the zero surface-value case, (b) the fixed surface-value case, and (c) the fixed surface-flux case. Plotted are the line contours of c with intervals 0.01, 0.04, and 0.02, respectively, and projections of velocity vectors on the cross-sections.

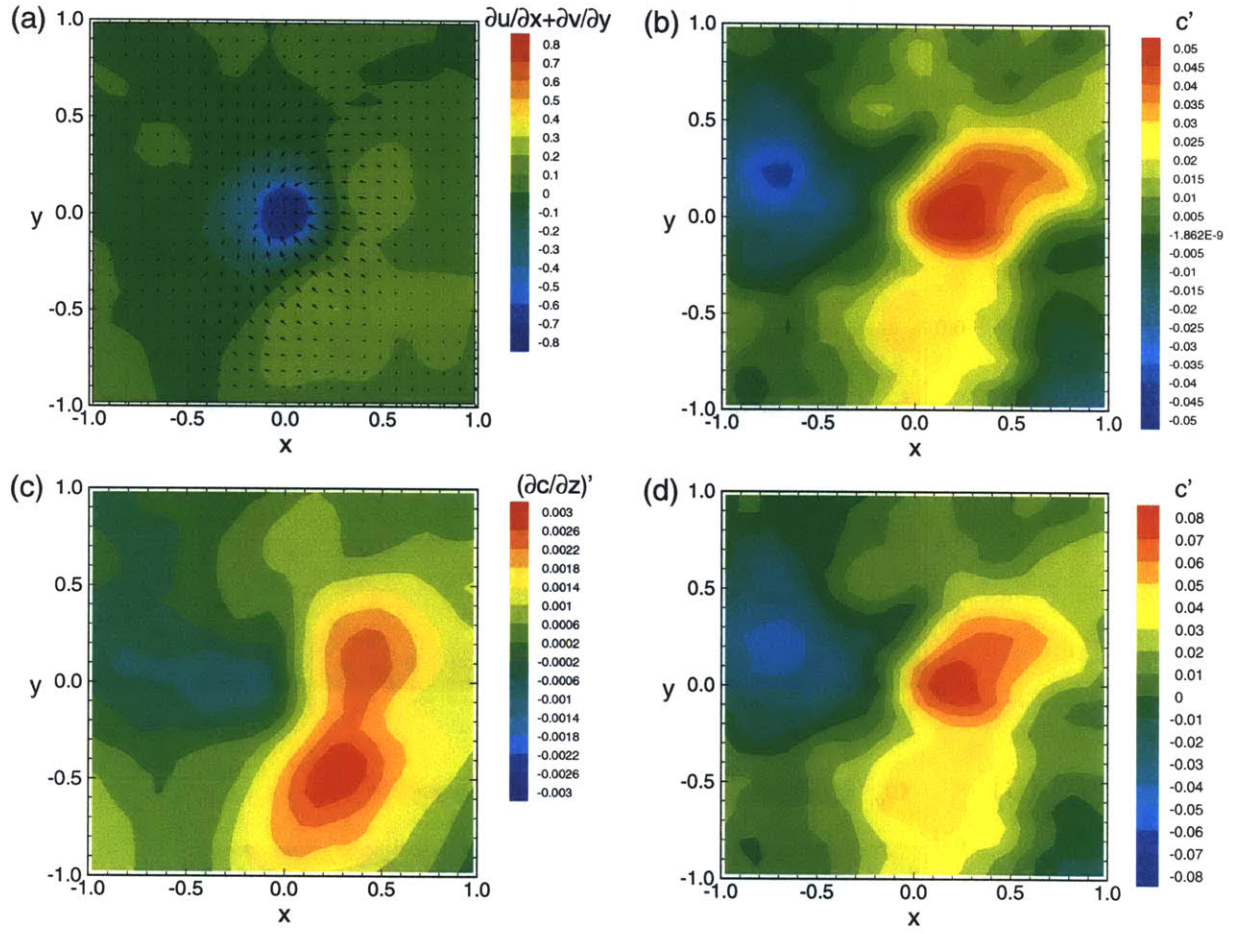

Figure 6-11: Free-surface features of the conditionally-averaged field around anti-splats: (a) contours of plane divergence $\partial u/\partial x + \partial v/\partial y = -\partial w/\partial z$ with velocity vectors (u', v'); (b) contours of c for the zero surface-flux case; (c) contours of $\partial c/\partial z/(R_e S_c)$ for the fixed surface-value case; and (d) contours of c for the fixed surface-flux case.

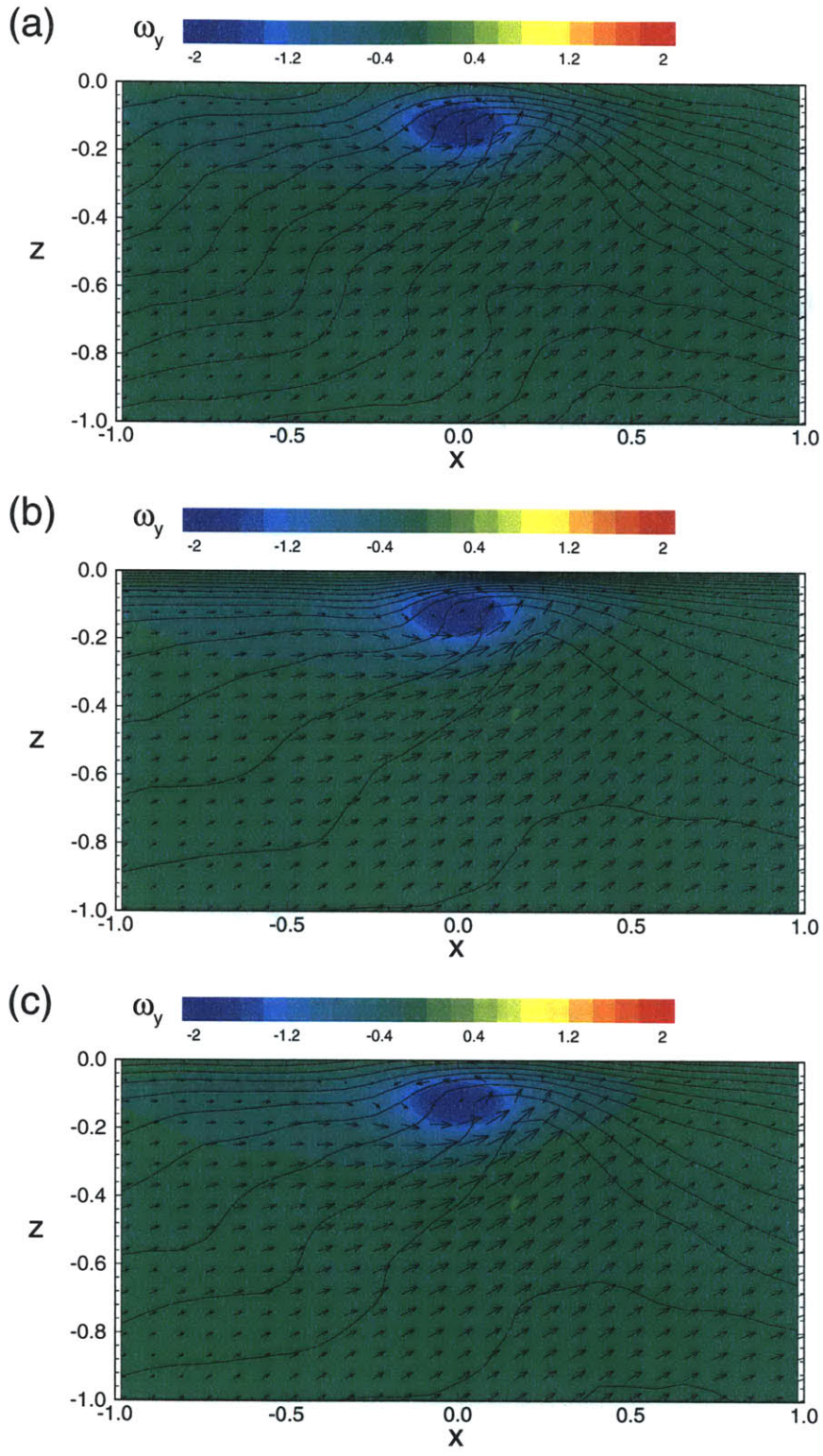

Figure 6-12: Vertical sections of the conditionally-averaged field around hairpin vortices for (a) the zero surface-flux case, (b) the fixed surface-value case, and (c) the fixed surface-flux case. Plotted are the color contours of ω_y, line contours of c with intervals 0.01, 0.04, and 0.02, respectively, and projection of velocity vectors on the cross section.

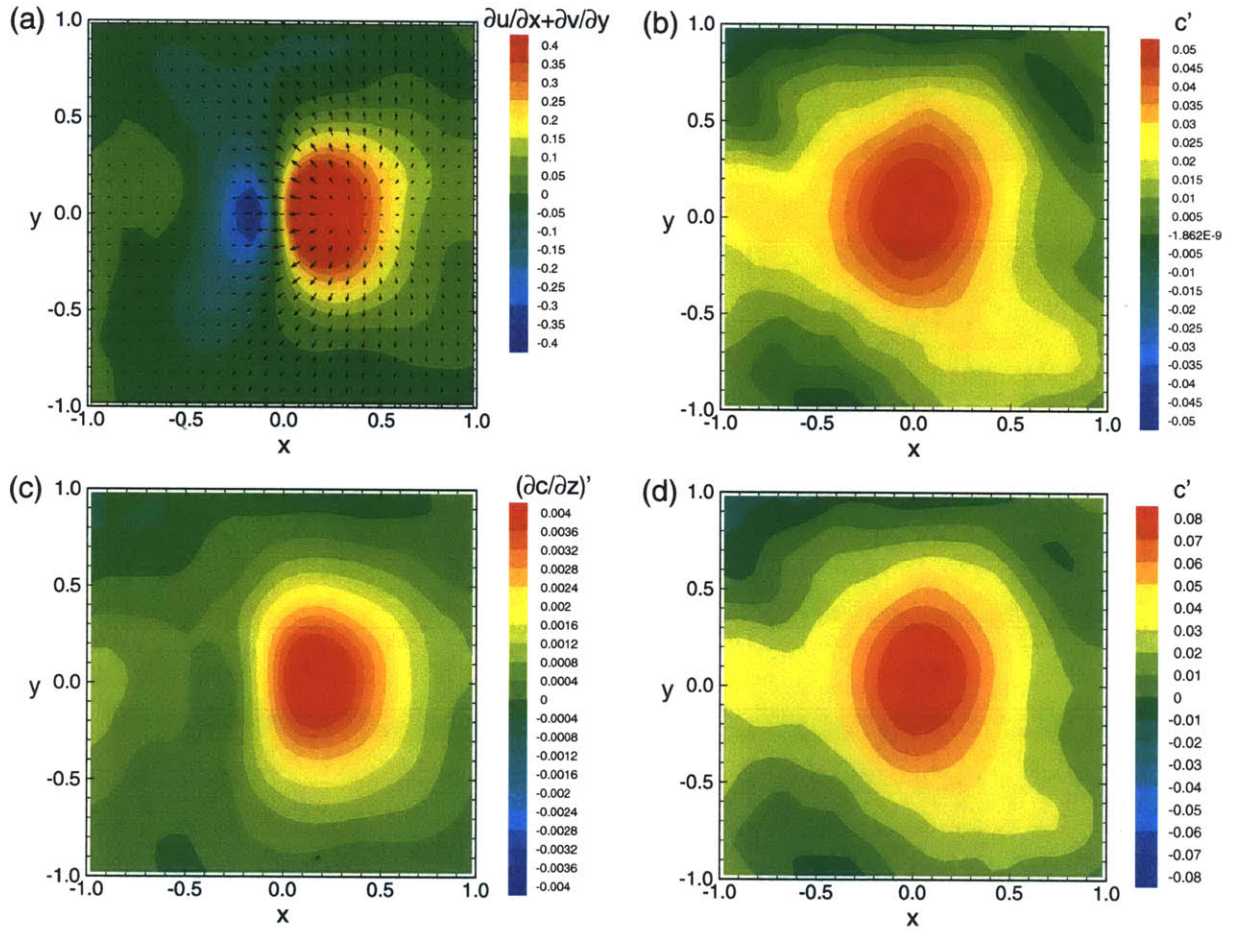

Figure 6-13: Free-surface features of the conditionally-averaged field around hairpin vortices: (*a*) contours of plane divergence $\partial u/\partial x + \partial v/\partial y = -\partial w/\partial z$ with velocity vectors (u', v'); (*b*) contours of c for the zero surface-flux case; (*c*) contours of $\partial c/\partial z/(R_e S_c)$ for the fixed surface-value case; and (*d*) contours of c for the fixed surface-flux case.

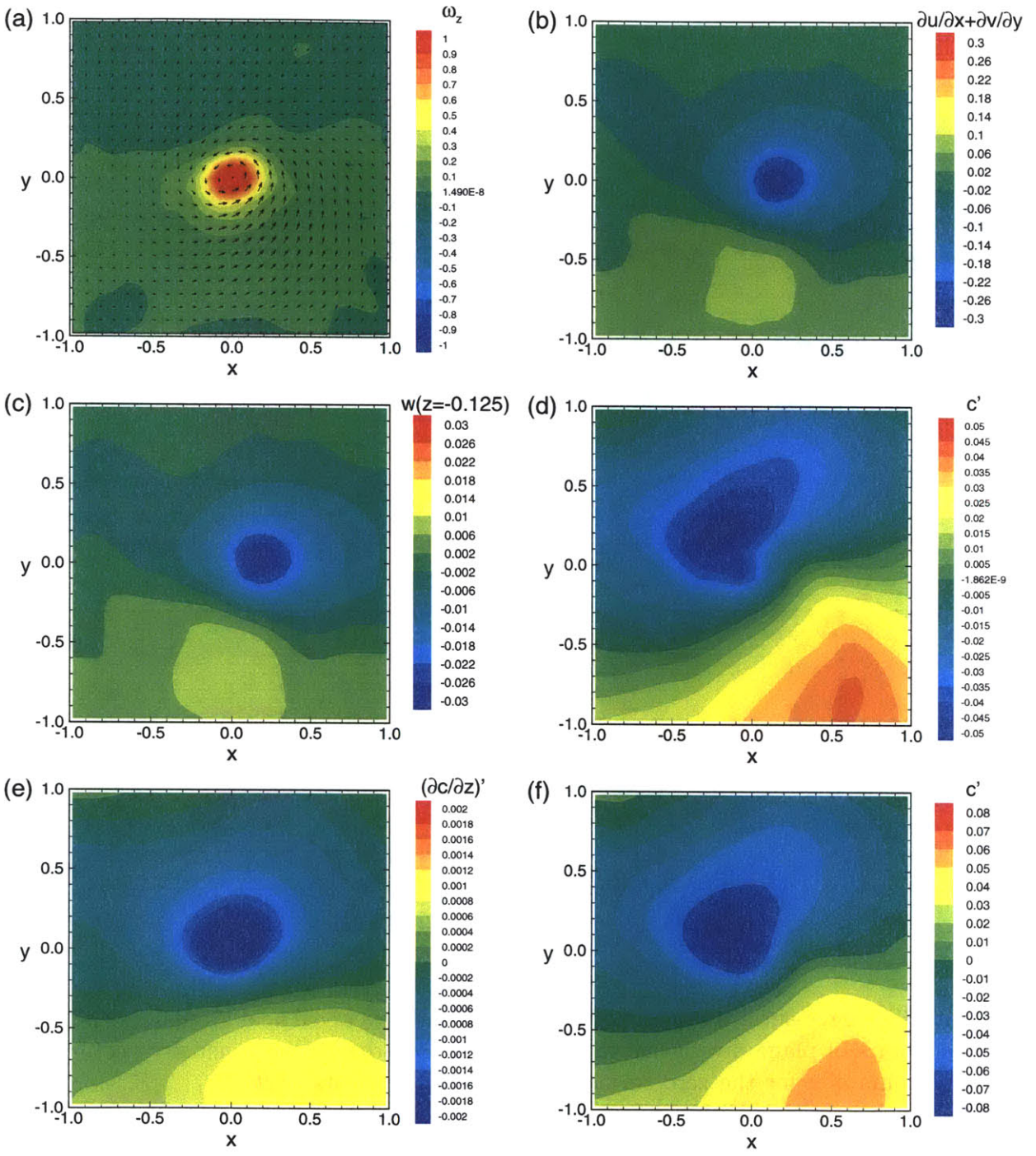

Figure 6-14: Free-surface features of the conditionally-averaged field around positive surface-connected vortices: (*a*) contours of ω_z with velocity vectors (u', v'); (*b*) contours of plane divergence $\partial u/\partial x + \partial v/\partial y = -\partial w/\partial z$; (*c*) contours of w at $z = -0.125$; (*d*) contours of c for the zero surface-flux case; (*e*) contours of $\partial c/\partial z/(R_e S_c)$ for the fixed surface-value case; and (*f*) contours of c for the fixed surface-flux case.

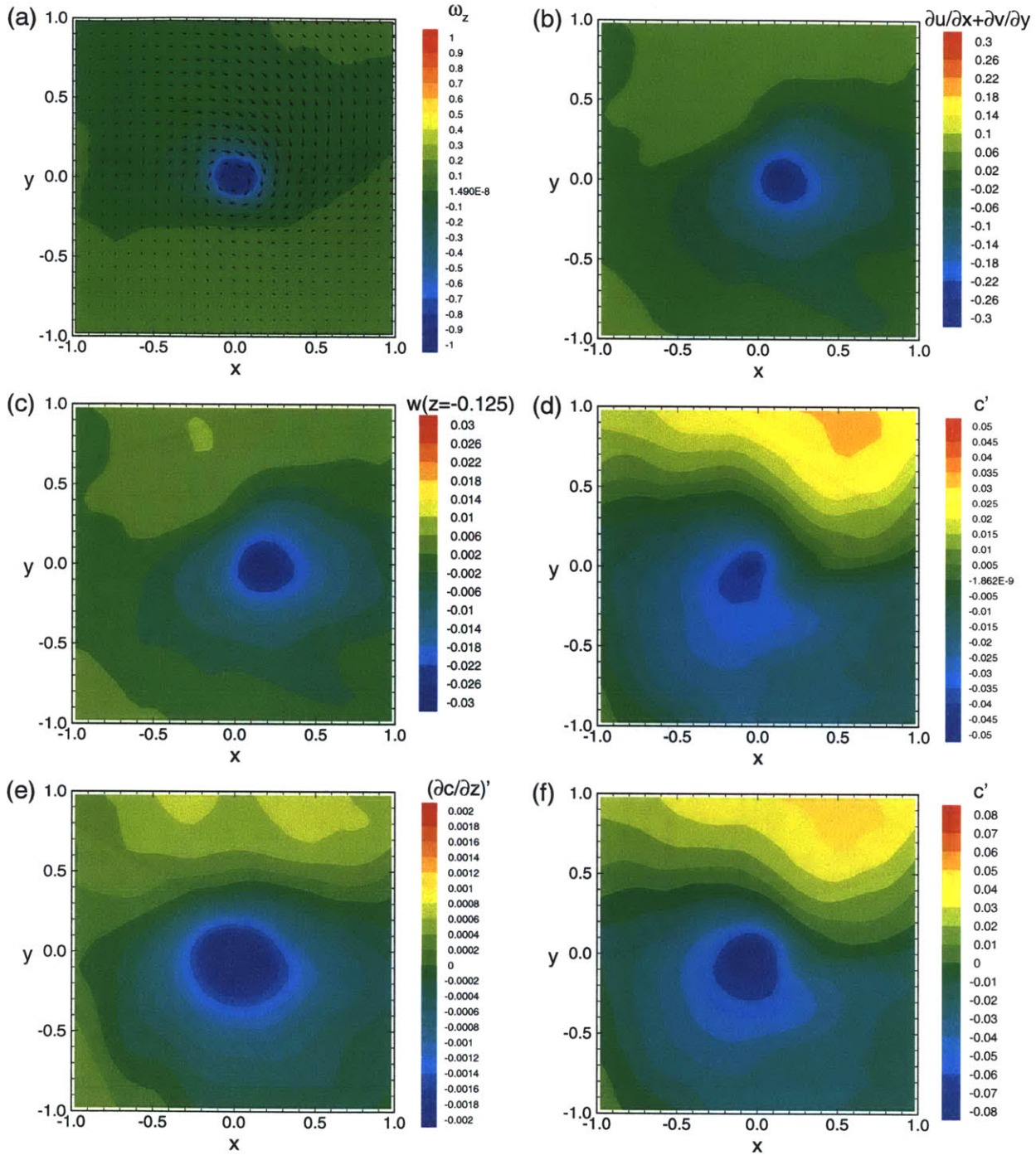

Figure 6-15: Free-surface features of the conditionally-averaged field around negative surface-connected vortices: (a) contours of ω_z with velocity vectors (u', v'); (b) contours of plane divergence $\partial u/\partial x + \partial v/\partial y = -\partial w/\partial z$; ($c$) contours of w at $z = -0.125$; (d) contours of c for the zero surface-flux case; (e) contours of $\partial c/\partial z/(R_e S_c)$ for the fixed surface-value case; and (f) contours of c for the fixed surface-flux case.

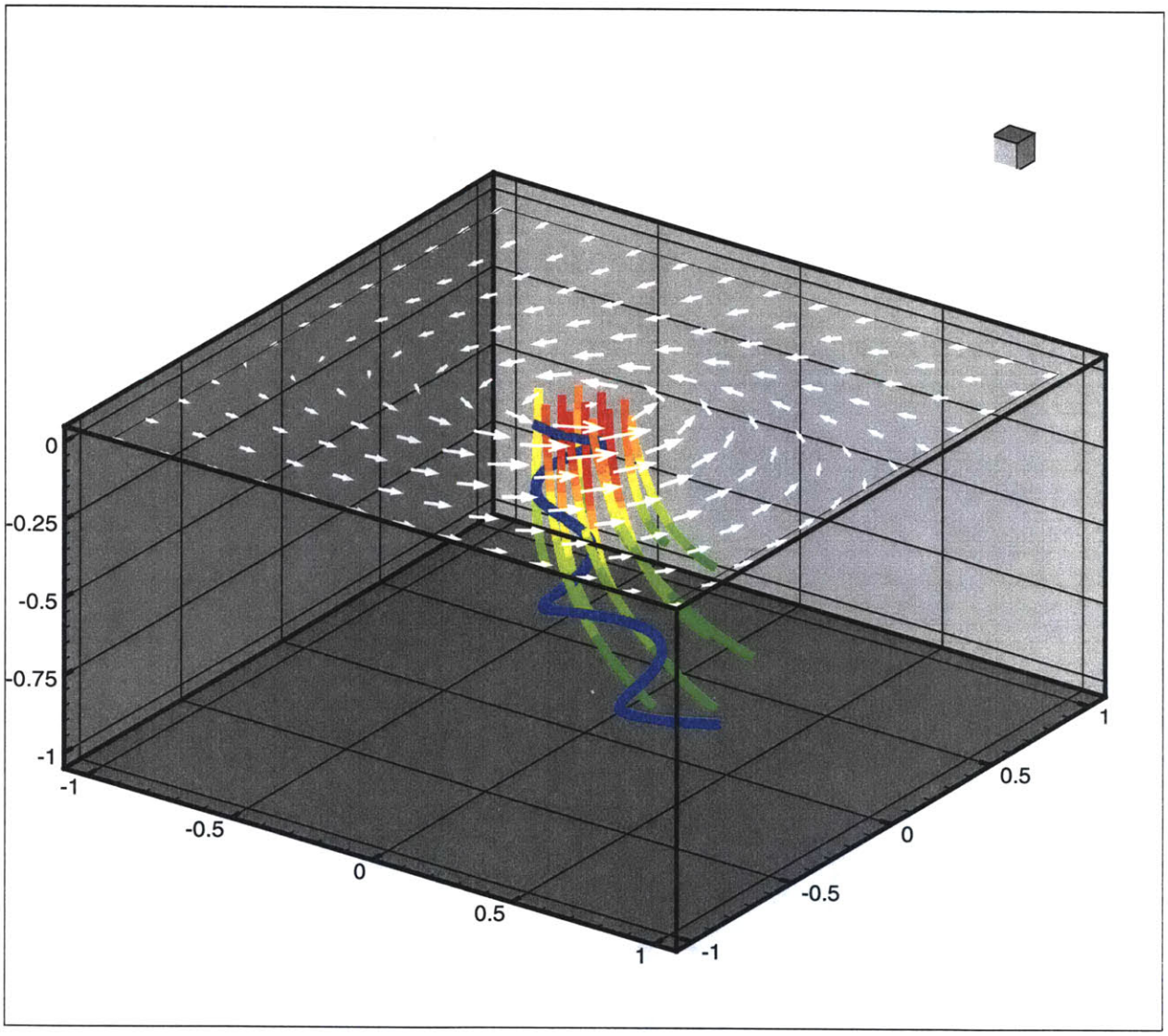

Figure 6-16: Spiral downdrought motion induced by surface-connected vortices. Plotted are velocity vectors on the free surface and vortex lines. The blue line is a typical streamline.

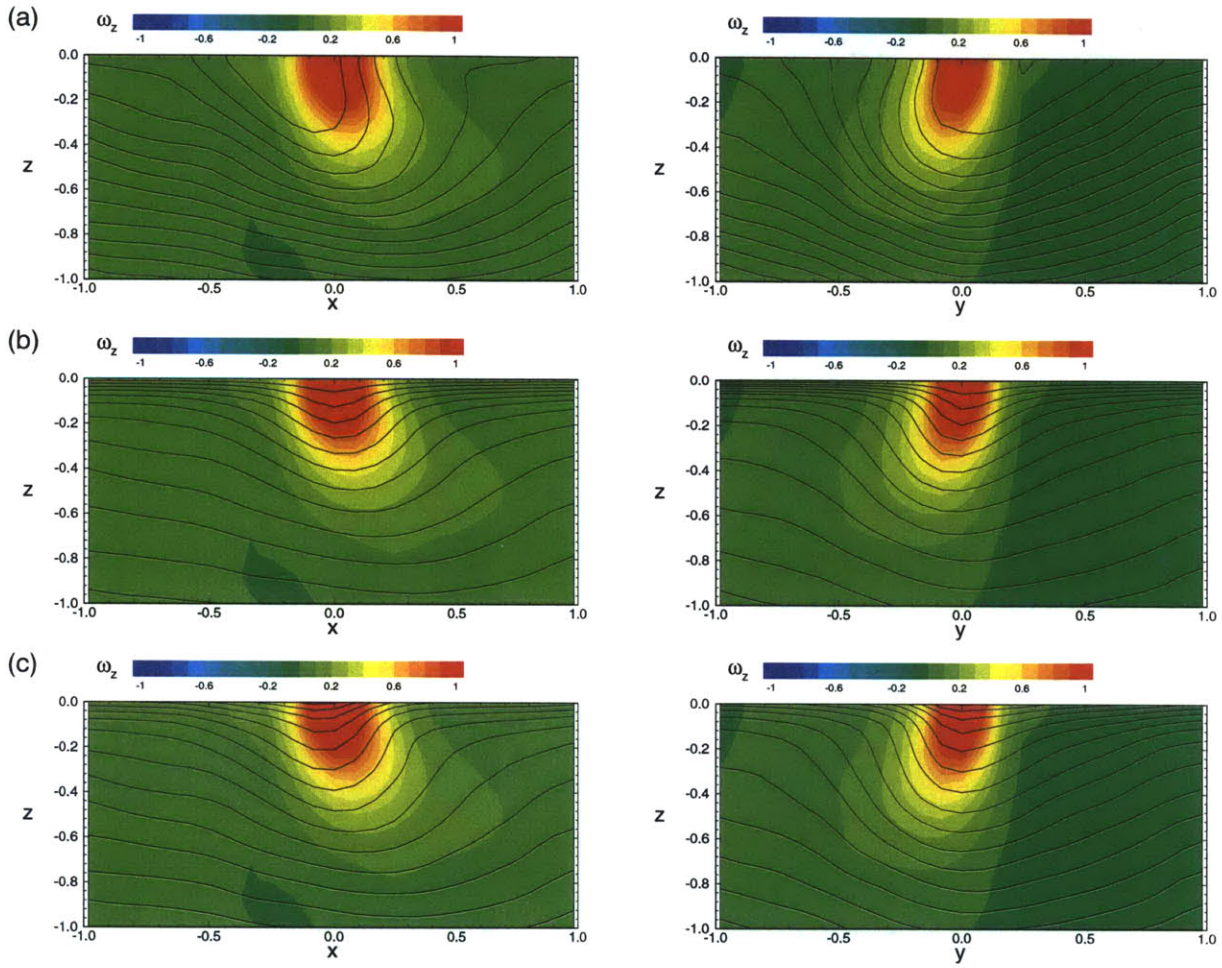

Figure 6-17: Vertical sections of the conditionally-averaged field around positive surface-connected vortices for (a) the zero surface-flux case, (b) the fixed surface-value case, and (c) the fixed surface-flux case. Plotted are the color contours of ω_z and line contours of c with intervals 0.01, 0.04, and 0.02, respectively.

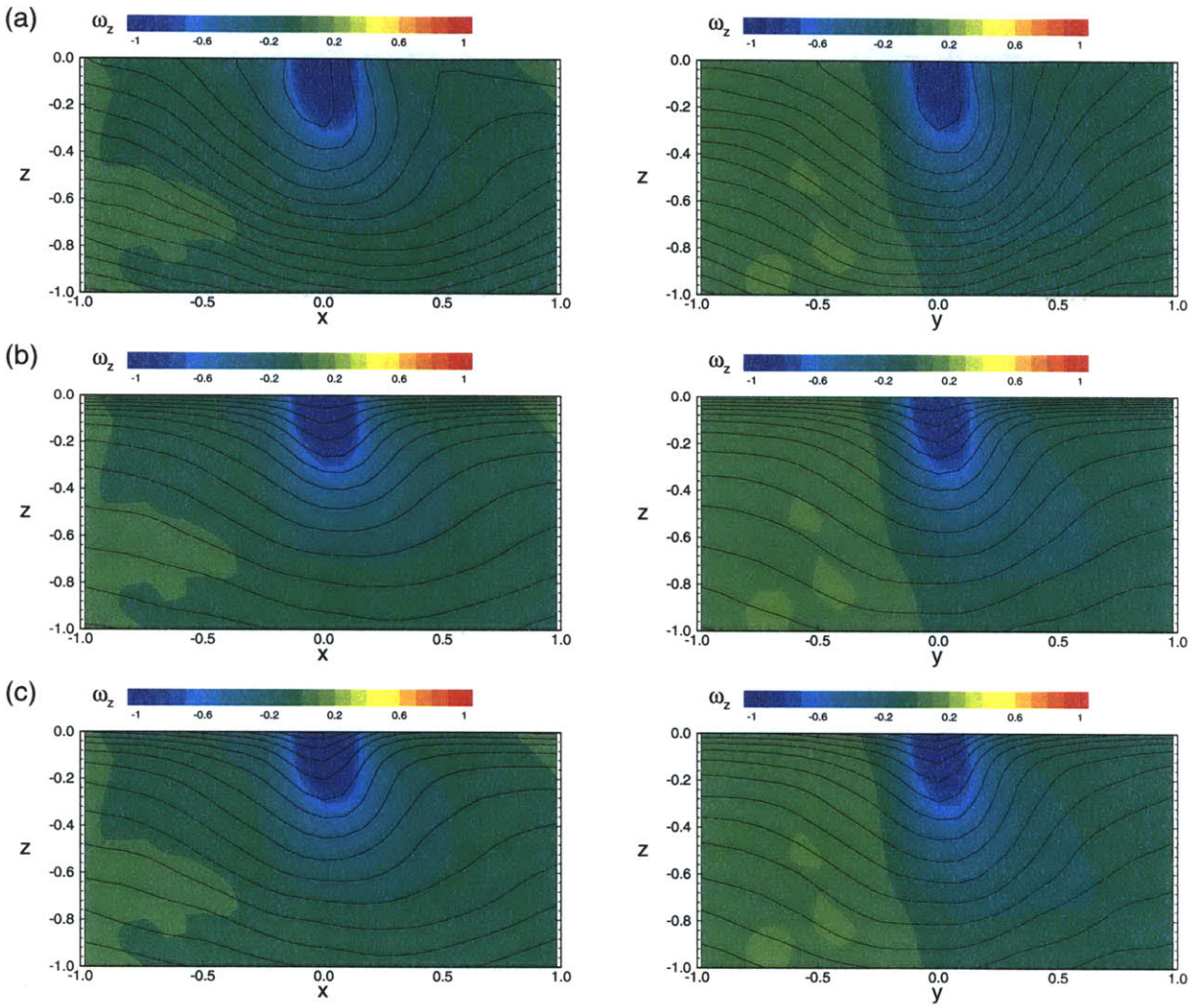

Figure 6-18: Vertical sections of the conditionally-averaged field around negative surface-connected vortices for (a) the zero surface-flux case, (b) the fixed surface-value case, and (c) the fixed surface-flux case. Plotted are the color contours of ω_z and line contours of c with intervals 0.01, 0.04, and 0.02, respectively.

In terms of coherent vortical structures, hairpin vortices convect scalars to the free surface, while surface-connected vortices draw scalars away from surface to the bulk flow below. In this section we quantify the contributions from each type of events.

We first consider the one-point correlation between the scalar and flow properties, which is plotted in Figures 6-19 to 6-21. Note that for quantities vanishing at the surface, surface values of correlation coefficients are not defined and extrapolations are used.

In Figures 6-19 to 6-21, plot (a) shows the correlation with vertical velocity and plot (c) shows the correlation with plane divergency, both represent vertical motions; plot (d) shows the correlation with horizontal vorticity $(\omega_x^2 + \omega_y^2)^{1/2}$, which corresponds to hairpin vortices. As expected, they all show positive correlations. Plot (b) shows the negative correlation with surface-normal vorticity, also in agreement with the results in §6.3. We also observe that among the three cases, the fixed surface-value case correlates with the flow field better than the other two cases. Nevertheless, we notice that the correlations are low.

The one-point correlation coefficient only provides a quantitative relation between the scalar and velocity field. In addition, it is unable to represent the cases where the scalar and velocity fields have an spatial shift, such as the hairpin vortex case shown in §6.3. To better quantify the contributions of each type of events to the scalar transport process, we develop a conditional statistical method based on the aforementioned VISA technique, which is described below.

In the VISA technique, for a certain type of coherent structures, we identify at most one event in each averaging window. Defining N as the number of the events detected and g as the quantity of interest, such as the scalar surface-concentration for the zero or fixed surface-flux cases or the scalar surface-gradient for the fixed surface-value case, the overall contribution of the detected events is expressed as

$$N \int \langle g \rangle_{cond} \mathrm{d}x\mathrm{d}y \ . \tag{6.8}$$

Here $\langle \ \rangle_{cond}$ represents the conditionally-averaged quantities, while the integration is performed in the averaging window.

For the expression (6.8) to accurately represent the contributions from all the events of

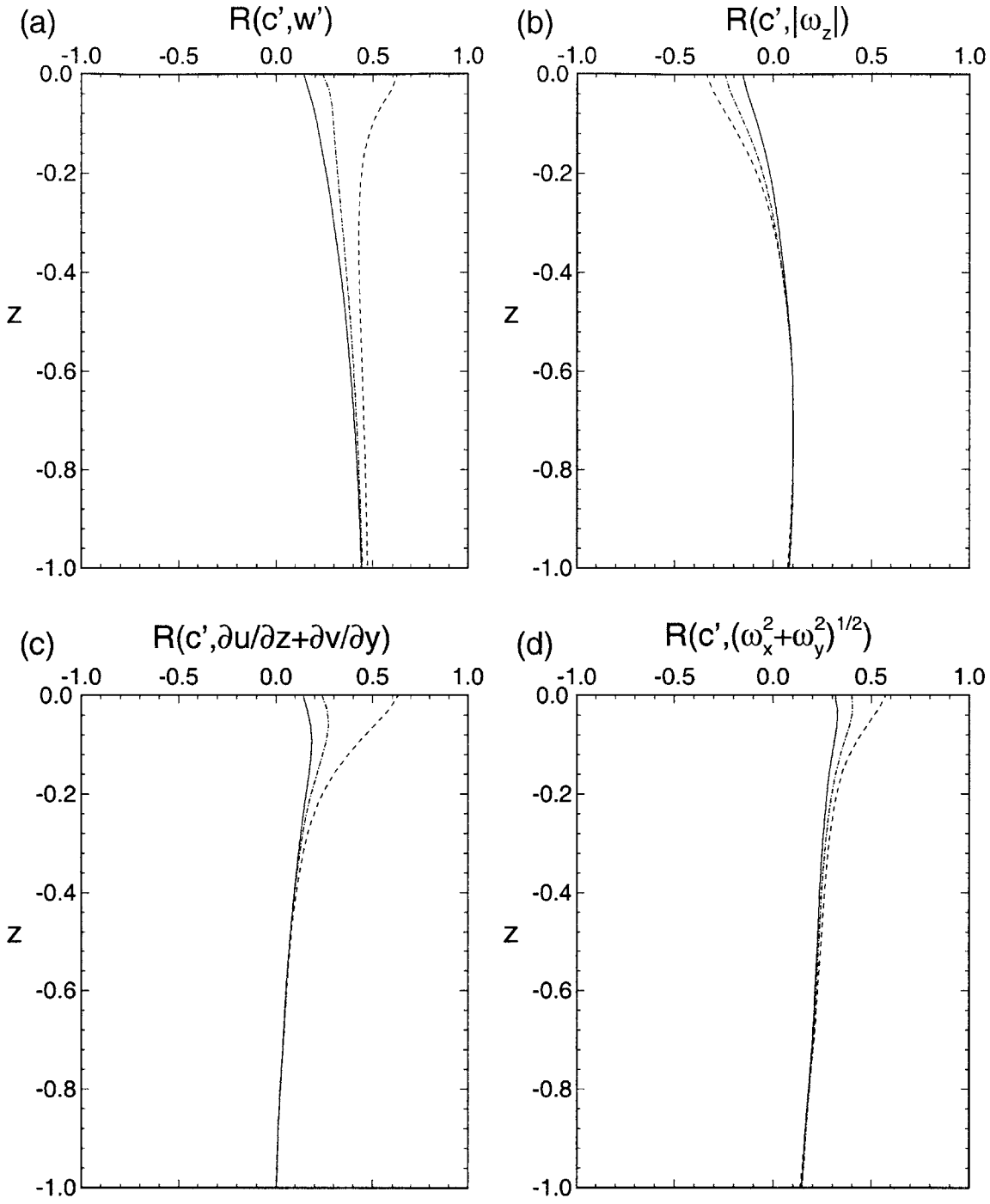

Figure 6-19: Correlation coefficients between scalar concentration c with (a) vertical velocity w, (b) surface-normal vorticity ω_z, (c) plane divergence $\partial u/\partial x + \partial v/\partial y = -\partial w/\partial z$, and ($d$) horizontal vorticity $(\omega_x^2 + \omega_y^2)^{1/2}$. ———— , the zero surface-flux case; – – – – , the fixed surface-value case; – · – · – , the fixed surface-flux case.

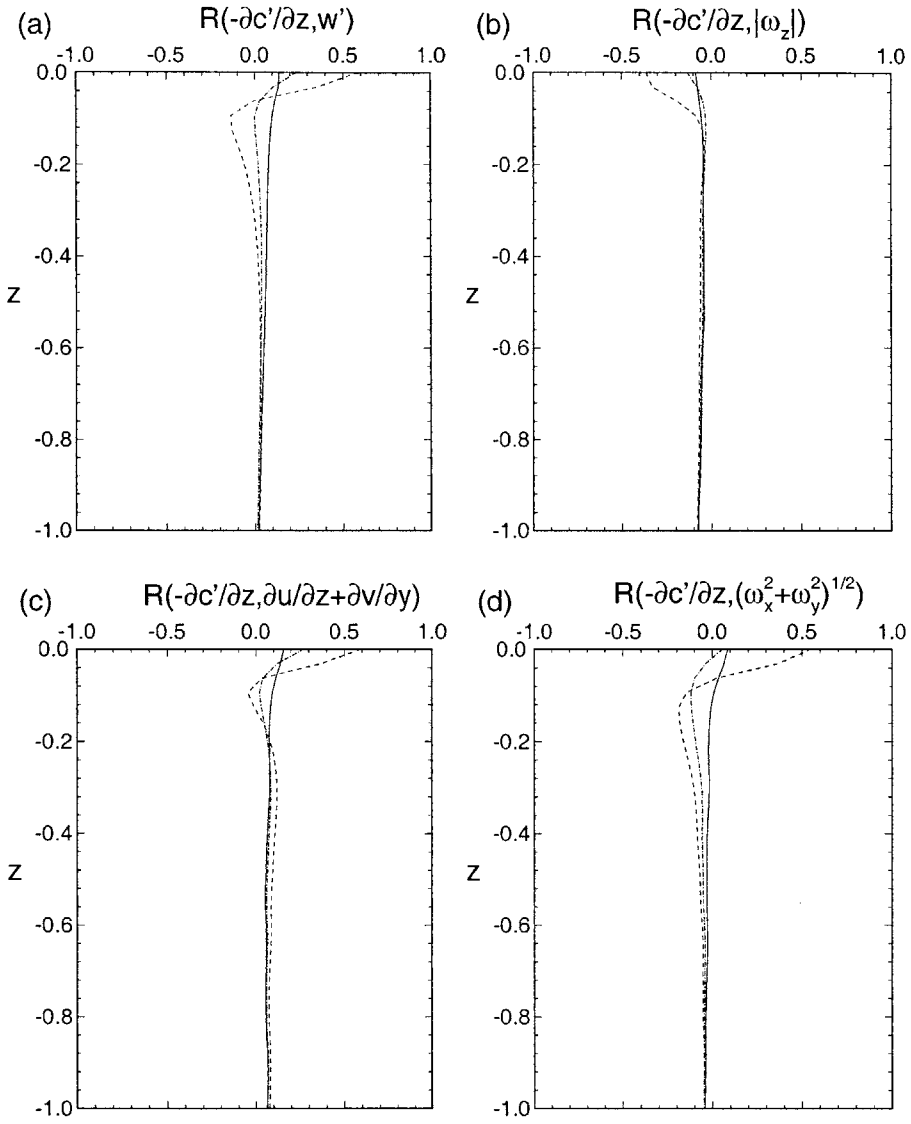

Figure 6-20: Correlation coefficients between scalar gradient $\partial c/\partial z$ with (a) vertical velocity w, (b) surface-normal vorticity ω_z, (c) plane divergence $\partial u/\partial x + \partial v/\partial y = -\partial w/\partial z$, and (d) horizontal vorticity $(\omega_x^2 + \omega_y^2)^{1/2}$. ———— , the zero surface-flux case; – – – – , the fixed surface-value case; – · – · – , the fixed surface-flux case.

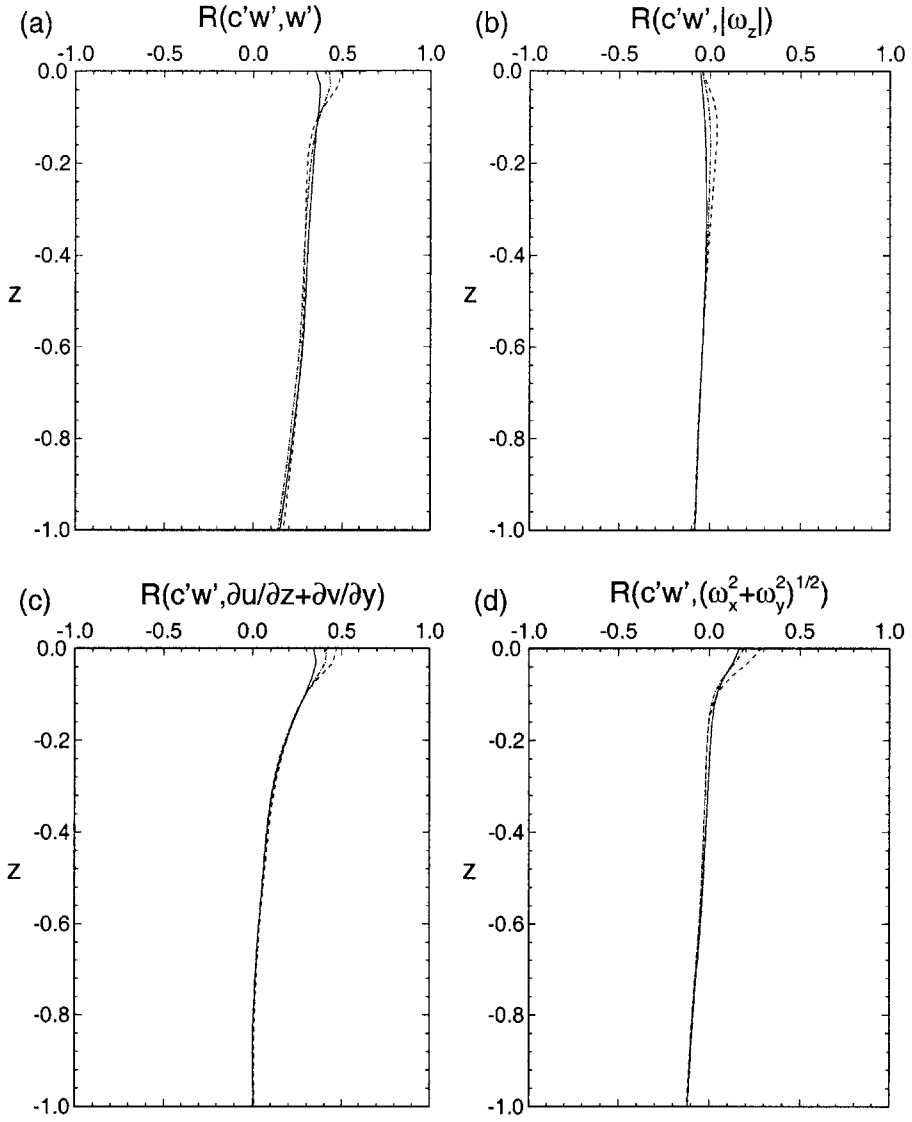

Figure 6-21: Correlation coefficients between scalar turbulence flux $c'w'$ with (a) vertical velocity w, (b) surface-normal vorticity ω_z, (c) plane divergence $\partial u/\partial x + \partial v/\partial y = -\partial w/\partial z$, and (d) horizontal vorticity $(\omega_x^2 + \omega_y^2)^{1/2}$. ———— , the zero surface-flux case; – – – – , the fixed surface-value case; – · – · – , the fixed surface-flux case.

the same type, an essential task is the determination of the averaging window size W. Small values of W tend to exclude some of the contributions out of the window; while large W will lose some of the events of the same type and include the effects of other types of events. A natural choice for the window size W is the integral scale of the detection function f. For the splats/anti-splats, hairpin vortices, and surface-connected vortices, the integral scales for the corresponding detection functions $f = \partial u/\partial x + \partial v/\partial y$, ω_y and ω_z are about 0.8, 0.65 and 0.5, respectively.

The quantified contributions from the events of splats, anti-splats, hairpin vortices, and surface-connected vortices are plotted in Figures 6-22 to 6-24 for the three cases, as functions of the threshold K. As shown, as K increases, the magnitude of the contribution quantities increases first and then decreases. The latter is easier to understand since less events are captured at higher threshold levels. The low contribution for small K, on the other hand, can be attributed to the fact that if the threshold level is too low, weak events are captured accompanied by other types of events. Nevertheless, Figures 6-22 to 6-24 show that the quantification of the contributions from the coherent events is insensitive to the threshold level K for a wide range.

The results in Figures 6-22 to 6-24 greatly agree with the observations from §6.3. The splats play an essential role in the enhancing of scalar transfer towards the free surface, of which the hairpin vortices contribute significantly. The quantification based on anti-splats, on the other hand, plays a much less significant role, also in agreement with the observation from §6.3. Of special note is that surface-connected vortices contribute considerably to the transport of scalar away from the surface, which is shown in the reduction of the surface concentration for the zero surface-flux case (Figure 6-22) and fixed surface-flux case (Figure 6-24), as well as the decreasing of surface gradient for the fixed surface-value case (Figure 6-23).

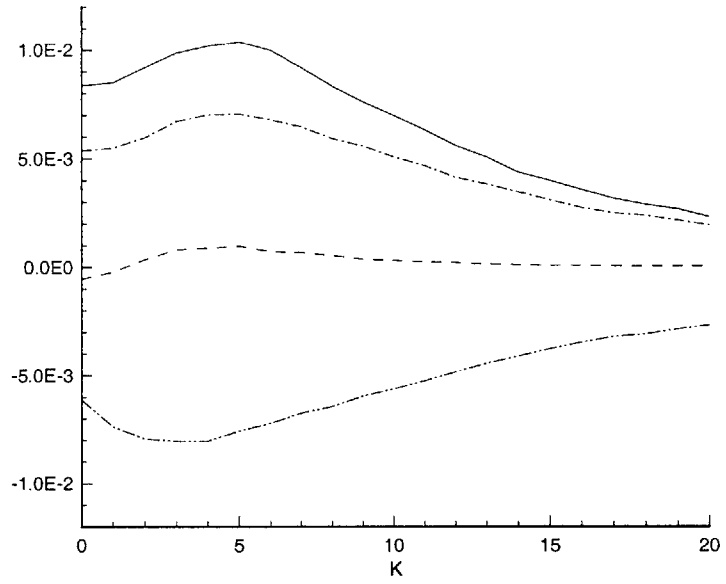

Figure 6-22: Contributions of turbulent structures to the scalar free-surface concentration for the zero surface-flux case. ———— , splats; – – – – , anti-splats; – · – · – , hairpin vortices; —··—··— , surface-connected vortices.

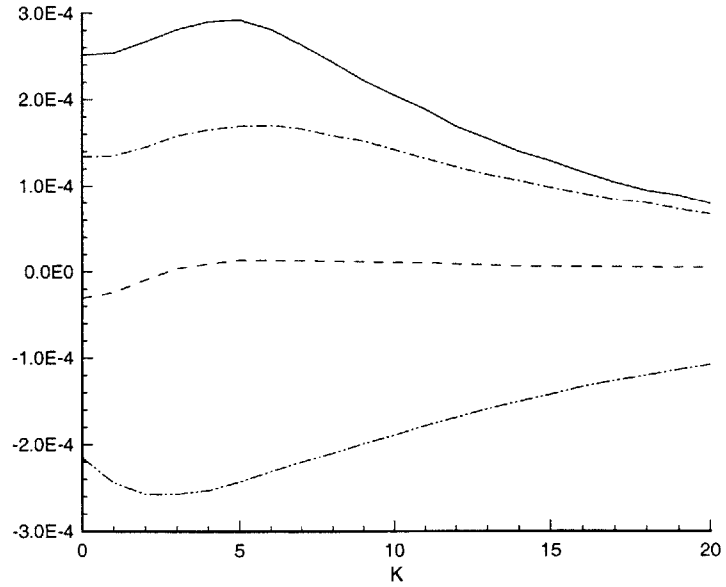

Figure 6-23: Contributions of turbulent structures to the scalar free-surface concentration for the fixed surface-value case. ———— , splats; – – – – , anti-splats; – · – · – , hairpin vortices; —··—··— , surface-connected vortices.

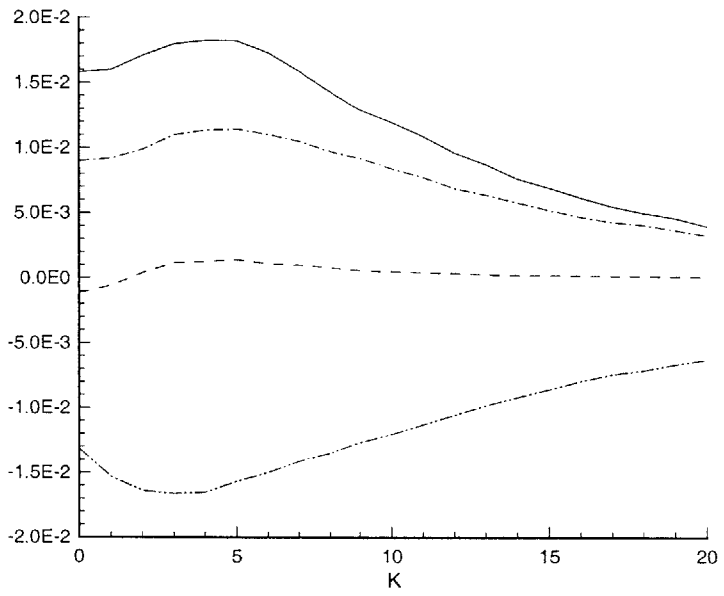

Figure 6-24: Contributions of turbulent structures to the scalar free-surface concentration for the fixed surface-flux case. ———— , splats; – – – – , anti-splats; – · – · – , hairpin vortices; —··—··— , surface-connected vortices.

6.5 Conclusions

In this chapter we perform direct numerical simulation for the transport of passive scalars with three different free-surface boundary conditions of a zero surface-flux-rate, a fixed surface-value, and a fixed surface-flux-rate, respectively. The three cases correspond respectively to the problems of pollutant spreading, gas transport and heat transfer. From the statistics of the scalar field, the structure of free-surface boundary layers is clearly shown, which is characterized by the dramatic change in the mean concentrations, the enhanced viscous flux rates, and the rapid reduction in the turbulent diffusivity.

The dependence of scalar transport process on the turbulent structures are elucidated. It is found that splats play a much significant role in the transport of scalars towards the free surface than the anti-splats do in convecting the scalars away from the surface. The coherent hairpin vortices and surface-connected vortices contribute considerably to the transport towards and away the surface, respectively. These processes are quantified by a novel conditional statistical technique based on the variable-interval space-averaging method.

Chapter 7

Inter-Scale Energy Transfer in Free-Surface Turbulence

In large-eddy simulation (LES) only the large scales (grid scales, GS) are computed explicitly while the effects of small scales (subgrid scales, SGS) are modeled. Obviously, the key to the success of LES lies in the accuracy of the SGS modeling. The most important role of SGS modeling is to represent the energy transfer between the grid scales and subgrid scales. In this chapter we study the inter-scale energy transfer in free-surface turbulence (FST). Our objective is to obtain the physical understanding necessary for the effective SGS modeling for the LES of FST.

The development of SGS modeling for FST LES has been limited until recently. Dommermuth & Novikov (1993) used DNS and LES to study the interaction between turbulence and a free surface with and without surface waves. They employed a number of local and global SGS models and their combinations, but with limited success in that, as resolution is decreased, the closure models they considered work as poorly as grid filters with no SGS models. They concluded that it would be important to obtain a better understanding of the structure of turbulence in question. Salvetti & Banerjee (1995) and Salvetti *et al.* (1997) developed a dynamic two-parameter model (DTM), which is a combination of the Smagorinsky model and the scale-similarity model (Bardina, Ferziger & Reynolds 1983) with both coefficients determined dynamically through the Germano identity (Germano *et al.* 1991).

Their tests with a decaying turbulence beneath a flat free-slip wall show that DTM obtains significant improvements over existing SGS models. Recently, Hodges & Street (1999) performed LES for a turbulent open-channel flow with a finite-amplitude surface wave. They employed DTM as the SGS model and obtained results for the turbulence wave interactions.

One of the major objectives of the present study is to further develop large-eddy simulation capabilities for free-surface turbulent flows. As a canonical problem, we consider the interaction of a turbulent shear flow with a free surface at low Froude numbers. From the DNS studies in proceeding chapters, it is known that free-surface turbulent shear flow possesses a number of unique features: (1) The flow field near the surface is highly anisotropic. The vanishing of the tangential stresses at the surface creates a thin *surface layer* where the velocity derivatives (e.g. vorticity and strain rate components) are highly anisotropic. On the other hand, the blockage effects of the surface cause anisotropy of the velocity components themselves over a much thicker region. (2) This multi-layer structure is manifest in the turbulent diffusion, which can be interpreted analytically through a similarity solution for the mean flow. (3) The free-surface turbulent flow is characterized by connection of coherent hairpin vortex structures at the free surface. Depending on the stage of the connection process, different vortex dynamics can be identified, which ultimately result in persistent surface-connecting vortices on the surface.

From the above, it is clear that the effectiveness of LES of free-surface turbulence would be enhanced if the characteristic features of the flow are taken into account and are captured by the SGS model(s) employed. In addition to the descriptions of the statistical and structural properties, of special importance in the context of LES is an understanding of the interaction and energy transfer mechanisms between resolved grid scales and the modeled subgrid scales of the flow. In this chapter we investigate these inter-scale turbulent mechanisms near the free surface. In Chapter 8, this understanding is used to develop specific SGS models which capture these underlying structures and mechanisms.

This chapter is organized as follows. In §7.1 we provide an overview of the FST flow field in terms of the characteristics of different turbulent length scales. We investigate in §7.2 the energy cascade in the free-surface turbulence. In §7.3 we then use a conditional

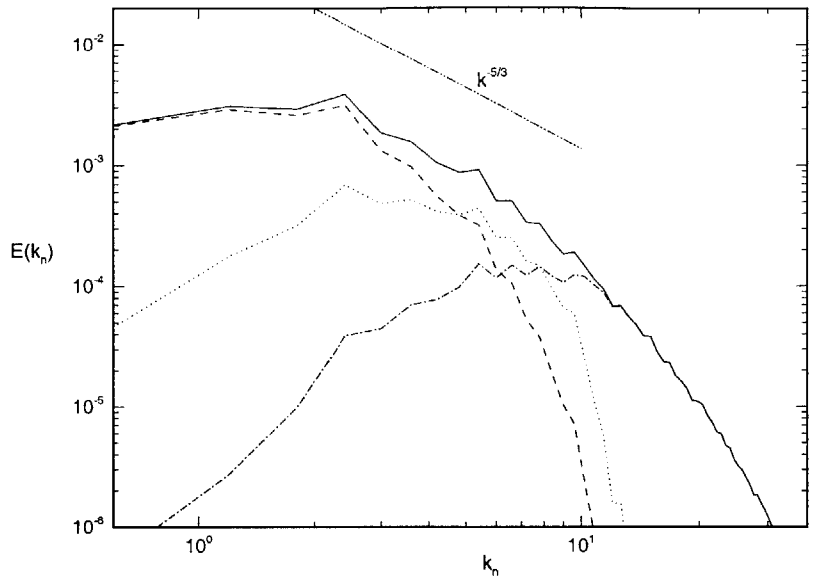

Figure 7-1: Kinetic energy spectra in the bulk flow ($z = -1.5$) for: the total velocity $E_{u_iu_i}$ (————); the grid-scale portion $E_{\overline{u}_i\overline{u}_i}$ (– – – –); the subgrid-scale portion $E_{u'_iu'_i}$ (– · – · –); and the cross portion $E_{\overline{u}_iu'_i}$ (· · · · · · ·). t=60.

averaging technique to study the role of coherent vortex structures in the inter-scale energy transfer. In §7.4 we examine the anisotropy of the flow field and the consequent effects on SGS modeling. Finally in §7.5, we present our conclusions.

7.1 Overview of the flow field

In this study, the DNS results on the interaction between a turbulent shear flow and a free surface at low Froude numbers, obtained in the proceeding chapters, are used to investigate the inter-scale energy transfer mechanism in FST. Here we first present an overview of the flow field in term of different turbulence length scales.

Figure 7-1 plots the horizontal energy spectrum $E_{u_iu_i}(k_n)$, which is defined as

$$E_{u_iu_i}(k_n;z) \equiv \sum_{k_n-\Delta_k/2\le k<k_n+\Delta_k/2} \frac{1}{2}\widetilde{u}_i(k_x,k_y;z)\widetilde{u}_i^*(k_x,k_y;z)/\Delta_k \ , \quad i=1,2,3. \tag{7.1}$$

Here k_n=$n\Delta_k$, n=1,2,3... with Δ_k=$2\pi/L_x$=$2\pi/L_y$. In (7.1), $\widetilde{u}_i$ is the (horizontal) Fourier mode ($\widetilde{u}_i^*$ is the complex conjugate) of the velocity component u_i:

$$u_i(x,y,z,t) = \sum_{k_x,k_y} \widetilde{u}_i(k_x,k_y,z,t) e^{ik_x x} e^{ik_y y} \ , \tag{7.2}$$

where

$$k_x = n_x\Delta_k, \quad k_y = n_y\Delta_k, \quad \text{and} \quad k \equiv \sqrt{k_x^2+k_y^2}, \tag{7.3}$$

$$n_x = -N_x/2, ..., N_x/2-1, \quad n_y = -N_y/2, ..., N_y/2-1 \ , \tag{7.4}$$

with N_x (N_y) the grids number in the x- (y-) direction.

Because of the low Reynolds number limited by the DNS, only a relatively small portion of the energy spectrum $E_{u_iu_i}$ in Figure 7-1 is close to the $k^{-5/3}$ high-wavenumber asymptote. Figure 7-1, however, shows clearly the overlap among the grid-scale portion of the kinetic energy, $E_{\overline{u}_i\overline{u}_i}$≡$\sum \widetilde{\overline{u}}_i\widetilde{\overline{u}}_i^*/(2\Delta_k)$; the subgrid scale portion of the energy, $E_{u'_iu'_i}$≡$\sum \widetilde{u'}_i\widetilde{u'}_i^*/(2\Delta_k)$; and the remaining cross portion, $E_{\overline{u}_iu'_i}$≡$\sum(\widetilde{\overline{u}}_i\widetilde{u'}_i^* + \widetilde{u'}_i\widetilde{\overline{u}}_i^*)/(2\Delta_k)$. Such overlaps are a characteristic of the (horizontal) Gaussian filters (2.34). The use of the Gaussian filter and the resulting energy overlap are the basis of the scale-similarity SGS models. The importance of including such SGS models in the LES is demonstrated in simulations in §4.4.

Similar to the energy spectrum, the turbulence kinetic energy $q^2/2$ itself can be separated into its scale components:

$$\frac{q^2}{2} \equiv \frac{1}{2}\langle (u_i - \langle u_i\rangle)^2\rangle = \underbrace{\frac{1}{2}\langle(\overline{u}_i - \langle\overline{u}_i\rangle)^2\rangle}_{\text{grid-scale component}} + \underbrace{\langle(\overline{u}_i - \langle\overline{u}_i\rangle)(u'_i - \langle u'_i\rangle)\rangle}_{\text{cross contribution}} + \underbrace{\frac{1}{2}\langle u'^2_i\rangle}_{\text{subgrid-scale component}} \ . \tag{7.5}$$

Likewise, the Reynolds stress $\langle -uw\rangle$ can be separated as:

$$\langle -uw\rangle = \underbrace{\langle -\overline{u}\ \overline{w}\rangle}_{\text{grid-scale component}} + \underbrace{\langle -\overline{u}w' - u'\overline{w}\rangle}_{\text{cross contribution}} + \underbrace{\langle -u'w'\rangle}_{\text{subgrid-scale component}} \ . \tag{7.6}$$

Figure 7-2 plots the vertical profiles of these components for the turbulence energy and the

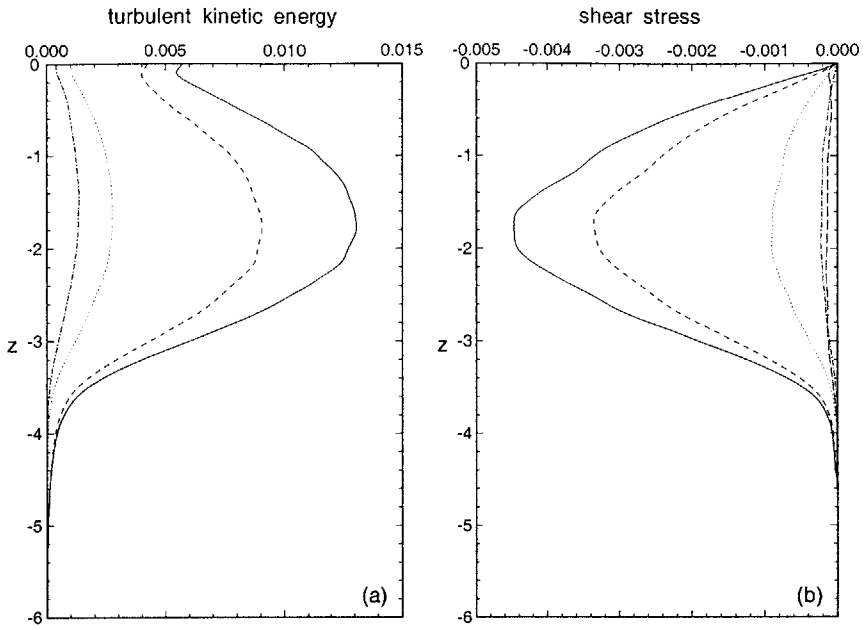

Figure 7-2: Profiles of the scale components of (a) turbulent kinetic energy $q^2/2$, and (b) Reynolds stress $\langle -uw \rangle$. ———— , total; – – – – , grid-scale component; ····· , cross contribution; – · – · – , subgrid-scale component. For reference, the viscous stress $Re^{-1}\partial\langle u \rangle/\partial z$ (— —) is also plotted in (b). t=60.

Reynolds stress $\langle -uw \rangle$. It is clear that the grid-scale portion, which contains most of the energy, is responsible for the main part of the turbulence transport.

7.2 Inter-scale energy transfer

Turbulence is characterized by the energy cascade throughout different length scales. The most important role of the SGS model is to account for the energy transfer between the resolved and subgrid scales. Figure 7-3(a) plots the horizontal plane-averaged energy transfer $\langle \epsilon \rangle$ from the grid scales to the subgrid scales, where $\epsilon \equiv \tau_{ij}\bar{s}_{ij}$ and $\bar{s}_{ij} \equiv (\partial\overline{u}_i/\partial x_j + \partial\overline{u}_j/\partial x_i)/2$. Positive/negative sign of ϵ corresponds to energy transfer to/from the grid scales from/to the subgrid scales. From the figure, it is seen that the average energy transfer is from grid to subgrid scales at all depths. The amount of the energy transferred into the subgrid scales is however much reduced near the free surface. For example, in the Smagorin-

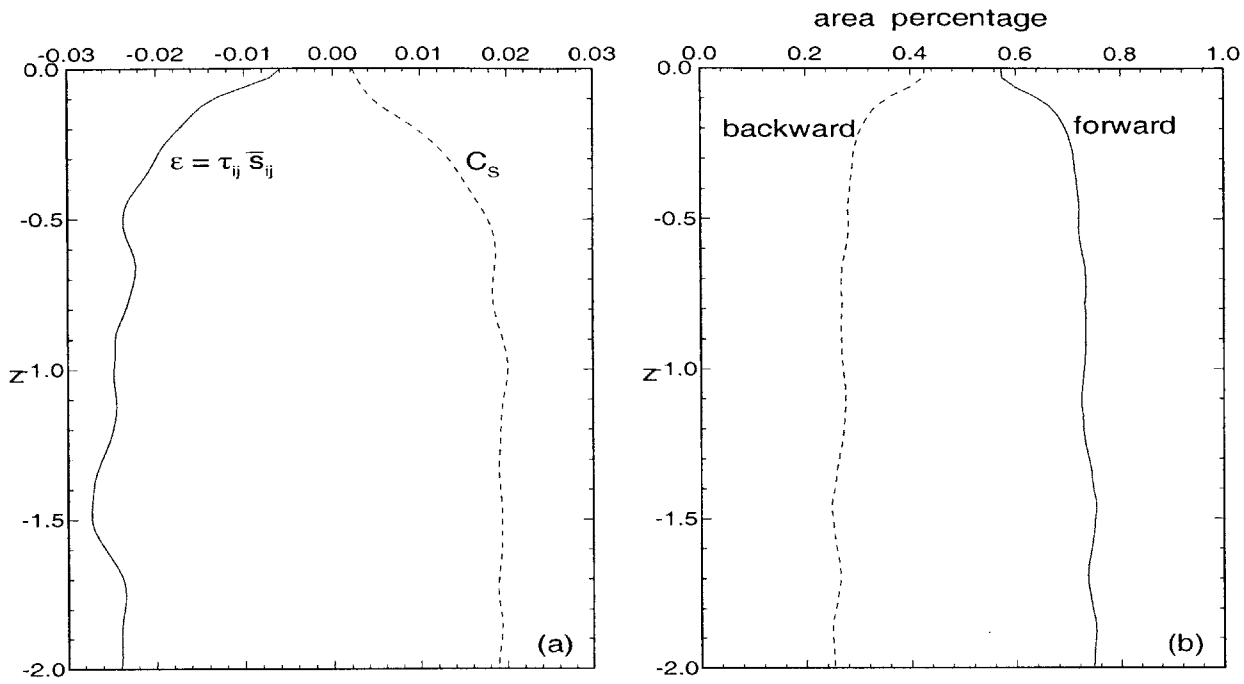

Figure 7-3: (a) Vertical variation of the energy transferred from the grid scales to the subgrid scales $\langle\epsilon\rangle$ (————) and the Smagorinsky coefficient C_S (– – – –). ϵ is normalized by the local turbulence kinetic energy $q^2(z)/2$. (b) Area percentages of grid points experiencing forward (grid to subgrid) transfer (————) and backward (subgrid to grid) transfer (– – – –). t=60.

sky model of the SGS stress,

$$\tau_{ij} - \frac{1}{3}\delta_{ij}\tau_{kk} = -2C_S\overline{\Delta}^2|\overline{s}|^2\overline{s}_{ij} \ , \tag{7.7}$$

the coefficient C_S will, as a result, decrease towards the free surface. This behavior of C_S is confirmed and shown in Figure 7-3(a). In Figure 7-3(a), C_S is obtained by assuming it to be constant in the horizontal plane and then calculated by best matching the two sides of (7.7) (cf. *a priori* tests by Clark, Ferziger & Reynolds 1979, and McMillan, Ferziger & Rogallo 1980).

Figure 7-3(b) plots the grid percentages at each horizontal plane where forward transfer (negative ϵ) or backward transfer (positive ϵ) occurs. In the bulk flow below, about 70% of the grids transfer energy forward while the remaining 30% experience energy backscatter. The

relatively high percentage of backscatter is consistent with previous studies. Piomelli *et al.* (1991) found that for turbulent channel flow, backscatter occurs at nearly 50% of the points in the flow when a Fourier cutoff filter is used; if a Gaussian filter is used, the backscatter fraction is reduced to 30%. Of significant importance to the study of free-surface turbulence is the near surface behavior in Figure 7-3(b) showing that the percentage of backscatter area increases from 30% to more than 40% as the free surface is approached.

The above results suggest that the inter-scale energy transfer near the free surface is significantly different from that in the bulk flow below and that energy backscatter must play a more important role near the surface. To further investigate these mechanisms, we study the energy cascade in the spectral space.

We denote the nonlinear advective terms as

$$\mathcal{N}_i \equiv -\frac{\partial u_i u_j}{\partial x_j} , \quad i = 1, 2, 3, \tag{7.8}$$

and the corresponding Fourier modes $\widetilde{\mathcal{N}}_i$. From (2.1) and (7.1), the effect of the nonlinear terms on $\partial E(k_n)/\partial t$ can be written as

$$\mathcal{T}(k_n) = \sum_{k_n - \Delta_k/2 \le \sqrt{k_x^2 + k_y^2} < k_n + \Delta_k/2} \mathcal{R}\{\widetilde{u}_i^*(k_x, k_y)\widetilde{\mathcal{N}}_i(k_x, k_y)\}/\Delta_k , \tag{7.9}$$

where $\mathcal{R}$ denotes the real part.

The wave vector of the quadratic nonlinear terms, (k_x, k_y), and those of the two velocity components in the nonlinear terms, (k_x^r, k_y^r) and (k_x^s, k_y^s), must satisfy the following triangular relation:

$$(k_x, k_y) = (k_x^r, k_y^r) + (k_x^s, k_y^s) . \tag{7.10}$$

In other words, it is the interaction between the two wavenumbers, $k^r = \sqrt{(k_x^r)^2 + (k_y^r)^2}$ and $k^s = \sqrt{(k_x^s)^2 + (k_y^s)^2}$, that results in the change at the third wavenumber $k = \sqrt{(k_x)^2 + (k_y)^2}$. For later reference, we use $\mathcal{T}^{k^r,k^s}(k)$ to denote the contribution to $\mathcal{T}(k)$ due to the quadratic interactions of the flow at two different wavenumbers k^r and k^s. To understand the contributions from the different scales, it is convenient to partition the k^r, k^s domain into dif-

ferent wavenumber regimes: $k^r, k^s \in$ M, I, II, III, A. These correspond to the regimes: M=$\{k : k = 0\}$ (mean flow); I=$\{k : 0.6 \leq k < 5.4\}$ (large scales); II=$\{k : 5.4 \leq k < 10.2\}$ (small resolved scales and large subgrid scales); III=$\{k : 10.2 \leq k < 15\}$ (small scales); and A=$\{k : k > 0\}$ (all turbulent fluctuation wavenumbers). For each of these energy transfer terms, we further define their directional components, $\mathcal{T}_j^{k^r,k^s}$, j=x, y, z, which correspond to the contributions to $\mathcal{T}^{k^r,k^s}$ due to the $j-$th component of the advection term, $-\partial u_i u_j/\partial x_j$ (no summation for j).

We first consider the interaction between the mean flow and the total turbulent fluctuations, $\mathcal{T}^{M,A}$. This is plotted in Figure 7-4 for the free-surface region (averaged over $-0.25 \leq z \leq 0$) and the deep region (averaged over $-1.625 \leq z \leq -1.375$). Here and hereafter, $\mathcal{T}$ is normalized by the local turbulent kinetic energy $q^2(z,t)/2$. Figure 7-4 shows clearly the energy extraction from the mean flow to turbulent fluctuations and that it is the low wavenumbers (largest eddies) that receive most of the energy directly. Figure 7-4 also shows that the turbulent production near the free surface is much less than that in the deep region. This is consistent with Shen *et al.* (1999) who considered the total production $<-uw>\ \partial<u>/\partial z$ in the physical space. This reduction was explained by Shen *et al.* (1999) through two mechanisms: (i) the annihilation of w due to the constraint on the vertical motion at the free surface; and (ii) the vanishing of $\partial<u>/\partial z$ caused by the shear-free free-surface boundary condition.

Next we investigate the interactions among the total turbulent fluctuations, $\mathcal{T}^{A,A}$, which is plotted in Figure 7-5(a) (the directional components in Figures b to d will be discussed later). The forward energy transfer (for the low wavenumbers) is manifest in the bulk region, as expected. This energy transfer is, however, very different near the free surface where it is predominately one of back-scattering (although at a smaller magnitude). This reverse energy transfer mechanism near the free surface is consistent with the finding in Figure 7-3 and was also observed in free-surface jet flows (e.g. Mangiavacchi, Gundlapalli & Akhavan 1994).

The overall picture is clarified if we consider the contributions to $\mathcal{T}^{A,A}$ from the different wavenumber scales, specifically: $\mathcal{T}^{I,A}$, $\mathcal{T}^{II,A}$, $\mathcal{T}^{III,A}$. These are plotted in Figures 7-6(a),

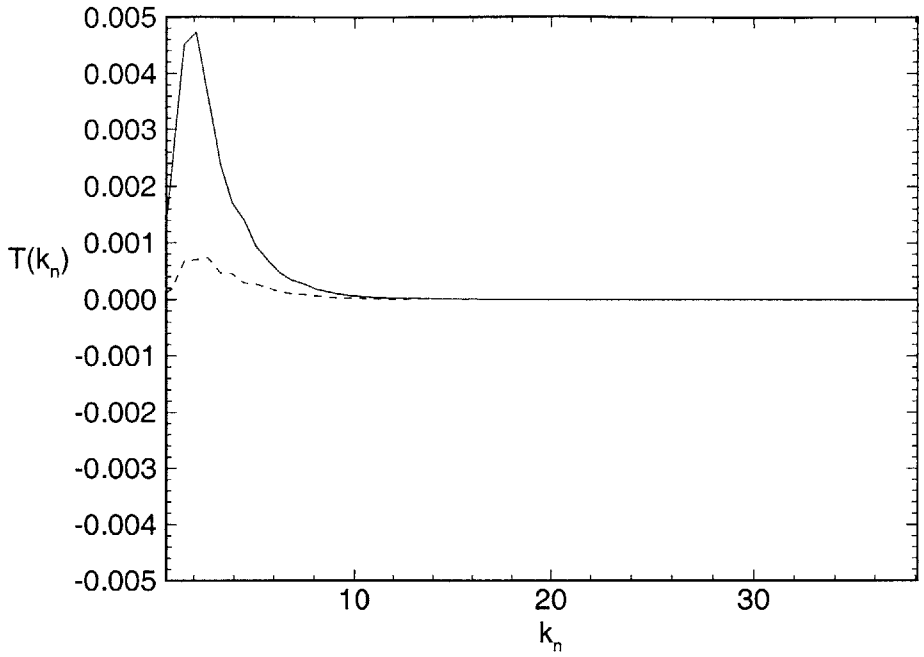

Figure 7-4: Energy transferred from the mean flow to all the scales of turbulent fluctuations $\mathcal{T}^{M,A}$. ———— , deep region; – – – – , free surface.

7-7(a), and 7-8(a), respectively. From these figures, we observe that, in the bulk region, the role of each band is to remove the energy from the larger scales to the smaller scales. This is in agreement with the previous studies on other types of flows (see e.g. Domaradzki & Rogallo 1990 for isotropic homogeneous turbulence, and Domaradzki *et al.* 1994 for wall-bounded turbulence). Near the free surface, band I (large scales) feeds energy into the low wavenumbers, similar to the backscatter shown in Figure 7-5(a), while the intermediate and small scales, bands II and III, continue to transfer energy forward. Nevertheless, the magnitudes of the forward energy transfer by bands II and III near the free surface are much less than the corresponding values in the bulk.

More insight into the inter-scale energy transfer can be obtained by considering the directional components of $\mathcal{T}$. Figures 7-5 to 7-8 (b), (c), (d) plot $\mathcal{T}_j^{A,A}$, $\mathcal{T}_j^{I,A}$, $\mathcal{T}_j^{II,A}$, $\mathcal{T}_j^{III,A}$, for j=x,y,z, respectively. For j=x and y, the difference between $\mathcal{T}$ in the bulk and at the free surface is insignificant: in both cases, energy is transferred from larger to smaller scales. It is the vertical component $\mathcal{T}_z$ that fundamental differences obtain between the bulk and free surface: the forward energy transfer in the bulk becomes negative and is comparable

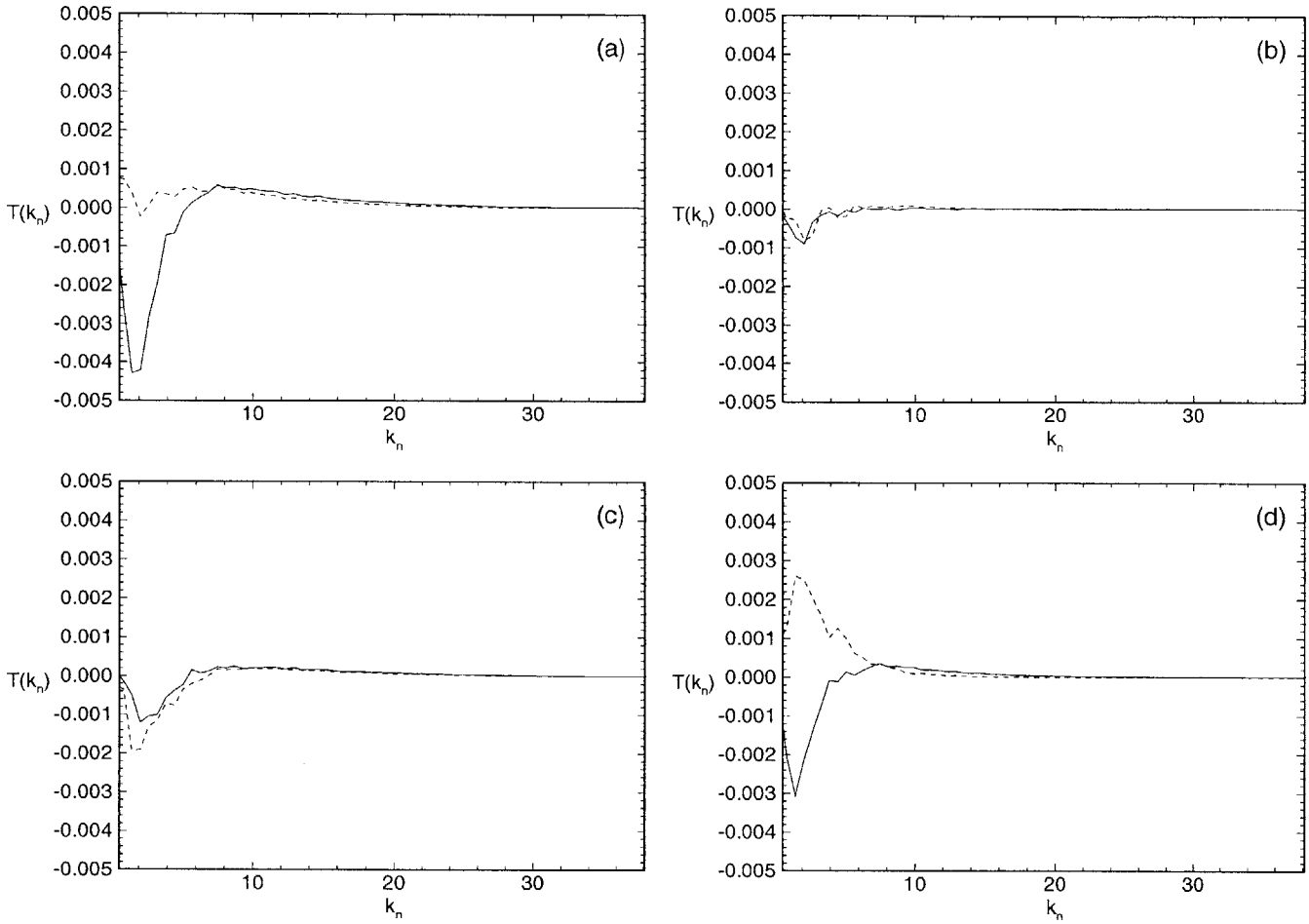

Figure 7-5: Inter-scale energy transfer among the turbulent fluctuations: (a) total $\mathcal{T}^{A,A}$; and contributions from (b) x-advection $\mathcal{T}_x^{A,A}$, (c) y-advection $\mathcal{T}_y^{A,A}$ and (d) z-advection $\mathcal{T}_z^{A,A}$. ———— , deep region; – – – – , free surface.

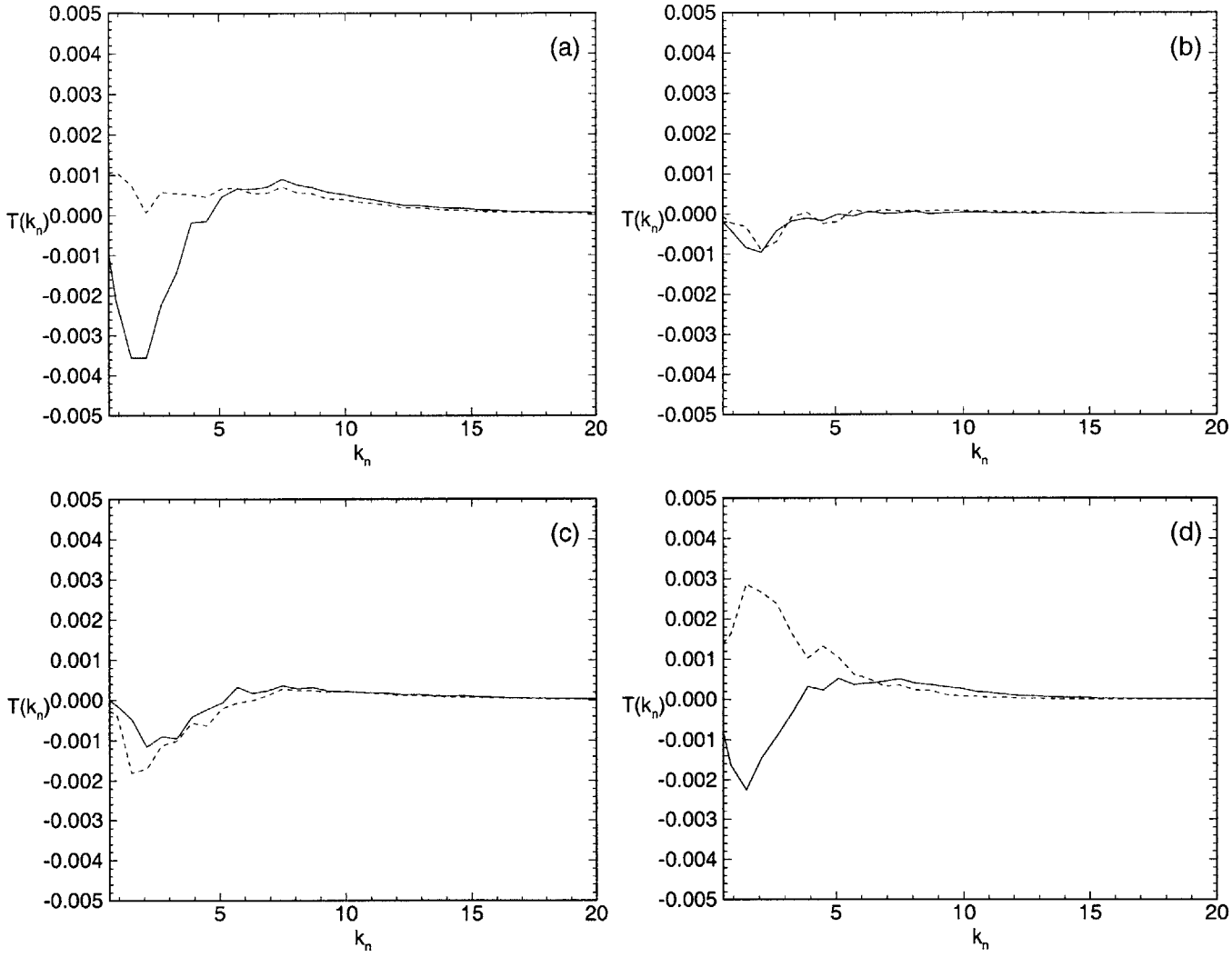

Figure 7-6: Inter-scale energy transfer associated with band I ($0.6 \leq k < 5.4$): (a) total $\mathcal{T}^{I,A}$; and contributions from (b) x-advection $\mathcal{T}_x^{I,A}$, (c) y-advection $\mathcal{T}_y^{I,A}$ and (d) z-advection $\mathcal{T}_z^{I,A}$. ———— , deep region; - - - - , free surface.

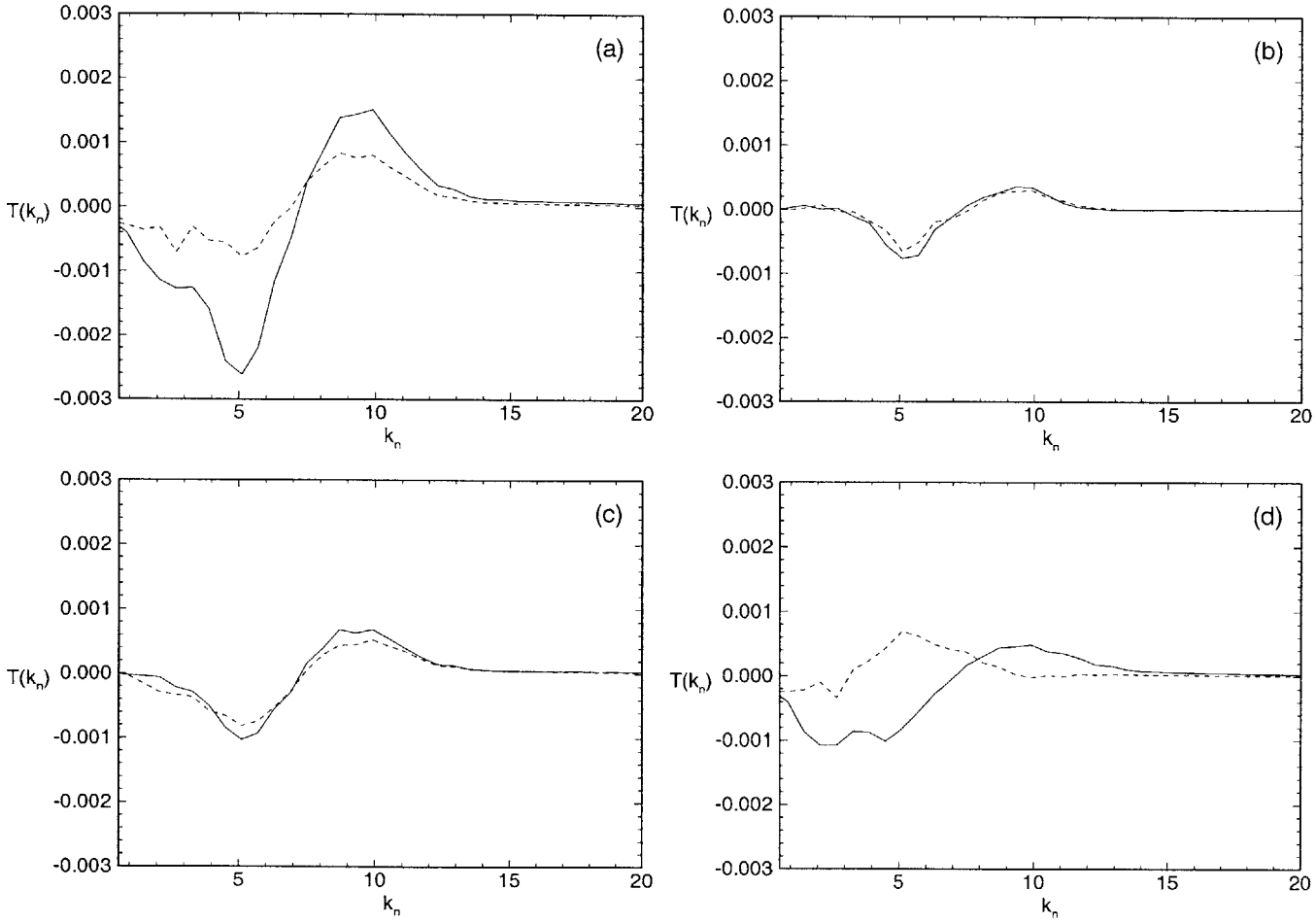

Figure 7-7: Inter-scale energy transfer associated with band II ($5.4 \leq k \leq 10.2$): (a) total $\mathcal{T}^{II,A}$; and contributions from (b) x-advection $\mathcal{T}_x^{II,A}$, (c) y-advection $\mathcal{T}_y^{II,A}$ and (d) z-advection $\mathcal{T}_z^{II,A}$. ———— , deep region; – – – – , free surface.

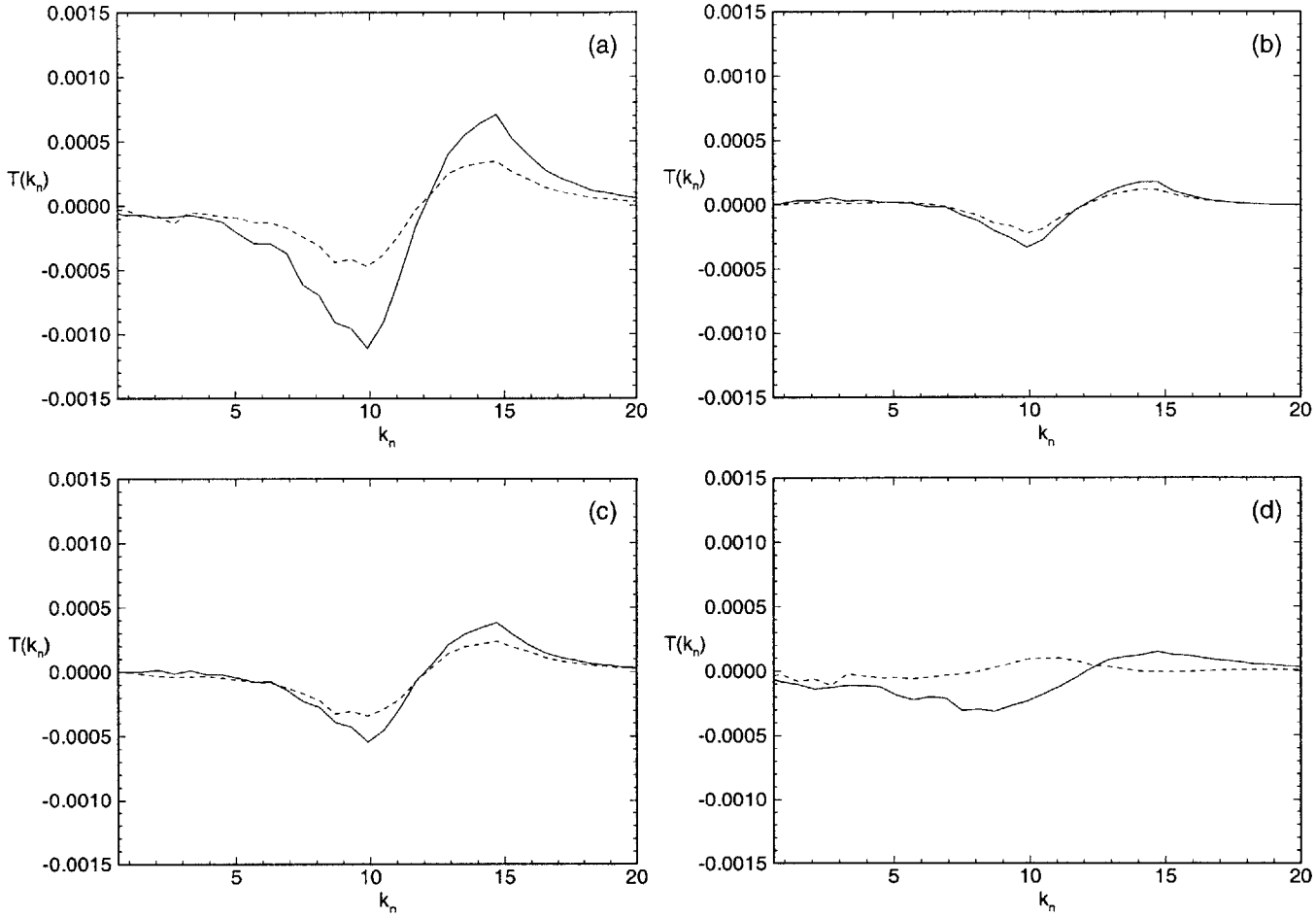

Figure 7-8: Inter-scale energy transfer associated with band III ($10.2 \leq k \leq 15$): (a) total $\mathcal{T}^{III,A}$; and contributions from (b) x-advection $\mathcal{T}_x^{III,A}$, (c) y-advection $\mathcal{T}_y^{III,A}$ and (d) z-advection $\mathcal{T}_z^{III,A}$. ———— , deep region; - - - - , free surface.

in magnitude at the free surface. Clearly this reversal is related to the vertical convective velocity term:

$$-\frac{\partial u_i w}{\partial z} = -w\frac{\partial u_i}{\partial z} - u_i\frac{\partial w}{\partial z}\,, \qquad i = 1, 2, 3. \tag{7.11}$$

The vertical velocity w is small near the free surface and hence the second term $-u_i\partial w/\partial z$ dominates. Since $\partial w/\partial z{=}-(\partial u/\partial x + \partial v/\partial y)$ measures the divergence at the horizontal plane, we conjecture that the energy backscatter in free-surface turbulence is likely related to the splat and anti-splat motions near the surface. This is confirmed in §3.3.

In summary, it is found that the mechanism of inter-scale energy transfer near a free surface is substantially different from that in the bulk flow. The typical energy cascade from large to small scales does not obtain near the free surface. This energy backscatter, which is found to be caused by vertical convection, plays a prominent role in the structure of free-surface turbulence.

7.3 Coherent vortical structures at the free surface

The reverse inter-scale energy transfer in free-surface turbulence is related to the presence of coherent vortex structures at the surface. The correlation between the turbulent structures and the forward/backward inter-scale energy transfer has received some attention in recent years. Hartel *et al.* (1994) showed that the backscatter near a solid wall is strongly enhanced by coherent motions such as bursting events. Piomelli, Yu & Adrian (1996) investigated the dependence of the inter-scale energy transfer on the large-scale turbulent structures in wall-bounded flows. These studies of wall-bounded flows provide important physical insights for the development of SGS models. For free-surface turbulence in an open-channel flow, Pan & Banerjee (1995) found strong backscatter in the upwellings, while strong forward energy transfers are at the outskirts of the surface-connecting vortices where the shear is high. The energy transfers at the vortex core regions are found to be weak. These features are also obtained in our present simulations (results not shown here).

From earlier studies (cf. Shen *et al.* 1999) it is shown that free-surface shear turbulence is characterized by the presence of hairpin vortices which are inclined with the mean flow

with head portions near the free surface and the two legs extending into the bulk region. As a hairpin vortex approaches the surface, the head portion is dissipated quickly within a surface layer and the two legs connect to the surface, resulting in a pair of persistent counter-rotating surface-connected vortices. (These processes are studied in some detail by Shen *et al.* 1999.) In our SGS modeling, we find that it is essential to capture the inter-dependence of near-surface vortex dynamics and inter-scale energy transfer in order to obtain adequate prediction of the surface signature.

To analyze the coherent turbulent structures, we employ the method of conditional averaging (cf. Antonia 1981 for a review of this method for turbulence studies). Specifically, we use a variable-interval space-averaging (VISA) technique (Kim 1983; Hartel *et al.* 1994; Piomelli *et al.* 1996), which is based on the variable-interval time-averaging (VITA) method developed by Blackwelder & Kaplan (1976). We summarize the VISA procedure used in the present study as follows. The event we want to capture is the head portion of the hairpin vortex near the free surface, i.e. large negative spanwise vorticity ω_y. For ω_y, its variable-interval space averaging is defined as

$$\underline{\omega}_y(x,y,z,t,W) \equiv \frac{1}{4W^2}\int_{x-W}^{x+W}\int_{y-W}^{y+W}\omega_y(\xi,\zeta,z,t)\mathrm{d}\xi\mathrm{d}\zeta\ , \tag{7.12}$$

where W is the half width of the averaging window, which has a value about 1 (macroscale) in this study. To identify strong ω_y events, a localized variance is introduced:

$$\omega_y^{var}(x,y,z,t,W) \equiv \omega_y^2(x,y,z,t) - \underline{\omega}_y^2(x,y,z,t,W)\ . \tag{7.13}$$

Strong hairpin head events are detected using the following criterion:

$$\mathcal{D}(x,y,z,t) = \begin{cases} 1, & \text{if } \omega_y^{var} > c(\omega_y^{rms})^2, \\ 0, & \text{otherwise.} \end{cases} \tag{7.14}$$

Here the detection function $\mathcal{D}(x,y,z,t)$=1 if the hairpin head exists; ω_y^{rms} is the root-mean-square variation of ω_y at the horizontal plane; and c is the threshold level, which has the value 15 in the present study. In this study, we detect hairpin head events at three horizontal

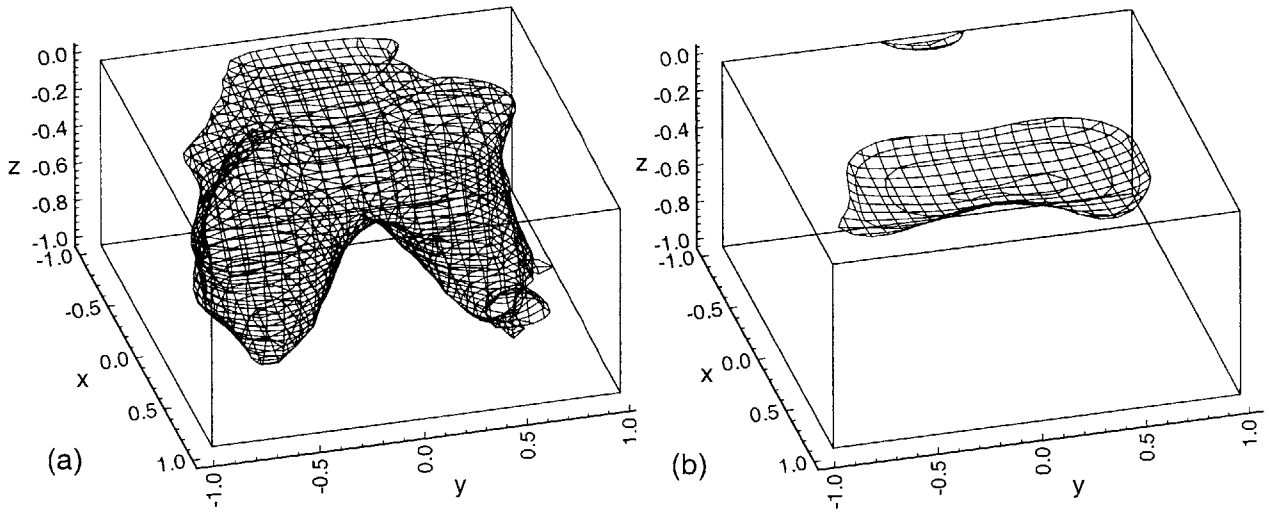

Figure 7-9: Coherent hairpin vortex structure in the conditionally-averaged VISA flow field (z_d=−0.25): (a) region where vorticity magnitude $|\vec{\omega}| \geq 0.2$; and (b) region where SGS dissipation $\tau_{ij}\overline{s}_{ij} \geq 0$ (energy backscatter). The mean flow is in the positive x-direction.

planes at z=z_d=−0.25, −0.125, −0.0625. Increasing z_d corresponds to later phases of the vortex connection process (cf. Shen *et al.* 1999). The three-dimensional flow field associated with each event is then ensemble averaged to yield the VISA field. (Before the averaging, the coordinates are transformed horizontally so that all the events are centered at $(0, 0, z_d)$.) In this study, we use the data from t=40 to 90 from 25 DNS realizations averaging over O(1000) events.

Figure 7-9 shows an example of the resulting VISA flow field. The hairpin heads are detected at z_d=−0.25 and thus the averaged hairpin head is centered at $(0, 0, -0.25)$ in the plots. Figure 7-9(a) shows the isosurface of the vorticity magnitude $|\omega|$. The head portion and the two legs of the hairpin are manifest with the legs inclined with the mean shear flow (cf. Figure 2-1).

One of the major findings in this study is shown in Figure 7-9(b), where the region with energy backscatter is plotted. Comparing Figures 7-9(a) and (b), it is seen that there is a distinct region of backwards energy transfer (positive $\tau_{ij}\overline{s}_{ij}$) downstream of the hairpin structure. The remaining of this sub-section is devoted to elucidating this feature.

Figure 7-10 plots vertical (x,z) sections at the center (y=0) of the VISA hairpin vortex detected at different values of z_d. Due to the induction of the hairpin head (which has negative ω_y component) and the two hairpin legs, the fluid downstream is advected to the free surface ('splats'); while the fluid upstream moves away the free surface ('anti-splats'). The contours of the SGS dissipation in Figure 7-10 show clearly the energy backscatter (positive $\tau_{ij}\bar{s}_{ij}$) region located downstream of the hairpin vortex. As the vortex approaches the free surface (Figures *a* to *c*), the backscatter region extends further downstream. Vertically however, the backscatter is always constrained to a thin region at the free surface. The thickness of this region is about 0.1 and is comparable to the thickness of the surface layer identified in Shen *et al.* (1999, 2000).

The surface characteristics of the VISA field are of immediate interest. Features of these are plotted in Figures 7-11 to 7-13 for hairpin heads detected at z_d=-0.25, -0.125, -0.0625, respectively. The surface contours of the spanwise vorticity, ω_y, (Figures *a*), which is induced by the primary vortex beneath, show that the surface vorticity is positive in the center region (the hairpin head has negative ω_y) and negative at the two sides. From the surface-normal vorticity ω_z (Figures *b*), it is seen that as the hairpin vortex approaches the surface, positive/negative ω_z appears upstream on either sides of the symmetry plane (y=0). These eventually evolve into a pair of counter-rotating surface-connected vortices (Figure 7-13*b*).

Surface contours of SGS dissipation $\tau_{ij}\bar{s}_{ij}$ are plotted in Figure (*c*). The energy backscatter in the downstream region is clearly seen. As the hairpin vortex approaches the surface (increasing z_d), the region of energy backscatter elongates in the streamwise direction and contracts somewhat in the spanwise direction. Figure (*d*) plots contours of the Smagorinsky coefficient C_S obtained by matching the model (7.7) point by point with the DNS-resolved SGS stresses. As expected, $C_S < 0$ in the region of energy backscatter.

According to Shen *et al.* (1999), the inclination angle of the vorticity at the surface, $\alpha \equiv \tan^{-1}(\sqrt{\omega_x^2+\omega_y^2}/|\omega_z|)$, is a good indicator of the temporal phase or 'age' of a surface-connecting hairpin vortex. During the connection, α is large ($\tilde{>}$ 25°), as shown in Figures 7-11 to 7-13 (*e*). After connection, ω_z becomes dominant while ω_x and ω_y are dissipated and

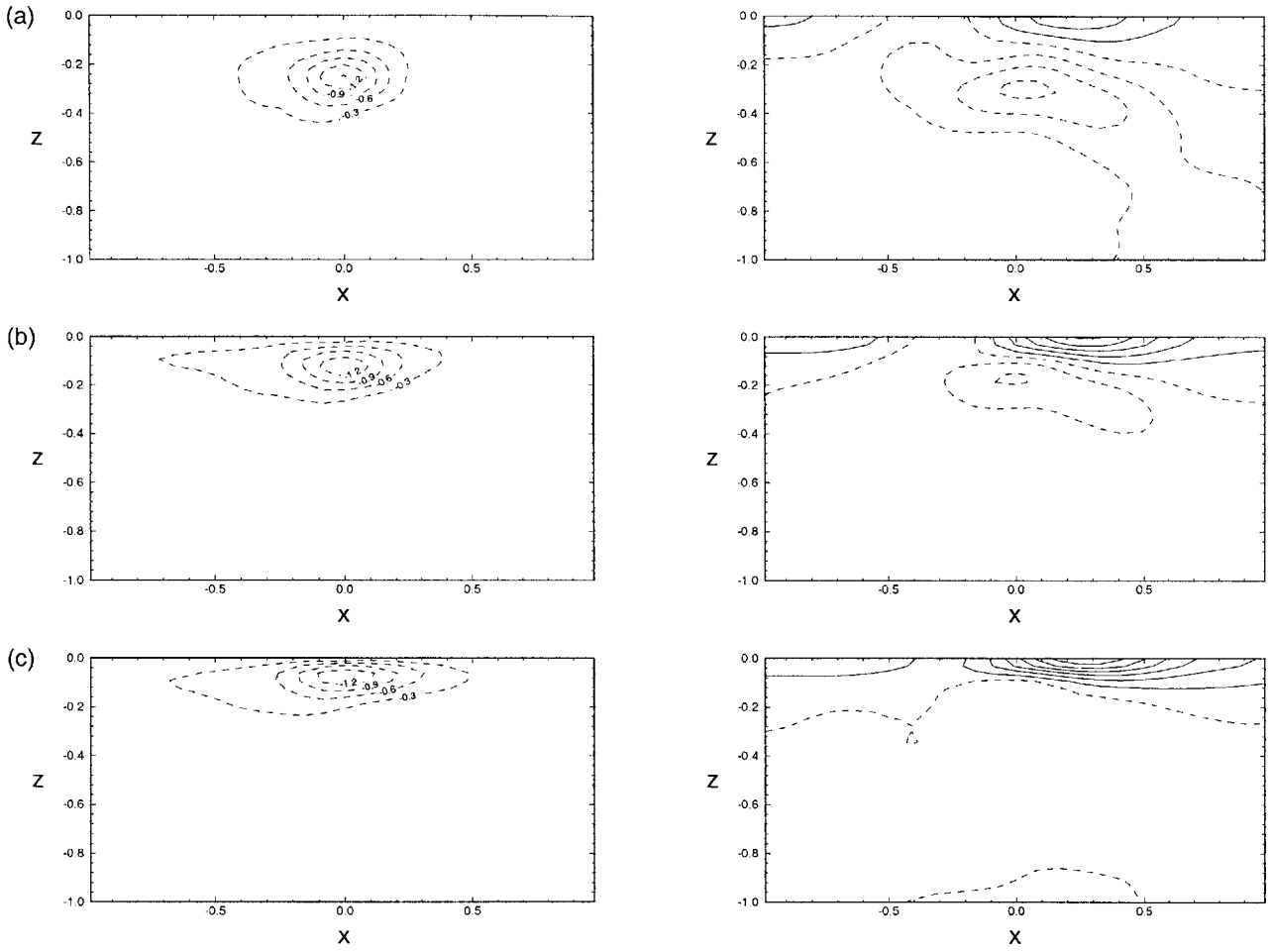

Figure 7-10: Vertical center-plane (y=0) sections of the VISA hairpin structure centered at: (a) z_d=−0.25; (b) z_d=−0.125; and (c) z_d=−0.0625. The left figures plot the contours of ω_y; the right figures plot the contours of $\tau_{ij}\overline{s}_{ij}$ with contours interval 0.0002. Dash lines represent negative values. The mean flow is in the positive x-direction.

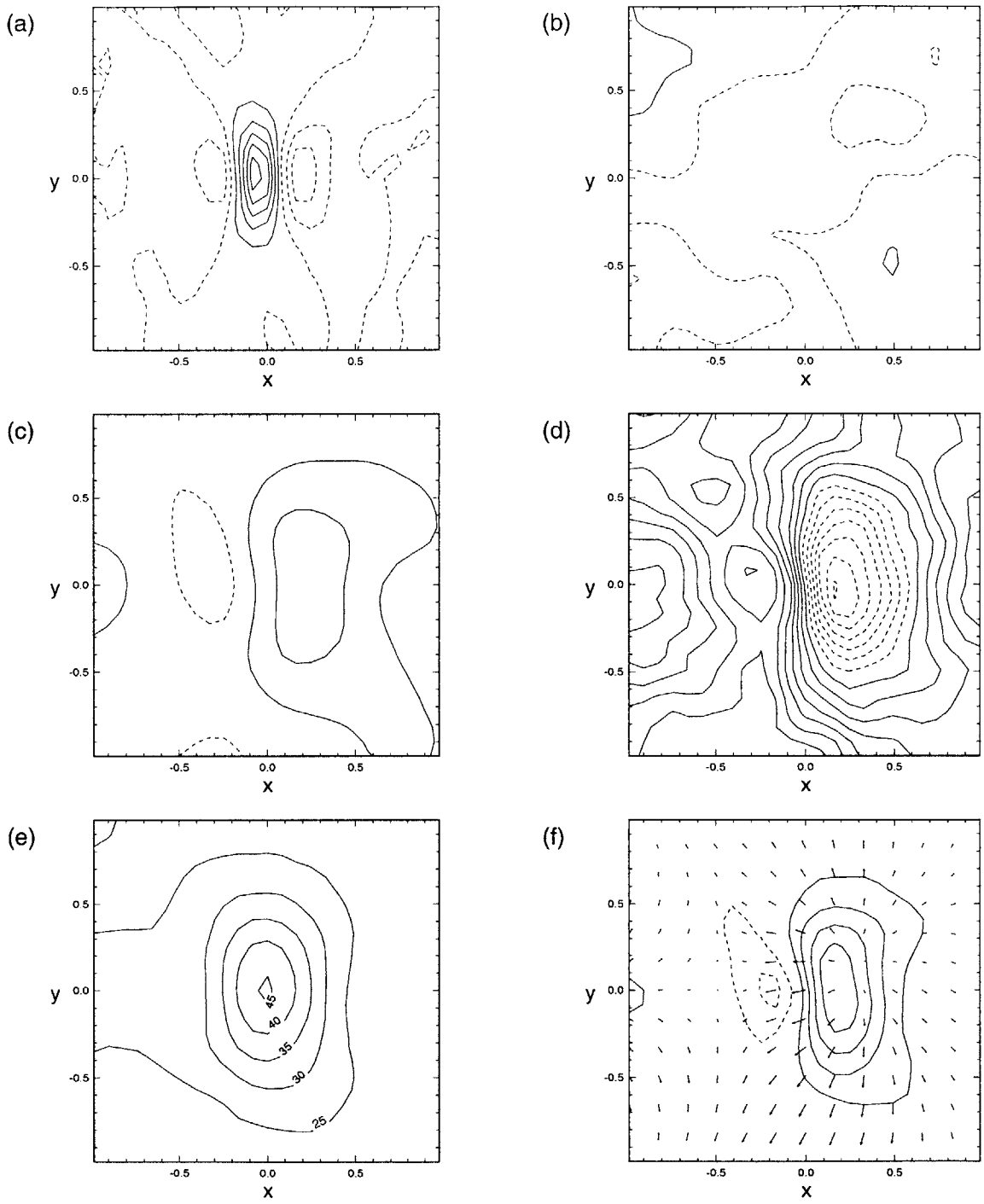

Figure 7-11: VISA surface features above the hairpin vortex which is located at z_d=−0.25: (a) contours of ω_y with contours interval 0.01; (b) contours of ω_z with contours interval 0.05; (c) contours of $\tau_{ij}\overline{s}_{ij}$ with contours interval 0.0002; (d) contours of C_S with contours interval 0.001; (e) contours of α; and (f) contours of $\partial u/\partial x + \partial v/\partial y$ with contours interval 0.05 and the fluctuation velocity vectors $(u - \langle u \rangle, v - \langle v \rangle)$. Dash lines represent negative values.

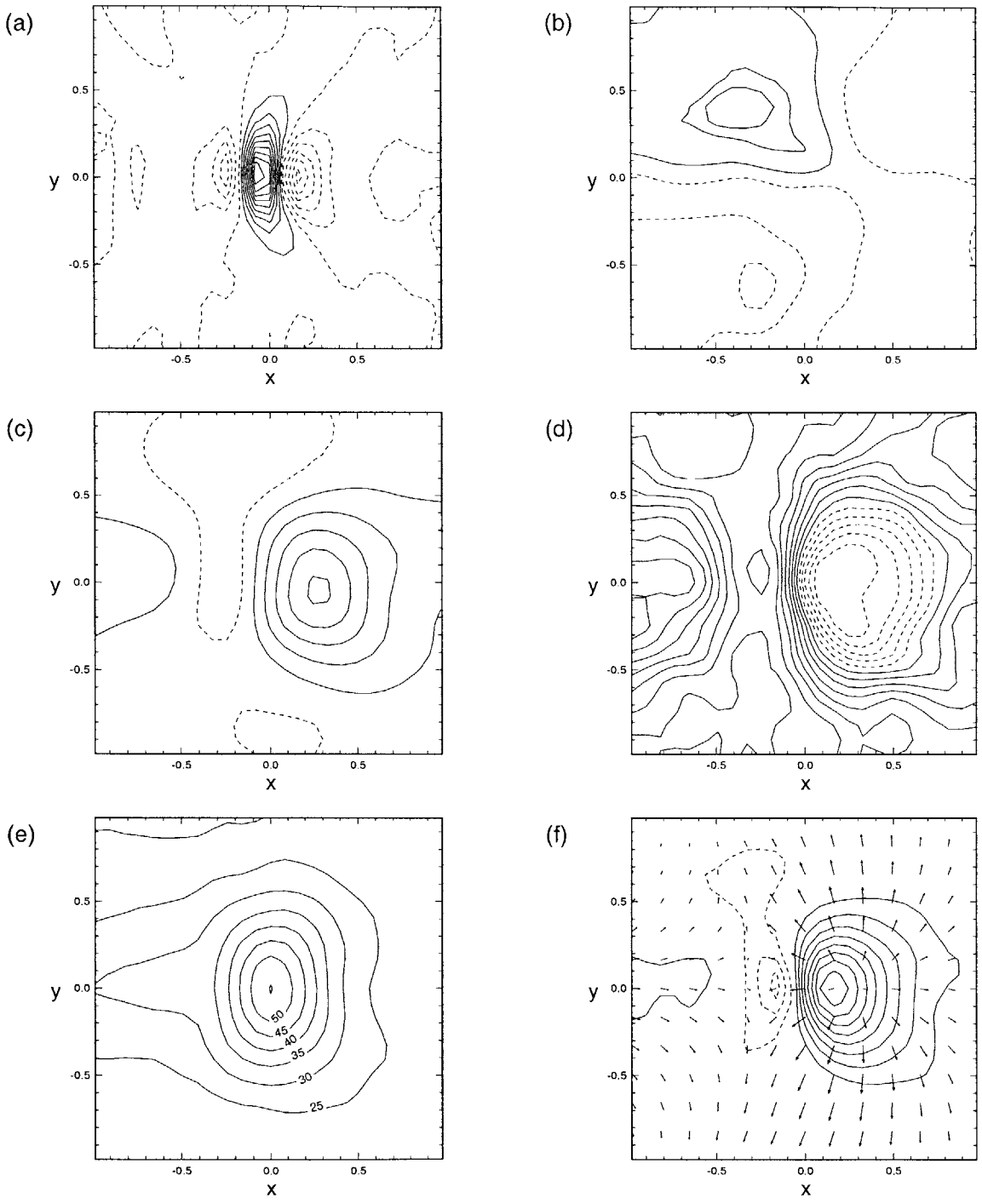

Figure 7-12: VISA surface features above the hairpin vortex which is located at z_d=−0.125. See caption for Figure 7-11.

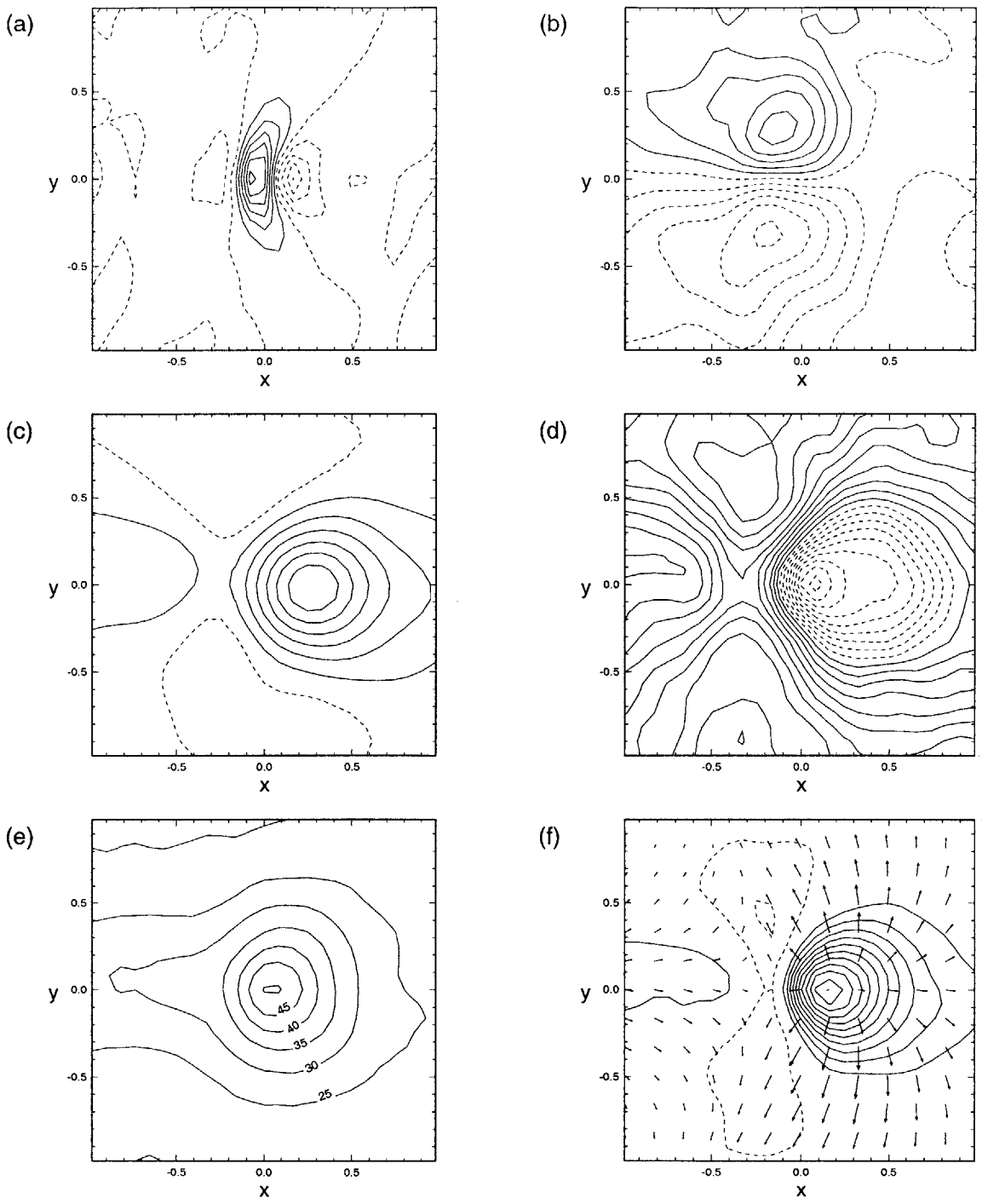

Figure 7-13: VISA surface features above the hairpin vortex which is located at z_d=−0.0625. See caption for Figure 7-11.

α becomes small ($\widetilde{<} 5^\circ$ in the present case). The detailed results for this latter condition are not shown here but were discussed extensively in Shen *et al.* (1999). It was found that surface-connected voticity is persistent and decays at a slow rate (more comparable to laminar condition). This is in agreement with Pan & Banerjee (1995) who observed that the energy cascade magnitude is small at the cores of surface-connected vortices.

Finally, Figure (*f*) plots the horizontal divergence $\partial u/\partial x + \partial v/\partial y = -\partial w/\partial z$ together with the horizontal velocity fluctuation vectors $(u - \langle u \rangle, v - \langle v \rangle)$. These show clearly the regions of splats and antisplats. The downstream splat region, when compared with Figures (*c*) and (*d*), is shown to correlate directly with the region of energy backscatter.

In summary, conditional averaging shows that energy backscatter at the free surface occurs at the downstream splat region of coherent hairpin structures approaching the surface. This region is also characterized by large vortex inclination angles (relative to the vertical) and positive horizontal velocity divergence $\partial u/\partial x + \partial v/\partial y$. The physics revealed herein is used directly in our later development of SGS stress models for free-surface turbulence in §4.

7.4 Anisotropy in the surface layer

In some sense, a necessary difference between isotropic turbulence and free-surface turbulence is anisotropy of the latter due to the imposition of kinematic and dynamic boundary conditions at the free surface (cf. e.g. Shen *et al.* 1999). Figure 7-14 plots the vertical profiles of the velocity and vorticity components in the four wavenumber bands I, II, III and A. The anisotropy in the velocity is a direct consequence of the kinematic free-surface condition which renders w much smaller than u and v near the free surface. The anisotropy in the velocity gradients is caused by the vanishing tangential-stress free-surface boundary conditions which results in horizontal vorticity components ω_x and ω_y much smaller than the vertical component ω_z. Comparing the results for the different wavenumber bands, it is significant that the free-surface anisotropy obtains qualitatively undiminished for different eddy wavenumbers. Thus, anisotropy is an essential feature that must be accounted for by free-surface turbulence SGS models.

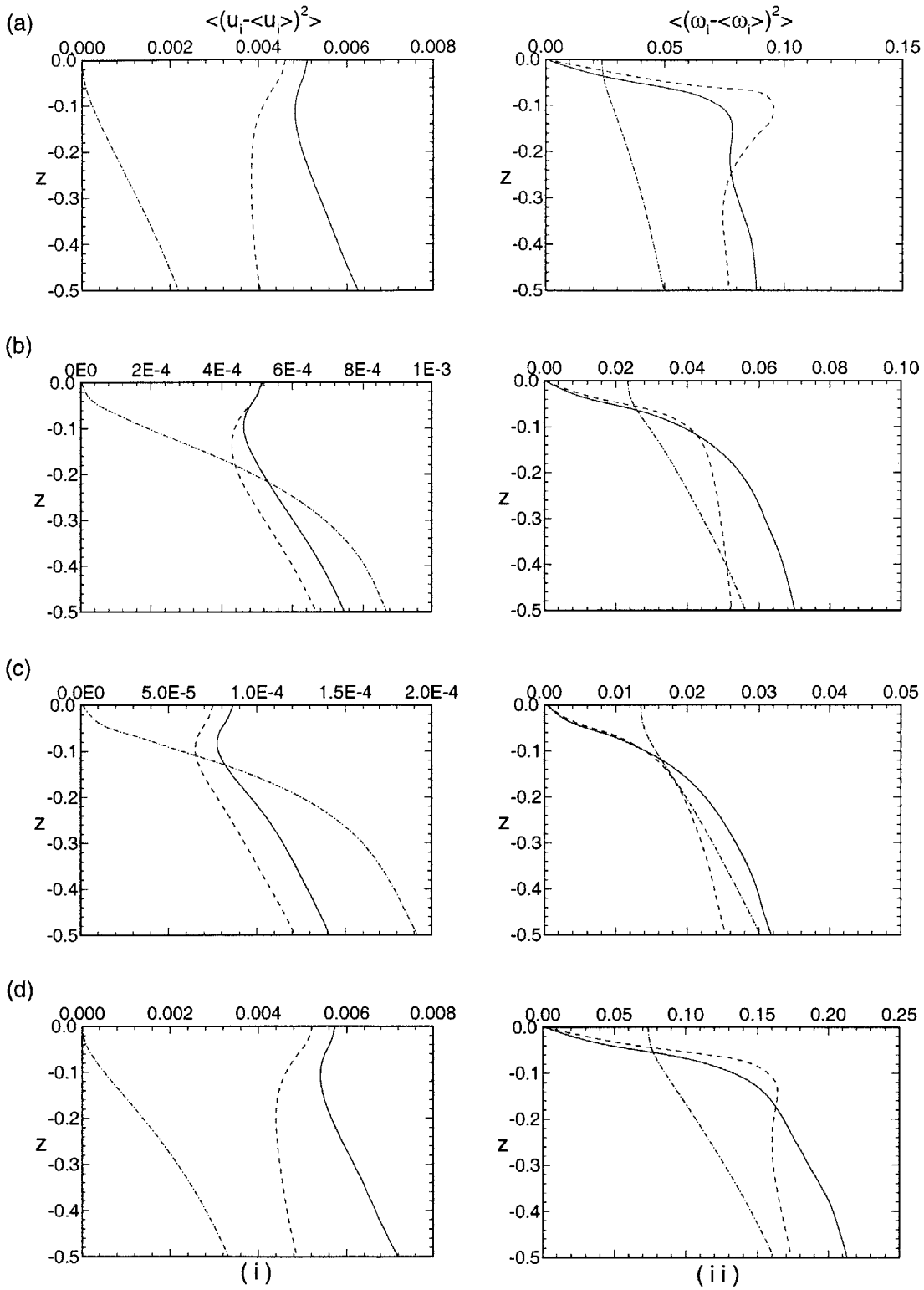

Figure 7-14: Vertical profiles of the turbulence fluctuation of (i) velocity and (ii) vorticity x- (————), y- (– – – –) and z-components (– · – · –); in wavenumber bands: $k \in$ (a) I; (b) II; (c) III and (d) A. t=60.

Figure 7-14 also reveals the vertical extents of the free-surface anisotropy regions as eddy wavenumber increases. To examine this further, we compare the normalized (by values in the bulk) vertical profiles for different wavenumber bands. Figure 7-15 plots typical results for w and ω_x. As a measure of the respective surface layer thickness, the point at which maximum (negative) curvature occurs on each profile is also indicated. For the velocity, the thickness generally decreases with increasing k as expected from physical reasoning. For ω_x (a similar result obtains for ω_y), there is little variation of the anistropy thickness with wavenumber, and the overall thickness is smaller than those for the velocity components as consistent with the respective inner versus outer (blockage) layer effects they manifest.

The double-layer structure near the free surface is elucidated by considering the vertical variation of the (horizontally averaged) turbulence diffusivity. This is in Shen *et al.* (2000) where it is found that the surface layer is characterized by a rapid reduction of the turbulence diffusivity. This behavior is well fitted by a Guassian profile and can be modeled by an analytical similarity solution for the mean flow. Of special relevance here is the fact that the outer and inner layer structure of the free-surface boundary layer can be quantified in terms of the mean flow profile. In particular, the outer and inner thicknesses are given by the local minimum and then the local maximum of the shear profile as the surface is approached (cf. Figure 4-3).

We now examine the extent of anisotropy in the SGS stress. Figure 7-16 plots the depth variation of the rms values of the (trace-free) SGS stress and the (grid-scale) strain rate components. As expected, there is significant anisotropy near the free surface: for both the SGS stress and strain rate, the 'horizontal' components ij=11, 12, 22, 33 increase towards the free surface, while the 'vertical' components ij=13, 23 decrease. Note that ij=33 is also a 'horizontal' component because w and thus $\tau_{33} \equiv \overline{ww} - \overline{w}\,\overline{w}$ is small near the free surface, so that $\tau_{33} - \tau_{kk}/3$ contains mainly contribution from τ_{11} and τ_{22}. We notice, however, that the extents over which the anisotropic variations occur are quite different for the stress versus the strain rate. The reason is that the anisotropy in the SGS stress is a direct result of the kinematic constraint on the vertical motion, while that in the strain is due to the dynamic condition of vanishing tangential stresses. Consequently, the SGS stress varies within a

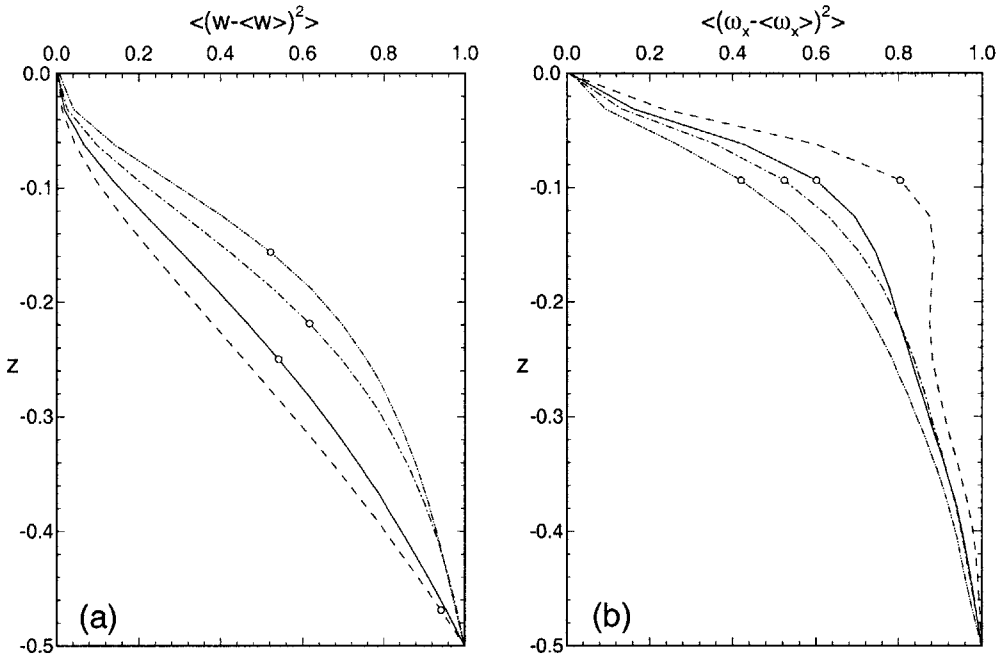

Figure 7-15: Normalized vertical profiles of the turbulence fluctuation: (a) vertical velocity w; and (b) streamwise vorticity ω_x; in wavenumber bands: $k \in$ I (– – – –); II (– · – · –); III (– ·· – ·· –) and A (————). t=60. The profiles are normalized by the bulk values. The point of maximum (negative) curvature on each curve is indicated by ○.

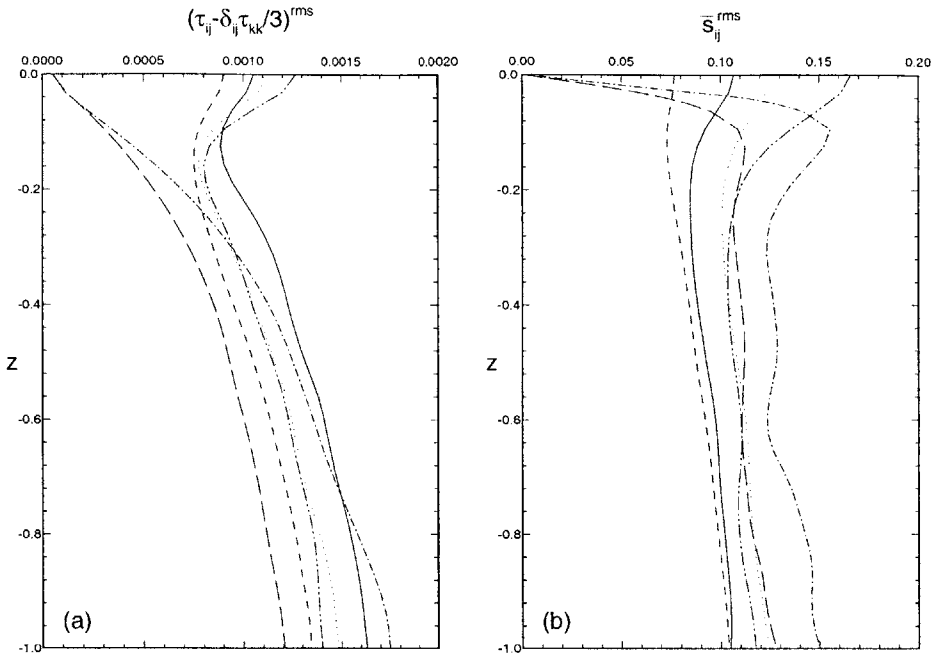

Figure 7-16: Vertical variation of the magnitudes of the different components of (a) trace-free SGS stress $(\tau_{ij} - \delta_{ij}\tau_{kk}/3)^{rms}$ and (b) strain rate $\bar{s}_{ij}^{rms}$. ———— , ij =11; - - - - , ij =12; - · - · - , ij =13; · · · · · · · , ij =22; —— —— , ij =23; —··—··— , ij =33. t=60.

'blockage' layer which is much thicker than the 'inner' layer over which the strain rate varies (cf. Shen *et al.* 1999).

A useful measure of the correlation between the SGS stress and strain rate is to consider *a priori* tests of a standard eddy-viscosity SGS (Smagorinsky) model (7.7). If we assume the Smagorinsky coefficient C_S to be constant horizontally but a function of depth, C_S can be determined *a priori* as in Figure 7-3. The goodness of fit of this model is measured by the correlation coefficient between the trace-free SGS stress and the SGS model:

$$Cor(z,t) \equiv \frac{< (\tau_{ij} - \delta_{ij}\tau_{kk}/3 - < \tau_{ij} - \delta_{ij}\tau_{kk}/3 >)(M_{ij} - < M_{ij} >) >}{(\tau_{ij} - \delta_{ij}\tau_{kk}/3 - < \tau_{ij} - \delta_{ij}\tau_{kk}/3 >)^{rms}(M_{ij} - < M_{ij} >)^{rms}} . \qquad (7.15)$$

This is plotted in Figure 7-17 (the model is labeled as 'DSM'). In the bulk flow, the correlation coefficient is about 0.2. This is in agreement with previous studies on other types of turbulent flows (see e.g. Clark *et al.* 1979, McMillan *et al.* 1980; Liu, Meneveau & Katz 1994). The reason for the low correlation between the actual SGS stress and the Smagorinsky model is

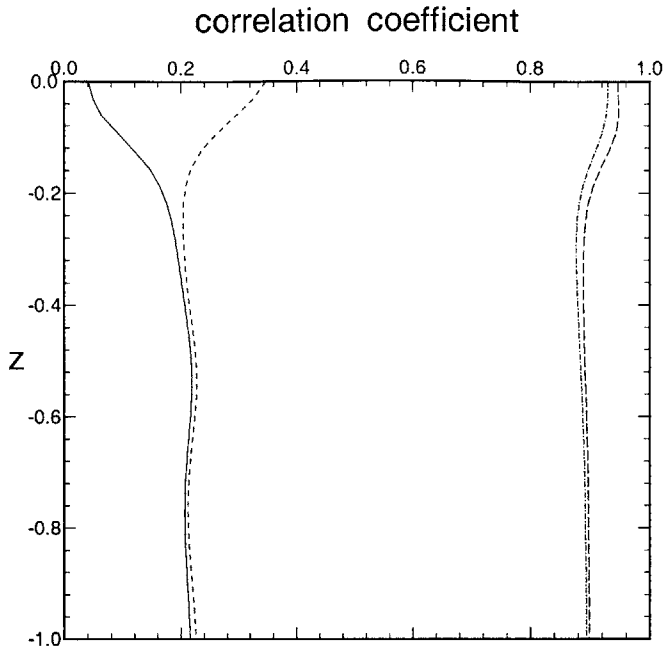

Figure 7-17: Correlation coefficient (7.15) between the trace-free SGS stress $\tau_{ij} - \delta_{ij}\tau_{kk}/3$ and: ———— , dynamic Smagorinsky model (DSM); - - - - , dynamic anisotropic selective model (DASM); – · – · – , DSM combined with a scale-similarity model (DSM+B); —— —— , DASM combined with a scale-similarity model (DASM+B). t=60.

that their principle axes are not aligned. Near a free surface, the correlation drops even lower. Clearly, a dynamic Smagorinsky model is not an effective model for free-surface turbulence.

7.5 Conclusions

In this paper we study the inter-scale energy cascade in a turbulent shear flow with a free surface. A detailed analysis of the DNS data reveals that:

- As the free surface is approached, the energy transfered from the large scales to small scales decreases significantly. This reduction in the energy cascade is caused by the increasing of the energy backscatter associated with the fluid vertical motions near the free surface.

- The inverse energy transfer is stongly correlated with the coherent pairpin vortex structures, which are characteristic of free-surface shear flows. Conditional sampling shows

that the backscatter occurs at the splat region as a pairpin vortex connects to the free surface.

- The flow field near the free surface is highly anisotropic. This anisotropy prevails throughout all the lengh scales and results in different behaviors in each component of SGS stress.

It is important for the large-eddy simulation of free-surface turbulence to utilize and capture the above physics. The reduction in the SGS disspiation near the free surface requires the corresponding decreasing in the coefficient of eddy-viscosity type of SGS models. The backscatter associated with the coherent vortex structures also indicates the sign change in the model coefficient. Furthermore, the anisotropy near the free surface suggests different treatments for the different components of SGS stress. These insights lead us to the development of new SGS models for the LES of free-surface turbulence, which are proven to be superior to existing SGS models, as shown in Chapter 8.

Chapter 8

Subgrid-Scale Modeling and Large-Eddy Simulation for Free-Surface Turbulence

Large-eddy simulation (LES) only computes the large scales (grid scales, GS) motions while the contributions from small scales (subgrid scales, SGS) are modeled. Since the small scales tend to be more isotropic and more universal, it is expected that the SGS modeling is simpler and thus more promising than other approaches like the Reynolds-averaging modeling.

Obviously, the key to the success of LES lies in the accuracy of the SGS modeling. Despite the fundamental importance of the SGS modeling and the efforts devoted to its development over the past several decades, people have not found yet a universal SGS model which can be applied to all the different types of flows without any empirical adjustment. The most widely used model is the Smagorinsky model (Smagorinsky 1963). Although the principle axes of the model tensor are not aligned with those of the real SGS stress and thus the correlation between the model and the SGS stress is rather poor, the Smagorinsky model predicts the overall dissipation rate accurately and has been used successfully.

One disadvantage of the Smagorinsky model is the inability to set a universal model coefficient for all the flows. For example, it has been found that the Smagorinsky model always over dissipates near solid walls or in transitional regimes. This drawback was largely

fixed by the dynamic procedure developed by Germano *et al.* (1991). The idea is to allow for spatial and temporal variability of the model coefficient, through the extrapolation at two filter levels by using an algebraic identity. Because strong fluctuations in the model coefficient have been found in the model implementation, averaging over direction of flow homogeneity is often used. This dynamic Smagorinsky model, hereafter designated as DSM, has been shown to yield results remarkably better than the constant-coefficient Smagorinsky model. Ghosal *et al.* (1995) further corrected a mathematical inconsistence in the DSM and proposed a dynamic localization model.

The low correlation between the Smagorinsky model and the SGS stress can be remedied by the combination with a scalar-similarity model, which was first developed by Bardina, Ferziger & Reynolds (1983) based on the idea that the grid/subgrid interactions involve mainly the smallest resolved scales and the largest subgrid scales. Zang, Street & Koseff (1993) used a dynamic mixed model (DMM), which is a linear combination of the scale-similarity model and the Smagorinsky model with the coefficient of the former fixed and the coefficient of the latter dynamically determined. They applied DMM to a lid-driven recirculating flow and found that not only the correlation between the model and the SGS stress is largely improved, the magnitude of the Smagorinsky coefficient is also reduced significantly, a desirable feature to avoid numerical instability. Salvetti & Banerjee (1995) and Salvetti *et al.* (1997) further developed a dynamic two-parameter model (DTM) in which both of the two model coefficients are determined dynamically. They tested the DTM with a decaying turbulent flow beneath a flat free surface and obtained satisfying results.

In this chapter we study the SGS modeling for the LES of free-surface turbulence at finite Froude numbers. From the preceding Chapter 7, it is shown that the SGS models for free-surface turbulence should recognize the reduction of energy cascade near the free surface, which is associated with the energy backscatter caused by the fluid vertical motion. More specifically, the inverse energy transfer is due to the splat motion associated with the connection of coherent hairpin vortex structures to the free surface. In this chapter, we apply this knowledge to the successful SGS modeling for the LES of free-surface turbulence. We first model the subgrid-scale contributions appearing in the free-surface kinematic and

dynamic boundary conditions in §8.1. The models for the SGS stress are then developed and evaluated in §8.2. Based on the physics of FST, we propose two new models for the SGS stress, a dynamic free-surface function model (DFFM) and a dynamic anisotropic selective model (DASM). These new models are evaluated in detail and are shown to be superior to existing models. Finally, we combine the new DFFM and DASM with a dynamic scale-similarity model to further improve the performance. In §8.3 we present our conclusions.

8.1 Modeling of SGS contributions in the free-surface boundary conditions

Large-eddy simulation models the subgrid-scale stress resulting from the nonlinear convective term $\tau_{ij}=\overline{u_i u_j} - \overline{u}_i\ \overline{u}_j$. As shown in Chapter 2, for flows with a free surface however, additional modeling for the subgrid-scale contributions to the free-surface boundary conditions is required. In this section we discuss the formulation for the modeling of the SGS energy in the Dirichlet dynamic condition for the pressure (§8.1.1) and the SGS flux in the kinematic boundary condition (§8.1.2), as well as the performance of the models (§8.1.3). After the numerical capability for the free-surface modeling is established, we investigate the modeling for the SGS stress τ_{ij} in §8.2.

8.1.1 SGS Modeling for the dynamic free-surface pressure

As shown in §2.2, usually it is the trace-free portion of the SGS stress $\tau_{ij} - \delta_{ij}\tau_{kk}/3$ that is modeled. The isotropic part is absorbed into the dynamic pressure $\overline{p}$ and, what appears in the governing equations is a modified pressure $\overline{P} = \overline{p} + \tau_{kk}/3$. For certain problems (e.g. incompressible flows with Neumann's boundary conditions for the pressure), $\overline{P}$ can be solved as a whole. However, in the free-surface problem where a Dirichlet condition is prescribed for the dynamic pressure $\overline{p}$ at the surface, the value of the SGS contribution $\tau_{kk}/3$ at z=0 must be known before the modified pressure $\overline{P}$ can be solved.

In this study, we model p_{SGS} by the Yoshizawa (1986)'s expression:

$$\frac{\tau_{kk}}{3} = 2C_p\overline{\Delta}^2|\overline{s}|^2 \,. \tag{8.1}$$

Here $|\overline{s}| \equiv (2\overline{s}_{ij}\overline{s}_{ij})^{1/2}$ and $\overline{s}_{ij} \equiv (\partial\overline{u}_i/\partial x_j + \partial\overline{u}_j/\partial x_i)/2$. In a dynamic scheme, the coefficient C_p can be determined through the procedure developed by Moin *et al.* (1991) based on the Germano identity (Germano *et al.* 1991). To do this, we introduce a test filter $\widehat{G}$ in addition to the grid filter $\overline{G}$ and, let $\widehat{\overline{G}} = \widehat{G}\overline{G}$. Applying $\widehat{\overline{G}}$ to the Navier–Stokes equations, we obtain the subgrid-scale stress at the coarse filter level:

$$T_{ij} = \widehat{\overline{u_i}\overline{u_j}} - \widehat{\overline{u}}_i\widehat{\overline{u}}_j \,, \quad i,j = 1,2,3 \,. \tag{8.2}$$

The Germano identity gives the algebraic relation

$$\mathcal{L}_{ij} = \widehat{\overline{u}_i\,\overline{u}_j} - \widehat{\overline{u}}_i\widehat{\overline{u}}_j = T_{ij} - \widehat{\tau_{ij}} \,, \tag{8.3}$$

where $\mathcal{L}_{ij}$ is a function of $\overline{u}_i$ and is computable from the resolved variables.

Assuming that the same Yoshizawa expression can be applied to $T_{kk}/3$ with the same coefficient C_p:

$$\frac{T_{kk}}{3} = 2C_p\widehat{\overline{\Delta}}^2|\widehat{\overline{s}}|^2 \,, \tag{8.4}$$

we obtain

$$\frac{\mathcal{L}_{kk}}{3} = 2C_p\widehat{\overline{\Delta}}^2|\widehat{\overline{s}}|^2 - 2\widehat{C_p\overline{\Delta}^2|\overline{s}|^2} \,. \tag{8.5}$$

Simplification can be obtained if the coefficient C_p in (8.5) can be extracted from the filter operation in the last term. In general, this cannot be done directly (cf. Ghosal *et al.* 1995). For simplicity, we assume that C_p is constant on the horizontal plane and let the test filter $\widehat{G}$ operate in the horizontal directions only. Equation (8.5) then becomes:

$$\frac{\mathcal{L}_{kk}}{3} = C_p(2\widehat{\overline{\Delta}}^2|\widehat{\overline{s}}|^2 - 2\overline{\Delta}^2\widehat{|\overline{s}|^2}) \,. \tag{8.6}$$

The coefficient C_p can be obtained by least-square to best match the two sides of (8.6) on

the free surface:

$$C_p = \frac{\langle m_I \mathcal{L}_{kk}/3 \rangle}{\langle m_I^2 \rangle} , \qquad \text{on } z = 0 , \tag{8.7}$$

where $m_I = 2\widehat{\overline{\Delta}}^2 |\widehat{\overline{s}}|^2 - 2\overline{\Delta}^2 |\widehat{\overline{s}}|^2$ and $\langle\ \rangle$ denotes the horizontal plane averaging.

8.1.2 Modeling of the free-surface SGS flux

The subgrid-scale flux appearing in the kinematic free-surface boundary condition (equations 2.32 and 2.33) is modeled by a scale-similarity model:

$$\begin{aligned} \tau_u^{kbc} &\equiv \overline{uh} - \overline{u}\,\overline{h} = C_{kbc}(\overline{\overline{u}\,\overline{h}} - \overline{\overline{u}}\,\overline{\overline{h}}) , \\ \tau_v^{kbc} &\equiv \overline{vh} - \overline{v}\,\overline{h} = C_{kbc}(\overline{\overline{v}\,\overline{h}} - \overline{\overline{v}}\,\overline{\overline{h}}) . \end{aligned} \tag{8.8}$$

The coefficient, C_{kbc}, above can again be determined dynamically as follows.

At the coarse filter level $\widehat{\overline{G}}$, the SGS flux is written as

$$\begin{aligned} T_u^{kbc} &\equiv \widehat{\overline{uh}} - \widehat{\overline{u}}\,\widehat{\overline{h}} = C_{kbc}(\widehat{\overline{\overline{u}\,\overline{h}}} - \widehat{\overline{\overline{u}}}\,\widehat{\overline{\overline{h}}}) , \\ T_v^{kbc} &\equiv \widehat{\overline{vh}} - \widehat{\overline{v}}\,\widehat{\overline{h}} = C_{kbc}(\widehat{\overline{\overline{v}\,\overline{h}}} - \widehat{\overline{\overline{v}}}\,\widehat{\overline{\overline{h}}}) . \end{aligned} \tag{8.9}$$

An algebraic identity similar to (8.3) gives:

$$\begin{aligned} \mathcal{L}_u^{kbc} &= \widehat{\overline{uh}} - \widehat{\overline{u}}\,\widehat{\overline{h}} = T_u^{kbc} - \widehat{\tau_u^{kbc}} = C_{kbc}(\widehat{\overline{\overline{u}\,\overline{h}}} - \widehat{\overline{\overline{u}}}\,\widehat{\overline{\overline{h}}}) , \\ \mathcal{L}_v^{kbc} &= \widehat{\overline{vh}} - \widehat{\overline{v}}\,\widehat{\overline{h}} = T_v^{kbc} - \widehat{\tau_v^{kbc}} = C_{kbc}(\widehat{\overline{\overline{v}\,\overline{h}}} - \widehat{\overline{\overline{v}}}\,\widehat{\overline{\overline{h}}}) . \end{aligned} \tag{8.10}$$

Here C_{kbc} is assumed to be constant on the free surface and is solved by least-square matching of (8.10) to give:

$$C_{kbc} = \frac{\langle \mathcal{L}_u^{kbc} m_u + \mathcal{L}_v^{kbc} m_v \rangle}{\langle m_u^2 + m_v^2 \rangle} , \qquad \text{on } z = 0 , \tag{8.11}$$

where $m_u = \widehat{\overline{\overline{u}\,\overline{h}}} - \widehat{\overline{\overline{u}}}\,\widehat{\overline{\overline{h}}}$ and $m_v = \widehat{\overline{\overline{v}\,\overline{h}}} - \widehat{\overline{\overline{v}}}\,\widehat{\overline{\overline{h}}}$.

8.1.3 Evaluation of SGS models for free-surface flux and dynamic pressure

In this study, the benchmark data is obtained from DNS of the free-surface shear flow on a fine 128^2 (horizontally) $\times$ 192 (vertically) grid with timestep 0.005. To obtain smooth statistics, a set of 25 DNS datasets (with different initial seeds) are obtained. For LES we use a coarse $32^2 \times 96$ grid with timestep 0.02. We start the LES with the filtered DNS field at t=60, and run the simulation for 10 time units, which is sufficient for the free-surface turbulence features (e.g. the surface-connecting vortices) to evolve significantly. A total of 25 LES runs corresponding to the DNS are also performed. The LES results are then compared with the filtered DNS data at t=70.

Figure 8-1 shows the *a priori* performances of the scale-similar SGS model (8.8) for the free-surface flux, and the Yoshizawa SGS model (8.1) for the free-surface dynamic pressure p_{SGS} in (2.31). The overall performance in terms of the correlation:

$$Cor < \tau, M > \equiv \frac{< (\tau - < \tau >)(M - < M >) >}{(\tau - < \tau >)^{rms}(M - < M >)^{rms}}. \tag{8.12}$$

is excellent ($\sim$0.9) for the SGS flux, and acceptable ($\sim$0.7) for the free-surface dynamic pressure. (Note that the mean value is subtracted from (8.12). If the mean value is not subtracted, the correlation coefficient for the p_{SGS} is close to 0.8.)

The efficacy of the modeling of the SGS free-surface terms τ_u^{kbc}, τ_v^{kbc} and p_{SGS} is demonstrated in *a posteriori* tests. Figure 8-2 compares the free-surface elevation and horizontal surface vorticity $\omega_s \equiv (\omega_x^2 + \omega_y^2)^{1/2}|_{z=0}$ between the LES and DNS results. For LES without SGS, the results depart from the DNS values and grow in time in a non-physical manner. Comparing the LES results (with DSM for the SGS stress) with and without SGS models for $\tau_{u,v}^{kbc}$ and p_{SGS}, the improvement with the latter is quite appreciable. Of the two, our results (not shown in Figure 8-2) show that the modeling of p_{SGS} accounts for about 70% of the total observed improvement.

Figure 8-3 plots the dynamic model coefficient values for C_{kbc} in (8.8) and C_p in (8.1) obtained in the DSM results of Figure 8-2. The coefficient C_{kbc} for the scale-similarity model

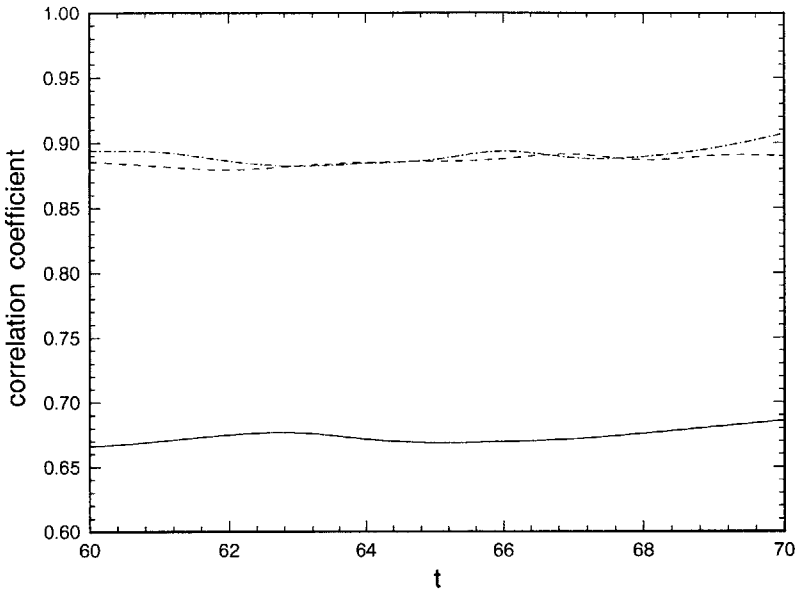

Figure 8-1: Correlation coefficients from *a priori* tests of SGS models for free-surface dynamic pressure p_{SGS} (————), and free-surface flux terms: τ_u^{kbc} (– – – –) and τ_v^{kbc} (– · – · –).

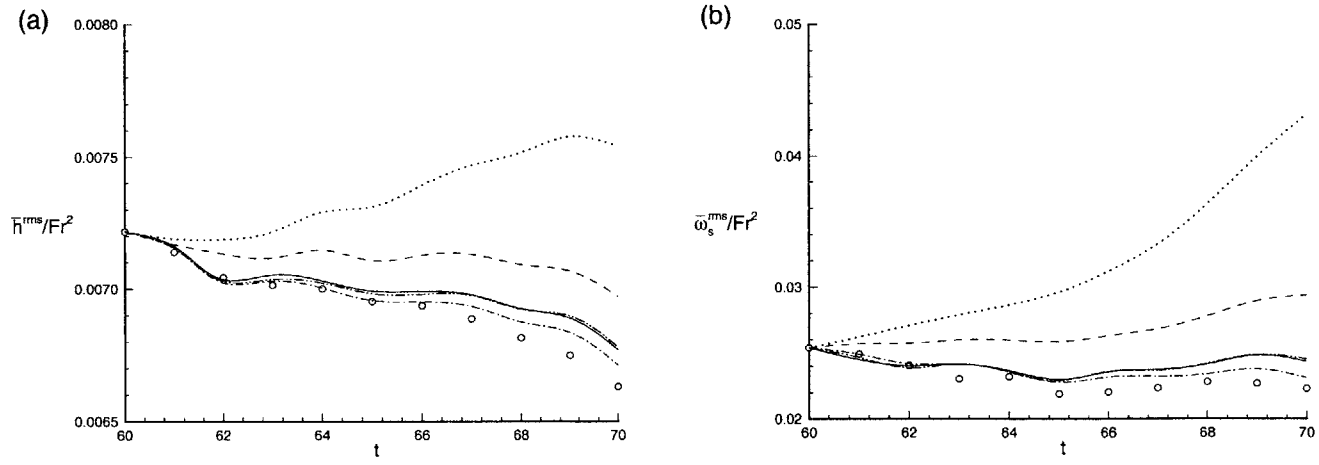

Figure 8-2: Time evolutions of (a) the free-surface elevation $\overline{h}^{rms}/Fr^2$, and (b) the horizontal surface-vorticity magnitude $\overline{\omega_s}^{rms}/Fr^2$ obtained using: ○, DNS; · · · · · · · , LES with no SGS model; – – – – , DSM without SGS models for free-surface flux and dynamic pressure; and with SGS models for free-surface flux and dynamic pressure: ———— , DSM; – · – · – , DFFM; and —··—··— , DASM.

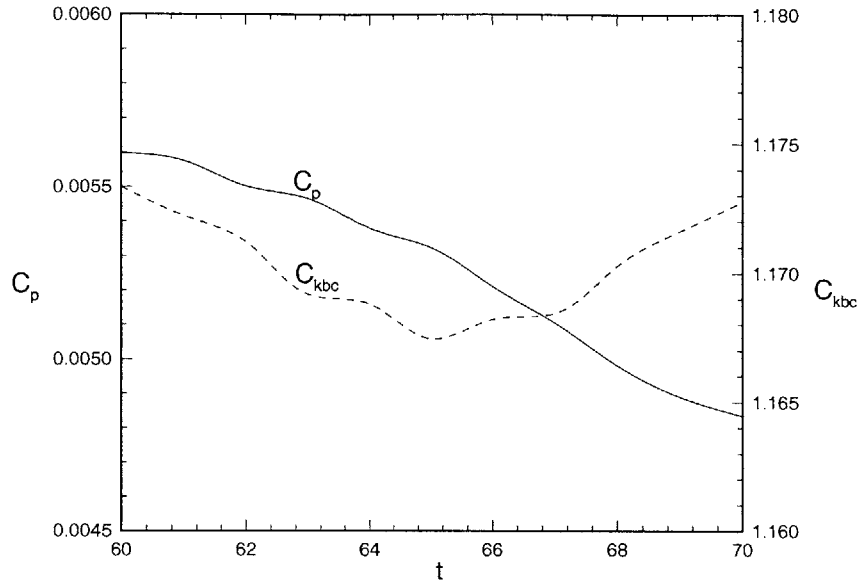

Figure 8-3: Time variations of the coefficients of the SGS models for the free-surface pressure p_{SGS}, C_p (————); and free-surface flux $\tau_{u,v}^{kbc}$, C_{kbc} (– – – –).

has the value around 1.17 which is close to the coefficient value of the scale-similarity model for the SGS stress (see Figure 8-17). The coefficient C_p in the Yoshizawa expression varies from 0.0056 to 0.0047, which is larger than the Smagorinsky coefficient near the free surface (cf. Figure 8-6).

For non-vanishing Froude numbers, it is clear that the modeling of the free-surface SGS terms p_{SGS} and $\tau_{u,v}^{kbc}$ is essential. In all subsequent LES results, the SGS models for these terms (8.1) and (8.8) are always used. We note that the need for SGS modeling in the kinematic boundary condition was also pointed out (but not implemented) by Hodges & Street (1999). The modeling of the SGS contribution to the dynamic pressure at the free surface appears to be new in the present context.

8.2 Development of LES for free-surface turbulence

We study here the modeling of the subgrid-scale stress for the large-eddy simulation of free-surface turbulence. From the analysis of DNS data in Chapter 7, we have obtained the

important physical insights to the SGS modeling for free-surface turbulence, which can be summarized as follows: (i) The energy cascade from the grid scales to the subgrid scales decreases significantly as the free surface is approached. As a result, the coefficient of the Smagorinsky model should also decrease towards the surface. (ii) The inter-scale energy transfer is strongly correlated with the coherent hairpin vortex structures. Energy backscatter occurs at the splat region during the connection of a hairpin vortex to the free surface. (iii) The SGS stress components are highly anisotropic. At the splat region, only the horizontal components of the SGS stress react to the backscattering. (iv) The correlation between the eddy-viscosity type SGS models and the real SGS stress is rather low near the surface. Armed with these physical observations, we now proceed to the development of effective SGS modeling and LES of free-surface turbulence.

In the following, a number of new SGS stress models for free-surface turbulence are introduced and compared with more standard approaches. The relative merits of these models tested against DNS dataset are then presented and discussed.

8.2.1 SGS stress models for free-surface turbulence

In general, the SGS stress (2.24) can be modeled with or without splitting it into separate components, for example, the Leonard stress, cross stress and 'true' SGS stress; or the modified definitions suggested by Germano (1986). In this work, we adopt the approach where the SGS stress is treated as a whole (cf. Lesieur & Métais 1996). All the models we present satisfy Galilean invariance (cf. Speziale 1985).

The base model we use here is the plane-averaged dynamic Smagorinsky model (DSM), which we use to compare against two new SGS models — a dynamic anisotropic selective model (DASM), which captures the dependence of energy backscatter on the coherent vortex structure and the anisotropy nature of free-surface turbulence; and a dynamic free-surface function model (DFFM), which directly accounts for the variation of the eddy viscosity in the surface layer.

Dynamic Smagorinsky model (DSM)

We consider the dynamic formulation of the Smagorinsky model (7.7) following the procedure of Germano *et al.* (1991) with the modification of Lilly (1992). At the coarse filter $\widehat{\overline{G}}$ level, the Smagorinsky model is written as:

$$T_{ij} - \frac{\delta_{ij} T_{kk}}{3} = -2C_S \widehat{\overline{\Delta}}^2 |\widehat{\overline{s}}|^2 \widehat{\overline{s}}_{ij} \ . \tag{8.13}$$

The Germano identity states that

$$\mathcal{L}_{ij} - \frac{\delta_{ij}\mathcal{L}_{kk}}{3} = T_{ij} - \widehat{\tau_{ij}} - \frac{\delta_{ij}(T_{kk} - \widehat{\tau_{kk}})}{3} = -2C_S \widehat{\overline{\Delta}}^2 |\widehat{\overline{s}}|^2 \widehat{\overline{s}}_{ij} + (2C_S \widehat{\overline{\Delta}^2 |\overline{s}|^2 \overline{s}_{ij}}) \ . \tag{8.14}$$

Assuming that C_S is constant over the horizontal plane and applying the test filter $\widehat{G}$ in the horizontal directions only, (8.14) reduces to:

$$\mathcal{L}_{ij} - \frac{\delta_{ij}\mathcal{L}_{kk}}{3} = C_S(2\overline{\Delta}^2 \widehat{|\overline{s}|^2 \overline{s}_{ij}} - 2\widehat{\overline{\Delta}}^2 |\widehat{\overline{s}}|^2 \widehat{\overline{s}}_{ij}) \ . \tag{8.15}$$

The coefficient C_S is chosen to best match the above equation on the horizontal plane using a least-square approach (Lilly 1992):

$$C_S(z,t) = \frac{\langle \mathcal{L}_{ij} m_{ij} \rangle}{\langle m_{ij}^2 \rangle} \ . \tag{8.16}$$

Here $m_{ij} = 2\overline{\Delta}^2 \widehat{|\overline{s}|^2 \overline{s}_{ij}} - 2\widehat{\overline{\Delta}}^2 |\widehat{\overline{s}}|^2 \widehat{\overline{s}}_{ij}$ and the fact that $\overline{s}_{kk} = \widehat{\overline{s}}_{kk} = 0$ is used, which is based on continuity.

Dynamic anisotropic selective model (DASM)

The poor correlation between the Smagorinsky model and the SGS stress near the free surface in Figure 7-17 can be attributed to the use of a single coefficient $C_S(z,t)$ for all the stress components in each entire horizontal plane. As pointed out earlier, the tangential components exhibit behaviors different from the other components because of the free-surface anisotropy, which may cause the principle axes of the model tensor to be far off from those of the actual SGS stress. In addition, the increase in backscatter near the free surface is also

not accounted for by (7.7): when a single positive model coefficient is used, the correlation in the backscatter region is necessarily negative, which reduces the overall correlation.

For this highly anisotropic flow, it is useful to consider different model coefficients in (7.7) for the different SGS stress components:

$$\tau_{ij} - \delta_{ij}\tau_{kk}/3 = -2C_{ij}\overline{\Delta}^2|\overline{s}|\overline{s}_{ij}, \qquad \text{no summation for } ij\,. \tag{8.17}$$

Since the flow is also highly-varying in space (see e.g. the horizontal variations in Figures 7-11 to 7-13), the (horizontal) spatial variation of C_{ij} is of interest.

Guided by the results of Chapter 7 (cf. e.g. Figure 7-16), we propose to model C_{ij} in two separate groups: the vertical coefficients ij=13, (31), 23, (32); and horizontal coefficients ij=11, 12, (21), 22, 33. The expectation (this is confirmed by extensive direct *a priori* tests) is that the horizontal coefficients will be positive in regions of forward energy cascade and negative in regions with energy backscatter; while the vertical coefficients will not be much affected by the energy forward/backward transfer. It is then natural to propose an anisotropic SGS model which has different coefficients for the horizontal and vertical components:

$$\tau_{ij} - \frac{\delta_{ij}\tau_{kk}}{3} = -2\overline{\Delta}^2|\overline{s}| \begin{pmatrix} C_H^n\overline{s}_{11} & C_H^n\overline{s}_{12} & C_V^n\overline{s}_{13} \\ C_H^n\overline{s}_{21} & C_H^n\overline{s}_{22} & C_V^n\overline{s}_{23} \\ C_V^n\overline{s}_{31} & C_V^n\overline{s}_{32} & C_H^n\overline{s}_{33} \end{pmatrix} \tag{8.18}$$

As in DSM, the model coefficients are functions of depth and time, $C_H^n(z,t)$, $C_V^n(z,t)$, but the subscripts 'H' and 'V' correspond to 'horizontal' and 'vertical', respectively. In addition to the anisotropy, we also allow the model coefficients to obtain different values in different regions of each horizontal plane using a selection based on the (resolved) coherent vortical structure. This is indicated by the superscript 'n' for regions within which different physical processes occur. Equation (8.18) represents a new model which we denote as *dynamic anisotropic selective model* (DASM). The different spatial regions n in each horizontal plane is selected as follows:

1. $n = a$, energy backscatter region. As shown in §7.3, energy backscatter occurs at the

splat region of hairpin vortex connection, where vortex surface-inclination angle α is large and horizontal divergence is positive. For our DASM implementation, we define region 'a' as all points which satisfy $\alpha > 25°$ and $\partial\overline{u}/\partial x + \partial\overline{v}/\partial y = -\partial\overline{w}/\partial z > 0$. Based on earlier discussions, we expect C_H^a to be negative near the free surface.

2. $n = b$, small inter-scale energy transfer region. As discussed in §3.3, in the region where coherent vorticity is connected to the free surface, the inter-scale energy transfer to expected be weak and SGS dissipation is small or can be neglected. In our DASM, this region is defined by $\alpha < 5°$ and $|\overline{\omega_z}| > 2\overline{\omega_z}^{rms}$; wherein we set $C_H^b = C_H^b = 0$.

3. $n = c$, remaining region (without strong coherent vortical interactions). This is the 'typical' region and is expected to be dominated by forward energy transfer.

We point out that the 'selective' idea for the SGS modeling is not new. David (1993) developed a selective structure-function model based on the angle between the vorticity at a grid point and the vorticity averaged over the neighboring points. When the angle is less than 20°, which means that the flow is not sufficiently three dimensional, the SGS model is turned off to allow molecular dissipation only. The model is turn on only when the angle exceeds 20°. This selective structure-function model has been applied successfully to stratified flow over a backward-facing step (cf. Lesieur & Métais 1996).

An indication of the efficacy of DASM over DSM is in *a priori* tests of the model against DNS data. Figure 7-17 plots also the correlation coefficient (3.20) between DASM and the SGS stress from DNS. Compared to DSM, DASM obtains better correlation especially near the free surface. This is suggestive of the fact that the anisotropic and selective nature of DASM is more able to capture the processes near the free surface. This is confirmed in Figure 8-4 which plots the vertical variations of the DASM model coefficients obtained from *a priori* test. In region 'a', it is seen that $C_H^a < 0$ as the free surface is approached indicating energy backscatter. On the other hand, the difference between C_V^a and C_V^c is insignificant and both remain positive throughout the depth (but diminish towards the free surface).

Finally, we discuss the dynamic procedure for obtaining the DASM coefficients, $C_H^n(z,t)$,

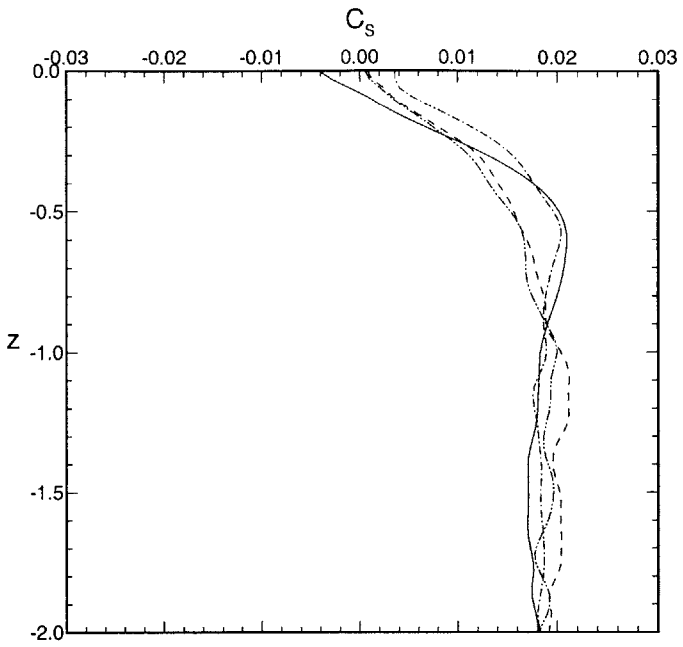

Figure 8-4: Vertical variations of DASM model coefficients: C_H^a (————), C_V^a (- - - -), C_H^c (- · - - · -) and C_V^c (—··—··—); obtained from *a priori* test. t=60.

$C_V^n(z,t)$, n=a,c, in LES. At the coarse filter level, the SGS model is written as:

$$T_{ij} - \frac{\delta_{ij}T_{kk}}{3} = -2\widehat{\overline{\Delta}}^2 |\widehat{\overline{s}}| \begin{pmatrix} C_H^n \widehat{\overline{s}}_{11} & C_H^n \widehat{\overline{s}}_{12} & C_V^n \widehat{\overline{s}}_{13} \\ C_H^n \widehat{\overline{s}}_{21} & C_H^n \widehat{\overline{s}}_{22} & C_V^n \widehat{\overline{s}}_{23} \\ C_V^n \widehat{\overline{s}}_{31} & C_V^n \widehat{\overline{s}}_{32} & C_H^n \widehat{\overline{s}}_{33} \end{pmatrix}. \tag{8.19}$$

The Germano identity then gives

$$\mathcal{L}_{ij} - \frac{\delta_{ij}\mathcal{L}_{kk}}{3} = \begin{pmatrix} C_H^n m_{11} & C_H^n m_{12} & C_V^n m_{13} \\ C_H^n m_{21} & C_H^n m_{22} & C_V^n m_{23} \\ C_V^n m_{31} & C_V^n m_{32} & C_H^n m_{33} \end{pmatrix} \tag{8.20}$$

where m_{ij} is as defined before. Finally, the DASM coefficients are solved by minimizing

$$\sum_{n=a,c} \sum_{ij=11,12,21,22,33} (\mathcal{L}_{ij} - \delta_{ij}\mathcal{L}_{kk}/3 - C_H^n m_{ij})^2 + \sum_{n=a,c} \sum_{ij=13,23,31,32} (\mathcal{L}_{ij} - C_V^n m_{ij})^2$$

on each horizontal plane. Note that the above procedure in effect neglects the variations of the model coefficients across boundaries between different regions but the net effect is found to be insignificant.

Dynamic free-surface function model (DFFM)

The results in §7.2 (cf. e.g. Figure 7-3) show that, as a result of (reverse) energy cascade, the eddy viscosity exhibits a characteristic decrease in the free-surface boundary layer. It is, therefore, desirable if this variation and the structure of the free-surface boundary layer can be represented explictly in a SGS model. As discussed in §7.4, the free-surface layer structure can be quantitatively defined in terms of the mean flow profile. We propose here a dynamic free-surface function model (DFFM). In this model, we assume that C_S has the similar behavior as the turbulence diffusivity (cf. Chapter 4):

$$C_S(z,t) = C_{Sa} - (C_{Sa} - C_{S0}) \exp[-z^2/(ra)^2] \; . \tag{8.21}$$

Here C_{Sa} is the value of the Smagorinsky coefficient in the bulk flow, C_{S0} its value at the free surface; a is the thickness of the outer free-surface boundary layer defined to be the depth of the minimum of the mean flow profile; and r is a length-scale ratio.

The model coefficients C_{Sa}, C_{S0} and a are determined dynamically from the resolved flow. The coefficient r is not directly available from the resolved flow and may, in general, depend on the LES filter width $\overline{\Delta}$. Figure 8-5 plots the variation of r as a function of $\overline{\Delta}$. The variation of r with $\overline{\Delta}$ is relatively small and justifies the use of a constant value of r in (8.21) which we set to be r=0.6 in our DFFM.

The dynamic scheme for the DFFM coefficients C_{Sa} and C_{S0} is derived from the model SGS equations under two filter levels $\overline{G}$ and $\widehat{\overline{G}}$:

$$\tau_{ij} - \frac{\delta_{ij}\tau_{kk}}{3} = -2\{C_{Sa} - (C_{Sa} - C_{S0}) \exp[-z^2/(ra)^2]\}\overline{\Delta}^2 |\overline{s}|^2 \overline{s}_{ij} \; , \tag{8.22}$$

and

$$T_{ij} - \frac{\delta_{ij}T_{kk}}{3} = -2\{C_{Sa} - (C_{Sa} - C_{S0}) \exp[-z^2/(ra)^2]\}\widehat{\overline{\Delta}}^2 |\widehat{\overline{s}}|^2 \widehat{\overline{s}}_{ij} \; . \tag{8.23}$$

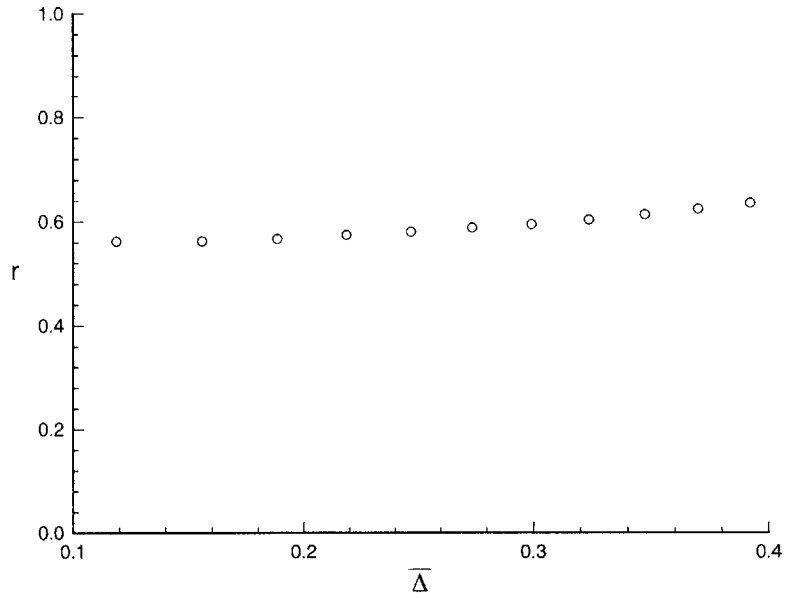

Figure 8-5: Dependence of the DFFM model coefficient r on the LES filter width $\overline{\Delta}$.

Using the Germano identity, we obtain:

$$\mathcal{L}_{ij} - \frac{\delta_{ij}\mathcal{L}_{kk}}{3} = \{C_{Sa} - (C_{Sa} - C_{S0})\exp[-z^2/(ra)^2]\}m_{ij} \ , \tag{8.24}$$

where m_{ij} is defined as before. Instead of averaging over each horizontal plane, the coefficients C_{Sa} and C_{S0} are determined by best matching (8.24) over the entire fluid volume. Least-square minimization then gives:

$$\int_{-D}^{0} \mathcal{W}(z)\langle(\mathcal{L}_{ij} - \frac{\delta_{ij}\mathcal{L}_{kk}}{3} - C_{Sa}\{1 - \exp[-z^2/(ra)^2]\}m_{ij} - C_{S0}\exp[-z^2/(ra)^2]m_{ij})^2\rangle dz \ .$$

In the above, $\mathcal{W}(z)$ is a weighting function which we choose to be $\mathcal{W}(z) = \exp[-z^2/(2ra)^2]$ to place more weight on the near free surface region.

Finally, the outer layer thickness $a(t)$ is determined from the resolved mean shear profile by the location where (local) minimum (first) occurs in the near surface region.

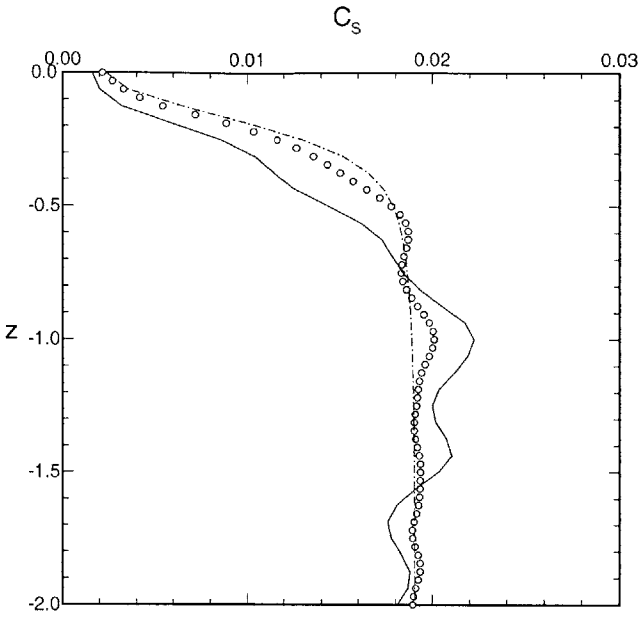

Figure 8-6: Profile of the model coefficient C_S from: ○, DNS; ———— , DSM; and – · – · – , DFFM. The profiles are averaged from t=60 to t=70.

8.2.2 Evaluation of SGS stress models for free-surface turbulence

The SGS stress models introduced in §8.2.1, DSM, DFFM and DASM, are tested in (*a posteriori*) LES simulations against DNS results. We examine in order: the variation of the model coefficients, predictions of turbulence intensity, mean flow and free-surface vortical statistics.

Model coefficients

In Chapter 7, we observe that the magnitude of the energy cascade from the resolved scales to the subgrid scales decreases significantly as the free surface is approached. Consequently, the Smagorinsky coefficient C_S should also decrease towards the surface (Figure 7-3). Figure 8-6 compares the model coefficients of DSM and DFFM against DNS-fitted values. Both models capture the decreasing trend of C_S towards the surface, but when a more physically-based form of the profile is used in DFFM, the comparison is appreciably improved and in both the vertical extent and quantitative value.

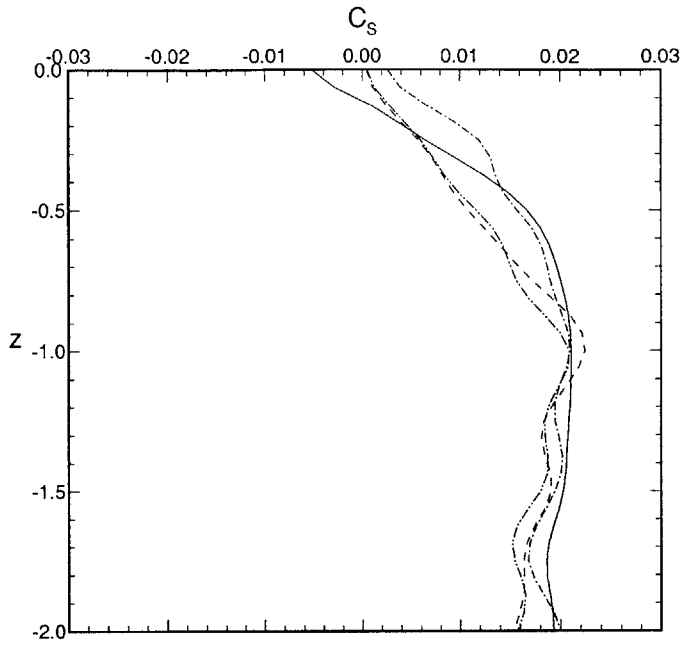

Figure 8-7: Profiles of the model coefficient in DASM: ———— , C_H^a; - - - - , C_V^a; - · - · - , C_H^c; and —··—··— , C_V^c. The profiles are averaged from t=60 to t=70.

Turning to DASM, the dynamic scheme provides, at each time, separate profiles for C_H^n, C_V^n for each region $n = a, c$ (we set $C_{H,V}^b \equiv 0$). The results are plotted in Figure 8-7. Comparing these to DNS-fitted curves in Figure 8-4, it is seen that the dynamic and DNS (*a priori*) values compare almost perfectly. The depths over which C_H and C_V vary are different; C_V^n are very close for $n = a, c$; while C_H^a and C_H^b differ qualitatively near the free surface.

Turbulence intensity

Figure 8-8 compares the DNS and LES predictions of the turbulent kinetic energy of grid-scale motions, $\overline{q}^2/2 \equiv \langle(\overline{u}_i - \langle\overline{u}_i\rangle)^2\rangle/2$. In the absence of any SGS model, $\overline{q}^2$ is over predicted at all depths as expected. In addition to DSM, DASM and DFFM, we plot for comparison the results using a constant Smagorinsky model (CSM) where a single constant value of C_S, set equal to the time-averaged bulk value obtained in DSM, is used for the LES. CSM, which does not capture the decrease in eddy viscosity at the surface, results in a $\overline{q}^2$ which is over dissipated there. Indeed the error in CSM at the surface is comparable in magnitude (but

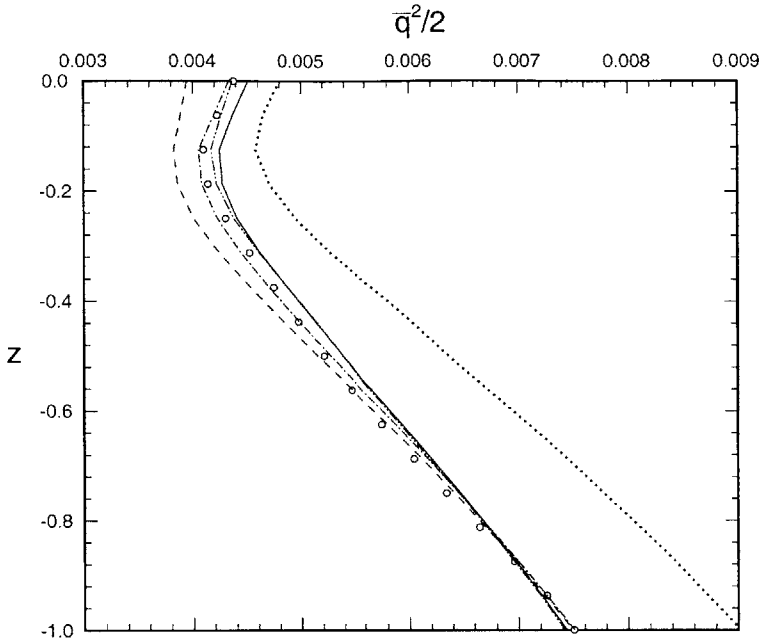

Figure 8-8: Grid-scale turbulent kinetic energy $\overline{q}^2/2$ obtained from: ○, DNS; and LES using: ····· , no SGS model; – – – – , CSM; ———— , DSM; – · – · – , DFFM; —··—··— , DASM. t=70.

with opposite sign) to that when no SGS model is used.

When vertical variation in the model coefficient is allowed, DSM obtains a reasonable kinetic energy profile, although since DSM slightly under predicts C_S at the surface (Figure 8-6), the corresponding prediction of $\overline{q}^2$ there is somewhat high. The new SGS models, DFFM and DASM, capture the variation of the model coefficients over the surface layer more precisely and obtain more accurate $\overline{q}^2$ predictions near the free surface. Of the two, DFFM, which captures more physically the near-surface turbulence diffusion mechanism (Shen *et al.* 2000), delivers a slightly better overall $\overline{q}^2$ prediction.

Figure 8-9 presents similar results for the components of $\overline{q}^2$ which reveals the anisotropy of the flow. Without SGS model, all components are substantially over predicted. CSM under predicts all the components but especially the horizontal ones relative to the other dynamic models. DSM is able to capture the anisotropy although the horizontal fluctuations are higher than the benchmark data because of the underestimation of C_S. With DFFM and DASM, improvements over DSM can be seen.

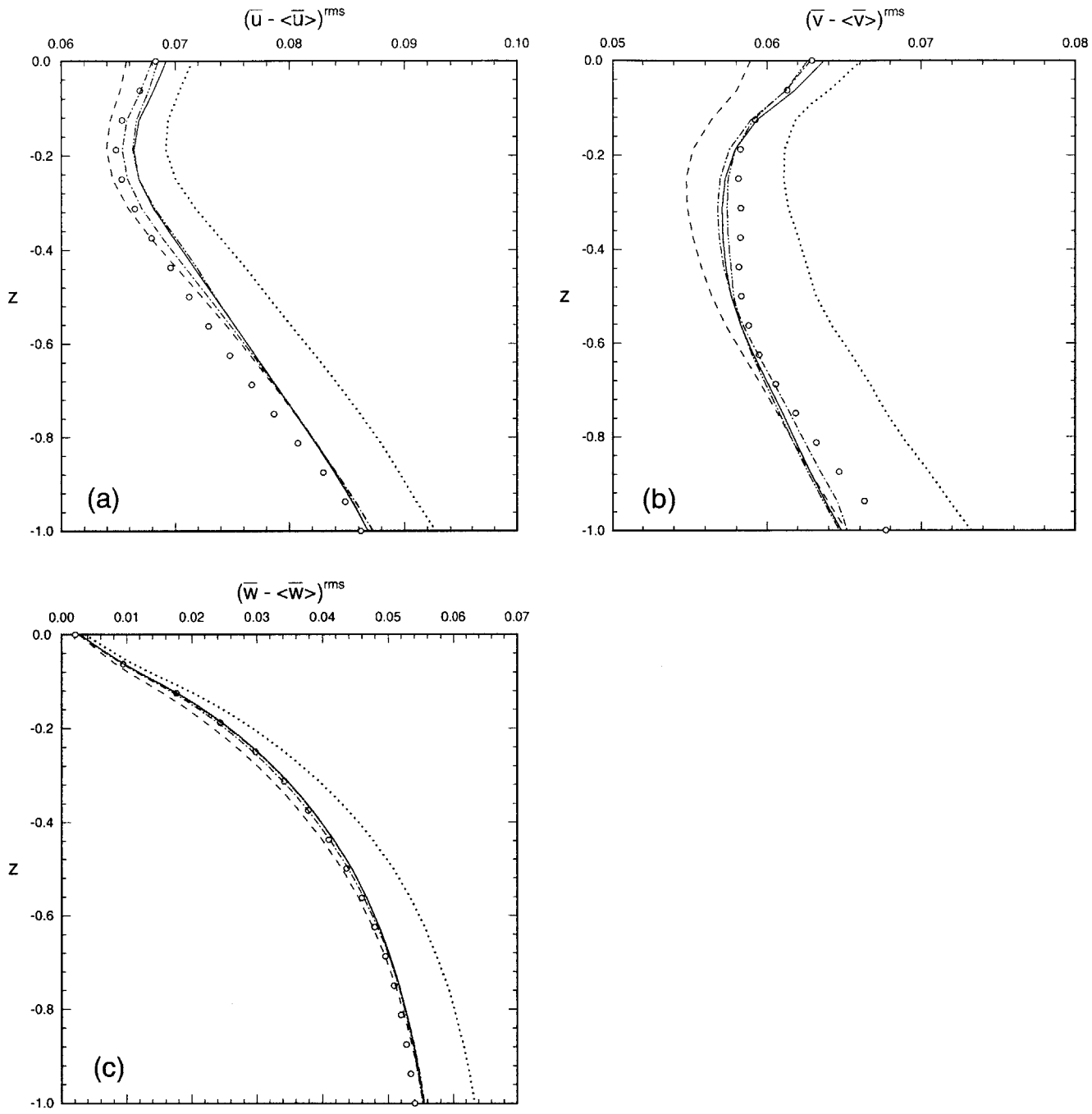

Figure 8-9: Profiles of the grid-scale velocity fluctuation components (a) $(\overline{u} - <\overline{u}>)^{rms}$; (b) $(\overline{v} - <\overline{v}>)^{rms}$; and (c) $(\overline{w} - <\overline{w}>)^{rms}$ obtained from: ∘, DNS; · · · · · · · , no SGS model; – – – – , CSM; ———— , DSM; – · – · – , DFFM; –··–··– , DASM. t=70.

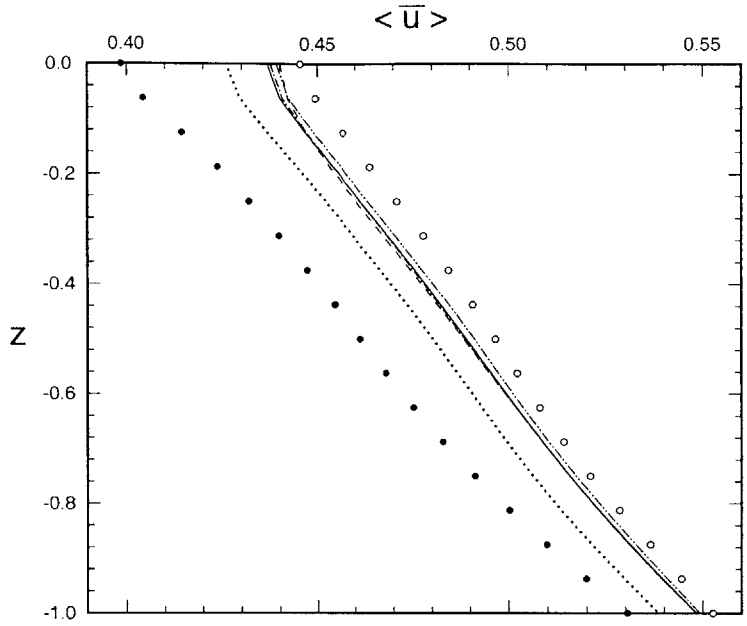

Figure 8-10: The mean velocity profile $< \overline{u} >$ at t=70: ○, DNS; · · · · · · · , no SGS model; – – – – , CSM; ———— , DSM; – · – · – , DFFM; —··—··— , DASM; •, the initial LES profile from DNS at t=60.

Mean flow

We compare the LES predicted mean velocity profiles in Figure 8-10. Although there is improvement over the no SGS model case, CSM, DSM, DFFM and DASM are all not satisfactory relative to their predictions of the kinetic energy. The reason is that, while eddy-viscosity models obtain the correct overall SGS dissipation, the correlation between the predicted and actual SGS stress itself is poor (cf. Figure 7-17). As will be shown in §4.4, a combination of such models with a scale-similarity (Bardina-type) model improves the mean velocity predictions significantly.

The most significant gain in using a surface-function type model like DFFM is in the prediction of the mean shear profile $< \overline{u}_z > (z)$ (Figure 8-11). The mean shear profile quantitatively defines the surface layer structure in that, as the free surface is approached, its magnitude initially increases over the outer boundary layer, reaches a maximum and then drops to zero inside a much thinner inner layer (cf. Shen *et al.* 2000). Figure 8-11 shows that CSM has a large error comparable to the no model case, and in particlar predicts a

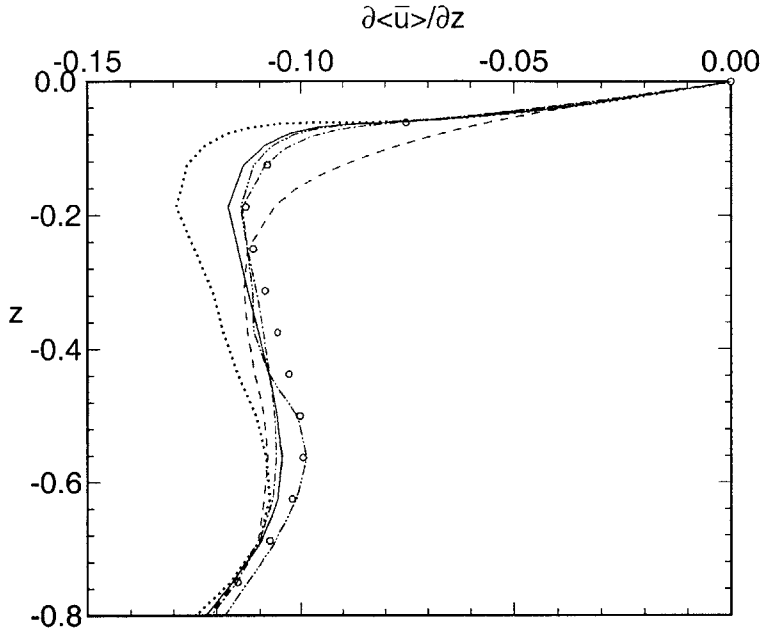

Figure 8-11: Mean shear profile $\partial < \overline{u} > /\partial z$ obtained from: ○, DNS; · · · · · · · , no SGS model; – – – – , CSM; ———— , DSM; – · – · – , DFFM; —··—··— , DASM. t=70.

much thicker surface layer. DSM and DASM, which obtain the decreasing trend in the eddy viscosity, capture the surface layer reasonably well. Since the physical functional behavior of the surface layer is represented in DFFM, it predicts $< \overline{u}_z > (z)$ with remarkable accuracy.

Free-surface vortical statistics

LES predictions of the free-surface roughness $\overline{h}^{\text{rms}}$ and horizontal surface vorticity $\overline{\omega}_s^{\text{rms}}$ are shown in Figure 8-2. As pointed out there, proper SGS modeling of free-surface flux and dynamic pressure is essential. With these models, DSM, DASM and DFFM all perform adequately for such averaged statistics.

The observable turbulence features on the surface are of immediate importance to applications. These features are dominated by near-surface vortical mechanisms such as surface connection which result in persistent and prominent surface signatures. Because of the uncertainty in the subgrid-scale motions (cf. Lesieur & Métais 1996), it is inappropriate to compare the evolution of a specific vortical structure in the LES. We resort instead to statistical measures of the structure of the coherent surface vorticity.

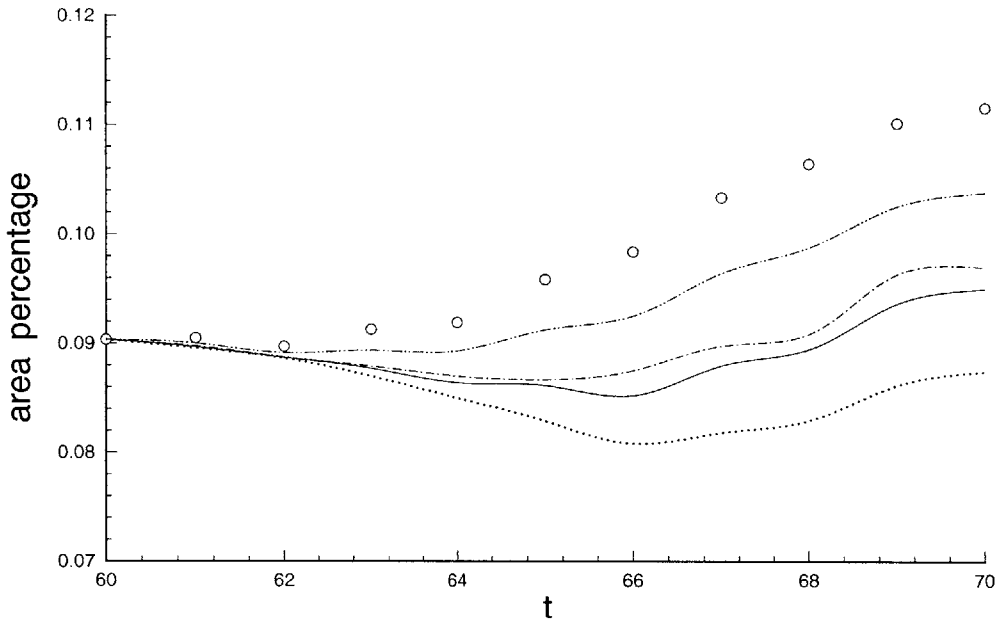

Figure 8-12: Time evolution of the area percentage of coherent surface-connected vortices $\mathcal{A}_b$ for: ○, DNS; · · · · · · · , no SGS model; ———— , DSM; – · – · – , DFFM; —··—··— , DASM.

Figure 8-12 plots the time evolution of the area percentage of coherent surface-connected vortices, $\mathcal{A}_b$, which we define as the percent of surface area satisfying $|\overline{\omega_z}| > 2\overline{\omega_z}^{rms} \cup \alpha < 5°$. Note that this is the same as region $n = b$ of DASM. Because of the persistence of such vorticity, $\mathcal{A}_b$ generally increases with time, as shown by the DNS data. DSM, which does not account for either energy backscatter during the vortex connection or reduced dissipation of surface-connected vortices, tends to over dissipate the surface vortices and hence under predicts $\mathcal{A}_b$. Since DFFM also uses a single model coefficient in the horizontal plane, the improvement of DFFM over DSM is small. On the other hand, since DASM uses a selective procedure based on the resolved vorticity structure information, it obtains a significantly better prediction for $\mathcal{A}_b$.

As discussed in §7.3, the surface-inclination angle α is an important measure of the evolution of surface-connecting vortices. To further elucidate the efficacy of the LES schemes for predicting surface signatures, we examine the distribution of percentage surface area $\mathcal{A}$ and surface enstrophy $\overline{\omega_z}^2$ as a function of the grid-scale inclination angle α. These are

plotted in Figure 8-13. The dominance of surface-connected vorticity (low α) is evident. Compared to DNS data, DSM and DFFM both tend to under predict the low-α values as a result of over dissipation of connection events (with a single C_S in the horizontal plane). DASM continues to perform well here although the peaks in $\mathcal{A}(\alpha)$ and $\overline{\omega_z}^2(\alpha)$ are under predicted since the number of selection regions n used is still relatively small.

The superiority of DASM for surface signatures is further seen in the conditionally-averaged flow field around LES-resolved coherent hairpin vortices. Figure 8-14 plots the VISA SGS dissipation rate around connecting hairpin vortices. Because of the negative values of C_H^a (Figure 8-7), DASM captures energy backscatter at the splat region of the hairpin vortex. This is in agreement with the *a priori* results in §7.3. In comparison, DSM, which uses a single model coefficient in the plane, does not capture the inverse energy transfer. Thus, although the plane-averaged value is correct in DSM, the local SGS dissipation rate around this event is off in both sign and magnitude.

Discussion

For free-surface turbulence, the above SGS stress model results show that it is important for eddy-viscosity models to capture the spatial variations of model coefficients both vertically and horizontally. Vertically because of the decrease in eddy viscosity over the surface layer due to energy backscatter; and horizontally because of its disparate behaviors associated with large-scale vortical events.

Dynamic procedures in the vertical direction in DSM and DASM have substantial advantage over CSM in obtaining the vertical variations, but a model that incorporated known physical structure(s) such as DFFM captures the surface layer with remarkable accuracy. When model coefficients in the horizontal plane are allowed to take on different values in a selective scheme, as in DASM (based on coherent vorticity dynamics and reflected differently in different directional components), the prediction of the statistics of coherent events are greatly improved. One may suggest that a point-by-point dynamic scheme would do even better. However, such procedures, without some *ad hoc* averaging, are prone to instability (when the model coefficient varies excessively) (cf. Germano *et al.* 1991). Advanced localization formulations (e.g. Ghosal *et al.* 1995) either constrain the occurrence of negative eddy

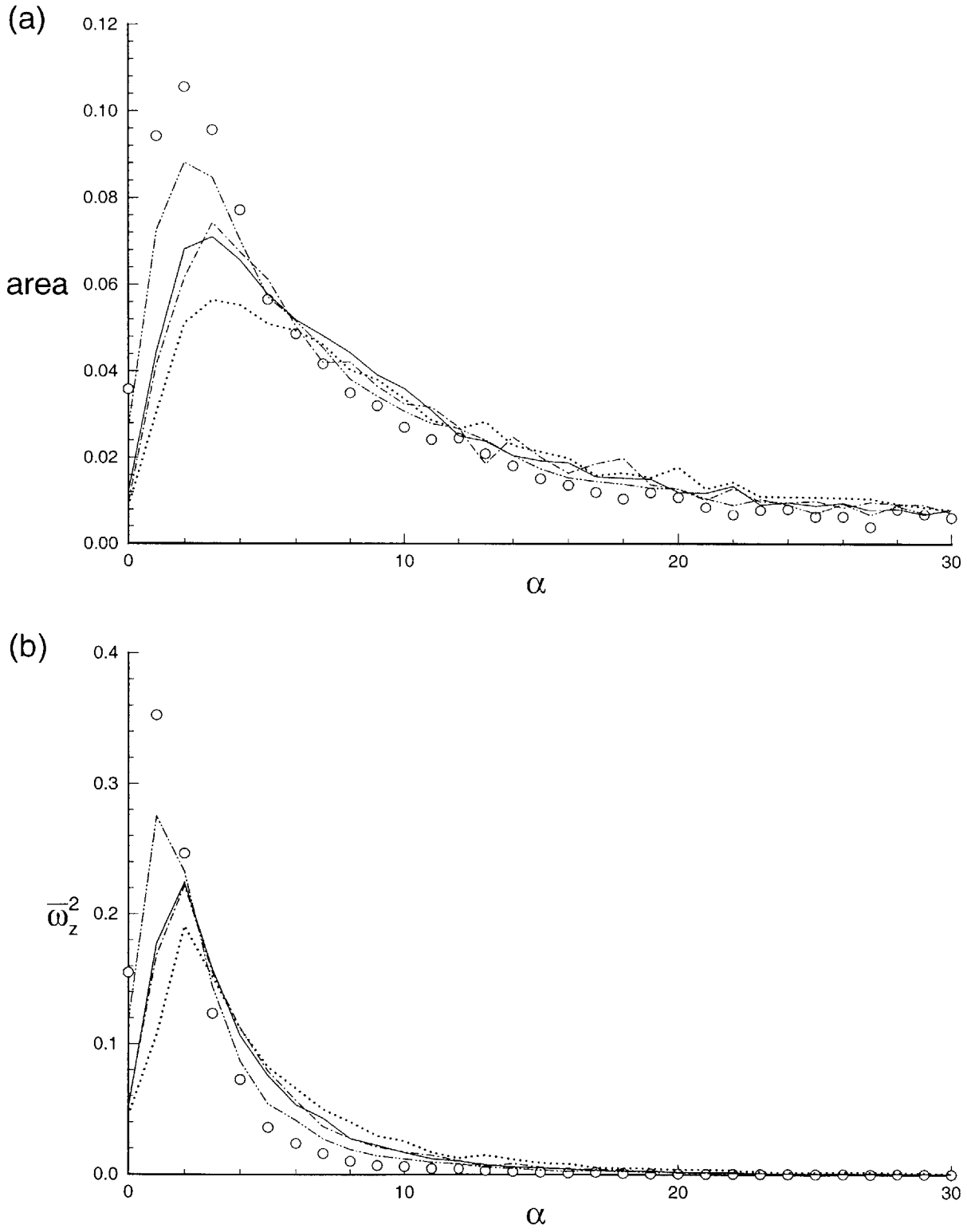

Figure 8-13: Distributions of (a) $\mathcal{A}(\alpha)$; and (b) $\overline{\omega_z}^2(\alpha)$; as functions of the vorticity surface-inclination angle α obtained with: $\circ$, DNS; $\cdots\cdots$, no SGS model; ————, DSM; – · – · –, DFFM; —··—··—, DASM.

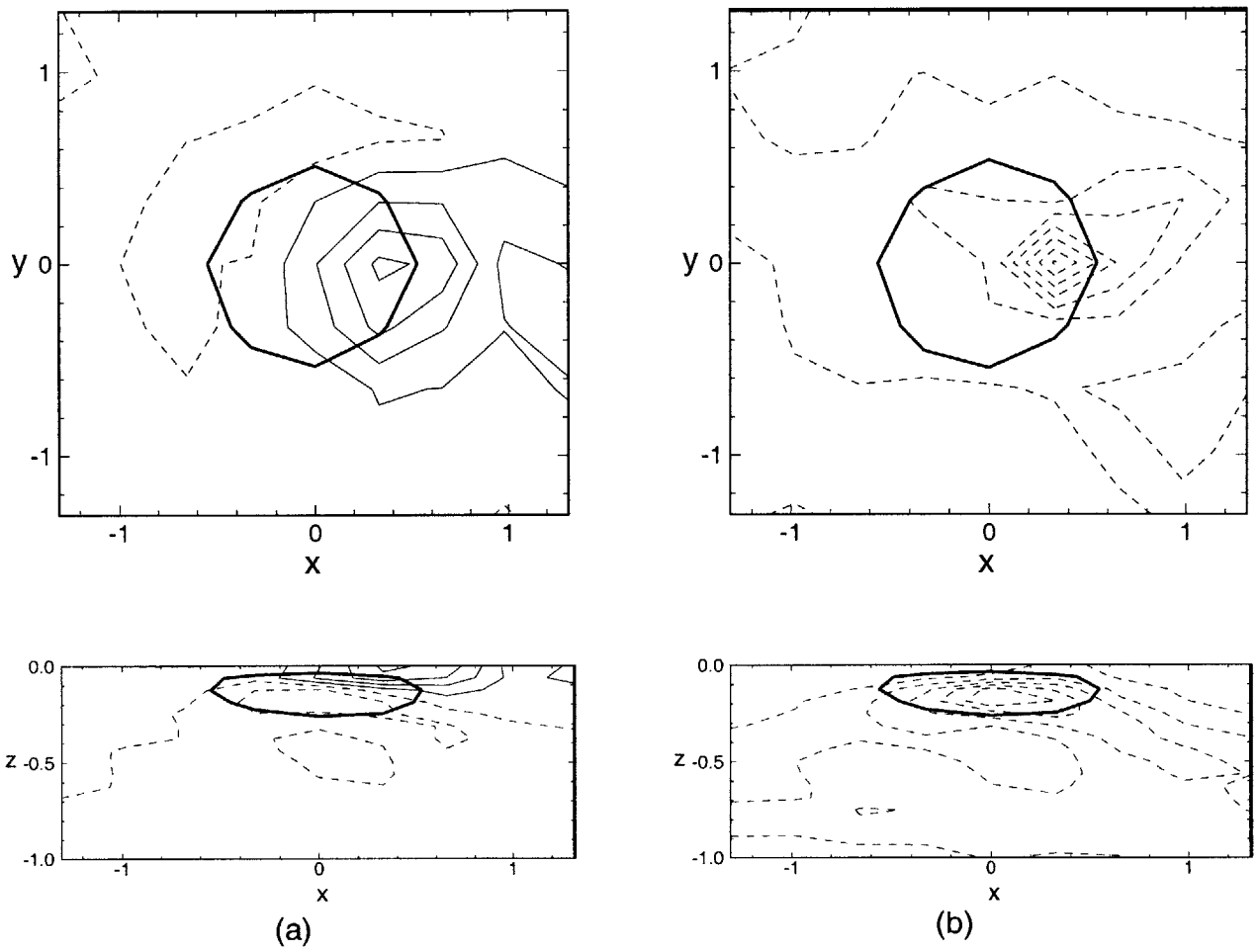

Figure 8-14: Contours of VISA SGS dissipation rate $\tau_{ij}\bar{s}_{ij}$ around hairpin vortices, with the head portion located at $(0, 0, -0.0625)$. Results obtained with: (a) DASM (contour interval 0.0002) ; and (b) DSM (contour interval 0.00002). Top (x-y plane) view (top figures). Side (x-z plane) view (bottom figures). Dash lines represent negative values. The thick line is the contour $\omega_y = -0.5$, which marks the location of the hairpin head.

viscosity, which does not allow energy backscatter, or introduce additional transport equations, which substantially increase the degree of complexity. Additional research in these areas is needed.

While eddy-viscosity models do an excellent job in modeling the total dissipation, they can be inadequate in select aspects, for example, in predicting the mean profile here. In this case, the correlation between the modeled and actual SGS stress is poor, because their principle axes are not generally aligned. As the free surface is approached, the correlation becomes even worse. To overcome this drawback, a powerful idea is to combine the eddy-viscosity model with a scale-similarity model (cf. Bardina *et al.* 1983; and e.g. Zang *et al.* 1993, Salvetti *et al.* 1997). This is pursued in the next section.

8.2.3 Combination of eddy-viscosity and scale-similarity models

Each of the SGS models in §8.2.1 can be used in combination with a dynamic scale-similarity model. In this case, the DSM, DFFM and DASM approaches become respectively:

$$\tau_{ij} - \frac{\delta_{ij}\tau_{kk}}{3} = -2C_S\overline{\Delta}^2|\overline{s}|^2\overline{s}_{ij} + C_B(L^m_{ij} - \frac{\delta_{ij}L^m_{kk}}{3}) \,, \tag{8.25}$$

$$\tau_{ij} - \frac{\delta_{ij}\tau_{kk}}{3} = -2\{C_{Sa} - (C_{Sa} - C_{S0})\exp[-z^2/(ra)^2]\}\overline{\Delta}^2|\overline{s}|^2\overline{s}_{ij} + C_B(L^m_{ij} - \frac{\delta_{ij}L^m_{kk}}{3}) \,, \tag{8.26}$$

and

$$\tau_{ij} - \frac{\delta_{ij}\tau_{kk}}{3} = -2\overline{\Delta}^2|\overline{s}| \begin{pmatrix} C^n_H\overline{s}_{11} & C^n_H\overline{s}_{12} & C^n_V\overline{s}_{13} \\ C^n_H\overline{s}_{21} & C^n_H\overline{s}_{22} & C^n_V\overline{s}_{23} \\ C^n_V\overline{s}_{31} & C^n_V\overline{s}_{32} & C^n_H\overline{s}_{33} \end{pmatrix} + C_B(L^m_{ij} - \frac{\delta_{ij}L^m_{kk}}{3}) \,. \tag{8.27}$$

These we denote by DSM+B, DFFM+B and DASM+B respectively. In the above, $L^m_{ij} \equiv \overline{\overline{u}_i\overline{u}_j} - \overline{\overline{u}}_i\overline{\overline{u}}_j$, and C_B is the coefficient of the scale-similarity model to be determined dynamically. Note that the combined model DSM+B (8.25) is identical to the dynamic two-parameter model (DTM) in Salvetti & Banerjee (1995) and Salvetti *et al.* (1997).

To determine the model coefficients, a similar dynamic procedure as before is applied. By using filters at two different levels and employing the Germano identity, we obtain re-

spectively:

$$\mathcal{L}_{ij} - \frac{\delta_{ij}\mathcal{L}_{kk}}{3} = C_S m_{ij} + C_B H_{ij} \ , \tag{8.28}$$

$$\mathcal{L}_{ij} - \frac{\delta_{ij}\mathcal{L}_{kk}}{3} = \{C_{Sa} - (C_{Sa} - C_{S0}) \exp[-z^2/(ra)^2]\} m_{ij} + C_B H_{ij} \ , \tag{8.29}$$

and

$$\mathcal{L}_{ij} - \frac{\delta_{ij}\mathcal{L}_{kk}}{3} = \begin{pmatrix} C_H^n m_{11} & C_H^n m_{12} & C_V^n m_{13} \\ C_H^n m_{21} & C_H^n m_{22} & C_V^n m_{23} \\ C_V^n m_{31} & C_V^n m_{32} & C_H^n m_{33} \end{pmatrix} + C_B H_{ij}. \tag{8.30}$$

Here $\mathcal{L}_{ij}$ and m_{ij} have the same definitions as before; while $H_{ij} \equiv \widehat{\overline{\overline{u}_i \overline{u}_j}} - \widehat{\overline{\overline{u}}_i \overline{\overline{u}}_j}$. Finally, the coefficients are solved by least-square matching of (8.28), (8.29) and (8.30) respectively.

The correlation coefficients between the actual SGS stress and those predicted by DSM+B and DASM+B have been plotted in Figure 7-17. As expected based on previous studies, the correlation is improved significantly at all depths when the scale-similarity model is added. In particular, the predictions of the combined models show no degradation in the surface layer in contrast to the Smagorinsky model alone.

The three combined models, DSM+B, DFFM+B and DASM+B, have been implemented and studied extensively in *a posteriori* LES tests. Overall, we obtain noticeable but not substantial improvements in the results for turbulent kinetic energy and free-surface statistics in §8.1.3 and §8.2.2. The most marked improvement of the combined models is in the prediction of the mean flow profile which we focus on. Figure 8-15 compares the performance of the three SGS schemes with and without the scale-similarity model. Relative to the results without SGS models, the improvement of the combined models over the eddy-viscosity models alone is quite substantial.

Finally, we plot the dynamic model coefficients for DSM+B, DFFM+B and DASM+B. Figure 8-16 shows that the coefficients of the eddy-viscosity portion of the models preserve the same qualitative trends as those in §8.2.2. The magnitudes of the coefficients of the combined models are, however, reduced significantly. This can be explained by the fact that less burden is put on the eddy-viscosity portion of the models to capture the SGS stress, a feature in favor of numerical stability (Zang *et al.* 1993; Salvetti *et al.* 1997). Figure 8-17

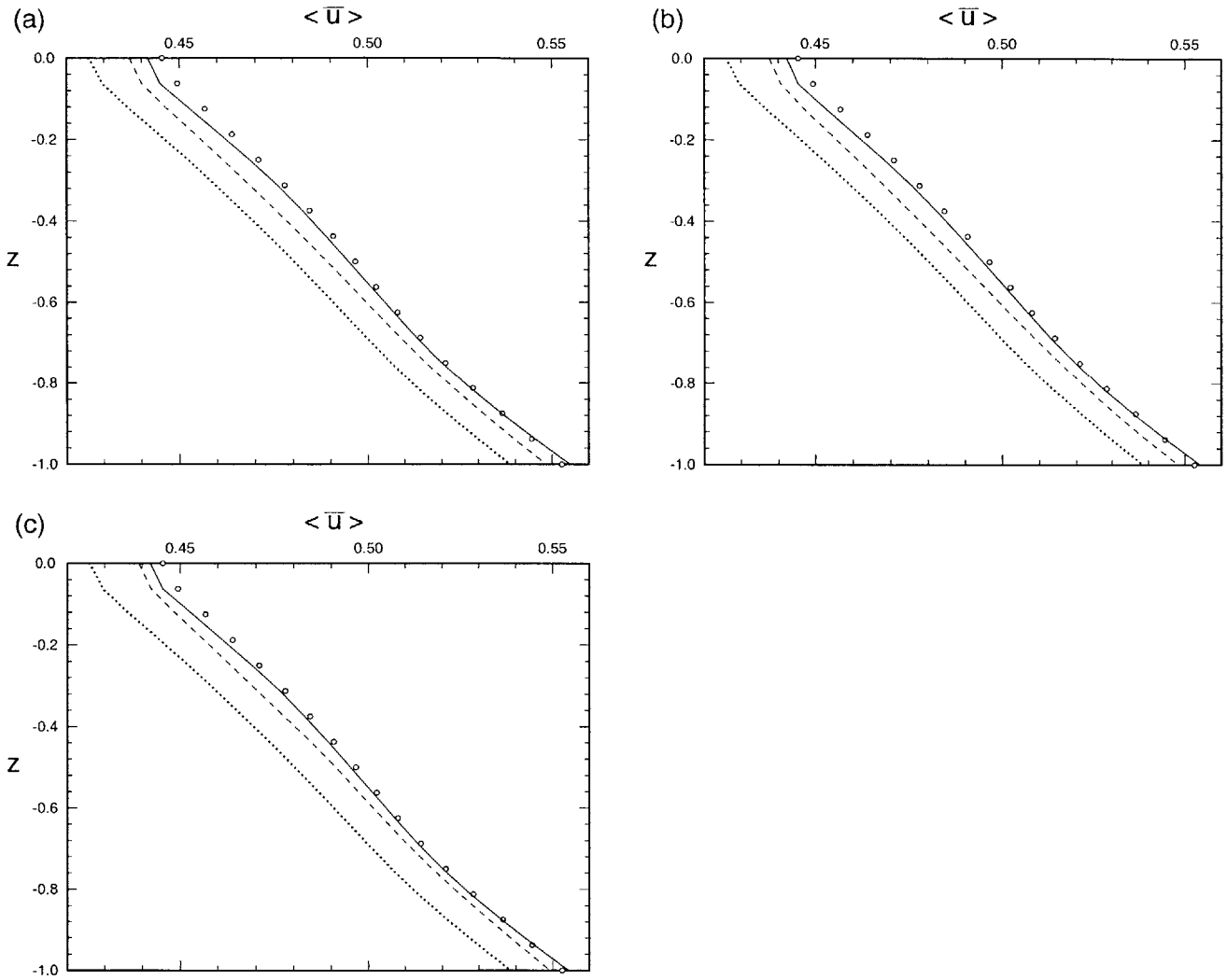

Figure 8-15: Mean velocity profile $< \overline{u} >$ obtained using: DNS ($\circ$), LES with no SGS model ($\cdots\cdots$), and eddy-viscosity models with (————) and without (– – – –) scale-similarity model for: (*a*) DSM; (*b*) DFFM; and (*c*) DASM. t=70.

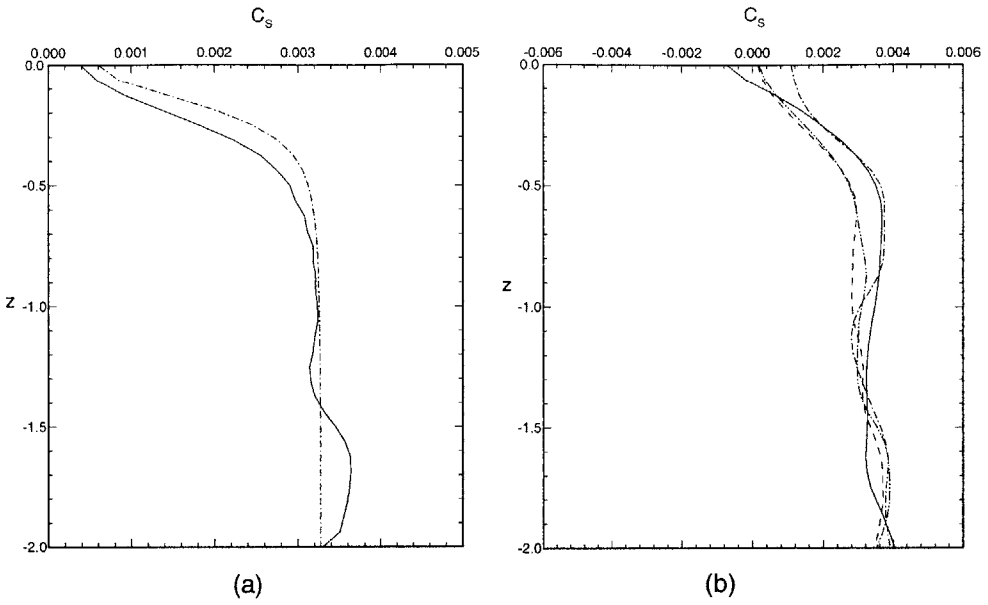

Figure 8-16: Profiles of eddy-viscosity model coefficients for: (a) ———— , DSM+B; and – · – · – , DFFM+B; and (b) DASM+B for ———— , C_H^a; – – – – , C_V^a; – · – · – , C_H^c; —··—··— , C_V^c. The profiles are averaged from t=60 to t=70.

plots the profiles of C_B for DSM+B and DASM+B. The variations of C_B within the surface layer is small and may justify the use of a single value of C_B for all the depths. This affords a simplification for DFFM+B where all the model coefficients are determined by least-square minimization over the whole volume.

8.3 Conclusions

In this study we develop the computational capability for the large-eddy simulation of free-surface turbulent flows. The canonical problem we study is the turbulent shear flow beneath a free surface at finite Froude numbers. The benchmark data is obtained from the direct numerical simulation on fine grid. Based on the physics of free-surface turbulence, subgrid-scale models have been developed. These include SGS models for free-surface fluxes which come from the kinematic free-surface boundary condition, and for a dynamic SGS pressure which results from the imposition of a boundary condition on the total pressure at the free

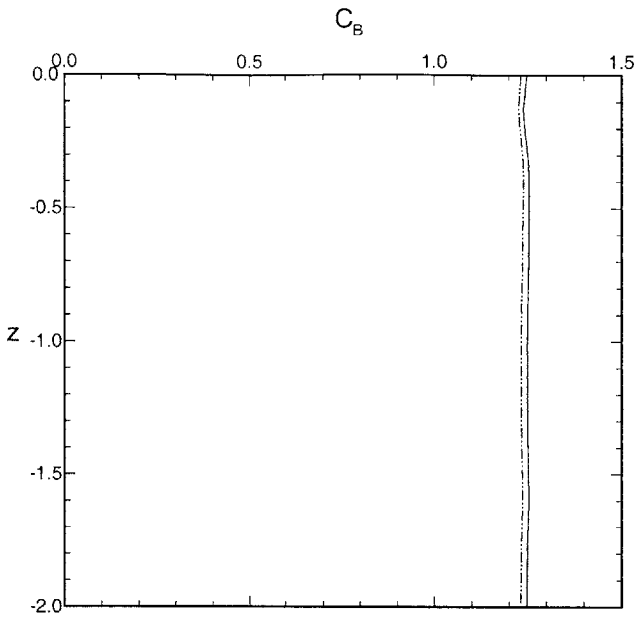

Figure 8-17: Profiles of the coefficient of the scale-similarity model C_B for: ———— , DSM+B; and —··—··— , DASM+B.

surface. These are obtained in the present context for the first time. For the SGS stress, we employ an existing dynamic Smagorinsky model (DSM), and develop two new models: a dynamic free-surface function model (DFFM) which captures the expected depth variation in the eddy viscosity (based on the similarity solution of Shen *et al.* 2000); and a dynamic anisotropic selective model (DASM), which recognizes the anisotropy of the flow field and the different energy cascade mechanisms which are coupled with the coherent surface vorticity dynamics.

Our numerical tests show that modeling of the free-surface SGS fluxes and dynamic pressure is important for the LES, especially in predicting the surface roughness. Compared with DSM, DFFM captures much better the structure of the free-surface boundary layer. On the other hand, DASM is superior in obtaining the statistics associated with free-surface signatures. The only shortcoming of these eddy-viscosity models is found in the prediction of the mean flow profile. This is overcome by the addition of a scale-similarity SGS model.

Chapter 9

Concluding Remarks

9.1 Summary of contributions of this thesis

In this study we combine theoretical and numerical efforts to study the interaction of turbulence with a free surface at low Froude numbers. Based on the simulations of free-surface turbulent flows, we obtain substantial understanding of the structures, mechanisms and statistical characteristics of low Froude number FST. Through this study, we are able to identify and quantify the key turbulent processes in the turbulent flows with a free surface. We also obtain important physical insights into the turbulence modeling and develop efficacious subgrid-scale (SGS) models for free-surface turbulent flows.

The major contributions of this work include:

- **Development of numerical capabilities of direct numerical simulation (DNS) for turbulent flows with a free surface.** The DNS enables the detailed analysis of the physics of FST. It also provides a framework for the development of large-eddy simulation capability.

- **Revelation of the surface-layer structure in FST.** We identify the multi-layer structure in the turbulent flows near a free surface and quantify the dynamics within these layers. The concept of free-surface inner and outer layers greatly facilitates the elucidation of the fundamental structures and physical mechanisms for turbulent flows

in the vicinity of a free surface.

- **Illustration of vortex dynamics in FST.** We identify the key coherent vortical structures in free-surface turbulence, namely hairpin eddies and surface-connected vortices. The vortex connection mechanisms at a free surface are investigated. We also study the vortex dynamics for the surface-connecting vortices during different evolutionary stages and reveal the underlying mechanisms for the persistence of surface-connected vortices.

- **Characterization and quantification of the near-surface diffusion mechanisms.** We derive an analytical-similarity solution for the mean flow to quantify the momentum diffusion mechanism. The theoretical results agree with numerical simulation with remarkable accuracy. The similarity theory also provides an accurate definition for the surface layers and suggests scaling properties for the thickness of these layers.

- **Demonstration and quantification of the processes of scalar mixing/transport at the air-water interface.** The similarity theory is extended to the problem of passive scalar mixing near a free surface at which the scalar flux rate vanishes. For the more general scalar transfer processes, we discover the dependence of transport processes on the structures of turbulent flows. The contributions of different types of coherent FST structures to the scalar transport processes are quantified.

- **Elucidation of the inter-scale energy cascade mechanism in free-surface turbulence.** We find that the amount of energy transferred from the grid scales to the subgrid scales (SGS) decreases significantly as the free surface is approached. This is a result of energy backscatter associated with the fluid vertical motions. Conditional averaging reveals that the energy backscatter occurs at the splat regions of coherent hairpin vortex structures as they connect to the free surface. The mechanism of inter-scale energy transfer is essential to the subgrid-scale modeling for free-surface turbulent flows.

- **Development of subgrid-scale models and establishment of LES capabilities for free-surface turbulent flows.** Based on the special physics of FST, we develop two new SGS models — a dynamic free-surface function model (DFFM) and a dynamic anisotropic selective model (DASM). The DFFM correctly represents the reduction of the Smagorinsky coefficient near the surface, while the DASM takes into account both the anisotropy nature of free-surface turbulence and the dependence of energy backscatter on specific coherent vorticity mechanisms. We also model for the first time the surface SGS flux and the dynamic SGS pressure, which are unique to the free-surface problems. Our LES with new SGS models obtains results substantially superior to the conventional approaches using existing models.

9.2 Future studies

This work is intended as a first step towards the understanding of the fundamental physics of free-surface turbulence. In this study, we simplify the problem by neglecting the surface tension effects, the wind stress, and the nonlinear wave effects. Through this research, we have obtained substantial understanding of this idealized flow in terms of the statistical, structural, and dynamical characteristics, which provides a framework for our next-step studies of more complicated cases. Some of the future research directions are discussed as follows.

9.2.1 Air-water coupled dynamics

The current study neglects the wind stress at the free surface, which may play a significant role in the real air-sea interactions, especially at moderate to high wind-speed cases. The understanding and prediction of the coupled air-ocean dynamics are of vital importance to applications such as global warming and pollutant transport, as well as many Navy operations.

Considerable work has been done to understand aspects of this problem in terms of simplified theory and modeling. Nevertheless, the representation of the true coupled air-

sea-wave interactions is far from satisfying. The majority of the body of numerical work involves idealized assumptions that capture only very limited aspects of the feedback coupling dynamics. For the ocean flow, numerical simulations generally treat the air-sea interface as a rigid lid, which does not include surface wave motions, or at most apply Craik-Leibovich type equations, which take into account Stokes drift as the sole wave effect. For the air flow, the most sophisticated simulations to date still treat the ocean surface as a stationary one or one prescribed by linear gravity wave solution. For the mass, momentum and energy fluxes across the air-sea interface, empirical constants or simple cycle models are often used instead of realistic values resulting from the coupling mechanisms. There does not exist realistic simulation that accounts for the truly coupled air-sea-wave interactions.

Based on the understanding of the fundamental physics of free-surface turbulence in terms of surface layers, the physics-based SGS models developed for FST, and the robust numerical capabilities established in this study, we are now in a position to perform a numerical simulation of both the air and ocean turbulent flows with coupled free-surface boundary conditions. The essential and immediate tasks of this research are: (1) development of DNS/LES capabilities for the coupled air-ocean flow field including the turbulent flows in both air and water; (2) elucidation of the structures and dynamics for turbulent flows in the vicinity of the air-sea interface; (3) assessment of the physical mechanisms of the key air-sea transport processes; and (4) obtain parameterizations of the momentum, mass and heat transfer for coupled air-ocean boundary modeling.

9.2.2 Turbulence-wave interaction

The interaction of turbulence with surface waves is a challenging problem involving numerous complicated processes such as, to name a few, the energy transfer among the turbulence, wave and current, the generation of surface vorticity, the enhanced turbulence dissipation introduced by the wave breaking, turbulent dissipation, scattering and production of waves, and turbulent roughening of the free surface. Our knowledge of the above processes are far from sufficient and numerical simulation may become a powerful tool for this research.

An immediate extension of the current work is the direct numerical simulation and large-

eddy simulation of free-surface turbulent flows at moderate to large Froude numbers. For small- to moderate-magnitude waves, we are going to use a boundary interface tracking method (BITM) which uses a boundary-fitted meshes; while for steep/breaking waves, other approaches based on levelset methodology, volume-of-fluid method, or smoothed particle hydrodynamics will be used.

For the study of turbulence-wave interaction, the major scientific and techniques issues are: (1) development of DNS/LES numerical capabilities in complex geometry; (2) development, calibration and validation of physics-based breaking dissipation models for LES of strong turbulence-wave interactions; (3) elucidation of the surface-layer structure near a wavy surface; (4) quantification of the turbulent dissipation, scattering and production of waves; and (5) assessment of the physical mechanisms of steep/breaking effects for ocean-wave boundary modeling.

9.2.3 Free-surface surfactant dynamics

The interaction between free-surface turbulence and surfactant (surface-active material, e.g. oil slicks) is of significant importance to many environmental concerns such as air-sea gas exchange and pollutant transport. From the viewpoint of basic scientific research, the turbulence-surfactant interaction is a profound problem which involves turbulence hydrodynamics, scalar diffusion/transport, and surface-tension phenomenon.

The contamination of surfactant on a free surface interacts with the underlying flow through the Marangoni effect. In general, the presence of surfactant lowers the local surface tension. Hydrodynamic disturbances result in a non-uniform distribution of surfactant concentration on the free surface, and consequently local interfacial tension gradients are created. The resulting shear stresses on the free surface, in return, interact and change the structure of the flow beneath. Thus the flow/surfactant interaction is a complicated closed-loop process (cf. Ananthakrishnan & Yeung 1994, Tsai & Yue 1995, and Willert & Gharib 1997).

Based on the current study of the fundamental physics of free-surface turbulence and the scalar transport processes in the vicinity of the free surface, we are now in a position where

a combined theoretical and computational effort will lead to an enormous step towards the description, understanding and prediction of free-surface turbulence/surfactant interaction. In the numerical simulation, fluid motions are described by the Navier-Stokes equations; the variation of surfactant concentration is solved as a scalar transport/diffusion problem; the effect of surfactant on fluid hydrodynamics is applied through the surface tension in the free-surface boundary conditions for fluid motions; and the dependence of surface tension variation on local surfactant concentration is quantified by equation of state.

For the free-surface surfactant dynamics, the main issues to resolve include: (1) development of computational capabilities for turbulent flows involving free surface and surfactant; (2) elucidation of physical mechanisms and structures for free-surface turbulence under the influence of surfactant; (3) revelation of basic physics for the transport of contaminants in free-surface turbulent flows; (4) establishment of physical basis for the quantification and prediction of contaminant spreading on the free surface; and (5) direct quantitative comparison and validation among theoretical analysis, computational prediction, and field/laboratory measurement.

Bibliography

[1] ANANTHAKRISHNAN, P. & YEUNG R. W. 1994 Nonlinear Interaction of a Vortex Pair with Clean and Surfactant-covered Free Surfaces. *Wave Motion* **19**, 343-365.

[2] ANTONIA, R. A. 1981 Conditional sampling in turbulence measurement. *Ann. Rev. Fluid. Mech.* **13**, 131–156.

[3] BALINT, J.-L., VUKOSLAVCEVIC, P. & WALLACE, J. M. 1988 The transport of enstrophy in a turbulent boundary layer. In *Near-Wall Turbulence, Zoran Zaric Memorial Conference* (ed. S. J. Kline & N. H. Afgan). Hemisphere, pp. 932–950.

[4] BARDINA, J., FERZIGER, J. H. & REYNOLDS, W. C. 1983 Improved turbulence models based on large eddy simulation of homogeneous, incompressible turbulent flows. *Rep.* TF-19, Mech. Engng Dept., Stanford University.

[5] BERNAL, L. P. & KWON J. T. 1989 Vortex ring dynamics at a free surface. *Phys. Fluids* A **1**, 449–451.

[6] BLACKWELDER, R. F. & KAPLAN, R. E. 1976 On the wall structure of the turbulent boundary layer. *J. Fluid Mech.* **76**, 89–112.

[7] BORUE, V., ORSZAG, S. A. & STAROSELSKY, I. 1995 Interaction of surface waves with turbulence: direct numerical simulations of turbulent open-channel flow. *J. Fluid Mech.* **286**, 1–23.

[8] BRADSHAW, P. & KOH, Y. M. 1981 A note on Poisson's equation for pressure in a turbulent flow. *Phys. Fluids* **24**, 777.

[9] BROWN, J. S., KHOO, B. S. & SONIN, A. A. 1990 Rate correlation for condensation of pure vapor on turbulent, subcooled liquid. *Intl J. Heat Mass Transfer* **33**, 2001–2018.

[10] BRUMLEY, B. & JIRKA, G. Near-surface turbulence in a grid-stirred tank. *J. Fluid Mech.* **183**, 235–263.

[11] CLARK, R. A., FERZIGER, J. H. & REYNOLDS, W. C. 1979 Evaluation of subgrid-scale models using an accurately simulated turbulent flow. *J. Fluid Mech.* **91**, 1–16.

[12] CORTESI, A. B., SMITH, B. L., YADIGAROGLU, G. & BANERJEE, S. 1999 Numerical investigation of the entrainment and mixing processes in neutral and stably-stratified mixing layers. *Phys. Fluids* **11**, 162–184.

[13] DANCKWERTS, P. V. 1951 Significance of liquid-film coefficients in gas absorption. *Ind. Engng Chem.* **43**, 1460–1467.

[14] DAVID, E. 1993 Modélisation des écoulements compressibles et hypersoniques: une approche instationnaire. PhD thesis, Natl. Polytech. Inst., Grenoble.

[15] DAVIS, J. T. 1972 *Turbulence Phenomena.* Academic.

[16] DIMAS, A. A. & TRIANTAFYLLOU, G. S. 1994 Nonlinear interaction of shear flow with a free surface. *J. Fluid Mech.* **260**, 211–246.

[17] DOMARADZKI, J. A., LIU, W., HARTEL, C. & KLEISER, L. 1994 Energy transfer in numerically simulated wall-bounded turbulent flows. *Phys. Fluids* **6**, 1583–1599.

[18] DOMARADZKI, J. A. & ROGALLO, R. S. 1990 Local energy transfer and nonlocal interactions in homogeneous, isotropic turbulence. *Phys. Fluids* A **2**, 413–426.

[19] DOMMERMUTH, D. G. & NOVIKOV, E. A. 1993 Direct-numerical and large-eddy simulations of turbulent free-surface flows. *Sixth international conference on numerical ship hydrodynamics*, Iowa City.

[20] ELLISON, T. H. 1960 A note on the velocity profile and longitudinal mixing in a broad open channel. *J. Fluid Mech.* **8**, 33–40.

[21] ENGEVIK, L. 2000 A note on the instabilities of a horizontal shear flow with a free surface. *J. Fluid Mech.* **406**, 337–346.

[22] FORTESCUE, G. E. & PEARSON, J. R. A. 1967 On gas absorption into a turbulent liquid. *Chem. Engng Sci.* **22**, 1163–1176.

[23] GERMANO, M. 1986 A proposal for a redefinition of the turbulence stresses in the filtered Navier-Stokes Equations. *Phys. Fluids* **29**, 2323–2324.

[24] GERMANO, M., PIOMELLI, U., MOIN, P. & CABOT, W. H. 1991 A dynamic subgrid-scale eddy viscosity model. *Phys. Fluids* A **3**, 1760–1765.

[25] GHARIB, M., DABIRI, D. & ZHANG, X. 1994 Interaction of small scale turbulence with a free surface. In *Free-Surface Turbulence* (ed. E. P. Rood & J. Katz), pp. 97–102. ASME.

[26] GHOSAL, S., LUND, T. S., MOIN, P. & AKSELVOLL, K. 1995 A dynamic localization model for large-eddy simulation of turbulent flows. *J. Fluid Mech.* **286**, 229–255.

[27] GOLDSTEIN, S. 1969 Fluid Mechanics in the first half of this century. *Ann. Rev. Fluid. Mech.* **1**, 1–28.

[28] HANDLER, R. A., SAYLOR, J. R., LEIGHTON, R. I. & ROVELSTAD, A. L. 1999 Transport of a passive scalar at a shear-free boundary in fully developed turbulent channel flow. *Phys. Fluids* **11**, 2607–2625.

[29] HANDLER, R. A., SWEAN, T. F. JR., LEIGHTON, R. I. & SWEARINGEN J. D. 1991 Length scales of turbulence near a free surface. *AIAA Paper* 91-1775.

[30] HANDLER, R. A., SWEAN, T. F. JR., LEIGHTON, R. I. & SWEARINGEN J. D. 1993 Length scales and the energy balance for turbulence near a free surface. *AIAA J.* **31**, 1998–2007.

[31] HARLOW, F. H. & WELCH, J. E. 1965 Numerical calculation of time-dependent viscous incompressible flow of fluid with free surface. *Phys. Fluids* **8**, 2182–2189.

[32] HARTEL, C., KLEISER, L., UNGER, F. & FRIEDRICH, R. 1994 Subgrid-scale energy transfer in the near-wall region of turbulent flows. *Phys. Fluids* **6**, 3130–3143.

[33] HINZE, J.O. 1975 *Turbulence.* McGraw-Hill.

[34] HODGES, B. R. & STREET, R. L. 1999 On simulation of turbulent nonlinear free-surface flows. *J. Comput. Phys.* **151**, 425–457.

[35] HUNT, J. N. 1954 The turbulent transport of suspended sediment in open channels. *Proc. R. Soc.* A **224**, 322–335.

[36] HUNT, J. C. R. & GRAHAM, J. M. R. 1978 Free-stream turbulence near plane boundaries. *J. Fluid Mech.* **84**, 209–235.

[37] JÄHNE, B. & HAUβECKER, H. 1998 Air-water gas exchange. *Ann. Rev. Fluid Mech.* **30**, 443–468.

[38] JOBSON, H. E. & SAYRE, W. W. 1970 Vertical transfer in open channel flow. *J. Hydraul. Div. ASCE* **96**, 703–724.

[39] KHOO, B. C., PATERA, A. T. & SONIN, A. A. 1989 Direct numerical simulation of pure vapor condensation at a turbulent liquid interface: an extracted-subdomain approach. In *Heat Transfer with Phase Change* (ed. I. S. Habib & R. J. Dallman), pp. 39–50. ASME.

[40] KHOO, B. C. & SONIN, A. A. 1992 Augmented gas exchange across wind-sheared and sheared-free air-water interfaces. *J. Geophys. Res.* **97**, 14413–14415.

[41] KIM, J. 1983 On the structure of wall-bounded turbulent flows. *Phys. Fluids* **26**, 2088–2097.

[42] KOMORI, S., MURAKAMI, Y. & UEDA, H. 1989 The relationship between surface-renewal and bursting motions in an open-channel flow. *J. Fluid Mech.* **203**, 103–123.

[43] KOMORI, S., MURAKAMI, Y. & UEDA, H. 1989 Detection of coherent structures associated with bursting events in an open-channel flow by a two-point LDV-measuring technique. *Phys. Fluids* A **1**, 339–348.

[44] KOMORI, S., NAGAOSA, N., MURAKAMI, Y., CHIBA, S., ISHII, K. & KUWAHARA, K. 1993 Direct numerical simulation of three-dimensional open-channel flow with zero-shear gas-liquid interface. *Phys. Fluids* **5**, 115–125.

[45] KOMORI, S., UEDA, H., OGINO, F. & MIZUSHINA, T. 1982 Turbulence structure and transport mechanism at the free surface in an open channel flow. *Intl J. Heat Mass Transfer* **25**, 513–521.

[46] KUMAR, S., GUPTA, R. & BANERJEE, S. 1998 An experimental investigation of the characteristics of free-surface turbulence in channel flow. *Phys. Fluids* **10**, 437–456.

[47] KWAK, D., REYNOLDS, W. C. & FERZIGER, J. H. 1975 Three-dimensional, time-dependent computation of turbulent flow. *Rep.* TF-5, Mech. Engng Dept., Stanford University.

[48] LAM, K. & BANERJEE, S. 1988 Investigation of turbulent flow bounded by a wall and a free surface. In *Fundamentals of Gas-Liquid Flows* (ed. E. Michaelides & M. P. Sharma), 29–38. ASME.

[49] LAM, K. & BANERJEE, S. 1992 On the condition of streak formation in a bounded turbulent flow. *Phys. Fluids* A **4**, 306–320.

[50] LEE, G. Y. & GILL, W. N. 1977 A note on velocity and eddy viscosity distributions in turbulent shear flows with free surfaces. *Chemical Engineering Science* **32**, 967–969.

[51] LEIGHTON, R. I., SWEAN, T. F., HANDLER, R. A. & SWEARINGEN J. D. 1991 Interaction of vorticity with a free surface in turbulent open channel flow. *AIAA Paper* 91-0236.

[52] LEONARD, A. 1974 Energy cascade in large-eddy simulation of turbulence fluid flows. *Adv. Geophys.* A **18**, 237–248.

[53] LESIEUR, M. 1997 *Turbulence in Fluids.* Kluwer.

[54] LESIEUR, M. & METAIS, O. 1996 New trends in large-eddy simulations of turbulence. *Ann. Rev. Fluid. Mech.* **28**, 45–82.

[55] LEVICH, V. G. 1962 *Physiochemical Hydrodynamics.* Prentice-Hall.

[56] LIDE, D. R. 2000 *Handbook of Chemistry and Physics.* CRC Press.

[57] LILLY, D. K. 1992 A proposed modification of the Germano subgrid-scale closure method. *Phys. Fluids* A **4**, 633–635.

[58] LIU, S., MENEVEAU, C. & KATZ, J. 1994 On the properties of similarity subgrid-scale models as deduced from measurements in a turbulence jet. *J. Fluid Mech.* **275**, 83–119.

[59] LOMBARDI, P., DE ANGELIS, V. & BANERJEE, S. 1996 Direct numerical simulation of near-interface turbulence in coupled gas-liquid flow. *Phys. Fluids* **8**, 1643–1665.

[60] LONGUET-HIGGINS, M. S. 1998 Instabilities of a horizontal shear flow with a free surface. *J. Fluid Mech.* **364**, 147–162.

[61] LUGT, H. J. & OHRING, S. 1994 The oblique rise of a viscous vortex ring toward a deformable free surface. *Meccanica* **29**, 313–329.

[62] MANGIAVACCHI, N., GUNDLAPALLI, R. & AKHAVAN, R. 1994 Dynamics of a turbulent jet interacting with a free surface. In *Free-Surface Turbulence* (ed. E.P.Rood & J.Katz), pp. 69–83. ASME.

[63] MARCUS, D. L. & BERGER, S. A. 1989 The interaction between a pair of counter-rotating potential vortices in vertical ascent and a free surface. *Phys. Fluids* A **1**, 1988–2000.

[64] MATTINGLY, G. E. & CRIMINALE, W. O. 1972 The stability of an incompressible two-dimensional wake. *J. Fluid Mech.* **51**, 233–272.

[65] McMillan, O. J., Ferziger, J. H. & Rogallo, R. S. 1980 Tests of new subgrid-scale models in strained turbulence. *AIAA Paper* 80-1339.

[66] Meneveau, C. & Katz, J. 2000 Scale-invariance and turbulence models for large-eddy simulation. *Ann. Rev. Fluid. Mech.* **32**, 1–32.

[67] Moin, P. & Mahesh, K. 1998 Direct numerical simulation: A tool in turbulence research. *Ann. Rev. Fluid. Mech.* **30**, 539–578.

[68] Moin, P. & Kim, J. 1985 The structure of the vorticity field in turbulent channel flow. Part 1. Analysis of instantaneous fields and statistical correlations. *J. Fluid Mech.* **155**, 441–464.

[69] Moin, P. & Kim, J. 1997 Tackling turbulence with supercomputers. *Sci. Am.* **276**, 62–68.

[70] Moin, P., Squires, K., Cabot, W. & Lee, S. 1991 A dynamic subgrid-scale model for compressible turbulence and scalar transport. *Phys. Fluids* A **3**, 2746–2757.

[71] Munk, W. H., Scully-Power, P. & Zachariasen F. 1987 Ships from space. *Proc. R. Soc. Lond.* A **412**, 231–254.

[72] Nagaosa, R. 1999 Direct numerical simulation of vortex structures and turbulent scalar transfer across a free surface in a fully developed turbulence. *Phys. Fluids* **11**, 1581–1595.

[73] Nakagawa, H. & Nezu, I. 1981 Structure of space-time correlation of bursting phenomena in an open channel flow. *J. Fluid Mech.* **104**, 1–43.

[74] Ohring, S. & Lugt, H. J. 1996 Interaction of an obliquely rising vortex ring with a free surface in a viscous fluid. *Meccanica* **31**, 623–655.

[75] Pan, Y. & Banerjee, S. 1995 A numerical study of free-surface turbulence in channel flow. *Phys. Fluids* **7**, 1649–1664.

[76] Papavassiliou, D. V. & Hanratty, T. J. 1997 Transport of a passive scalar in a turbulent channel flow. *Intl J. Heat Mass Transfer* **40**, 1303–1311.

[77] Perot, B. & Moin, P. 1995 Shear-free turbulent boundary layers. Part 1. Physical insights into near-wall turbulence. *J. Fluid Mech.* **295**, 199–227.

[78] Piomelli, U., Cabot, W. H., Moin, P. & Lee, S. 1991 Subgrid-scale backscatter in turbulent and transitional flows. *Phys. Fluids* A **3**, 1766–1771.

[79] PIOMELLI, U., YU, Y. & ADRIAN R. J. 1996 Subgrid-scale energy transfer and near-wall turbulence structure. *Phys. Fluids* **8**, 215–224.

[80] RASHIDI, M. 1997 Burst-interface interactions in free surface turbulent flows. *Phys. Fluids* **9**, 3485–3501.

[81] RASHIDI, M. & BANERJEE, S. 1988 Turbulence structure in free surface channel flows. *Phys. Fluids* **31**, 2491–2503.

[82] RASHIDI, M. & BANERJEE, S. 1990 Streak characteristics and behavior near wall and interface in open channel flows. *J. Fluids Engineering* **112**, 164–170.

[83] RASHIDI, M. & BANERJEE, S. 1990 The effects of boundary conditions and shear rate on streak formation and breakdown in turbulent channel flows. *Phys. Fluids* A **32**, 1827–1838.

[84] RASHIDI, M., HETSRONI, G. & BANERJEE, S. 1991 Mechanisms of heat and mass transport at gas-liquid interfaces. *Intl J. Heat Mass Transfer* **34**, 1799–1810.

[85] ROGALLO, R. S. & MOIN, P. 1984 Numerical simulation of turbulent flows. *Ann. Rev. Fluid. Mech.* **16**, 99–137.

[86] SALVETTI, M. V. & BANERJEE, S. 1995 *A priori* tests of a new dynamic subgrid-scale model for finite-difference large-eddy simulations. *Phys. Fluids* **7**, 2831–2847.

[87] SALVETTI, M. V., ZANG, Y., STREET, R. L. & BANERJEE, S. 1997 Large-eddy simulation of free-surface decaying turbulence with dynamic subgrid-scale models. *Phys. Fluids* **9**, 2405–2419.

[88] SARPKAYA, T. 1996 Vorticity, free surface, and surfactants. *Ann. Rev. Fluid. Mech.* **28**, 83–128.

[89] SHEN, L., TRIANTAFYLLOU, G. S. & YUE, D. K. P. 2000 Turbulent diffusion near a free surface. *J. Fluid Mech.* **407**, 145–166.

[90] SHEN, L., ZHANG, X., YUE, D. K. P. & TRIANTAFYLLOU, G. S. 1999 The surface layer for free-surface turbulent flows. *J. Fluid Mech.* **386**, 167–212.

[91] SMAGORINSKY, J. 1963 General circulation experiments with the primitive equations. Part I: The basic experiment. *Mon. Weather Rev.* **91**, 99–164.

[92] SONIN, A. A., SHIMKO, M. A. & CHUN, J.-H. 1986 Vapor condensation onto a turbulent liquid — I. The steady condensation rate as function of liquid-side turbulence. *Intl J. Heat Mass Transfer* **29**, 1319–1332.

[93] SPEZIALE, C. 1985 Galilean invariance of subgrid-scale stress models in the large-eddy simulation of turbulence. *J. Fluid Mech.* **156**, 55–62.

[94] SWEAN, T. F., JR., LEIGHTON, R. I., HANDLER, R. A. & SWEARINGEN, J. D. 1991 Turbulence modeling near the free surface in open channel flow. *AIAA Paper* 91-0613.

[95] TENNEKES, H. & LUMLEY, J. L. 1972 *A First Course in Turbulence.* The MIT Press.

[96] THEOFANOUS, T. G. 1984 Conceptual models of gas exchange. In *Gas Transfer at Water Surfaces* (ed. W. Brutsaert & G. H. Jirka), pp. 271–281. Reidel.

[97] THOMAS, N. H. & HANCOCK, P. E. 1977 Grid turbulence near a moving wall. *J. Fluid Mech.* **82**, 481–496.

[98] TRIANTAFYLLOU, G. S. & DIMAS, A. A. 1989 Interaction of two-dimensional separated flows with a free surface at low Froude numbers. *Phys. Fluids* A **1**, 1813–1821.

[99] TSAI, W. T. 1998 A numerical study of the evolution and structure of a turbulent shear layer under a free surface. *J. Fluid Mech.* **354**, 239–276.

[100] TSAI, W. T. & YUE, D. K. P. 1995 Effects of soluble and insoluble surfactant on laminar interactions of vortical flows with a free-surface. *J. Fluid Mech.* **289**, 315–349.

[101] UEDA, H., MOLLER, R., KOMORI, S. & MIZUSHINA, T. 1977 Eddy diffusivity near the free surface of open channel flow. *Intl J. Heat Mass Transfer.* **20**, 1127–1136.

[102] UZKAN, T. & REYNOLDS, W. C. 1967 A shear-free turbulent boundary layer. *J. Fluid Mech.* **28**, 803–821.

[103] VAN HAARLEM, B., BOERSMA, B. J. & NIEUWSTADT, F. T. M. 1998 Direct numerical simulation of particle deposition onto a free-slip and no-slip surface. *Phys. Fluids* **10**, 2608–2620.

[104] WALKER, D. T., LEIGHTON, R. I. & GARZA-RIOS, L. O. 1996 Shear-free turbulence near a flat free surface. *J. Fluid Mech.* **320**, 19–51.

[105] WILLERT, C. E. & GHARIB, M. 1997 The interaction of spatially modulated vortex pairs with free surfaces. *J. Fluid Mech.* **345**, 227–250.

[106] YOSHIZAWA, A. 1986 Statistical theory for compressible turbulent shear flows, with the application to subgrid modeling. *Phys. Fluids* **29**, 2152–2164.

[107] ZANG, Y., STREET, R. L. & KOSEFF, I. R. 1993 A dynamic mixed subgrid-scale model and its application to turbulence recirculation flows. *Phys. Fluids* A **5**, 3186–3196.

[108] ZHANG, C. 1996 Turbulent free-surface wakes behind towed model — experimental measurements, numerical simulations and stability analysis. PhD thesis, Department of Ocean Engineering, MIT.

[109] ZHANG, C., SHEN, L. & YUE, D.K.P 1999 The mechanism of vortex connection at a free surface. *J. Fluid Mech.* **384**, 207–241.